Molecular Density Functional Theory under homogeneous reference fluid approximation

Lu Ding

NNT : 2017SACLV004

THESE DE DOCTORAT
DE
L'UNIVERSITE PARIS-SACLAY
PREPAREE A
L'UNIVERSITE VERSAILLES SAINT-QUENTIN EN YVELINES

ECOLE DOCTORALE N°573
Interfaces : approches interdisciplinaires / fondements, applications et innovation

Spécialité de doctorat : chimie

Par

Mlle Lu Ding

Théorie de la Fonctionnelle de la Densité Moléculaire
Sous l'Approximation du Fluide de Référence Homogène

Thèse présentée et soutenue à la Maison de la Simulation, Saclay ; le 27 février 2017 :

Composition du Jury :

M. LUC BELLONI	CEA Saclay	Directeur de these
M. Rodolphe VUILLEUMIER	Université Pierre et Marie Curie	Rapporteur
M. Olivier BERNARD	CNRS	Rapporteur
M. Bernard ROUSSEAU	CNRS	Président du jury
Mme Rosa RAMIREZ	Université d'Evry-Val-d'Essonne	Examinatrice
M. Daniel BORGIS	CNRS	Directeur de thèse
M. Maximilien LEVESQUE	CNRS	Co-directeur de thèse

Université Paris-Saclay
Espace Technologique / Immeuble Discovery
Route de l'Orme aux Merisiers RD 128 / 91190 Saint-Aubin, France

Molecular Density Functional Theory

under homogeneous reference fluid approximation

LU DING

Under the direction of
DANIEL BORGIS, LUC BELLONI & MAXIMILIEN LEVESQUE

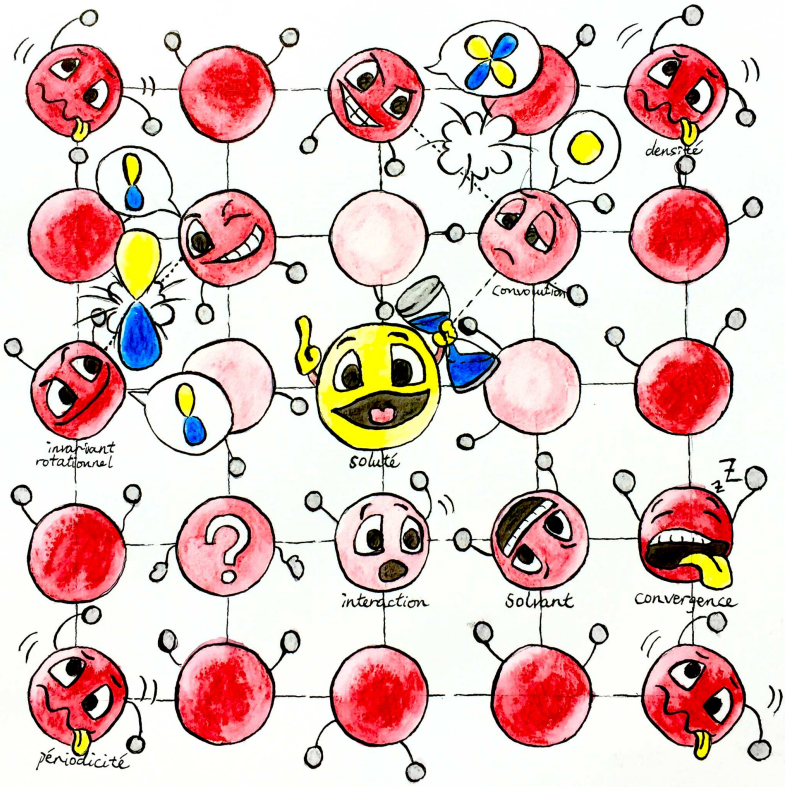

AN ADVANCED MOLECULAR-SCALE LIQUID THEORY
FOR SOLVATION PROPERTY PREDICTION

16 November 2016 @ Maison de la Simulation, CEA Saclay

When you are studying any matter, or considering any philosophy, ask yourself only,
what are the facts and what is the truth that the facts bear out.
Never let yourself be diverted either by what you wish to believe, or by what you think
would have beneficent social effects if it were believed.
But look only, and solely, at what are the facts.

— Bertrand Russell

Acknowledgements

First of all, I would like to express my most respectful gratitude to my thesis advisors, Daniel Borgis and Luc Belloni, who have developed the main theories used in this thesis and whose great knowledge of liquid theory as well as the genius way of thinking and explaining have given me a solid guide for doing this research. I would also like to thank them for their tireless work in correcting this manuscript.

I'm also grateful to Maximilien Levesque, the other main developer of MDFT who joined the supervision of my thesis and the correction of this manuscript. Thanks as well for sharing some results and data that have proven useful to my research.

I wish to acknowledge all the great minds willing to evaluate and give ideas about my work: Rodolphe Vuilleumier, Olivier Bernard, Bernard Rousseau, Rosa Ramirez; thank you for agreeing to be part of the jury of this thesis.

As a master student issued from pure chemistry speciality, a lack of knowledge about Informatics brought to me a lot of difficulties. I would like to express my sincere gratitude to my colleagues Pierre Kestener, Matthieu Haefele, and Yacine Ould-Rouis for their huge aid in Informatics and very useful advices during this thesis.

This thesis was produced at *Maison de la Simulation, CEA Saclay*, financially supported by the scholarship IDEX-CEA. I acknowledge all the organizations and staff that gave me the chance to have this three-year experience.

I am also grateful to Thomas Wiggins for help in correcting the huge amount of grammar faults in this manuscript.

Looking back through all those years of schooling, I'm deeply indebted to my tutors during my bachelor and master, respectively Mr. Hongwei Tan and Mrs. Michelle Gupta, whose clear logic and warm encouragement gave me all that I needed to be in love with theoretical chemistry.

And I should also thank my friends Yiting Cui, Qirong Zhu, Yu Wu and Bo Gao for taking care of me at the very end of the thesis when I was seriously ill.

Finally I would like to thank my father, who made the right decision to send me here in France and support me in every aspect.

Abstract

Solvation properties play an important role in chemical and bio-chemical issues. The molecular density functional theory (MDFT) is one of the frontier numerical methods to evaluate these properties, in which the solvation free energy functional is minimized for an arbitrary solute in a periodic cubic solvent box. In this thesis, we work on the evaluation of the excess term of the free energy functional under the homogeneous reference fluid (HRF) approximation, which is equivalent to hypernetted-chain (HNC) approximation in integral equation theory. Two algorithms are proposed: the first one is an extension of a previously implemented algorithm, which makes it possible to handle full 3D molecular solvent (depending on three Euler angles) instead of linear solvent (depending on two angles); the other one is a new algorithm that integrates the molecular Ornstein-Zernike (OZ) equation treatment of angular convolution into MDFT, which in fact expands the solvent density and the functional gradient on generalized spherical harmonics (GSHs). It is shown that the new algorithm is much more rapid than the previous one. Both algorithms are suitable for arbitrary three-dimensional solute in liquid water, and are able to predict the solvation free energy and structure of ions and molecules.

Résumé

Les propriétés de solvatation jouent un rôle important dans les problèmes chimiques et biochimiques. La théorie fonctionnelle de la densité moléculaire (MDFT) est l'une des méthodes frontières pour évaluer ces propriétés, dans laquelle une fonction d'énergie libre de solvatation est minimisée pour un soluté arbitraire dans une boîte de solvant cubique périodique. Dans cette thèse, nous travaillons sur l'évaluation du terme d'excès de la fonctionnelle d'énergie libre sous l'approximation du fluide de référence homogène (HRF), équivalant à l'approximation de la chaîne hypernettée (HNC) dans la théorie des équations intégrales. Deux algorithmes sont proposés : le premier est une extension d'un algorithme précédent, qui permet de traiter le cas d'un solvant moléculaire à trois dimensions (en fonction de trois angles d'Euler) au lieu d'un solvant linéaire (selon deux angles) ; L'autre est un nouvel algorithme qui intègre le traitement de la convolution angulaire de l'équation Ornstein-Zernike (OZ) moléculaire dans MDFT, et en fait développe la densité du solvant et le gradient fonctionnel en harmoniques sphériques généralisées (GSHs). On montre que le nouvel algorithme est beaucoup plus rapide que le précédent. Les deux algorithmes sont appropriés pour des solutés arbitraires tridimensionnels dans l'eau liquide, et pour prédire l'énergie libre et la structure de solvatation d'ions et de molécules.

Contents

1 INTRODUCTION 1

1.1 Modeling of solvent effects, 1
1.2 Scope of this thesis, 3

I STATE OF THE ART: SOLVATION, MODELS AND METHODS 5

2 MODEL OF SOLUTION SYSTEM 7

2.1 Continuum solvation models, 7
2.1.1 Poisson-Boltzmann methods, 8
2.1.2 Born / Onsager / Generalized Born models, 9
2.2 Model potential of explicit molecules, 10
2.2.1 Interaction of spherical particle, 11
2.2.2 Site-site interactions, 12
2.2.3 Multipole and spherical harmonic expansion, 13
2.2.4 SPC/E water model, 13
2.2.5 Flexible and polarizable models, 14
2.3 Model of solute, 15

3 STATISTICAL MECHANICS OF ATOMIC FLUIDS 16

3.1 Hamiltonian and ensemble properties, 16
3.2 Functional derivatives and distribution functions, 17
3.3 Classical density functional theory, 19
3.4 Integral equation theory, 20
3.5 Equivalence between cDFT and IET for a dilute solution system, 21

4 APPROACH TO MOLECULAR SOLVENTS 22

4.1 Molecular density functional theory, 22
4.1.1 The ideal term, 22
4.1.2 The external term, 23
4.1.3 The excess term, 24
4.2 Molecular integral equation theory, 25
4.2.1 Translational and rotational invariance, 25
4.2.2 Blum's reduction of molecular OZ equation, 26

5 CODE MDFT 28

5.1 Supercell discretization, 28
5.2 Minimizer L-BFGS-B, 28
5.3 Treatment to avoid unphysical density, 29
5.4 Fast Fourier transform, 29

II THEORY: HRF APPROXIMATION, FOR MOLECULAR SOLVENT 31

6 ANGULAR INTEGRATION IN EXCESS FUNCTIONAL 33

6.1 Using full intermolecular DCF, 34
6.1.1 Zero-order interpolation of DCF, 35
6.1.2 Linear interpolation of DCF, 36
6.2 Direct calculation of DCF from rotational invariant projections, 36
6.2.1 Using projections in the form of $\hat{c}^{mnl}_{\mu\nu}(k)$, 37
6.2.2 Using projections in the form of $\hat{c}'^{mn}_{\mu\nu,\chi}(k)$, 37

7 ANGULAR CONVOLUTION, A BETTER ALGORITHM 38

7.1 Angular convolution using Blum's reduction, 38
7.2 Fast generalized spherical harmonic transform, 40
7.2.1 Equivalence of order in angular quadratures and projections, 40
7.2.2 Integration of Φ, Ψ using FFT, 41
7.3 Operational algorithm, 43
7.3.1 Commutativity between operations, 44
7.3.2 Reduction by symmetry, 45

8 SOLVATION PROPERTIES 47

8.1 Free energy correction for single ions, 47
8.1.1 Correction of type B, 47
8.1.2 Correction of type C, 48
8.2 Solvation structure, 48
8.2.1 Radial and site-site distribution function, 49
8.2.2 Radial polarization function, 49
8.2.3 Rotational invariant expansion, 50
8.2.4 Equivalence between the curves, 50

III IMPLEMENTATION 51

9 ALGORITHMS AND BRANCHES 53

9.1 Branches "naive", 54
9.2 Branches "convolution", 55
9.3 Testing branches for $n_{\max} = 1$, 55
9.4 Other paths, 55

10 NUMERICAL ACCURACY 56

10.1 Significant digits and curve resolution, 56
10.2 Generalized spherical harmonics transform, 57
10.2.1 $m_{\max}$ and $n_{\max}$ of projections, 58
10.2.2 From ρ to γ, 58
10.3 Comparison between branches, 60
10.3.1 Difference in energy evaluation, 61
10.3.2 A single k-kernel, 62

10.3.3 k-border effect, 62
10.3.4 Difference in γ for "naive" and "convolution" methods, 63
10.4 Intrinsic variation of free energy, 64
10.5 Series of charged LJ centers, 66
10.5.1 Box length dependance and charge dependance of free energy, 66
10.5.2 Comparison with IET after corrections, 69
10.5.3 Dependence on $m_{\max}$ and $n_{\max}$, 70
10.6 Uncharged LJ centers, 73
10.7 Linear solutes, 74
10.8 First conclusion, 75

11 COMPUTING PERFORMANCE 77

11.1 FFT, 77
11.2 FGSHT, 78
11.3 k-kernel, 79
11.4 Entire iteration of $\mathcal{F}_{\text{exc}}$ evaluation, 80
11.4.1 "naive" methods and "convolution_pure_angular", 80
11.4.2 "convolution_standard" and "convolution_pure_angular", 81
11.4.3 "convolution_standard" and "convolution_asymm", 81
11.4.4 Distinction of $m_{\max}$ and $n_{\max}$, 82
11.5 Global view of the code performance, 82

IV APPLICATIONS 83

12 COMPARISON TO MD SIMULATION 85

12.1 LJ centers, 85
12.2 Charged CH_4 series, 86
12.3 Solvation free energy of single ions, 86
12.4 Small molecules, 88

V CONCLUSION AND PERSPECTIVES 95

13 CONCLUSION 97

14 PERSPECTIVES 99

14.1 Reduce memory footprint in MDFT, 99
14.2 Site-based grid, 99
14.3 Theories beyond the HRF approximation and other improvements, 99
14.4 MDFT Viewer, 100
14.5 Application to real biological systems, and entropy, 100

VI APPENDIX 101

A BASICS OF ALGORITHM COMPLEXITY 103

B DIRECT CORRELATION FUNCTION OF WATER 104

B.1 Dipole DCF from molecular dynamics simulation, 104
B.2 DCF projections from bulk Monte Carlo simulation, 105
B.3 Comparison between DCFs, 105

C ERROR EVALUATION OF INTERPOLATION STRATEGIES FOR DCF IN LOCAL FRAME 107

D ANGULAR CONVOLUTION USING BLUM'S REDUCTION 109

E EQUIVALENCE OF QUADRATURE-PROJECTION ORDER 112

E.1 Gaussian quadrature, 112
E.2 Angular integration in GSHT, 112

F ROTATIONAL INVARIANT EXPANSION 114

F.1 Orthogonality of Φ, 114
F.2 Rotational invariance of Φ, 115
F.3 Transform in local frame, 116
F.4 Transform in fixed frame, 118
F.5 Symmetry, 119
F.5.1 Symmetric rules of $F(\boldsymbol{\omega}_1, \boldsymbol{\omega}_2)$ in intermolecular form, 119
F.5.2 Symmetric rules of rotational invariant projections, 119

G CALCULATION OF ROTATION MATRIX ELEMENTS $R^m_{\mu\mu'}$ BY RECURRENCE 121

G.1 Case of $m_{\max} \leq 1$, 121
G.2 Case of $m_{\max} > 1$, 122

H PROPERTIES OF WIGNER 3J-SYMBOL AND GSH 124

H.1 Properties of Wigner 3j-Symbol, 124
H.2 Properties of GSH, 125
H.3 Convention of GSH, 126

BIBLIOGRAPHY 127

List of Figures

Figure 1.1 The solvation process, 2
Figure 2.1 Continuum solvent model, 7
Figure 2.2 Definition of cavity surfaces, 8
Figure 2.3 Euler angles, 11
Figure 2.4 LJ pair potential, 12
Figure 2.5 Water models, 13
Figure 2.6 Interactions in a flexible model, 14
Figure 2.7 Hierarchy of solute models, 15
Figure 4.1 Solute charge density projected onto grids, 23
Figure 5.1 Main structure of code MDFT, 29
Figure 6.1 Molecules 1 and 2 in different coordinate systems, 33
Figure 6.2 Rotation matrices, 34
Figure 6.3 Rotation to k-frame, 34
Figure 6.4 $\phi_1 - \phi_2$ distribution, 36
Figure 7.1 Indices arrangement in a complete forward-backward FFT-2D process of m'×m elements, 43
Figure 7.2 Commutativity of operations, 44
Figure 7.3 Distribution of points to be calculated according to symmetry in a 2D plan, 46
Figure 8.1 IQ model and summation scheme, 48
Figure 9.1 Process "find equilibrium density" in MDFT, 53
Figure 9.2 Possible algorithms for γ evaluation, 53
Figure 10.1 RDF with different resolution parameter, 57
Figure 10.2 The minimum value of $\Delta\rho(\mathbf{r},\mathbf{\Omega})/\rho_0$ after a forward-backward GSHT process, 60
Figure 10.3 $\rho_{0\nu}^{0nl}(r)$ and $\gamma_{0\nu}^{0nl}(r)$ of an artificial charged LJ center $CH_4^{+0.4}$, 61
Figure 10.4 A k-kernel, 62
Figure 10.5 k-border effect, 63
Figure 10.6 Absolute differences in $\hat{\gamma}(\mathbf{k},\mathbf{\Omega})$ and $\gamma(\mathbf{r},\mathbf{\Omega})$, 64
Figure 10.7 Comparison of projections $\gamma_{0\nu}^{0nl}(r)$ for branches "naive_standard" and "convolution_standard", 65
Figure 10.8 Space-grid and Ψ dependence of code MDFT, 65
Figure 10.9 Original free energy of charged CH_4, "naive_nmax1", 67
Figure 10.10 Original free energy of charged CH_4, "naive_interpolation" with DCF of $n_{\max} = 5$, 68
Figure 10.11 Original free energy of charged CH_4, "convolution_standard" with DCF of $n_{\max} = 1$, 68
Figure 10.12 Quadratic charge dependence of free energy in CH_4^q series, 69
Figure 10.13 Free energy of charged CH_4 compared to IET, without P-scheme correction, 69
Figure 10.14 Free energy difference of CH_4^q series compared to IET, with all corrections, 70
Figure 10.15 Free energy of CH_4^q series, with all corrections, 70

Figure 10.16 Free energy of $CH_4^{\mathfrak{q}}$ series (with corrections) for different $n_{\max}$ ($m_{\max} = 5$), 71
Figure 10.17 The projections $\rho_{0\nu}^{0nl}(r)$ of some selected charges of $CH_4^{\mathfrak{q}}$ series comparing to IET, 72
Figure 10.18 RDF and RPF of some selected charges of $CH_4^{\mathfrak{q}}$ series with different $m_{\max}$ and $n_{\max}$, 73
Figure 10.19 Test linear solutes, 74
Figure 10.20 The projections $\rho_{\mu\nu}^{mnl}(r)$ of CO_2 comparing to IET, 75
Figure 11.1 Timing of FFT for real-to-complex and complex-to-complex processes with respect to grid number N, 77
Figure 11.2 Timing of real-to-complex FFT processes with respect to its complex-to-complex process of the same grid number N, 78
Figure 11.3 Computing time of GSHT and FGSHT, 78
Figure 11.4 Timing of real-to-complex FGSHT processes with respect to its complex-to-complex process of the same $m_{\max}$ and $n_{\max}$, 79
Figure 11.5 Timing of a k-kernel, 79
Figure 11.6 Entire iteration of $\mathcal{F}_{\text{exc}}$ evaluation, 80
Figure 11.7 Performance comparison of "convolution_standard" and "convolution_pure_angular", 81
Figure 11.8 Performance comparison of "convolution_standard" and "convolution_asymm", 81
Figure 11.9 Performance comparison of "convolution_standard" for $m_{\max} = n_{\max}$ and $m_{\max} = 5$, 82
Figure 11.10 Timing of the whole $\mathcal{F}$ iteration, 82
Figure 12.1 RDF of rare gases compared to MD result, 85
Figure 12.2 RDF of charged CH_4 series compared to MD result, 86
Figure 12.3 Test solutes, 89
Figure 12.4 Site-O RDF of test solutes, 91
Figure 12.5 Volume slice of solvent number density $n(\mathbf{r})$ for pyrimidine, 94
Figure 12.6 Iso-surface of solvent number density $n(\mathbf{r}) = 2.4$ for test water molecules, 94
Figure 14.1 Site-site grid model, 100
Figure A.1 Function growth, 103
Figure B.1 Comparison between DCF projections, 106
Figure C.1 Error of finding $\hat{c}(\mathbf{k}, \mathbf{\Omega}_1, \mathbf{\Omega}_2)$ by interpolation, 108
Figure F.1 Symmetry operations of a 2-molecule system, 119

List of Tables

Table 1.1 Solvation theories, 3
Table 2.1 Structural parameters of SPC and SPC/E water, 14
Table 7.1 Number of FE needed by OZ equation of different form, 40
Table 9.1 Branch option in MDFT, 54
Table 10.1 Minimized free energy given by different convergence criteria, 56
Table 10.2 Maximum absolute error $E_a^{\max}$ of some function $f(\mathbf{\Omega})$ introduced by a forward-backward GSHT process, 59
Table 10.3 Minimized free energy via different branches MDFT, 60

Table 10.4 Parameters of charged CH_4 LJ centers for test usage, 66
Table 10.5 Methods and parameters for charged CH_4 series test, 66
Table 10.6 Free energy of CH_4^q series (with corrections) for different $m_{\max}$ and $n_{\max}$, 71
Table 10.7 Free energy of rare gases, 74
Table 10.8 Parameters of test solutes, 74
Table 10.9 Free energy of solutes, 75
Table 11.1 Timing of loop k, 80
Table 12.1 Free energy and first maximum of ion-water oxygen RDF for alkali and halide ions from experimental and MD simulation results, 87
Table 12.2 Free energies and first RDF maximum of single ions from MDFT results, 87
Table 12.3 Parameters of test solutes, 90

Notations

Ω	Grand potential $[\mathrm{kJ}\cdot\mathrm{mol}^{-1}]$
Ξ	Grand partition function, dimensionless
F	Helmholtz free energy $[\mathrm{kJ}\cdot\mathrm{mol}^{-1}]$
$\mathcal{F}[\rho]$	Solvation free energy functional $[\mathrm{kJ}\cdot\mathrm{mol}^{-1}]$
$\rho(\mathbf{r},\mathbf{\Omega})$	Density variable of solvent $[\mathrm{Å}^{-3}]$
$\mathbf{\Omega}$	Orientation variable in laboratory coordinate system, $\mathbf{\Omega}\equiv(\Theta,\Phi,\Psi)$
$\boldsymbol{\omega}$	Orientation variable in intermolecular coordinate system, $\boldsymbol{\omega}\equiv(\theta,\phi,\psi)$
$n(\mathbf{r})$	Number density of solvent $[\mathrm{Å}^{-3}]$, $n(\mathbf{r})=\int \mathrm{d}\mathbf{\Omega}\rho(\mathbf{r},\mathbf{\Omega})$
ρ_0	Bulk solvent angular density, $n_0=(\int \mathrm{d}\mathbf{\Omega})\,\rho_0$ is the bulk solvent number density, both of unity $[\mathrm{Å}^{-3}]$; in this thesis, $n_0=0.0332891$ is used as given by the original code
$\mathcal{F}_{\mathrm{id}}[\rho]$	Ideal free energy functional $[\mathrm{kJ}\cdot\mathrm{mol}^{-1}]$
$\mathcal{F}_{\mathrm{ext}}[\rho]$	External free energy functional $[\mathrm{kJ}\cdot\mathrm{mol}^{-1}]$
V_{ext}	External potential imposed by the solute $[\mathrm{kJ}\cdot\mathrm{mol}^{-1}]$
μ	Chemical potential of unity $[\mathrm{kJ}\cdot\mathrm{mol}^{-1}]$
$\mathcal{F}_{\mathrm{exc}}[\rho]$	Excess free energy functional $[\mathrm{kJ}\cdot\mathrm{mol}^{-1}]$
γ	Normalized gradient of excess free energy functional, dimensionless
g	Pair distribution function (PDF), dimensionless
h	Pair correlation function (PCF), or total correlation function (TCF) in certain references, dimensionless
c	Direct correlation function (DCF), dimensionless
$R^m_{\mu'\mu}$	Generalized spherical harmonics (GSH)
$\Phi^{mnl}_{\mu u}$	Rotational invariant bases defined in appendix F
$\mathbf{P}$	Polarization $[\mathrm{Å}^{-3}]$
q_e	Elementary charge, $q_e=1.602176565\cdot10^{-19}$ [C]

q	Charge of unity [C]; $\mathfrak{q} = q/q_e$ is the number charge, dimensionless
ε_0	Vacuum permittivity, $\varepsilon_0 = 8.854187817 \cdot 10^{-12}\,[\mathrm{C}^2 \cdot \mathrm{J}^{-1} \cdot \mathrm{m}^{-1}]$
ε	Dielectric constant (relative permittivity) of solvent, dimensionless
N_A	Avogadro constant, $N_\mathrm{A} = 6.02214129 \cdot 10^{23}\,[\mathrm{mol}^{-1}]$
f_Q	$f_Q = q_e^2 10^{-3} N_\mathrm{A}/(4\pi\varepsilon_0 10^{-10})$, electrostatic potential unit so that $f_Q \cdot \mathfrak{q}^2/r$ is in $[\mathrm{kJ} \cdot \mathrm{mol}^{-1}]$, where $\mathfrak{q}$ is the number charge without unity, r in [Å]
K_B	Boltzmann constant, $K_\mathrm{B} = 1.3806488 \cdot 10^{-23}\,[\mathrm{J} \cdot \mathrm{K}^{-1}]$
β	$\beta = (K_\mathrm{B} T)^{-1}$, reciprocal of the thermodynamic temperature $[\mathrm{mol} \cdot \mathrm{kJ}^{-1}]$

Acronyms

DCF direct correlation function

DFT discret Fourier transform, also refers to density functional theory

FE function evaluation

FFT fast Fourier transform

FGSHT fast generalized spherical harmonic transform

GSH generalized spherical harmonic

GSHT generalized spherical harmonic transform

HNC hypernetted-chain (approximation)

HRF homogeneous reference fluid (approximation)

IET integral equation theory

MC Monte Carlo

MD molecular dynamics

MDFT molecular density functional theory

MOZ molecular Ornstein-Zernike (equation)

MRSO molecule rotation symmetry order, $s = 1$ or 2 according to symmetry axis

OZ Ornstein-Zernike (equation)

PCF pair correlation function

PDF pair distribution function

QM quantum mechanics

RDF radial distribution function

RPF radial polarization function

1 Introduction

This thesis aims to develop an original numerical toolkit for physical chemists and structural biologists based on the molecular density functional theory (MDFT), which makes it possible to predict the solvation properties of arbitrary molecular objects in arbitrary molecular solvents (mainly water) efficiently and with microscopic accuracy. The introduction will seek to highlight the objective of this thesis and help explain such topics as why theorists are interested in the nature of solvation, what are the present computing trends in solvation simulations, and where our work situates in this frame of solvation theories.

1.1 Modeling of solvent effects

Solvation is a fundamental phenomenon in chemistry. The chemical behavior of numerous systems strongly depends on the nature of solvation; for example, this is the case for the reaction mechanisms in metal-organic reacting centers [1, 2], or pharmaceutical studies [3–5]. The solvation properties demanded by scientific studies are highly diverse; they include the free energy of solvation, solubility, concentration, partition coefficient, saturated vapor pressure, pH value, the 3D solvation structure, etc. Overall, interest in these solvation properties touches many fields of study such as chemistry and biochemistry, as well as pharmaceutical, environmental, and agrochemical industries. Unlike the well-studied quantum mechanics (QM) for chemical interactions at a microscopic scale, and the finite element models for macroscopic physical processes, the theories of solvation lie in-between these description scales and are still under development, owing to the ambiguous compromise between accuracy and computing cost, and the rapid development of computer hardware which makes complicated calculations more and more accessible. In a word, the studies in this domain are quite vibrant.

To change a phenomenon into a model, we must first understand its process. Solvation is defined as the process of moving a molecule from the gas phase (or vacuum) to a condensed phase (figure 1.1), which builds a stabilizing interaction with the solute (or solute moiety, e.g., residues, interfaces, etc.) [6]. Such interactions are mostly classical interactions, involving electrostatic and van der Waals forces; but there are also additional specific chemical effects such as hydrogen bond formation, and quantum effects for some small solvent molecules whose vibrational or rotational energy states are at the same magnitude as $k_{\mathrm{B}}T$, as well as other effects, etc.

As not all kinds of interactions are important in applications, different models and methods have been developed according to the usage.

For most of the 20th century, the study of solvation effects has been dominated by continuum (implicit) models [7, 8], which mostly rely on the continuum dielectric description of the solvent and are not costly in terms of computation resources. They provide an accurate way to treat the strong, long-range electrostatic interactions which dominate many solvation phenomena, but lack detailed information on the first solvation shell. This information mainly includes the cavity formation energy and solute-solvent van der Waals interactions, which are often roughly treated by introducing an artificial form of cavity that links to the form of the solute. The methods for testing electrostatic

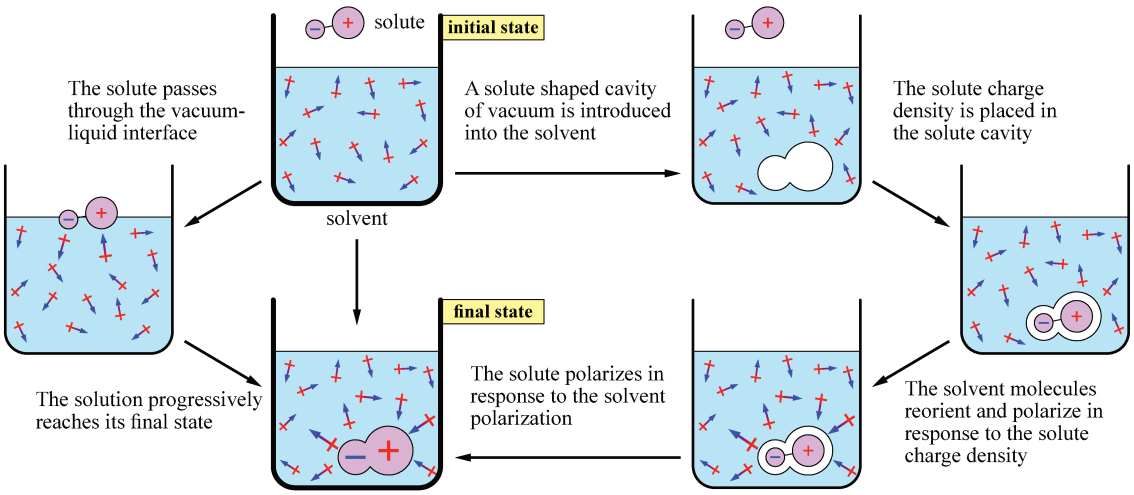

Figure 1.1: The solvation process. A thermodynamic system, whose properties only depend on the initial and final states, can go through different paths. The physical process of solvation (left path) takes the solute from vacuum into bulk solvent, progressively passing through the vacuum-liquid interface. Theoretically, the solvation energy is defined as the energy consumed in such a process. In theoretical studies, the process can also be decomposed into some artificial unphysical process (right path), involving the growth of an uncharged solute-sized cavity within the bulk solvent, the transfer of the solute charge distribution from vacuum into cavity, and the interaction between the solute and solvent.

interactions include the Generalized Born (GB) approximation or, for better estimates, Poisson-Boltzmann (PB) calculations. These are widely integrated within QM calculations by adding extra solvation terms onto the Fock or Kohn-Sham operator [9, 10]. However, the improper treatment of the first shell, where the microscopic interactions are primarily located, often introduces potentially huge errors in free energy evaluation, especially for polar solvents (such as water), despite the accuracy that the QM calculation alone can achieve. Therefore, classical molecular simulations, which describe the individual solvent molecules explicitly (explicit solvent), particularly the molecular dynamics (MD) and Monte Carlo method (MC), have become the alternative solution during the last few decades. They generate trajectories and configurations, and from there estimate free energy changes by statistical mechanical techniques, such as free energy perturbation (FEP) theory or thermodynamic integration (TI) [11]. These calculations are very demanding in computing cost, due to the need for numerous (hundreds or thousands) solvent molecules to form a realistic model, and an even greater number of configurations (millions) in order to be statistically significant.

Recently, a third domain of theory to describe solvents based on the statistical mechanics of fluids has been growing rapidly. It mainly involves the integral equation theory (IET), and the classical density functional theory (cDFT) for liquids. These approaches are capable of giving the molecular nature of the first solvation shell, not by calculating all the instantaneous micro-states with respect to time, but rather by theoretically integrating over positions and momenta. Therefore, they are orders of magnitude faster than the simulations done by micro-states.

The integral equation theory focuses on solving the Ornstein-Zernike (OZ) equation with a specific closure equation [12, 13]. It was initially limited to so-called “simple liquids” - a system of spherical particles. The extension to molecular fluids, composed of polyatomic molecules with non-spherical shapes, was done in two different directions. On the one hand, Chandler and Andersen in 1971 [14] developed the reference interaction site

model (RISM), which discretizes the distribution and correlation functions into site-site functions, and solves somewhat phenomenological OZ and closure equations in a matrix form [15]. On the other hand, Blum [16–18], Fries and Patey [19] extend the OZ equation into a full molecular form, where the distribution and correlation functions depend on both position and orientation. In their theory, the orientation part of OZ equation is simplified by expanding the distribution and correlation functions onto rotational invariants, which can be expressed in terms of Wigner generalized spherical harmonics.

The classical density functional theory approach deals with inhomogeneous liquids, and uses the same variation principle and minimization strategy [20–22] as electronic density functional theory (eDFT) for electron-electron interactions. The latter has received immense success in computational chemistry. Classical DFT gives the solvation free energy of the grand potential (usually named as free energy for simplification) and the equilibrium solvent density by minimizing the free energy functional of the solvent density in the presence of a given external potential. Borgis and collaborators [23–32] have recently generalized it into the molecular case, leading to molecular density functional theory (MDFT), where the solvent density depends on both position and orientation, $\rho(\mathbf{r}, \mathbf{\Omega})$. The main theoretical difficulty lies in the definition of well-funded and reliable functionals of the excess free energy $\mathcal{F}_{\text{exc}}[\rho]$, accounting for the geometric complexity of the solvent molecule. Some recent research has shown that MDFT is capable of describing linear solvents like acetonitrile, but still has some caveats for the most complex solvent, water [32]. MDFT can be proven as mathematically equivalent to the two-component molecular IET, in the limit that the functional is continuous (grid infinitely fine) and in an infinite system.

The majority of work of all these theories has been focused on water, since it is one of the most difficult systems to model due to its molecular geometry, unavoidable multibody character, quantum effects, and hydrogen bonds, to name a few. The importance of including instantaneous polarization in potential functions is also an issue [33, 34]. However, since polarizable force fields are not yet in common use, the simulations by micro-states and the liquid theory which feed on force fields also have their own limits, compared to the continuum model which can be totally polarizable. The advantages and disadvantages of each branch of theory are listed in table 1.1.

THEORY	SPEED	LONG-RANGE	FIRST-SHELL	POLARIZABLE SOLVENT
Continuum model	fast	yes	no	fully
Classical molecular simulations	costly	yes	yes	partially, very costly
Theory of liquids	fast	yes	yes	partially

Table 1.1: Solvation theories

1.2 SCOPE OF THIS THESIS

This thesis aims at developing the theory and the code of MDFT, focusing on the generalization and algorithmic acceleration of the excess free energy functional $\mathcal{F}_{\text{exc}}$ evaluation under homogenous reference fluid (HRF) approximation, which will be discussed in detail in later chapters.

Chapter I reviews a selection of models and methods to describe solvent effects. It includes the implicit and explicit models, the basics of liquid-state theory, as well as its two frontier research domains, MDFT and IET. Some details of the code MDFT, associated to the MDFT approach, on which all the developments of this thesis are based, are also included.

Chapter II presents all the theory developed and newly used in this thesis. Two algorithms for the excess energy functional evaluation under HRF approximation are proposed. One is an extension of the previous algorithm which could be applied to only linear solvents (or linearized molecular solvents), to a full 3D molecular solvent case; while the other is a new algorithm that integrates the molecular OZ equation treatment of angular convolution into MDFT. The solvation properties that the code generates are also presented, mainly containing the corrections of free energy and solvent structure profiles.

Chapter III reports all the implementation results, which are divided into two aspects: the "accuracy", which involves the error evaluations, comparisons between algorithms, and with IET results; and the "performance", which evaluates the computing cost, from the parts of the code to the entire branches.

Chapter IV gives applications to some LJ centers, ions and small molecules. Some works that remain unachieved are put in the perspectives.

Chapter I

State of the Art: Solvation, Models and Methods

This chapter gives a brief review of all the basic concepts and previous work that this thesis is based on.

In section 2, we begin by introducing the frequent models of solvent in a simulation, from the simplest implicit continuum model to the most complex explicit one. The overview of these models then helps to understand the choice of description scale used in our study, as well as its limits.

Once the model is chosen, all the theories become mathematical problems. Section 3 reviews some basic concepts of statistical mechanics for liquids (i.e. theory of liquids), which present some brief formalisms deduced for an atomic solvent model. Two frontier approaches are introduced with a few deductions: the classical density functional theory (cDFT), and the integral equation theory (IET). A mathematical equivalence between these two theories is also presented.

The following section 4 gives the extension of the two theories to the molecular solvent case, i.e. the molecular density functional theory (MDFT) that this thesis works upon, and the molecular Ornstein-Zernike (MOZ) approach for IET. The equivalence between these two theories gave us the idea to use the expansion techniques in IET to serve MDFT.

Section 5 gives some supplementary presentation of the initial code MDFT, which the development of this thesis is based on.

2

Model of Solution System

Computing models of solvents are broadly divided into two types: those treating the solvent as a continuous medium (implicit models) and those describing the individual solvent molecules (explicit models). In the continuum model, the solvent is characterized by the dielectric constant ε and contains an artificially shaped cavity. The explicit models can have more specific microscopic scales. Within the scope of classical mechanics, the most detailed (and thus the most expensive) methods involve flexible and polarizable explicit models, while in computational chemistry, less detailed models often have wider usage (for example, the proteins are treated in the unity of residues). As the theory of liquids was initially established for spherical atom-like solvent particles, the model adopted by such a theory is a rigid entity carrying distributed point charges, characterized by their position and orientation, i.e. there is no internal movement considered. This approximation has been proven reasonable [13]. There also exist models in which the scale lies somewhere between the implicit and explicit models; for example, so-called coarse-grained models [35], which gather groups of atoms into a single interaction site.

In this section, we will give a brief introduction of the implicit model in order to facilitate later discussion on solvation free energy corrections. We will then focus on the rigid solvent models and discuss the limits of such approximations. The flexible and polarizable models will also be briefly mentioned.

2.1 Continuum Solvation Models

Continuum models [7–9], which are popular in QM calculations, consider the solvent as a polarizable medium with dielectric constant ε, with the solute M placed in the cavity within this medium (figure 2.1)

The dielectric constant ε is the key parameter characterizing the solvent. It is normally a constant value, but that can depend on the position in space. (see §2.1.1)

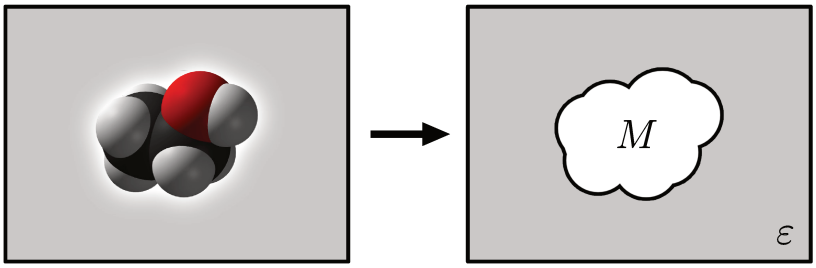

Figure 2.1: Continuum solvent model

According to this model the solvation Gibbs free energy is

$$\Delta G_{\text{solvation}} = \Delta G_{\text{cavity}} + \Delta G_{\text{dispersion}} + \Delta G_{\text{elec}} \tag{2.1}$$

where $\Delta G_{\text{cavity}} > 0$ is the energy needed to create a hole in the medium, and $\Delta G_{\text{dispersion}}$ is the dispersion interaction, which is roughly the van der Waals energy $\Delta G_{\text{vdW}} < 0$ between the solvent and solute. In principle, there may also be a repulsive component, and the dispersion term is sometimes denoted dispersion/repulsion. $\Delta G_{\text{elec}} < 0$ is the contribution of electrostatic interactions, introduced by electric charge distribution of M

which polarizes the medium, and the action back of the medium on the molecule (reaction field).

The initial two terms in eq. (2.1) are linked to the configuration of the first solvation shell (cavity). The definition of cavity varies from the simplest sphere or ellipsoid to the ensemble of atomic surfaces defined by the van der Waals radii in the solute. It is somewhat reasonable to consider the cavity area as proportional to the number of solvent molecules in the first solvation shell. This number can be calculated as the area passing through the middle region of first shell solvent. This area, named the solvent-accessible surface area (SASA) [36, 37], can be calculated by adding the radius of the probe solvent ball to the solvent excluded surface area (figure 2.2).

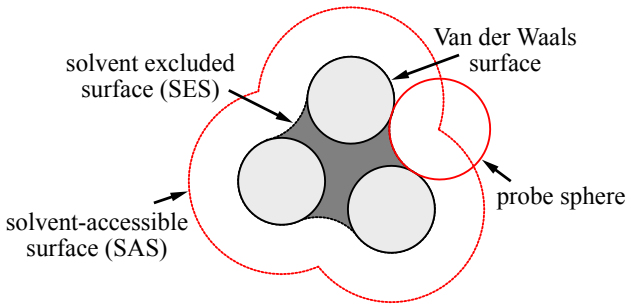

Figure 2.2: Definition of cavity surfaces. The solvent accessible surface (SAS) traced out by the center of the probe representing a solvent molecule. The solvent excluded surface (SES) is the topological boundary of the union of all possible probes that do not overlap with the molecule.

The energy required to create such a cavity and the stabilization due to van der Waals interactions between the solute and solvent, assumed to be proportional to the surface area of the cavity, is expressed as

$$\Delta G_{\text{cavity}} + \Delta G_{\text{dispersion}} = \gamma S_{\text{SASA}} + \beta \tag{2.2}$$

or parameterized by having a constant ξ specific for each atom type, with the ξ parameters being determined by fitting to experimental solvation data:

$$\Delta G_{\text{cavity}} + \Delta G_{\text{dispersion}} = \sum_{i}^{\text{atoms}} \xi_i S_i \tag{2.3}$$

The models and methods employed to calculate the electrostatic contribution ΔG_{elec} have varied greatly according to their usage. The sections below list the most common examples. On another topic, the integration of continuum models into QM calculations is also a very important field; these developments will not be detailed here as they do not connect yet to our work. Such kinds of methods are called the self-consistent reaction field (SCRF) models, which integrate the calculation of the solute-solvent interaction in addition to that of the solute wave function by an iterative procedure. Some examples are presented in the list of Gaussian keyword SCRF [38], and the field is well reviewed by, for example, Tomasi [9, 10] and Jensen [7].

2.1.1 *Poisson-Boltzmann methods*

The Poisson-Boltzmann equation (PBE) [39] makes it possible to calculate the position-dependent electrostatic potential $V_{\text{elec}}(\mathbf{r})$ in the continuum model, such that the electrostatic component of the free energy can be written as

$$\Delta G_{\text{elec}} = \frac{1}{2} \int \mathrm{d}\mathbf{r} \rho_q(\mathbf{r}) V_{\text{elec}}(\mathbf{r}) \tag{2.4}$$

where ρ_q is the charge distribution of the solute.

The Maxwell-Gauss equation in SI units convention gives

$$\nabla \cdot D(\mathbf{r}) = \frac{\rho_q(\mathbf{r})}{\varepsilon_0} \tag{2.5}$$

where $D(\mathbf{r}) = \varepsilon_0 E(\mathbf{r}) + P(\mathbf{r})$ is the electric displacement field, $P(\mathbf{r})$ is the system polarization, $E(\mathbf{r})$ the electric field, and ε_0 the vacuum permittivity. $D(\mathbf{r})$ can also be expressed in terms of the position-dependent dielectric constant $\varepsilon(\mathbf{r})$, $D(\mathbf{r}) = \varepsilon(\mathbf{r})E(\mathbf{r})$, which thus gives

$$\nabla \cdot \varepsilon(\mathbf{r})E(\mathbf{r}) = \frac{\rho_q(\mathbf{r})}{\varepsilon_0} \tag{2.6}$$

or in terms of electrostatic potential:

$$\nabla \cdot [\varepsilon(\mathbf{r})\nabla V_{\text{elec}}(\mathbf{r})] = -\frac{\rho_q(\mathbf{r})}{\varepsilon_0} \tag{2.7}$$

This second-order differential equation (2.7) is called the Poisson equation.

This equation cannot be solved analytically for complex geometries (such as a protein). Therefore it is done numerically using appropriate methods; for example, as mentioned in the article of Roux and Simonson [40] or Holst [39]. A density functional approach based on the minimization of the polarization density can also be used to solve this equation [41, 42].

If the solvent is ionic, the Poisson equation can be modified by taking into account a (thermal) Boltzmann distribution of ions in the solvent, i.e.,

$$\rho_{\text{tot}}(\mathbf{r}) = \rho_q(\mathbf{r}) - 2qn_{\text{ion}} \sinh(\frac{q}{k_{\text{B}}T} V_{\text{elec}}(\mathbf{r})) \tag{2.8}$$

for a salt composed of ions of charge $+\mathtt{q}$ and $-\mathtt{q}$ and of density n_{ion}. Replacing in eq. (2.7) leads to the Poisson-Boltzmann Equation:

$$\nabla \cdot (\varepsilon(\mathbf{r})\nabla V_{\text{elec}}(\mathbf{r})) - \frac{2qn_{\text{ion}}}{\varepsilon_0} \sinh\left(\frac{qV_{\text{elec}}(\mathbf{r})}{k_{\text{B}}T}\right) = -\frac{\rho(\mathbf{r})}{\varepsilon_0} \tag{2.9}$$

2.1.2 *Born / Onsager / Generalized Born models*

For simple geometries, the Poisson equation (2.7) can be solved analytically. The simplest model is a spherical cavity. For a net charge q in a cavity of radius a, the electrostatic free energy of a medium with a dielectric constant of ε is given by the Born formula:

$$\Delta G_{\text{elec}}(q) = -\frac{1}{8\pi\varepsilon_0}\left(1 - \frac{1}{\varepsilon}\right)\frac{q^2}{2a} \tag{2.10}$$

Other similar models include the Onsager model, in which a point dipole (characterized by the dipole moment μ) is put in a spherical cavity. The Kirkwood model refers to a general multipole expansion in a spherical cavity, while the Kirkwood-Westheimer model arises for an ellipsoidal cavity. Those simplified models are not fully able to predict the solvent behavior in many realistic cases [7].

The generalized Born (GB) model is an empirical model based on the superposition of several net charges in spherical cavities as the Born model describes, with a similar formula:

$$\Delta G_{\text{elec}} = -\frac{1}{8\pi\varepsilon_0}\left(1 - \frac{1}{\varepsilon}\right)\sum_i \sum_j \frac{q_i q_j}{f_{ij}} \tag{2.11}$$

where the function f_{ij} depends on the internuclear distance r_{ij} between the centers of atoms i and j and on the Born radii for each pair of atoms a_i and a_j:

$$f_{ij} = \sqrt{r_{ij}^2 - a_i a_j \exp\left(\frac{r_{ij}^2}{4a_i a_j}\right)} \tag{2.12}$$

The key (empirical) point is to be able to attribute an effective Born radius a_i to each atom inside the complex, non-spherical cavity formed by the solute. Once this is accomplished, the GB model provides a very fast method, with an overall accuracy comparable to that of Poisson-Boltzmann calculations. That makes it widely used in computational structural biology to perform structure optimization and molecular dynamics simulations.

2.2 MODEL POTENTIAL OF EXPLICIT MOLECULES

The model potential frequently used in the theory of liquids is a classical, rigid, pairwise additive model [12, 13]. It is based on three assumptions.

1. Firstly, the quantum effects should be ignored. It is assumed that the rotational and transitional motion of solvent particles are continuous and classical, which means the separation of both transitional and rotational states are largely inferior of $k_{\mathrm{B}}T$. For light molecules, that is not always convincing. Some molecules containing hydrogen (e.g. H_2O, NH_3, and particularly H_2) exhibit obvious quantum effects at low temperatures in the liquid state. Gaseous H_2O and NH_3 also need quantum effect corrections. However, for the liquid of most interest to us, H_2O at room temperature, the contribution of this effect is small enough to be neglected. And obviously, there should not be any chemical interaction of the solvent with the solute.

Compared to atomic models that only depend on $\mathbf{r}^N$, the angular correlations can give influence on both structural and thermodynamic proprieties. That is why our theory is extended to linear case, $\boldsymbol{\Omega} \equiv (\Theta, \Phi)$, then molecular case, $\boldsymbol{\Omega} \equiv (\Theta, \Phi, \Psi)$.

2. Secondly, the intramolecular movement (vibration and internal rotation) should be either independent of transitional and rotational movement or absent. This rigid molecule approximation assumes that the intermolecular potential $\mathcal{U}(\mathbf{r}^N, \boldsymbol{\Omega}^N)$ for N particles only depends on the positions of the N molecular centers $\mathbf{r}^N \equiv (\mathbf{r}_1, \mathbf{r}_2, \ldots, \mathbf{r}_N)$ and on their orientations $\boldsymbol{\Omega}^N \equiv (\boldsymbol{\Omega}_1, \boldsymbol{\Omega}_2, \cdots, \boldsymbol{\Omega}_N)$, where $\boldsymbol{\Omega} \equiv (\Theta, \Phi, \Psi)$ represents the Euler angles (figure 2.3). The natural choice for the molecular center is the center of mass. This is, however, arbitrary if only equilibrium properties are considered.

   The rigid approximation is quite realistic for molecules in which the separation of vibrational states largely exceeds $k_{\mathrm{B}}T$, implying that the molecule stays in its ground vibrational state. This is the case for many small solvent molecules such as N_2, CO_2, C_6H_6, and indeed for the bending and stretching modes of water.

3. Finally, the intermolecular forces have to be assumed as pairwise additive:

$$\mathcal{U}(\mathbf{r}^N, \boldsymbol{\Omega}^N) = \frac{1}{2}\sum_{i \neq j} u(\mathbf{r}_{ij}, \boldsymbol{\Omega}_\mathbf{i}, \boldsymbol{\Omega}_\mathbf{j}) = \sum_{i<j} u(\mathbf{r}_{ij}, \boldsymbol{\Omega}_\mathbf{i}, \boldsymbol{\Omega}_\mathbf{j}) \tag{2.13}$$

   This means that the model potential only depends on the intermolecular separation $\mathbf{r}$ and on the molecular orientations $\boldsymbol{\Omega}_1$ and $\boldsymbol{\Omega}_2$. This approximation is quasi-exact for low density gases, where the contribution of the three and more body terms decreases rapidly. But for dense fluids, in most of the cases the multi-body potential cannot be ignored. The complete model potential with higher-order corrections can be written in the form of

$$\mathcal{U}(\mathbf{r}^N, \boldsymbol{\Omega}^N) = \sum_{i<j} u(ij) + \sum_{i<j<k} u(ijk) + \sum_{i<j<k<l} u(ijkl) + \ldots \tag{2.14}$$

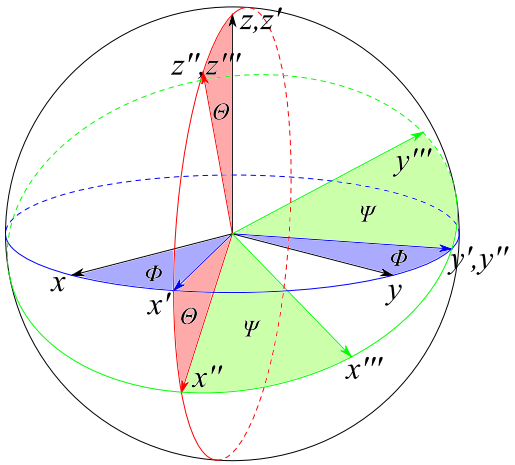

Figure 2.3: Euler angles. The basis vectors of the new orientation are obtained by 3 sequential operations: (1) A rotation ϕ $(0 < \phi < 2\pi)$ about the z-axis, bringing the frame of axes from the initial position $\mathbf{S}$ into the position $\mathbf{S}'$ (2) A rotation θ $(0 < \theta < \pi)$ about the y-axis of the frame $\mathbf{S}'$, which is transformed into $\mathbf{S}''$ (3) A rotation ψ $(0 < \psi < 2\pi)$ about the z-axis of the frame $\mathbf{S}''$.

where $u(ij) = u(\mathbf{r}_{ij}, \mathbf{\Omega_i}, \mathbf{\Omega_j})$ and $u(ijk) = u(\mathbf{r}_{ij}, \mathbf{r}_{jk}, \mathbf{r}_{ki}, \mathbf{\Omega_i}, \mathbf{\Omega_j}, \mathbf{\Omega_k})$, etc. The omission of the three-body and higher-order terms can cause errors, for example, in surface tension and surface energy calculation [43]. However the higher order terms are often accounted for by an effective pair potential (measured by experiments or calculated by simulations), which reduces considerably the computational cost for simulations, or the degree of theory needed. Such models are presented below, going from simple to molecular liquids. For the molecular solvent considered in this thesis, water, most publications have stayed at this two-body level of description.

2.2.1 *Interaction of spherical particle*

The simplest model of a fluid is the hard sphere model. With d the hard-sphere diameter, the pair potential is defined as:

$$u(r) = \begin{cases} \infty & r < d \\ 0 & r > d \end{cases} \tag{2.15}$$

This model is indeed a fundamental reference model in statistical mechanics, and it can represent some physical systems, such as neutral colloidal suspensions [44]. However, the absence of attractive force, which precludes the existence of a liquid-gas transition, makes it too simple for realistic fluids. More realistic neutral particle models, like the Lenard-Jones (LJ) model, exhibit a potential energy curve that has the same shape as the real interaction of rare gas, as shown in figure 2.4.

The Lennard-Jones (LJ) interaction gives

$$u_{LJ}(r) = 4\varepsilon \left[\left(\frac{\sigma}{r}\right)^{12} - \left(\frac{\sigma}{r}\right)^{6} \right] \tag{2.16}$$

where r is the distance from centre to centre, σ is the collision diameter or the particles separation where $u(r) = 0$, and ϵ is the well depth of the potential (of unity of energy). The well minimum occurs at $r_{\min} = 2^{1/6}\sigma$ and $u(r_{\min}) = -\epsilon$. The parameters σ and ϵ can be extracted from experiments.

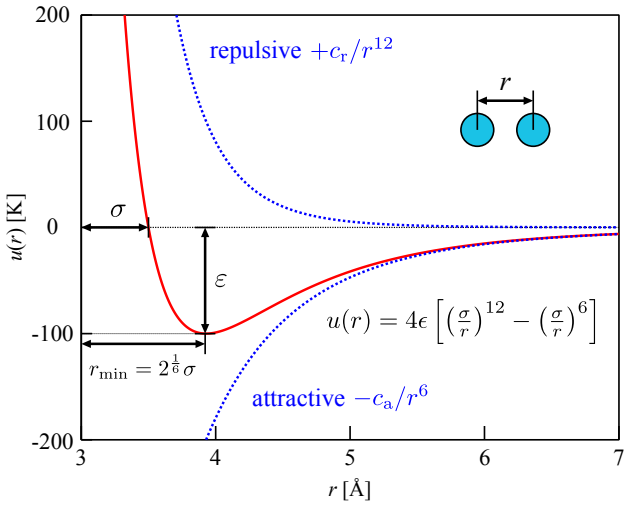

Figure 2.4: LJ pair potential. The plot gives the potential energy $u(r)$ versus internuclear distance r of two particles. At large distances, both attractive and repulsive interactions are small. As the distance between the atoms decreases, the attractive electron-proton interactions dominate, and the energy of the system decreases. At the observed bond distance, the repulsive electron-electron and proton-proton interactions just balance the attractive interactions, preventing a further decrease in the internuclear distance. At very short internuclear distances, the repulsive interactions dominate, making the system less stable than the isolated atoms.

Theoretically, all terms in the multipole series represent attractive contributions to the potential. The leading term, varying as r^{-6}, describes the quantum dipole-dipole interaction. Higher-order terms represent dipole-quadrupole (r^{-8}), quadrupole-quadrupole (r^{-10}) interactions, and so on, but these are negligible compared to r^{-6}. The short-range interaction is difficult to define properly, and for the sake of simplicity and numerical efficiency, it is defined as r^{-12} in the LJ model.

If the spherical particles are charged (as in molten salts), the electrostatic interaction between them is described by the Coulomb point charge interaction:

$$u_{\text{Coul}}(r) = \frac{q_1 q_2}{4\pi\varepsilon_0 r} \tag{2.17}$$

For such charged simple fluids, the overall pair $u(r)$ is a sum of LJ and Coulomb interactions. Such decomposition can be extended to molecular fluids in terms of site-site interactions, which are discussed in the following section.

2.2.2 *Site-site interactions*

Indeed, a spherical description of interactions is not sufficient to fully describe molecular fluids. The site-site model is a further extension of atomic models in which the solvent molecule is represented by a set of discrete interaction sites. The total potential energy is a sum of spherical interaction potentials:

$$u(1,2) = \sum_{\alpha}\sum_{\beta} u_{\alpha\beta}(|\mathbf{r}_{2\beta} - \mathbf{r}_{1\alpha}|) \tag{2.18}$$

where $\mathbf{r}_{is}$ is the coordinates of site s in molecule i, $u_{\alpha\beta}(r)$ the interatomic potential energy of pairs of sites α and β, as discussed above. More specifically, it is generally decomposed into a Lennard-Jones and a Coulombic contribution:

$$u(1,2) = \sum_{\alpha}\sum_{\beta}\left\{4\epsilon_{\alpha\beta}\left[\left(\frac{\sigma_{\alpha\beta}}{r_{12}^{\alpha\beta}}\right)^{12} - \left(\frac{\sigma_{\alpha\beta}}{r_{12}^{\alpha\beta}}\right)^{6}\right] + \frac{1}{4\pi\varepsilon_0}\frac{q_\alpha q_\beta}{r_{12}^{\alpha\beta}}\right\} \tag{2.19}$$

where $r_{12}^{\alpha\beta} = |\mathbf{r}_{2\beta} - \mathbf{r}_{1\alpha}|$, $\epsilon_{\alpha\beta}$ and $\sigma_{\alpha\beta}$ are the site-site LJ parameters and q_α the partial charge on each site. This model is the most commonly adopted, and it will be so in this thesis for the calculation of external free energy functional.

2.2.3 *Multipole and spherical harmonic expansion*

To obtain fewer terms in the calculation, the model potential can be presented in convergent series via multipole or spherical harmonic expansion.

For polar liquids, the dipole-dipole interaction should be mainly taken into account. Thus the model considers dipole-dipole interactions in addition to a spherically symmetric Lennard-Jones-like potential:

$$u(1,2) = u_0(r) - \boldsymbol{\mu}_1 \cdot \mathbf{T}(\mathbf{r}) \cdot \boldsymbol{\mu}_2 \tag{2.20}$$

where $\mathbf{r}$ is the vector separation of the molecular centers, $u_0(r)$ is the spherically symmetric term discussed above, $\boldsymbol{\mu}_i$ is the dipole moment vector of particle i and $\mathbf{T}(\mathbf{r})$ is the dipole-dipole interaction tensor:

$$T(\mathbf{r}) = \nabla^2 \left(\frac{1}{r}\right) = 3\mathbf{rr}/r^5 - \mathbf{I}/r^3 \tag{2.21}$$

and $\mathbf{I}$ is the unit tensor. Note that this model can be made more realistic by including higher-order electrostatic interactions, such as dipole-quadrupole, quadrupole-quadrupole, etc. Such a systematic multipolar approach has previously been proposed for water [45].

Alternatively, the intermolecular potential can be expanded onto rotational invariants in the form:

$$u(\mathbf{r}_{12}, \boldsymbol{\Omega}_1, \boldsymbol{\Omega}_2) = \sum_{mnl\mu\nu} u_{\mu\nu}^{mnl}(r_{12}) \Phi_{\mu\nu}^{mnl}(\hat{\mathbf{r}}_{12}, \boldsymbol{\Omega}_1, \boldsymbol{\Omega}_2) \tag{2.22}$$

where the angular basis functions $\Phi_{\mu\nu}^{mnl}(\hat{\mathbf{r}}_{12}, \boldsymbol{\Omega}_1, \boldsymbol{\Omega}_2)$ can be expressed in terms of generalized spherical harmonics (GSHs) [13]. A detailed description of rotational invariant transform is in appendix F.

2.2.4 *SPC/E water model*

As water cannot be perfectly described by a pair potential (due to multi-body effects, quantum effects, hydrogen bond, etc.), various models have been developed to fit a maximum number of properties. Those models contain several sites, which can be placed possibly elsewhere than at the center of atoms (figure 2.5). The more sites the model has, the more precise it can be. There is a great work done by Martin Chaplin [46] to summarize the most widely used water models.

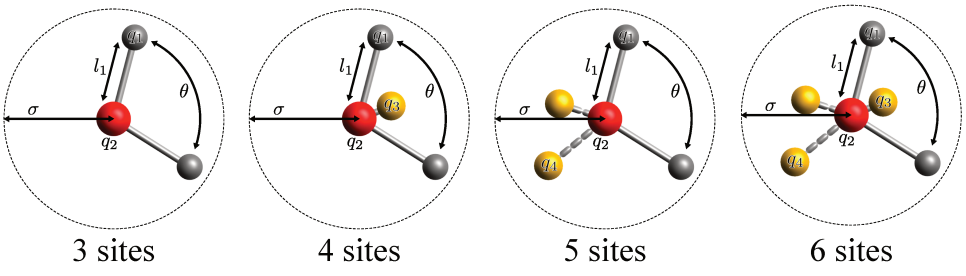

Figure 2.5: Water models

In this thesis, we use the extended simple point charge model (SPC/E) of water [47] as our solvent model throughout. It is a 3-site model, the electrostatic interaction being

modeled using Coulomb's Law and the dispersion and repulsion forces using the Lennard-Jones potential, as described above.

With respect to the original SPC model, the SPC/E model takes into account the polarization in an implicit and phenomenological way, re-normalizing the dipole of the effective pair model, and thus increasing the partial charge slightly compared to SPC (table 2.1; the center of water molecule has been placed at atom O, for convenance). The SPC/E model gives a better radial distribution function and diffusion constant than the SPC model. It is the most commonly used model for applications.

It should be noted that any rigid solvent model is compatible with the theory that this thesis is based on, e.g. acetonitrile used in [32].

MODEL	σ [Å]	ε [kJ · mol^{-1}]	l_1 [Å]	$\mathfrak{q}_1$ [q_e]	$\mathfrak{q}_2$ [q_e]	θ [°]
SPC [48]	3.166	0.650	1.0000	+0.410	-0.8200	109.47
SPC/E [47]	3.166	0.650	1.0000	+0.4238	-0.8476	109.47
experiment [49]	-	-	0.991	-	-	105.5

Table 2.1: Structural parameters of SPC and SPC/E water

2.2.5 *Flexible and polarizable models*

Up to this point, molecules were considered as rigid bodies. Flexible models give extra degrees of freedom in vibration and internal rotation. In that case, the interaction potential contains several extra terms, yielding typically five kinds of forces: three for the direct interactions in addition to the two indirect interactions (LJ and Coulomb).

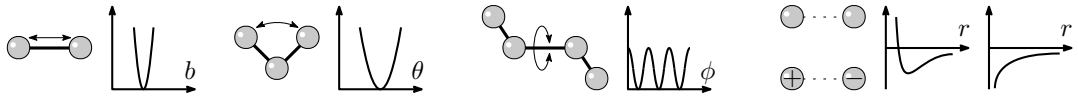

$$U = \sum_{\text{bonds}} K_r(r - r_{\text{eq}})^2 + \sum_{\text{angles}} K_\theta(\theta - \theta_{\text{eq}})^2 + \sum_{\text{dihedrals}} \frac{V_n}{2}[1 + \cos(n\phi - \gamma)] + \sum_{i<j} \left[\frac{A_{ij}}{r_{ij}^{12}} - \frac{B_{ij}}{r_{ij}^{6}} + \frac{q_i q_j}{\varepsilon r_{ij}} \right]$$

stretch terms bend terms torsional terms non-bonded interactions

Figure 2.6: Interactions in a flexible model

The flexible yielding can deal with the non-rigidity of the solvent, which is partially polarized owing to the vibrational degrees of freedom (the so-called atomic polarizability). On the other hand, electronic polarizability (the deformation of the molecule electron cloud under the action of the external electric field) can be taken into account even in a rigid model. This polarizability can be described by introducing a modifiable charge distribution, for example by adding an induced dipole at the molecular center of the molecule, or even on each of its atomic sites, and by solving the set of induced dipoles self-consistently. Introducing variable atomic charges is possible too [50]. Optimizing the induced charges/dipoles has a large computational overhead compared to fixed charges.

Complex models require expensive computing cost, but still can have large fluctuations due to use of imposed small system size. There is a compromise between the choice of model and the choice of system size. For this reason, the rigid models are still the most popular nowadays. On the other hand, computing technologies have greatly developed compared to the theories themselves, which makes it possible to use more and more precise models in computation.

2.3 MODEL OF SOLUTE

The model of solute also has a substantial influence on the predicted energy and structure of solvation. The solute can eventually be treated by QM calculations in terms of wave function and electron density. This is the case for the implicit SCRF method, which for apolar solvents (i.e. toluene) has been proven to work well. There is a clear mismatch, however, between the very refined description of the solute and the rather primitive continuous-medium treatment of the solvent. The compromise to have a better model of solvent or solute is debatable, and should vary according to the applications. On the other extreme, one never uses a quantum solvent model with an implicit solute; this would not be profitable even if the solute is of simple geometry (wall). In the case of molecular solutes, it is consistent to require the solute to have at least the same scale of description as the solvent. A hierarchy of possible potential models for solutes is described in figure (2.7).

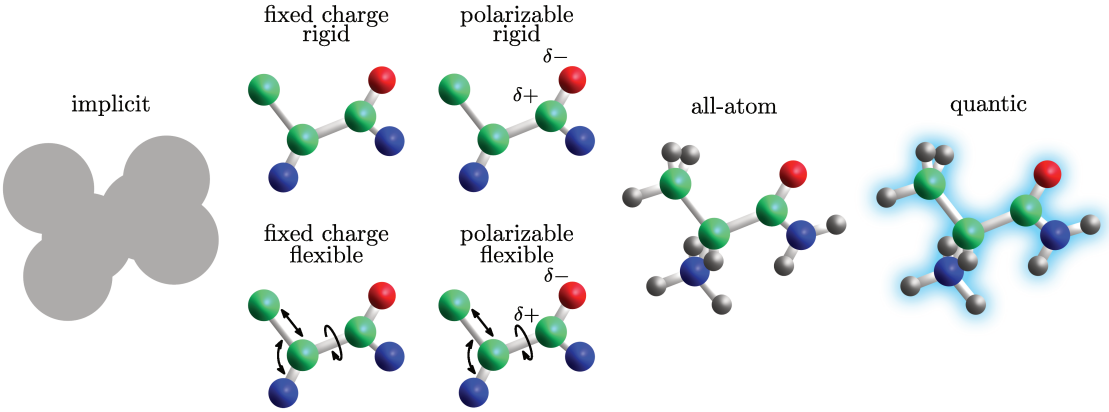

Figure 2.7: Hierarchy of solute models

In this thesis, our first step will be to use a rigid molecular model to describe the solute. This is coherent with IET, which cannot treat the solvent and solute at different scales of description. Polarizable and/or flexible models of solute, and the coupling of a QM solute to the molecular solvent, will be described in perspective.

In conclusion, the choice of model for the solute/solvent system is a compromise between the required precision according to the application, and the computing cost that the research can afford.

3

Statistical Mechanics of Atomic Fluids

Statistical mechanics serves to deduce thermodynamic quantities from the Hamiltonian of any given system. In this section, we present some basic formalism for a classical atom-like spherical solvent model in grand canonical ensemble (μ,V,T). Firstly, we introduce the relations between the statistical mechanics and thermodynamic quantities. Then we change the view to the structure of the solvent. The two theories we use in this thesis, here referred to as IET and cDFT, as well as their equivalency, are presented with brief derivations in the following content. The majority of this section is based on the book by Hansen & McDonald [12, 51], and the articles and notes of Evans [21, 52, 53]. A very detailed review is done by Wu *et al.* [54] to the same purpose, thus here we only introduce the concepts that will be useful to understand this thesis.

3.1 Hamiltonian and Ensemble Properties

Once we define a spherical solvent model, of which the movement only depends on its position and momentum $(\mathbf{r}, \mathbf{p})$, the instantaneous state (phase point, micro-state) of an N-particle solvent system is specified by $3N$ coordinates $\mathbf{r}^N \equiv \mathbf{r}_1, \ldots, \mathbf{r}_N$ and $3N$ momenta $\mathbf{p}^N \equiv \mathbf{p}_1, \ldots, \mathbf{p}_N$. The internal energy of particles in a system is characterized by its Hamiltonian:

$$H_N(\mathbf{r}^N, \mathbf{p}^N) = K_N(\mathbf{p}^N) + V_N(\mathbf{r}^N) + V_N^{\text{ext}}(\mathbf{r}^N) \tag{3.1}$$

where

$K_N(\mathbf{p}^N) = \sum_{i=1}^{N} \frac{\mathbf{p}_i^2}{2m}$ is the kinetic energy;

$V_N(\mathbf{r}^N) = \sum_{i<j}^{N} u(|\mathbf{r}_i - \mathbf{r}_j|) + 3\,\text{body} + \ldots$ is the interatomic potential energy $\mathcal{U}(\mathbf{r}^N)$;

$V_N^{\text{ext}}(\mathbf{r}^N) = \sum_{i=1}^{N} V_{\text{ext}}(\mathbf{r}_i)$ is the potential energy arising from the interaction of the particles with the external field (e.g. a solute).

The grand potential, characteristic thermodynamic state function for the grand canonical ensemble, which depends on the chemical potential μ, the volume V and the temperature T, is linked with the statistical mechanics quantities with the relation:

$$\Omega(\mu, V, T) = -k_{\text{B}} T \ln \Xi \tag{3.2}$$

where

$$\Xi = \sum_{N=0}^{\infty} \frac{e^{\beta\mu N}}{h^{3N} N!} \int \mathrm{d}\mathbf{r}^N \mathrm{d}\mathbf{p}^N e^{-\beta H_N(\mathbf{r}^N, \mathbf{p}^N)} \tag{3.3}$$

$$= \sum_{N=0}^{\infty} \frac{1}{N!} \int \mathrm{d}\mathbf{r}^N e^{-\beta V_N(\mathbf{r}^N)} \left(\prod_{i=1}^{N} \frac{e^{\beta V_{\text{int}}(\mathbf{r}_i)}}{\Lambda^3} \right) \tag{3.4}$$

is the grand partition function, with $\Lambda = \left(2\pi\beta\hbar^2/m\right)^{-\frac{1}{2}}$ the de Broglie thermal wavelength, and

$$V_{\text{int}}(\mathbf{r}_i) = \mu - V_{\text{ext}}(\mathbf{r}_i) \tag{3.5}$$

the intrinsic chemical potential.

We can also define the intrinsic free energy:

$$\begin{aligned} F_{\text{int}} &= F - \int \mathrm{d}\mathbf{r}\bar{n}(\mathbf{r})V_{\text{ext}}(\mathbf{r}) \\ &= \Omega + \mu N - \int \mathrm{d}\mathbf{r}\bar{n}(\mathbf{r})V_{\text{ext}}(\mathbf{r}) \\ &= \Omega + \int \mathrm{d}\mathbf{r}\bar{n}(\mathbf{r})V_{\text{int}}(\mathbf{r}) \end{aligned} \tag{3.6}$$

$N = \int \mathrm{d}\mathbf{r}\bar{n}(\mathbf{r})$ is the number of particles in canonical ensemble, but the formulae (3.6) and (3.8) are also available for grand canonical ensemble.

where F is the Helmholtz free energy and

$$\bar{n}(\mathbf{r}) = \langle \varrho(\mathbf{r}) \rangle = \left\langle \sum_{i=1}^{N} \delta(\mathbf{r} - \mathbf{r}_1) \right\rangle \tag{3.7}$$

is the density profile of instantaneous density $\varrho(\mathbf{r})$ distribution at equilibrium.

The differential form of F_{int} is

$$\delta F_{\text{int}} = -S\delta T + \int \mathrm{d}\mathbf{r}\delta\bar{n}(\mathbf{r})V_{\text{int}}(\mathbf{r}) \tag{3.8}$$

with S the entropy.

The internal energy of the solvent contains two contributions, one due to the kinetic energy of the particles, $K_N(\mathbf{p}^N)$, and the other linked to the interaction between particles, $V_N(\mathbf{r}^N)$. When the fluid is a perfect gas, which means $V_N = 0$, it can be easily derived from eq. (3.2-3.5) that F_{int} has the following expression:

$$F_{\text{id}} = k_{\text{B}}T \int \mathrm{d}\mathbf{r}\bar{n}(\mathbf{r}) \left[\ln\left(\Lambda^3\bar{n}(\mathbf{r})\right) - 1 \right] \tag{3.9}$$

When interactions between particles are accounted for, the total expression of F_{int} is:

$$F_{\text{int}} = F_{\text{id}} + F_{\text{exc}} \tag{3.10}$$

and the form of F_{exc} will be detailed in later sections.

3.2 FUNCTIONAL DERIVATIVES AND DISTRIBUTION FUNCTIONS

The structure of the solvent in the grand canonical ensemble can be characterized by its n-particle density

$$\rho^{(n)}(\mathbf{r}^n) = \frac{1}{\Xi} \sum_{N=n}^{\infty} \frac{1}{(N-n)!} \int \mathrm{d}\mathbf{r}^{(N-n)} e^{-\beta V_N(\mathbf{r}^N)} \left(\prod_{i=1}^{N} \frac{e^{\beta V_{\text{int}}(\mathbf{r}_i)}}{\Lambda^3} \right) \tag{3.11}$$

which means the probability to find n particles in a volume element $\mathrm{d}\mathbf{r}^n$. In particular, the probability to find one particle in a volume element is the solvent density $\rho^{(1)}(\mathbf{r}) = \bar{n}(\mathbf{r})$, that

$$\int \rho^{(1)}(\mathbf{r})\mathrm{d}\mathbf{r} = \langle N \rangle \tag{3.12}$$

where $\langle N \rangle$ is the ensemble average of the number of particles, that is to say the average number of particles at equilibrium. $\rho^{(n)}(\mathbf{r}^n)$ becomes ρ^n if the system is homogeneous. It can be proven that

$$\frac{\delta\Omega}{\delta V_{\text{int}}(\mathbf{r})} = -\rho^{(1)}(\mathbf{r}) \tag{3.13}$$

The corresponding n-particle distribution function is defined as:

$$g^{(n)}(\mathbf{r}^n) = \frac{\rho^{(n)}(\mathbf{r}^n)}{\prod_{i=1}^{n}\rho^{(1)}(\mathbf{r}_i)} \tag{3.14}$$

such that $g^{(n)}(\mathbf{r}^n) \to 1$ when all pairs of particles becomes sufficiently large.

The two-particle pair distribution function (PDF), $g^{(2)}(\mathbf{r}_1, \mathbf{r}_2)$, is one of the most important quantities in the theory of liquids. Its corresponding pair correlation function (PCF) is defined as:

$$h^{(2)}(\mathbf{r}_1, \mathbf{r}_2) = g^{(2)}(\mathbf{r}_1, \mathbf{r}_2) - 1 \tag{3.15}$$

which vanishes when $|\mathbf{r}_1 - \mathbf{r}_2| \to \infty$.

For any ensemble.

If we define the density-density correlation function as:

$$H^{(2)}(\mathbf{r}_1, \mathbf{r}_2) = \rho^{(1)}(\mathbf{r}_1)\rho^{(1)}(\mathbf{r}_2)h^{(2)}(\mathbf{r}_1, \mathbf{r}_2) + \rho^{(1)}(\mathbf{r}_1)\delta(\mathbf{r}_1 - \mathbf{r}_2) \tag{3.16}$$

which means the correlation [55] between the instantaneous fluctuation of particle density from its ensemble average, it can be proven that

$$\frac{\delta\Omega^2}{\delta V_{\text{int}}(\mathbf{r}_1)\delta V_{\text{int}}(\mathbf{r}_2)} = -\beta H^{(2)}(\mathbf{r}_1, \mathbf{r}_2) = -\frac{\delta\rho^{(1)}(\mathbf{r}_1)}{\delta V_{\text{int}}(\mathbf{r}_2)} \tag{3.17}$$

As an analogue, the direct correlation function (DCF) is defined as the derivative of the excess free energy functional $F_{\text{exc}}[\rho]$:

$$c^{(1)}(\mathbf{r}) = -\frac{\delta(\beta F_{\text{exc}}[\rho^{(1)}])}{\delta\rho^{(1)}(\mathbf{r})} \tag{3.18}$$

$$c^{(2)}(\mathbf{r}_1, \mathbf{r}_2) = \frac{\delta c^{(1)}(\mathbf{r}_1)}{\delta\rho^{(1)}(\mathbf{r}_2)} = -\frac{\delta^2(\beta F_{\text{exc}}[\rho^{(1)}])}{\delta\rho^{(1)}(\mathbf{r}_1)\delta\rho^{(1)}(\mathbf{r}_2)} = c^{(2)}(\mathbf{r}_2, \mathbf{r}_1) \tag{3.19}$$

$$c^{(n)}(\mathbf{r}_1, \ldots, \mathbf{r}_n) = \frac{\delta c^{(n-1)}(\mathbf{r}_1, \ldots, \mathbf{r}_{n-1})}{\delta\rho^{(1)}(\mathbf{r}_n)} \tag{3.20}$$

According to the definition of F_{int}, as well as the expression of δF_{int} in eq. (3.8):

$$\begin{aligned} \beta V_{\text{int}}(\mathbf{r}) &= \beta\frac{\delta F_{\text{int}}[\rho^{(1)}]}{\delta\rho^{(1)}(\mathbf{r})} = \beta\frac{\delta F_{\text{id}}[\rho^{(1)}]}{\delta\rho^{(1)}(\mathbf{r})} + \beta\frac{\delta F_{\text{exc}}[\rho^{(1)}]}{\delta\rho^{(1)}(\mathbf{r})} \\ &= \ln\left(\Lambda^3\rho^{(1)}(\mathbf{r})\right) - c^{(1)}(\mathbf{r}) \end{aligned} \tag{3.21}$$

The functional derivative chain rule leads to

$$\begin{aligned} \int \mathrm{d}\mathbf{r}_3 \frac{\delta V_{\text{int}}(\mathbf{r}_1)}{\delta\rho^{(1)}(\mathbf{r}_3)} \cdot \frac{\delta\rho^{(1)}(\mathbf{r}_3)}{\delta V_{\text{int}}(\mathbf{r}_2)} &= \int \mathrm{d}\mathbf{r}_3 \frac{\delta V_{\text{int}}[\rho^{(1)}(\mathbf{r}_1)]}{\delta\rho^{(1)}(\mathbf{r}_3)} \cdot \beta H^{(2)}(\mathbf{r}_3, \mathbf{r}_2) \\ &= \int \mathrm{d}\mathbf{r}_3 \left[\frac{1}{\rho^{(1)}(\mathbf{r}_1)}\delta(\mathbf{r}_1 - \mathbf{r}_3) - c^{(2)}(\mathbf{r}_1, \mathbf{r}_3)\right] \cdot H^{(2)}(\mathbf{r}_3, \mathbf{r}_2) \\ &= \delta(\mathbf{r}_1 - \mathbf{r}_2) \end{aligned} \tag{3.22}$$

in addition to the definition of H in eq. (3.16) gives

$$h^{(2)}(\mathbf{r}_1, \mathbf{r}_2) = c^{(2)}(\mathbf{r}_1, \mathbf{r}_2) + \int \mathrm{d}\mathbf{r}_3 \left(c^{(2)}(\mathbf{r}_1, \mathbf{r}_3)\rho^{(1)}(\mathbf{r}_3)h^{(2)}(\mathbf{r}_3, \mathbf{r}_2)\right) \tag{3.23}$$

which is called the Ornstein-Zernike (OZ) equation.

3.3 CLASSICAL DENSITY FUNCTIONAL THEORY

The density functional theory is based on two theorems :

1. For a given choice of V_N, T and μ, the intrinsic free energy F_{int} is a unique functional of the equilibrium one-particle density $\bar{n}(\mathbf{r})$, expressed by $F_{\text{int}}[\bar{n}]$.

2. Let $n(\mathbf{r})$ be some arbitrary one-particle microscopic density, and define the grand potential functional $\Omega[n]$ as:

$$\Omega[n] = F_{\text{int}}[n] - \int \mathrm{d}\mathbf{r} n(\mathbf{r}) V_{\text{int}}(\mathbf{r}) \tag{3.24}$$

Then the variational principle states that

$$\Omega[n] \geq \Omega[\bar{n}] \tag{3.25}$$

with the equal sign takes at $n(\mathbf{r}) = \bar{n}(\mathbf{r})$. The differentiation of eq. (3.24) with respect to $n(\mathbf{r})$ gives

$$\left.\frac{\delta\Omega[n]}{\delta n(\mathbf{r})}\right|_{n=\bar{n}} = \left.\frac{\delta F_{\text{int}}[n]}{\delta n(\mathbf{r})}\right|_{n=\bar{n}} - V_{\text{int}}(\mathbf{r}) = 0 \tag{3.26}$$

The fact that the right hand vanishes at equilibrium is agreed with eq. (3.8).

The solvation free energy functional $\mathcal{F}$ is defined as the difference between the grand potential functional of the solution system $\Omega[n]$ and of the correspondent reference bulk solvent at equilibrium $\Omega[\bar{n}_0]$:

$$\mathcal{F}[n] = \Omega[n] - \Omega[\bar{n}_0] \tag{3.27}$$

Here the character $\mathcal{F}$ is used for "free-energy functional"; it is a free energy of grand ensemble, but differs from Helmholtz free energy F. However, it can be proven that all the free energies become the same when the fluctuations in N and V are negligible [56].

As the external potential is absent for bulk solvent, we define:

$$\begin{aligned}
\mathcal{F}_{\text{int}}[n] &= \mathcal{F}[n] - \int \mathrm{d}\mathbf{r} n(\mathbf{r}) V_{\text{ext}}(\mathbf{r}) && (3.28)\\
&= F_{\text{int}}[n] - F_{\text{int}}[\bar{n}_0] - \mu \int \mathrm{d}\mathbf{r} \Delta n(\mathbf{r}) \\
&= k_{\text{B}}T \int \mathrm{d}\mathbf{r} n(\mathbf{r}) \left[\ln\left(\Lambda^3 n(\mathbf{r})\right) - 1\right] + F_{\text{exc}}\left[n(\mathbf{r})\right] && (3.29)\\
&\quad -k_{\text{B}}T \int \mathrm{d}\mathbf{r} \bar{n}_0 \left[\ln\left(\Lambda^3 \bar{n}_0\right) - 1\right] - F_{\text{exc}}\left[\bar{n}_0\right] - \mu \int \mathrm{d}\mathbf{r} \Delta n(\mathbf{r})
\end{aligned}$$

where $\Delta n(\mathbf{r}) = n(\mathbf{r}) - \bar{n}_0$.

If we write the external free energy $F_{\text{exc}}\left[n(\mathbf{r})\right]$ in Taylor expansion around $\bar{n}_0$:

$$\begin{aligned}
F_{\text{exc}}\left[n\right] &\equiv F_{\text{exc}}\left[\bar{n}_0\right] + \int \mathrm{d}\mathbf{r} \left.\frac{\delta F_{\text{exc}}\left[n\right]}{\delta n(\mathbf{r})}\right|_{n=\bar{n}_0} \Delta n(\mathbf{r}) \\
&\quad + \frac{1}{2} \int \mathrm{d}\mathbf{r}_1 \mathrm{d}\mathbf{r}_2 \left.\frac{\delta^2 F_{\text{exc}}\left[n\right]}{\delta n(\mathbf{r}_1)\delta n(\mathbf{r}_2)}\right|_{n=\bar{n}_0} \Delta n(\mathbf{r}_1)\Delta n(\mathbf{r}_2) + \mathcal{O}(\Delta n^3) \\
&= F_{\text{exc}}\left[\bar{n}_0\right] - k_{\text{B}}T \int \mathrm{d}\mathbf{r} c_0^{(1)}(\mathbf{r}) \Delta n(\mathbf{r}) \\
&\quad - \frac{k_{\text{B}}T}{2} \int \mathrm{d}\mathbf{r}_1 \mathrm{d}\mathbf{r}_2 c_0^{(2)}(\mathbf{r}_1, \mathbf{r}_2) \Delta n(\mathbf{r}_1) \Delta n(\mathbf{r}_2) + \mathcal{O}(\Delta n^3) && (3.30)
\end{aligned}$$

where $c_0^{(n)}(\mathbf{r})$ is the corresponding bulk DCF at equilibrium defined in eq. (3.20). According to eq. (3.21):

$$c_0^{(1)}(\mathbf{r}) = \ln\left(\Lambda^3 \bar{n}_0\right) - \beta\mu \tag{3.31}$$

we can find

$$\begin{aligned}\mathcal{F}_{\text{int}}[n] &= k_{\text{B}}T\int \mathrm{d}\mathbf{r}\left[n(\mathbf{r})\ln\left(\frac{n(\mathbf{r})}{\bar{n}_0}\right)-n(\mathbf{r})+\bar{n}_0\right] \\ &\quad -\frac{k_{\text{B}}T}{2}\int \mathrm{d}\mathbf{r}_1\mathrm{d}\mathbf{r}_2 c_0^{(2)}(\mathbf{r}_1,\mathbf{r}_2)\Delta n(\mathbf{r}_1)\Delta n(\mathbf{r}_2)+\mathcal{O}(\Delta n^3)\end{aligned} \tag{3.32}$$

Therefore, if we define:

$$\mathcal{F}_{\text{id}}[n] = k_{\text{B}}T\int \mathrm{d}\mathbf{r}\left[n(\mathbf{r})\ln\left(\frac{n(\mathbf{r})}{\bar{n}_0}\right)-n(\mathbf{r})+\bar{n}_0\right] \tag{3.33}$$

$$\mathcal{F}_{\text{exc}}[n] = -\frac{k_{\text{B}}T}{2}\int \mathrm{d}\mathbf{r}_1\mathrm{d}\mathbf{r}_2 c_0^{(2)}(\mathbf{r}_1,\mathbf{r}_2)\Delta n(\mathbf{r}_1)\Delta n(\mathbf{r}_2)+\mathcal{O}(\Delta n^3) \tag{3.34}$$

$$\mathcal{F}_{\text{ext}}[n] = \int \mathrm{d}\mathbf{r} n(\mathbf{r})V_{\text{ext}}(\mathbf{r}) \tag{3.35}$$

the free energy functional can be written as:

$$\mathcal{F}[n] = \mathcal{F}_{\text{int}}+\mathcal{F}_{\text{ext}} = \mathcal{F}_{\text{id}}+\mathcal{F}_{\text{exc}}+\mathcal{F}_{\text{ext}} \tag{3.36}$$

Up to this point a brilliant approach has been built, in that for a given choice V_N, T and μ, one can obtain the equilibrium density of solvent $\bar{n}(\mathbf{r})$ by minimizing the free energy functional:

$$\left.\frac{\delta\mathcal{F}[n]}{\delta n(\mathbf{r})}\right|_{n=\bar{n}} = 0 \tag{3.37}$$

Note that the two terms $\mathcal{F}_{\text{id}}[n]$ and $\mathcal{F}_{\text{ext}}[n]$ are physically exact, while the excess term $\mathcal{F}_{\text{exc}}[n]$, which can be rewritten as:

$$\mathcal{F}_{\text{exc}}[n] = -\frac{k_{\text{B}}T}{2}\int \mathrm{d}\mathbf{r}_1\mathrm{d}\mathbf{r}_2 C(\mathbf{r}_1,\mathbf{r}_2)\Delta n(\mathbf{r}_1)\Delta n(\mathbf{r}_2) \tag{3.38}$$

depends on the exact correlation function $C(\mathbf{r}_1,\mathbf{r}_2)$ which is a priori unknown.

If we ignore the three-body and higher order terms in eq. (3.34), $C(\mathbf{r}_1,\mathbf{r}_2)$ becomes that of the homogeneous reference fluid, which only depends on the relative distance, i.e. $c^{(2)}(\mathbf{r}_1,\mathbf{r}_2) = c(r_{12})$, so that

$$\mathcal{F}_{\text{exc}}[n] \simeq -\frac{k_{\text{B}}T}{2}\int \mathrm{d}\mathbf{r}_1\mathrm{d}\mathbf{r}_2 c(r_{12})\Delta n(\mathbf{r}_1)\Delta n(\mathbf{r}_2) \tag{3.39}$$

This was called the homogenous reference fluid (HRF) approximation. The generalization to a molecular, non-spherical solvent for which orientations matter is described in §4.

3.4 INTEGRAL EQUATION THEORY

Similar to the DFT approach which aims to find the equilibrium solvent density $\rho^{(1)} = \bar{n}$ and the free energy functional $\mathcal{F}$, the integral equation theory (IET) can also give structural and energetic informations by solving a pair of integral equations of $h^{(2)}(\mathbf{r}_1,\mathbf{r}_2)$ and $c^{(2)}(\mathbf{r}_1,\mathbf{r}_2)$ to find the pair distribution function g and the difference of correlation functions $\gamma = h - c$ which is directly linked to the free energy. One of the relations for h and c is the OZ equation shown as eq. (3.23). Note that in k-space eq. (3.23) can take advantage of the convolution properties to give a simple product relation:

$$\gamma(\mathbf{k}) = h(\mathbf{k})-c(\mathbf{k}) = \rho\left(\gamma(\mathbf{k})+c(\mathbf{k})\right)c(\mathbf{k}) \tag{3.40}$$

The second relation is a closure equation, which can be deduced from eq. (3.37), giving the minimum density

$$\rho^{(1)}(\mathbf{r}_1) = \rho_0^{(1)} \exp\left(-\beta V_{\text{ext}}(\mathbf{r}_1) + \int \mathrm{d}\mathbf{r}_2 \Delta\rho^{(1)}(\mathbf{r}_2) c^{(2)}(\mathbf{r}_1, \mathbf{r}_2) + \mathcal{O}(\Delta\rho^2)\right) \tag{3.41}$$

which gives, for example, when $\mathcal{O}(\Delta\rho^2) = 0$, one of the simplest closure equations, the hypernetted-chain HNC approximation:

$$g(1,2) = 1 + h(1,2) = \exp\left[-\beta u(1,2) + h(1,2) - c(1,2)\right] \tag{3.42}$$

Here u corresponds to V_{ext} in eq. (3.41) when the particles 1 and 2 are respectively the solute and solvent.

The general form of OZ closure is:

$$g(1,2) = \exp\left[-\beta u(1,2) + h(1,2) - c(1,2) + b(1,2)\right] \tag{3.43}$$

where the b is the bridge function. Other closures are also possible, such as Percus-Yevick (PY) approximation (a linear expansion of the second exponential term in HNC) specifically for systems with short-range forces, or mean-spherical approximation (MSA) in the limit of low density.

3.5 EQUIVALENCE BETWEEN CDFT AND IET FOR A DILUTE SOLUTION SYSTEM

The generalization of the OZ equation in eq. (3.23) to n components can be written as

$$h_{\nu\mu}(1,2) = c_{\nu\mu}(1,2) + \rho \sum_{\lambda} x_\lambda \int h_{\lambda\mu}(1,3) c_{\nu\lambda}(2,3) \mathrm{d}3 \tag{3.44}$$

where $x_\nu = N_\nu / N$ is the number concentration of species $\nu \in [1, n]$.

For a two-component homogeneous solute-solvent mixture, where the solute (M) is infinitely diluted in the solvent (S) ($x_S \to 1$), the coupled OZ relations are written as

$$h_{\text{SS}}(1,2) = c_{\text{SS}}(1,2) + \rho \int h_{\text{SS}}(1,3) c_{\text{SS}}(2,3) \mathrm{d}3 \tag{3.45}$$

$$h_{\text{SM}}(1,2) = c_{\text{SM}}(1,2) + \rho \int h_{\text{SS}}(1,3) c_{\text{SM}}(2,3) \mathrm{d}3 \tag{3.46}$$

$$h_{\text{MS}}(1,2) = c_{\text{MS}}(1,2) + \rho \int h_{\text{MS}}(1,3) c_{\text{SS}}(2,3) \mathrm{d}3 \tag{3.47}$$

$$h_{\text{MM}}(1,2) = c_{\text{MM}}(1,2) + \rho \int h_{\text{MS}}(1,3) c_{\text{SM}}(2,3) \mathrm{d}3 \tag{3.48}$$

Eq. (3.45) is the OZ equation for bulk solvent. Eqs. (3.46) and (3.47) describe the correlations between the solute and solvents, which are equivalent. From eq. (3.47) we can deduce eq. (3.34) for the DFT approach, if we impose $\mathcal{O}(\Delta\rho^3) = 0$, i.e. the HNC approximation. And in IET, eq. (3.46) is normally used for two-component solution. Eq. (3.48) is rarely used. The difficulty to solve such equation lies in finding a proper closure equation. As the approximations like HNC are already quantitatively far from sufficient to describe solute-solvent correlation, it becomes very bad for solute-solute.

4

Approach to Molecular Solvents

In the case of non-spherical solvents like water, the solvent particle carries a molecular structure described by a collection of distributed atomic interaction sites (LJ and Coulombic). The two theories mentioned in the previous section are now formulated in the molecular picture in which each solvent molecule is considered as a rigid body and characterized by its position $\mathbf{r}$ (e.g. the position of center of mass), and its orientation $\mathbf{\Omega}$. In MDFT, the solvent is characterized by an angle-dependent inhomogeneous density, $\rho(\mathbf{r},\mathbf{\Omega})$; in IET, an angle-dependent form of the pair distribution function $g(\mathbf{X}_1,\mathbf{X}_2)$ ($X \equiv (\mathbf{r},\mathbf{\Omega})$) is proposed, while the molecular OZ equation is expanded on rotational invariants. The reference interaction site model (RISM) [15], which provides another way for IET to treat molecular solvents, will not be discussed here for the sake of simplicity.

4.1 Molecular density functional theory

In molecular density functional theory (MDFT), the free energy functional is rewritten as:

$$\mathcal{F}[\rho(\mathbf{r},\mathbf{\Omega})] = \Omega[\rho(\mathbf{r},\mathbf{\Omega})] - \Omega[\rho_0] \tag{4.1}$$

where $\Omega[\rho_0]$ is the correspondent reference bulk fluid grand potential at equilibrium. $\rho(\mathbf{r},\mathbf{\Omega})$ is the angle-dependent fluid density function, depending on 3 variables for spatial coordinates $\mathbf{r}$, and also 3 for orientation $\mathbf{\Omega} \equiv (\Theta,\Phi,\Psi)$. In the case of linear solvents, this number can be reduced to 2, i.e. $\mathbf{\Omega} \equiv (\Theta,\Phi)$. The homogeneous bulk density ρ_0 is normalized to $n_0/\int \mathrm{d}\mathbf{\Omega}$, to keep coherent with the relation

$$\int \mathrm{d}\mathbf{\Omega}\rho(\mathbf{r},\mathbf{\Omega}) = \int \mathrm{d}\cos\Theta\mathrm{d}\Phi\mathrm{d}\Psi\rho(\mathbf{r},\mathbf{\Omega}) = n(\mathbf{r}) \tag{4.2}$$

which reduces eq. (4.1) to eq. (3.27) in §3.3.

According to the variation principle described in §3.3, the equilibrium density can be found by minimizing the free energy functional

$$\mathcal{F}[\rho] = \mathcal{F}_{\mathrm{id}}[\rho] + \mathcal{F}_{\mathrm{ext}}[\rho] + \mathcal{F}_{\mathrm{exc}}[\rho] \tag{4.3}$$

regarding to $\rho(\mathbf{r},\mathbf{\Omega})$:

$$\left.\frac{\delta\mathcal{F}[\rho]}{\delta\rho(\mathbf{r},\mathbf{\Omega})}\right|_{\rho=\bar{\rho}} = 0 \tag{4.4}$$

4.1.1 *The ideal term*

The ideal term $\mathcal{F}_{\mathrm{id}}[\rho]$ deduced from the particle interaction-free condition is:

$$\mathcal{F}_{\mathrm{id}}[\rho] = k_{\mathrm{B}}T\int \mathrm{d}\mathbf{r}\mathrm{d}\mathbf{\Omega}\left[\rho(\mathbf{r},\mathbf{\Omega})\ln\left(\frac{\rho(\mathbf{r},\mathbf{\Omega})}{\rho_0}\right) - \rho(\mathbf{r},\mathbf{\Omega}) + \rho_0\right] \tag{4.5}$$

The differentiation of $\mathcal{F}_{\mathrm{id}}[\rho]$ used for the minimization, which will be discussed later, has the form:

$$\frac{\delta\mathcal{F}_{\mathrm{id}}[\rho]}{\delta\rho(\mathbf{r},\mathbf{\Omega})} = k_{\mathrm{B}}T\ln\left(\frac{\rho(\mathbf{r},\mathbf{\Omega})}{\rho_0}\right) \tag{4.6}$$

4.1.2 *The external term*

The solute, like the solvent, is described in microscopic detail by a molecular non-polarizable force field involving atomic Lennard-Jones and partial charge parameters, creating at each point in space an external potential $V_{\text{ext}}(\mathbf{r}, \mathbf{\Omega})$, containing two components:

$$V_{\text{ext}}(\mathbf{r}, \mathbf{\Omega}) = V_{\text{LJ}}(\mathbf{r}) + V_{\text{coul}}(\mathbf{r}, \mathbf{\Omega}) \tag{4.7}$$

The external potential term calculates the contribution of V_{ext}:

$$\mathcal{F}_{\text{ext}}[\rho] = \int \mathrm{d}\mathbf{r}\mathrm{d}\mathbf{\Omega}\rho(\mathbf{r}, \mathbf{\Omega})V_{\text{ext}}(\mathbf{r}, \mathbf{\Omega}) \tag{4.8}$$

The Lennard-Jones potential is given by:

$$V_{\text{LJ}}(\mathbf{r}) = \sum_u \sum_v 4\epsilon_{uv} \left[\left(\frac{\sigma_{uv}}{r_{uv}} \right)^{12} - \left(\frac{\sigma_{uv}}{r_{uv}} \right)^{6} \right] \tag{4.9}$$

where u stands for solute, v stands for solvent, $\epsilon_{uv} = \sqrt{\epsilon_u \epsilon_v}$ and $\sigma_{uv} = (\sigma_u + \sigma_v)/2$ are the geometric and arithmetic average Lennard-Jones parameters between solute and solvent, according to the Lorentz-Berthelot mixing rules. r_{uv} is the norm of relative site-site vector

$$\mathbf{r}_{uv} = \mathbf{r} + \mathbf{R}(\mathbf{\Omega})\mathbf{s}_v - \mathbf{r}_u \tag{4.10}$$

where $\mathbf{r}_u$ and $\mathbf{s}_v$ are the coordinates of solute/solvent molecules in the molecular frame, and $\mathbf{R}(\mathbf{\Omega})$ is the rotation matrix of the Euler angles $\mathbf{\Omega}$. In cases where the solvent site wears only one LJ centre, eq. (4.10) reduces to

$$\mathbf{r}_{uv} = \mathbf{r} - \mathbf{r}_u \tag{4.11}$$

which is actually what we use in the code as the solvent is SPC/E water.

The Coulomb interaction is calculated by solving the Poisson equation. The charge density of the solute is projected onto a space grid $\mathbf{r}$,

$$\rho_q(\mathbf{r}) = \sum_u q_{ijk}/\Delta v \tag{4.12}$$

where q_{ijk} is the charge on the space grid distributed by its nearby point charge as shown in figure 4.1, and Δv is the volume of the unit cube that this point charge situates in.

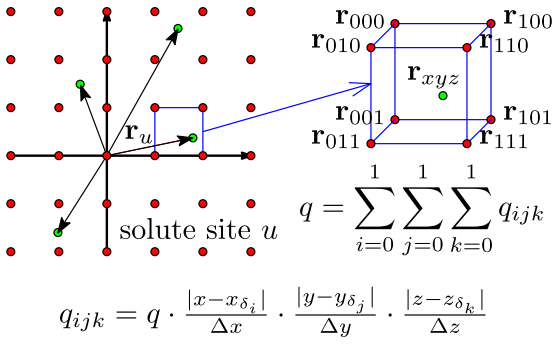

Figure 4.1: Solute charge density projected onto grids

The electrostatic potential created by the charge distribution $\rho_q(\mathbf{r})$, $V_q(\mathbf{r})$, can thus be computed using a periodic Poisson Solver. The Poisson equation (2.7)

$$\nabla^2 V_q(\mathbf{r}) = -\frac{\rho_q(\mathbf{r})}{\varepsilon_0} \tag{4.13}$$

gives in Fourier space

$$\hat{V}_q(\mathbf{k}) = \frac{\hat{\rho}_q(\mathbf{k})}{\varepsilon_0 k^2} \tag{4.14}$$

where $\hat{V}_q(\mathbf{k})$ and $\hat{\rho}_q(\mathbf{k})$ are the Fourier transform of $V_q(\mathbf{r})$ and $\rho_q(\mathbf{r})$ respectively. These two equations provide a fast way to calculate $V_q(\mathbf{r})$ from $\rho_q(\mathbf{r})$.

The Coulomb potential is expressed as a sum of solvent partial charge contributions at each grid node:

$$V_{\text{coul}}(\mathbf{r}, \mathbf{\Omega}) = \sum_v q_v V_q(\mathbf{r}_v) \tag{4.15}$$

where q_v is the point charge of solvent, and

$$\mathbf{r}_v = \mathbf{r} + \mathbf{R}(\mathbf{\Omega})\mathbf{s}_v \tag{4.16}$$

is the Cartesian coordinate of a solvent site v; $V_q(\mathbf{r}_u)$ is the electrostatic potential, given by a linear interpolation of the nearby point of $V_q(\mathbf{r})$ obtained in the last step from the Poisson solver.

Another method to calculate $V_{\text{coul}}(\mathbf{r}, \mathbf{\Omega})$ is direct summation, which gives a non-periodic external potential, but in the implementation it usually leads to better convergence for non-spherical molecules. Here we describe its expression, without going into the reason behind the convergence:

In this thesis we only work on the $\mathcal{F}_{\text{exc}}$ term.

$$V_{\text{coul}}(\mathbf{r}, \mathbf{\Omega}) = \sum_{u \in \text{solute}} \sum_{v \in \text{solvent}} \left(\frac{q_u q_v}{4\pi\varepsilon_0 r_{uv}} \right) \tag{4.17}$$

where r_{uv} is calculated as in eq. (4.10). For this thesis, the direct summation is only used in the minimization of non-spherical solutes, specifically in the chapters of implementation and application.

4.1.3 *The excess term*

As shown in §3.3, we invoke here the HRF approximation which amounts to a second-order Taylor expansion around the homogeneous fluid at density ρ_0:

$$\mathcal{F}_{\text{exc}}[\rho] = -\frac{k_B T}{2} \int \mathrm{d}\mathbf{r}_1 \mathrm{d}\mathbf{\Omega} \gamma(\mathbf{r}_1, \mathbf{\Omega}) \rho(\mathbf{r}_1, \mathbf{\Omega}) \tag{4.18}$$

where γ is the normalized gradient of the excess functional:

$$\gamma(\mathbf{r}_1, \mathbf{\Omega}_1) = -\frac{\delta \beta F_{\text{exc}}}{\delta \rho} = \int \mathrm{d}\mathbf{r}_2 \mathrm{d}\mathbf{\Omega}_2 \Delta\rho(\mathbf{r}_2, \mathbf{\Omega}_2) c(\mathbf{r}_{12}, \mathbf{\Omega}_1, \mathbf{\Omega}_2) \tag{4.19}$$

which can be related to the solute-solvent 2-component IET with its definition:

$$\gamma_{\text{MS}}(1,2) = h_{\text{MS}}(1,2) - c_{\text{MS}}(1,2) \tag{4.20}$$

To evaluate the integration $\int \mathrm{d}\mathbf{r}_2 \mathrm{d}\mathbf{\Omega}_2$ for each gradient $\gamma(\mathbf{r}_1, \mathbf{\Omega}_1)$ in eq. (4.19), a total number of $N^2 \equiv N_{\mathbf{r}}^2 N_{\mathbf{\Omega}}^2 = O(N^2)$ function evaluations (FE) are required, which, with typically $N_{\mathbf{r}} = 64^3$ and $N_{\mathbf{\Omega}} = 50 \sim 100$, is far too costly for current computing technology. For this reason, Fourier transform is used to treat the spatial convolution.

A convolution

$$h(x_1) \equiv f(x_2) \otimes g(x_2) \equiv \int f(x_2) g(x_1 - x_2) dx_2 \tag{4.21}$$

has the property that

$$\mathfrak{F}[h(x_1)] = \mathfrak{F}[f(x_2)]\mathfrak{F}[g(x_2)] \tag{4.22}$$

$\mathfrak{F}$ being the Fourier transform operation. As $\mathbf{r}_{12} = \mathbf{r}_1 - \mathbf{r}_2$, eq. (4.19) is a 3D convolution, which leads to

$$\hat{\gamma}(\mathbf{k}, \mathbf{\Omega}_1) = \int \mathrm{d}\mathbf{\Omega}_2 \Delta\hat{\rho}(\mathbf{k}, \mathbf{\Omega}_2)\hat{c}(\mathbf{k}, \mathbf{\Omega}_1, \mathbf{\Omega}_2) \tag{4.23}$$

Here we put the hat symbol on the physical quantities to represent the Fourier transform of their original function.

In eq. (4.23), the integral $\int \mathrm{d}\mathbf{r}_2$ of eq. (4.19) is transformed into a simple product; only $N_\mathbf{r} N_\mathbf{\Omega}^2$ FE are needed to obtain $\hat{\gamma}(\mathbf{k}, \mathbf{\Omega}_1)$ with given $\Delta\hat{\rho}(\mathbf{k}, \mathbf{\Omega}_2)$. To this computational cost should be added the transform from $\Delta\rho(\mathbf{r}, \mathbf{\Omega})$ to $\Delta\hat{\rho}(\mathbf{k}, \mathbf{\Omega})$ and the backward transform from $\hat{\gamma}(\mathbf{k}, \mathbf{\Omega})$ to $\gamma(\mathbf{r}, \mathbf{\Omega})$ which are both of order $N_\mathbf{\Omega} \cdot O(N_\mathbf{r} \log_2 N_\mathbf{r})$ due to the properties of Fast Fourier Transform (FFT). The total number of FE is thus reduced from quadratic complexity $O(N_\mathbf{r}^2 N_\mathbf{\Omega}^2)$ to $N_\mathbf{r} N_\mathbf{\Omega}^2 + 2N_\mathbf{\Omega} \cdot O(N_\mathbf{r} \log_2 N_\mathbf{r}) = O(N_\mathbf{r} \log_2 N_\mathbf{r} N_\mathbf{\Omega}^2)$. As the total number of spatial grid $N_\mathbf{r}$ is of magnitude $10^5 \sim 10^6$, this procedure, which is mathematically equivalent to the direct evaluation (4.19), offers a great advantage in terms of computational efficiency (figure A.1 in appendix A).

The angular-dependent DCF of the homogeneous solvent, $\hat{c}(\mathbf{k}, \mathbf{\Omega}_1, \mathbf{\Omega}_2)$, is an input data which can be obtained from MD or MC simulations. A detailed presentation of the DCFs used in this thesis is available in appendix B.

4.2 MOLECULAR INTEGRAL EQUATION THEORY

To adapt the IET formalism to non-spherical solvent, Blum [16–18] proposed to expand the angle-dependent correlation functions $F(\mathbf{X}_1, \mathbf{X}_2) \equiv F(\mathbf{r}_1, \mathbf{r}_2, \mathbf{\Omega}_1, \mathbf{\Omega}_2)$ onto rotational invariants, such that the OZ equation can be reduced to only a few FE. This theory is then adopted by Fries & Patey [19], who proposed a numerical solution for full HNC closure. The test below describes the theory of Blum, but based on the convention of Fries & Patey, where Messiah's definition of generalized spherical harmonics (GSHs) is used. A detailed explication of different conventions of GSH is given in appendix H.

4.2.1 *Translational and rotational invariance*

If F describes a homogeneous fluid, the translational invariance ($\mathbf{r}_{12} \equiv \mathbf{r}_1 - \mathbf{r}_2$) should be presented, then the number of independent variables is reduced from 12 to 9:

$$F(\mathbf{X}_1, \mathbf{X}_2) = F(\mathbf{r}_{12}, \mathbf{\Omega}_1, \mathbf{\Omega}_2) = F(r, \hat{\mathbf{r}}_{12}, \mathbf{\Omega}_1, \mathbf{\Omega}_2) \tag{4.24}$$

We can further expand F on Wigner GSHs of the three orientations; then F becomes a sum of an infinite number of projections that depending on r and 8 indices:

$$F(\mathbf{X}_1, \mathbf{X}_2) = \sum_{m,n,l=0}^{\infty} \sum_{|\mu',\mu| \le m, |\nu',\nu| \le n, |\lambda'| \le l} F^{mnl}_{\mu'\mu\nu'\nu\lambda'}(r) R^m_{\mu'\mu}(\mathbf{\Omega}_1) R^m_{\nu'\nu}(\mathbf{\Omega}_2) R^l_{\lambda' 0}(\hat{\mathbf{r}}_{12}) \tag{4.25}$$

Assuming that this expansion converges, which is normally the case for correlation functions, the expansion can be expressed in a limited number of projections. If we also take into account the rotational invariance by recombining some terms, only r and 5 independent indices are necessary to describe all the projections:

$$F^{mnl}_{\mu\nu}(r) = \sum_{\mu'\nu'\lambda'} \begin{pmatrix} m & n & l \\ \mu' & \nu' & \lambda' \end{pmatrix} F^{mnl}_{\mu'\mu\nu'\nu\lambda'}(r) \tag{4.26}$$

The projections $F^{mnl}_{\mu\nu}(r)$ with a finite order of expansion have much fewer of terms compared to the angular form in eq. (4.24) with the same precision of description.

We can define a basis set of rotational invariant as:

$$\Phi^{mnl}_{\mu\nu}(\mathbf{\Omega}_1,\mathbf{\Omega}_2,\hat{\mathbf{r}}_{12}) = f^{mnl}\sum_{\mu'\nu'\lambda'}\begin{pmatrix} m & n & l \\ \mu' & \nu' & \lambda' \end{pmatrix} R^m_{\mu'\mu}(\mathbf{\Omega}_1)R^n_{\nu'\nu}(\mathbf{\Omega}_2)R^l_{\lambda'0}(\hat{\mathbf{r}}_{12}) \tag{4.27}$$

where the normalization factor f^{mnl} can be any arbitrary non-zero constant, depending only on indices m, n, l. In Blum's convention, it is taken as $[(2m+1)\,(2n+1)]^{\frac{1}{2}}$.

With these definitions, the relation between the projections and the original function is:

$$F(\mathbf{X}_1,\mathbf{X}_2) = \sum_{mnl\mu\nu}\tilde{F}^{mnl}_{\mu\nu}(r)\Phi^{mnl}_{\mu\nu}(\mathbf{\Omega}_1,\mathbf{\Omega}_2,\hat{\mathbf{r}}_{12}) \tag{4.28}$$

where $\tilde{F}^{mnl}_{\mu\nu}(r) = F^{mnl}_{\mu\nu}(r)/f^{mnl}$.

4.2.2 *Blum's reduction of molecular OZ equation*

The molecular Ornstein-Zernike (MOZ) equation is defined as:

$$\gamma(\mathbf{X}_1,\mathbf{X}_2) = h(\mathbf{X}_1,\mathbf{X}_2) - c(\mathbf{X}_1,\mathbf{X}_2) = \frac{\rho}{8\pi^2}\int \mathrm{d}\mathbf{X}_3 h(\mathbf{X}_1,\mathbf{X}_3)c(\mathbf{X}_3,\mathbf{X}_2) \tag{4.29}$$

The rotational invariant expansion gives:

$$c(\mathbf{X}_1,\mathbf{X}_2) = \sum_{mnl\mu\nu} c^{mnl}_{\mu\nu}(r)\Phi^{mnl}_{\mu\nu}(\mathbf{\Omega}_1,\mathbf{\Omega}_2,\hat{\mathbf{r}}_{12}) \tag{4.30}$$

$$\gamma(\mathbf{X}_1,\mathbf{X}_2) = \sum_{mnl\mu\nu} \gamma^{mnl}_{\mu\nu}(r)\Phi^{mnl}_{\mu\nu}(\mathbf{\Omega}_1,\mathbf{\Omega}_2,\hat{\mathbf{r}}_{12}) \tag{4.31}$$

and also in k-space:

$$\hat{c}(\mathbf{k},\mathbf{\Omega}_1,\mathbf{\Omega}_2) = \sum_{mnl\mu\nu} \hat{c}^{mnl}_{\mu\nu}(k)\Phi^{mnl}_{\mu\nu}(\mathbf{\Omega}_1,\mathbf{\Omega}_2,\hat{\mathbf{k}}) \tag{4.32}$$

$$\hat{\gamma}(\mathbf{k},\mathbf{\Omega}_1,\mathbf{\Omega}_2) = \sum_{mnl\mu\nu} \hat{\gamma}^{mnl}_{\mu\nu}(k)\Phi^{mnl}_{\mu\nu}(\mathbf{\Omega}_1,\mathbf{\Omega}_2,\hat{\mathbf{k}}) \tag{4.33}$$

The relation between these projections in r and k-space is built by the Hankel transform:

$$\hat{c}^{mnl}_{\mu\nu}(k) = 4\pi i^l \int \mathrm{d}r\, r^2 j_l(kr) c^{mnl}_{\mu\nu}(r) \tag{4.34}$$

$$\hat{\gamma}^{mnl}_{\mu\nu}(k) = 4\pi i^l \int \mathrm{d}r\, r^2 j_l(kr) \gamma^{mnl}_{\mu\nu}(r) \tag{4.35}$$

where $j_l(kr)$ are the spherical Bessel functions of order l. Eq. (4.34) and (4.35) are built in the same purpose as eq. (3.40) in atomic case, where FFT is used. As an analogue to FFT, the fast Hankel transform is available for such a process.

Note that if function $f(\mathbf{X}_1,\mathbf{X}_2)$ is real and the molecules processes a symmetry axis C_{2v}, like water, the projections $f^{mnl}_{\mu\nu}(r)$ are real, therefore $\hat{f}^{mnl}_{\mu\nu}(k)$ is real if l is even, and pure imaginary if l is odd. The complete symmetry relations are listed in §F.5.

The MOZ equation based on the rotational invariants $\hat{f}^{mnl}_{\mu\nu}(k)$ can be found in the article of Blum [16], but the form is a bit complicated. To provide a simpler form, Blum defined the χ-transform:

$$\hat{c'}^{mn}_{\mu\nu,\chi}(k) = \sum_{l=|m-n|}^{m+n}\begin{pmatrix} m & n & l \\ \chi & -\chi & 0 \end{pmatrix}\hat{c}^{mnl}_{\mu\nu}(k) \tag{4.36}$$

$$\hat{\gamma}'^{mn}_{\mu\nu,\chi}(k) = \sum_{l=|m-n|}^{m+n} \begin{pmatrix} m & n & l \\ \chi & -\chi & 0 \end{pmatrix} \hat{\gamma}^{mnl}_{\mu\nu}(k) \tag{4.37}$$

where we use the apostrophe to represent functions in an intermolecular frame.

The result MOZ equation is:

$$\hat{\gamma}'^{mn}_{\mu\nu,\chi}(k) = \rho \sum_{n_1} \sum_{\nu_1=-n_1}^{n_1} (-)^{\chi+\nu_1} \left[\hat{\gamma}'^{mn_1}_{\mu\nu_1,\chi}(k) + \hat{c}'^{mn_1}_{\mu\nu_1,\chi}(k)\right] \hat{c}'^{n_1 n}_{\underline{\nu_1}\nu,\chi}(k) \tag{4.38}$$

This simple form of MOZ equation reduces the calculation of $\int \mathrm{d}\mathbf{X}_3$ for each $(\mathbf{X}_1, \mathbf{X}_2)$ in eq. (4.29) to only a sum of terms of n_1, ν_1 for each index of projection.

5

Code MDFT

The code MDFT upon which all the development in this thesis is based is a Fortran 95 sequential code developed by Maximilien Levesque, Daniel Borgis *et al.* [23–32], which implements the MDFT theory. It reads the force field (Lennard-Jones and Coulomb parameters) describing the solute and the solvent as input, as well as necessary parameters like the temperature T, number density of solvent n_0, etc. It minimizes the functional and gives the equilibrium density $\rho(\mathbf{r}, \mathbf{\Omega})$, then computes output properties.

5.1 Supercell discretization

$L_x \times L_y \times L_z \left[\text{Å}^3\right]$ space is discretized on a regular grid of $\text{nfft}_1 \times \text{nfft}_2 \times \text{nfft}_3$ nodes. The solute center is at $\mathbf{r}_T = \left(\frac{L_x}{2}, \frac{L_y}{2}, \frac{L_z}{2}\right)$ of the box. If the internal coordinates of solute $\mathbf{r}_M$, the solute coordinates in the box $\mathbf{r} = \mathbf{r}_M + \mathbf{r}_T$.

Angular grid is discretized with Lebedev (L) quadrature for $\mathbf{\Omega} \equiv (\Theta, \Phi)$, $\Theta \in [0, \pi]$, $\Phi \in [0, 2\pi]$, or Gauss-Legendre (GL) quadrature for Θ and trapezoidal quadrature for Φ. $\Psi \in [0, \pi]$ as we used the code mainly for water, is discretized with trapezoidal quadrature. The number of each angular dimension is linked to the order of quadrature, $m_{\max}$, which is discussed mainly in the chapter of theory.

5.2 Minimizer L-BFGS-B

The minimizer adopted by MDFT is the L-BFGS-B [57, 58] package version 3.0 written in Fortran 77, implementing the limited-memory Broyden-Fletcher-Goldfarb-Shanno (BFGS) algorithm with constraints of the form $l \leq x \leq u$ to the variable x.

The functional $\mathcal{F}[x_i]$ and the gradient of functional $\nabla\mathcal{F}[x_i] = \frac{\delta\mathcal{F}}{\delta x}(x_i)$ are required by L-BFGS to minimize the functional. It saves the variables x_i and gradients of the past m iterations, which requires a lot of memory.

The functional in MDFT to be minimized is eq. (4.3):

$$\mathcal{F}[\rho] = \mathcal{F}_{\text{id}}[\rho] + \mathcal{F}_{\text{ext}}[\rho] + \mathcal{F}_{\text{exc}}[\rho] \tag{5.1}$$

and its gradient is

$$\frac{\delta\mathcal{F}[\rho]}{\delta\rho(\mathbf{r}, \mathbf{\Omega})} = k_{\text{B}}T \ln\left(\frac{\rho(\mathbf{r}, \mathbf{\Omega})}{\rho_0}\right) + V_{\text{exc}}(\mathbf{r}, \mathbf{\Omega}) + V_{\text{ext}}(\mathbf{r}, \mathbf{\Omega}) \tag{5.2}$$

where ρ_0 is the angular density of bulk solvent,

$$\rho_0 = \begin{cases} n_0 & \text{if atomic, } \Omega \equiv 1 \\ n_0/4\pi & \text{if linear, } \Omega \equiv (\Theta, \Phi) \\ n_0/8\pi^2 & \text{if non-linear, } \Omega \equiv (\Theta, \Phi, \Psi) \end{cases} \tag{5.3}$$

such that $\int \mathrm{d}\mathbf{\Omega}\rho(\mathbf{r}, \mathbf{\Omega})/\rho_0 = n(\mathbf{r})/n_0$ is normalized to 1 when $r \to \infty$.

5.3 TREATMENT TO AVOID UNPHYSICAL DENSITY

During minimization, the density variable $\rho(\mathbf{r}, \mathbf{\Omega})$ can have unphysical negative numbers, which also cause the divergence of the minimization. To avoid this phenomenon, a normalized $\varphi(\mathbf{r}, \mathbf{\Omega})$ is used as the variable during the minimization in place of $\rho(\mathbf{r}, \mathbf{\Omega})$, so that:

$$\rho(\mathbf{r}, \mathbf{\Omega}) = \rho_0 \varphi^2(\mathbf{r}, \mathbf{\Omega}) \tag{5.4}$$

According to the definition (5.4), we see:

$$\frac{\delta\rho(\mathbf{r}, \mathbf{\Omega})}{\delta\varphi} = 2\rho_0\varphi(\mathbf{r}, \mathbf{\Omega}) \tag{5.5}$$

Therefore the gradient to feed the L-BFGS minimizer is:

$$\frac{\delta\mathcal{F}}{\delta\varphi} = \frac{\delta\mathcal{F}}{\delta\rho} \cdot \frac{\delta\rho}{\delta\varphi} = 2\rho_0\varphi(\mathbf{r}, \mathbf{\Omega}) \cdot \left[\beta^{-1} \ln\varphi^2 + V_{\text{exc}} + V_{\text{ext}}\right] \tag{5.6}$$

The main structure of the code is shown in figure 5.1.

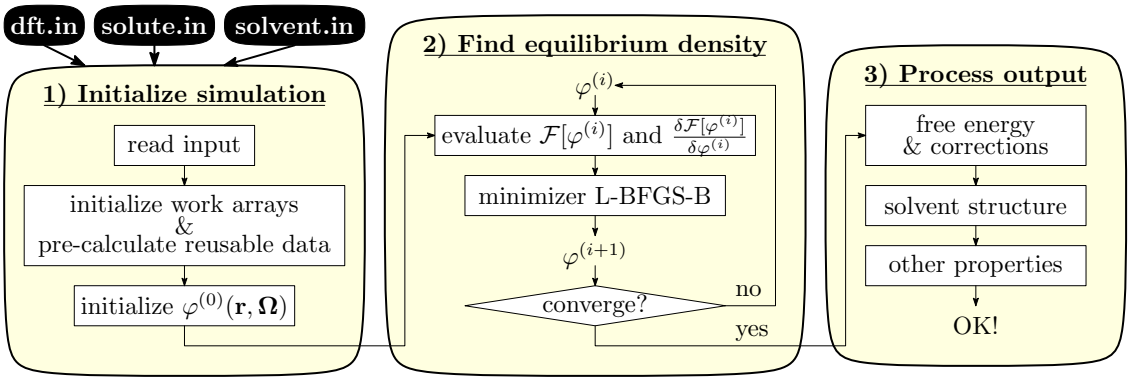

Figure 5.1: Main structure of code MDFT

5.4 FAST FOURIER TRANSFORM

The fast Fourier transform (FFT) is used, for example, in the evaluation of excess functional in eq. (4.23); in this thesis, the FFTW3 library [59] is used for implementation, which performs discrete Fourier Transform (DFT) as defined below:

$$Y_k = \sum_{j=0}^{n-1} X_j e^{-2\pi ijk/n} \quad \text{(forward)} \tag{5.7}$$

$$X_j = \sum_{k=0}^{n-1} Y_k e^{2\pi ijk/n} \quad \text{(backward)} \tag{5.8}$$

Note that after a forward-backward Fourier transform, the original function is multiplied by a normalization factor N_k, which is the total number of nodes k.

For input function Y_k ($k = 0, \ldots, n-1$) in real numbers, FFTW3 only outputs elements $k = 0, \ldots, \lfloor n/2 \rfloor$ ($\lfloor n/2 \rfloor + 1$ complex numbers of X_j are stocked; $\lfloor n/2 \rfloor$ being the floor function of $n/2$), with the "Hermitian" symmetry

$$Y_k = Y^*_{n-k} \tag{5.9}$$

used to regenerate elements of $k > \lfloor n/2 \rfloor$. The resulting X_j issued from the corresponding backward transform is purely real.

The definition of FFT can differ in some literature, with the "+" sign in the exponential of forward transform and "−" sign in the exponential of backward transform. According to the Hermitian symmetry, we should use the quantities in k-space issued from the definition with its conjugate form.

Chapter II

Theory: HRF Approximation, For Molecular Solvent

This chapter presents a complete theory of the $\mathcal{F}_{\text{exc}}$ evaluation under HRF approximation.

As presented in section 5, to complete the minimization process of MDFT, we need to evaluate the excess functional

$$\mathcal{F}_{\text{exc}} = -\frac{k_{\text{B}}T}{2}\int \mathrm{d}\mathbf{r}_1\mathrm{d}\mathbf{r}_2\mathrm{d}\mathbf{\Omega}_1\mathrm{d}\mathbf{\Omega}_2\Delta\rho(\mathbf{r}_1,\mathbf{\Omega}_1)\Delta\rho(\mathbf{r}_2,\mathbf{\Omega}_2)c(\mathbf{r}_{12},\mathbf{\Omega}_1,\mathbf{\Omega}_2) \quad \text{(II.1)}$$

as well as its gradient (normalized as dimensionless)

$$\gamma(\mathbf{r}_1,\mathbf{\Omega}_1) = \int \mathrm{d}\mathbf{r}_2\mathrm{d}\mathbf{\Omega}_2\Delta\rho(\mathbf{r}_2,\mathbf{\Omega}_2)c(\mathbf{r}_{12},\mathbf{\Omega}_1,\mathbf{\Omega}_2) \quad \text{(II.2)}$$

As discussed in §4.1.3, eq. (II.2) is a 3D convolution, which leads to

$$\hat{\gamma}(\mathbf{k},\mathbf{\Omega}_1) = \int \mathrm{d}\mathbf{\Omega}_2\Delta\hat{\rho}(\mathbf{k},\mathbf{\Omega}_2)\hat{c}(\mathbf{k},\mathbf{\Omega}_1,\mathbf{\Omega}_2) \quad \text{(II.3)}$$

such that the integral $\int \mathrm{d}\mathbf{r}_2$ in eq. (II.2) is transformed into a simple product in eq. (II.3), giving a great advantage in terms of computational efficiency for huge spatial grids.

From the previous work [32], $\hat{c}(\mathbf{k},\mathbf{\Omega}_1,\mathbf{\Omega}_2)$ in eq. (II.3) is evaluated with a pre-tabulated intermolecular DCF, $\hat{c}(k,\cos\theta_1,\cos\theta_2,\phi_{12})$, which is appropriate for linear molecules. Section 6 gives a complete evaluation of $\hat{c}(\mathbf{k},\mathbf{\Omega}_1,\mathbf{\Omega}_2)$ using either a full intermolecular DCF $\hat{c}(k,\cos\theta_1,\cos\theta_2,\phi_{12},\psi_1,\psi_2)$ or rotational invariant projections.

On the other hand, the increased precision of DCF evaluation makes the computing cost of the original algorithm no longer reasonable. Section 7 presents a new algorithm to treat the angular convolution in eq. (II.3), which takes advantage of the rotational invariance by expanding the density variable $\rho(\mathbf{r},\mathbf{\Omega})$ on Wigner generalized spherical harmonics. In this algorithm, the OZ equation is largely simplified, and the memory needed for the storage of DCF is no longer important.

The solvent properties involved in this thesis are presented in section 8 and organized in two aspects, the energy and the structure. The solvation free energy corrections and some forms of structure are presented.

6

Angular Integration in Excess Functional

As discussed in last chapter, the Fourier transform of the excess functional gradient is:

$$\hat{\gamma}(\mathbf{k}, \mathbf{\Omega}_1) = \int \mathrm{d}\mathbf{\Omega}_2 \Delta\hat{\rho}(\mathbf{k}, \mathbf{\Omega}_2)\hat{c}(\mathbf{k}, \mathbf{\Omega}_1, \mathbf{\Omega}_2) \tag{6.1}$$

It should be pointed out that the direct correlation function (DCF), $\hat{c}(\mathbf{k}, \mathbf{\Omega}_1, \mathbf{\Omega}_2)$, used as input data in eq. (6.1) is very memory-costly. In the previous work [23, 32, 60], the DCF was stocked in the intermolecular form $\hat{c}(k, \boldsymbol{\omega}_1, \boldsymbol{\omega}_2)$ to take advantage of an economy of memory, where $(\boldsymbol{\omega}_1, \boldsymbol{\omega}_2) \equiv (\cos\theta_1, \cos\theta_2, \phi_{12})$, and the correspondence of $(\mathbf{\Omega}_1, \mathbf{\Omega}_2)$ to $(\boldsymbol{\omega}_1, \boldsymbol{\omega}_2)$ is calculated directly in the code. These works adapt well with linear solvents, but are proven less powerful for molecular solvents such as water. However, in the case of full Euler angles intermolecular DCF (fig. 6.1),

$$\hat{c}(k, \boldsymbol{\omega}_1, \boldsymbol{\omega}_2) \equiv \hat{c}(k, \cos\theta_1, \cos\theta_2, \phi, \psi_1, \psi_2) \tag{6.2}$$

neither the storage of $\hat{c}(\mathbf{k}, \mathbf{\Omega}_1, \mathbf{\Omega}_2)$ which is definitively impossible, nor the direct calculation of correspondence $(\mathbf{\Omega}_1, \mathbf{\Omega}_2)$ to $(\boldsymbol{\omega}_1, \boldsymbol{\omega}_2)$ due to the increased complexity and resulting cost, can be regarded as possible solutions. For instance, with a normal setting of 64^3 spatial grid and a Lebedev quadrature of order 2 (14 angles for Θ and Φ), and 3 Ψ-angles, even if the DCF is stocked in simple precision (complex number), it takes $64^3 \times 42^2 \times 4\,\text{bytes} \times 2 = 3.52\text{GB}$, and for a Lebedev quadrature of order 5 and correspondingly 5 Ψ-angles, it takes $64^3 \times 250^2 \times 4\,\text{bytes} \times 2 = 131\text{GB}$. As a normal PC has only 4 to 16 GB of RAM, this can cause a memory leak.

Therefore, two strategies are developed to treat the full DCF case. The first one is a direct extension of the previous work, which uses the full intermolecular DCF with a more complicated angle correspondence pre-tabulated in the beginning of the implementation. The other calculates the DCF directly from rotational invariant projections. Here we give a complete discussion of these two strategies.

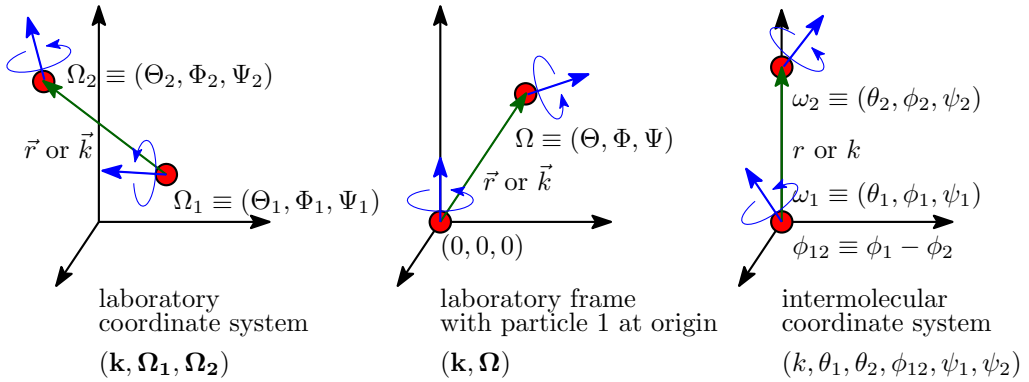

Figure 6.1: Molecules 1 and 2 in different coordinate systems. The laboratory coordinate system is the system of our grid with a fixed reference view. When one of the molecules is considered as the reference, e.g. the solute in the case of $\rho(\mathbf{r}, \mathbf{\Omega})$, only one $\mathbf{\Omega}$ needs to be described. For the intermolecular frame, in $\mathbf{r}$-space, the z axis is oriented along the vector $\mathbf{r}_{12} = \mathbf{r}_2 - \mathbf{r}_1$, or in $\mathbf{k}$-space along the vector $\mathbf{k}$. An orientation $\mathbf{\Omega} \equiv (\Theta, \Phi, \Psi)$ in laboratory frame corresponds to $\boldsymbol{\omega} \equiv (\theta, \phi, \psi)$ in intermolecular frame.

6.1 USING FULL INTERMOLECULAR DCF

For the full DCF in intermolecular coordinates system, $\hat{c}(k, \boldsymbol{\omega}_1, \boldsymbol{\omega}_2)$, only 6 variables are needed instead of 9 for $\hat{c}(\mathbf{k}, \boldsymbol{\Omega}_1, \boldsymbol{\Omega}_2)$, and the storage is considerably reduced. The transformation from $\hat{c}(\mathbf{k}, \boldsymbol{\Omega}_1, \boldsymbol{\Omega}_2)$ to $\hat{c}(k, \boldsymbol{\omega}_1, \boldsymbol{\omega}_2)$ relies on the correspondence $\boldsymbol{\omega}(\mathbf{k}, \boldsymbol{\Omega}) \equiv (\cos\theta, \phi, \psi)$, which is here pre-calculated as a table of data.

Finding $\boldsymbol{\omega}$ from $\boldsymbol{\Omega}$ amounts to defining the correspondence between the rotation matrices of the two coordinate systems. The rotation matrix $\hat{\mathbf{R}}_{\boldsymbol{\Omega}}$ that rotates the solvent molecule from $\mathbf{I}$ to its orientation $\hat{\mathbf{R}}_{\boldsymbol{\Omega}}$

$$\hat{\mathbf{R}}_{\boldsymbol{\Omega}}\mathbf{I} = \hat{\mathbf{R}}_{\boldsymbol{\Omega}} \tag{6.3}$$

can be expressed by 3 rotation operations $\hat{\mathbf{R}}_{\Phi}$, $\hat{\mathbf{R}}_{\Theta}$, and $\hat{\mathbf{R}}_{\Psi}$ which rotate along z-y-z axes (the same convention as defined in Messiah [61] and Gray-Gubbins [13]):

$$\begin{aligned}
\hat{\mathbf{R}}_{\boldsymbol{\Omega}} &= \begin{bmatrix} R_{xx} & R_{xy} & R_{xz} \\ R_{yx} & R_{yy} & R_{yz} \\ R_{zx} & R_{zy} & R_{zz} \end{bmatrix} \\
&= \begin{bmatrix} \cos\Phi & -\sin\Phi & 0 \\ \sin\Phi & \cos\Phi & 0 \\ 0 & 0 & 1 \end{bmatrix} \begin{bmatrix} \cos\Theta & 0 & \sin\Theta \\ 0 & 1 & 0 \\ -\sin\Theta & 0 & \cos\Theta \end{bmatrix} \begin{bmatrix} \cos\Psi & -\sin\Psi & 0 \\ \sin\Psi & \cos\Psi & 0 \\ 0 & 0 & 1 \end{bmatrix} \\
&= \begin{bmatrix} \cos\Phi\cos\Theta\cos\Psi - \sin\Phi\sin\Psi & -\cos\Phi\cos\Theta\sin\Psi - \sin\Phi\cos\Psi & \cos\Phi\sin\Theta \\ \sin\Phi\cos\Theta\cos\Psi + \cos\Phi\sin\Psi & -\sin\Phi\cos\Theta\sin\Psi + \cos\Phi\cos\Psi & \sin\Phi\sin\Theta \\ -\sin\Theta\cos\Psi & \sin\Theta\sin\Psi & \cos\Theta \end{bmatrix}
\end{aligned} \tag{6.4}$$

As shown in fig. 6.2, the rotation matrix to transform the DCF from the intermolecular coordinates to laboratory coordinates $\hat{\mathbf{R}}_{\boldsymbol{\omega}}$ can be written as:

$$\hat{\mathbf{R}}_{\boldsymbol{\omega}} = \hat{\mathbf{R}}_{\mathbf{k}}^{-1}\hat{\mathbf{R}}_{\boldsymbol{\Omega}} \tag{6.5}$$

with the rotation matrix related to $\mathbf{k}$ vector:

$$\hat{\mathbf{R}}_{\mathbf{k}}^{-1} = \begin{bmatrix} \cos\theta_k\cos\phi_k & \cos\theta_k\sin\phi_k & -\sin\theta_k \\ -\sin\phi_k & \cos\phi_k & 0 \\ \sin\theta_k\cos\phi_k & \sin\theta_k\sin\phi_k & \cos\theta_k \end{bmatrix} \tag{6.6}$$

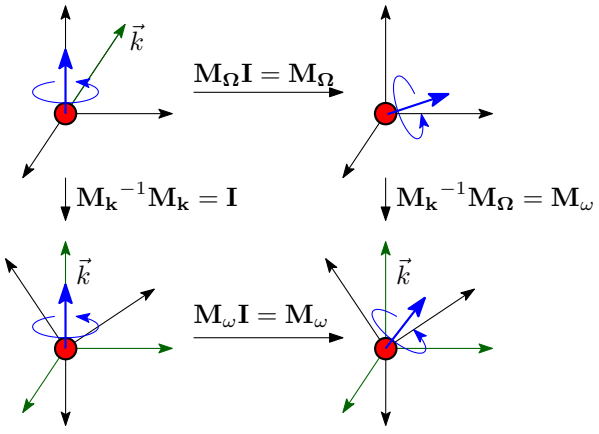

Figure 6.2: Rotation matrices

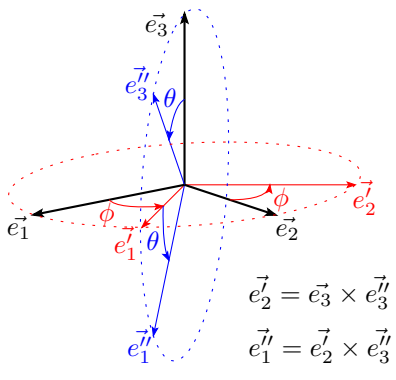

Figure 6.3: Rotation to k-frame

Here we fix $\psi_k = 0$. θ_k and ϕ_k are calculated from Cartesian coordinates (k_x, k_y, k_z). In extreme cases where we cannot define θ_k (for $\|\mathbf{k}\| = 0$) and ϕ_k (for $k_x^2 + k_y^2 = 0$), we can arbitrarily fix those angles to zero.

A faster way to find the rotation matrix of $\mathbf{k}$, avoiding the evaluation of trigonometric functions, is shown in figure 6.3, where the matrix can be calculated by the cross products of basis vectors from z axis and $\mathbf{k}$ vector ($\mathbf{k} = \mathbf{e}_3''$):

$$\left[\begin{array}{ccc} \mathbf{e}_1'' & \mathbf{e}_2' & \mathbf{e}_3'' \end{array} \right] = \left[\begin{array}{ccc} \mathbf{e}_1 & \mathbf{e}_2 & \mathbf{e}_3 \end{array} \right] \hat{\mathbf{R}}_{\mathbf{k}} = \hat{\mathbf{R}}_{\mathbf{k}} \tag{6.7}$$

The two ways to calculate $\mathbf{k}$ differ only in the case of $\hat{\mathbf{k}} = \left[\begin{array}{ccc} 0 & 0 & -1 \end{array} \right]^T$, where one is the inverse of the other. This is due to the different definitions of ϕ_k (0 or π when $\overrightarrow{k_z'}$ superposes with $\overrightarrow{k_z}$) in the two cases. Tests have shown that it has no influence on the final result of the excess functional evaluation.

The elements of $\hat{\mathbf{R}}_{\boldsymbol{\omega}}$ can be calculated according to eq. (6.5), which possesses the form:

$$\begin{aligned} \hat{\mathbf{R}}_{\boldsymbol{\omega}} &= \left[\begin{array}{ccc} u_x & v_x & w_x \\ u_y & v_y & w_y \\ u_z & v_z & w_z \end{array} \right] \\ &= \left[\begin{array}{ccc} \cos\phi\cos\theta\cos\psi - \sin\phi\sin\psi & -\cos\phi\cos\theta\sin\psi - \sin\phi\cos\psi & \cos\phi\sin\theta \\ \sin\phi\cos\theta\cos\psi + \cos\phi\sin\psi & -\sin\phi\cos\theta\sin\psi + \cos\phi\cos\psi & \sin\phi\sin\theta \\ -\sin\theta\cos\psi & \sin\theta\sin\psi & \cos\theta \end{array} \right] \end{aligned} \tag{6.8}$$

The angles $\boldsymbol{\omega}$ are thus found as:

$$\begin{aligned} \cos\theta &= w_z \\ \phi &= \arccos(w_x/(w_x^2 + w_y^2)^{\frac{1}{2}}) \\ \psi &= \arccos(-u_z/(u_z^2 + v_z^2)^{\frac{1}{2}}) \end{aligned} \tag{6.9}$$

The resulting angles are between normal intervals, $\cos\theta \in [-1, 1]$, $\phi \in [0, 2\pi]$. As water possesses C_{2v} symmetry, we take $\psi \in [0, \pi]$.

Here the DCF $c(k, \boldsymbol{\omega}_1, \boldsymbol{\omega}_2) \equiv c(k, \cos\theta_1, \cos\theta_2, \phi_{12}, \psi_1, \psi_2)$ is stored in a discrete set of angles for each value of k (typically $(8, 8, 8, 8, 8)$ in the case of water, which uses the symmetries in §F.5.1 to reduce the number of ϕ and ψ by two) such that the correspondence from $(\boldsymbol{\Omega}_1, \boldsymbol{\Omega}_2)$ to $(\boldsymbol{\omega}_1, \boldsymbol{\omega}_2)$ usually falls in between angular grid points of the intermolecular grid. An interpolation can be done at different orders: zeroth order interpolation, which directly takes the nearest point, or linear interpolation.

6.1.1 *Zero-order interpolation of DCF*

At this order, for each possible value of $\mathbf{k}$ and $\boldsymbol{\Omega}$, the corresponding $\cos\theta$ and ψ which relate to a single solvent molecule are stored as an index (single precision integer), which gives the nearest angle in a pre-defined table:

$$\begin{aligned} i_{\cos\theta} &= \lfloor (\cos\theta + 1)(n_{\cos\theta}/2) \rfloor + 1 \\ i_{\psi} &= \mathrm{mod}(\lfloor \psi(n_{\psi}/\pi) \rfloor, n_{\psi}) + 1 \end{aligned} \tag{6.10}$$

where $\lfloor f \rfloor$ is the floor function. For the angle ϕ which relates to two solvent molecules, the operation $\phi = \phi_1 - \phi_2$ introduces a double error when integer indices are used, as shown in figure 6.4.

In the actual implementation, as an integer takes 4 bytes and a real takes 8 bytes, there is no profit to tabulate ϕ in integer form two times, thus ϕ is stored directly in real.

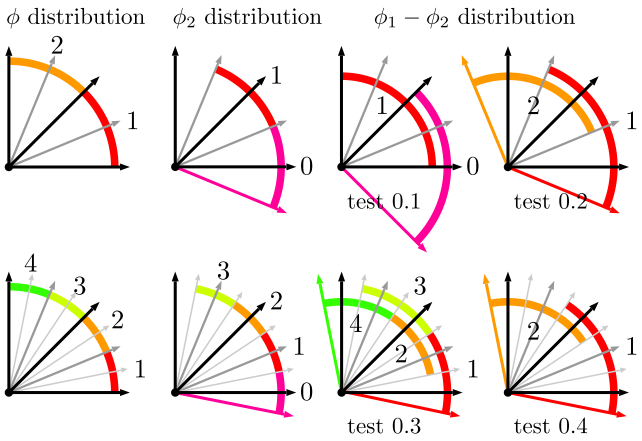

Figure 6.4: $\phi_1 - \phi_2$ distribution: Test 0.1 is the direct subtraction of ϕ established in the same way with θ and ψ, as shown in the top first schema. Test 0.2 tabulates ϕ_2 by taking the nearest point in another manner, as shown in the second schema. In test 0.3-0.4, all ϕ or only ϕ_2 is doubled.

6.1.2 *Linear interpolation of DCF*

At this order, $\boldsymbol{\omega}(\mathbf{k}, \boldsymbol{\Omega})$ is stored in double precision. All angles are stored in real number form, and the corresponding DCF is calculated as

$$c(\omega) = w_0 c(\omega_0) + w_1 c(\omega_1) \tag{6.11}$$

w is the weight, and ω is the angle set.

where $w_0 = \dfrac{\omega_1 - \omega}{\omega_1 - \omega_0}$ and $w_1 = \dfrac{\omega - \omega_0}{\omega_1 - \omega_0}$. Here ω is one of the 5 dimensions in $\tilde{\boldsymbol{\omega}}(\mathbf{k}, \boldsymbol{\Omega}_1, \boldsymbol{\Omega}_2) \equiv (\cos\theta_1, \cos\theta_2, \phi, \psi_1, \psi_2)$, ω_0 and ω_1 are the 2 nearest value points, while other variables are fixed. If we express the weight for each dimension as $w^i_{n_i}$ where $i = 1, 2, 3, 4, 5$ is the ith variable, the total equation with 5 variables is:

$$c(\tilde{\boldsymbol{\omega}}) = \left[\sum_{n_1=0}^{1} \sum_{n_2=0}^{1} \sum_{n_3=0}^{1} \sum_{n_4=0}^{1} \sum_{n_5=0}^{1} \left(\prod_{i}^{5} w^i_{n_i} c(\tilde{\boldsymbol{\omega}}_{n_1,n_2,n_3,n_4,n_5}) \right) \right] \tag{6.12}$$

These two equations are available for both interpolation and extrapolation, where the latter applies, e.g., for $\cos\theta_1$ and $\cos\theta_2$.

An error evaluation of the two strategies of interpolation presented in §6.1.1 and §6.1.2 is shown in appendix C. Results demonstrate that the linear interpolation scheme is absolutely essential. On the other hand, as seen in eq. (6.12), it is computationally much more expensive than the simple histogram scheme as it requires $2^5 = 32$ times the number of operations.

6.2 DIRECT CALCULATION OF DCF FROM ROTATIONAL INVARIANT PROJECTIONS

Another strategy to calculate $\hat{c}(\mathbf{k}, \boldsymbol{\Omega}_1, \boldsymbol{\Omega}_2)$ is to use the DCF expressed in terms of rotational invariant projections, which takes far less memory than in the intermolecular function form thanks to their angular independence and symmetric properties.

6.2.1 *Using projections in the form of $\hat{c}^{mnl}_{\mu\nu}(k)$*

As described by Blum [16], $\hat{c}(\mathbf{k}, \mathbf{\Omega}_1, \mathbf{\Omega}_2)$ can be expanded as

$$\hat{c}(\mathbf{k}, \mathbf{\Omega}_1, \mathbf{\Omega}_2) = \sum_{mnl\mu\nu} \hat{c}^{mnl}_{\mu\nu}(k) \Phi^{mnl}_{\mu\nu}(\hat{\mathbf{k}}, \mathbf{\Omega}_1, \mathbf{\Omega}_2) \tag{6.13}$$

where $\Phi^{mnl}_{\mu\nu}(\hat{\mathbf{k}}, \mathbf{\Omega}_1, \mathbf{\Omega}_2)$ are rotational invariants that depend on both the spatial and angular coordinates of the two particles (detailed in appendix F).

For projections of order $n_{\max} = 1$ ($n, m \leq 1$), the DCF can be expressed in very simple form. Only 4 projections $\hat{c}^{mnl}(k)$ are independent: $\hat{c}_{\mathrm{S}} \equiv \hat{c}^{000}$, $\hat{c}_{\Delta} \equiv \hat{c}^{110}$, $\hat{c}_{\mathrm{D}} \equiv \hat{c}^{112}$ and $\hat{c}^{011} = -\hat{c}^{101}$, with the corresponding rotational invariants expressed below both in laboratory and intermolecular frames:

$$\begin{aligned}
\Phi^{000} &= 1 \\
\Phi^{011} &= i\mathbf{k} \cdot \mathbf{\Omega}_1 = i \cos\theta_1 \\
\Phi^{101} &= i\mathbf{k} \cdot \mathbf{\Omega}_2 = i \cos\theta_2 \\
\Phi^{110} &= -\sqrt{3}\mathbf{\Omega}_1 \cdot \mathbf{\Omega}_2 = -\sqrt{3}(\sin\theta_1 \sin\theta_2 \cos\phi_{12} + \cos\theta_1 \cos\theta_2) \\
\Phi^{112} &= \sqrt{\frac{3}{10}} \left[3(\mathbf{k} \cdot \mathbf{\Omega}_1)(\mathbf{k} \cdot \mathbf{\Omega}_2) - \mathbf{\Omega}_1 \cdot \mathbf{\Omega}_2\right] \\
&= \sqrt{\frac{3}{10}} \left(2\cos\theta_1 \cos\theta_2 - \sin\theta_1 \sin\theta_2 \cos\phi_{12}\right)
\end{aligned} \tag{6.14}$$

where the orientations in laboratory frame $\mathbf{\Omega}$ are here expressed as an orientational vector $\mathbf{\Omega} = (\sin\Theta\cos\Phi, \sin\Theta\sin\Phi, \cos\Theta)$ in the Cartesian coordinate system.

To express the DCF at higher orders, the number of FE needed for $\Phi^{mnl}_{\mu\nu}(\hat{\mathbf{k}}, \mathbf{\Omega}_1, \mathbf{\Omega}_2)$ becomes huge and the DCF should be calculated in intermolecular frame as indicated below.

6.2.2 *Using projections in the form of $\hat{c}'^{mn}_{\mu\nu,\chi}(k)$*

Compared to the expression of $\Phi^{mnl}_{\mu\nu}(\hat{\mathbf{k}}, \mathbf{\Omega}_1, \mathbf{\Omega}_2)$ in laboratory frame (eq. (F.2)), its intermolecular form has far fewer terms (eq. (F.18)), such that

$$\hat{c}(k, \boldsymbol{\omega}_1, \boldsymbol{\omega}_2) = \frac{1}{2l+1} \sum_{mn\mu\nu\chi} \hat{c}'^{mn}_{\mu\nu,\chi}(k) r^m_{\chi\mu}(\theta_1) r^n_{\underline{\chi}\nu}(\theta_2) e^{-i\chi(\phi_{12} \equiv \phi_1 - \phi_2)} e^{-i\mu\psi_1} e^{-i\nu\psi_2} \tag{6.15}$$

where r is the generalized Legendre polynomial, $m, n \leq n_{\max}$, $|\mu| \leq m$, $|\nu| \leq n$, and $\chi \in [-\min(m,n), \min(m,n)]$; $\underline{\chi} = -\chi$.

$r^m_{\chi\mu}(\theta)$, $e^{-i\chi\phi}(\phi)$ and $e^{-i\mu\psi}(\psi)$ can be separately pre-tabulated for each given $\mathbf{k}$, to avoid repetitive evaluation of each term.

Eq. (6.15) replaces the interpolation of eq. (6.12) by an exact formula, and it requires the projections $\hat{c}'^{mn}_{\mu\nu,\chi}(k)$ to be stored in memory rather than the full angular representation $\hat{c}(k, \boldsymbol{\omega}_1, \boldsymbol{\omega}_2)$. It also requires the passage from orientations in laboratory frame to orientations in intermolecular frame, i.e. use of the formulae (6.9) for each $\mathbf{k}$ vector.

7

Angular Convolution, A Better Algorithm

In previous sections, the spatial convolution in the excess functional gradient is treated by FFT thanks to the transitional invariance that leads to $\mathbf{r}_{12} = \mathbf{r}_1 - \mathbf{r}_2$. However, as the angular grid is not homogeneous, the relative coordinates of two angles cannot be simply represented $\mathbf{\Omega}_{12} = \mathbf{\Omega}_1 - \mathbf{\Omega}_2$, therefore for the angles we cannot take advantage of the convolution property shown in eq. (4.21-4.22). On the other hand, these two-particle quantities have rotational invariance. As proposed by Blum [16, 17], a rotational invariant expansion technique is used to reduce the molecular Ornstein-Zernike (MOZ) equation into smaller irreducible matrix equations (§4.2). Owing to the mathematical equivalence between IET and DFT approach (§3.5), where eq. (6.1) about the Fourier transform of the excess functional gradient can be regarded as the MOZ equation, the formalism of Blum can also be applied to MDFT.

7.1 angular convolution using blum's reduction

To build an analogue of the irreducible form of MOZ equation for homogeneous fluid deduced by Blum (detailed in §4.2)

$$\hat{\gamma'}^{lm}_{\lambda\mu,\chi}(k) = \sum_{n=0}^{n_{\max}} \sum_{\nu=-n}^{n} (-)^{\chi+\nu} \Delta\hat{\rho'}^{ln}_{\lambda\underline{\nu},\chi}(k) \hat{c'}^{nm}_{\nu\mu,\chi}(k) \tag{7.1}$$

Here the projections $F'^{mn}_{\mu\nu,\chi}$ are defined as in [19]. Eq. (7.1) is mathematically identical with those in [16, 17] but using $R^m_{\mu'\mu} = D^{m*}_{\mu\mu'}$. The difference between the conventions of GSH are listed in §H.3.

for the MDFT formalism, a generalized spherical harmonic transform (GSHT) treatment is proposed by developing the functional gradient $\hat{\gamma}$ and the density $\hat{\rho}$ in eq. (6.1) on Wigner generalized spherical harmonics (GSH):

$$\hat{\gamma}(\mathbf{k}, \mathbf{\Omega}_1) = \sum_{m\mu'\mu} f_m \hat{\gamma}^m_{\mu'\mu}(\mathbf{k}) R^m_{\mu'\mu}(\mathbf{\Omega}_1) \tag{7.2}$$

$$\Delta\hat{\rho}(\mathbf{k}, \mathbf{\Omega}_2) = \sum_{n\nu'\nu} f_n \Delta\hat{\rho}^n_{\nu',\nu}(\mathbf{k}) R^n_{\nu',\nu}(\mathbf{\Omega}_2) \tag{7.3}$$

where $0 \le m, n \le n_{\max}$, $|\mu'|, |\mu| \le m$ and $|\nu'|, |\nu| \le n$. $f_m = (2m+1)^{\frac{1}{2}} = \left\| R^m_{\mu'\mu} \right\|^{-1}$ is the normalization factor.

The DCF can also be expanded on rotational invariants:

$$\hat{c}(k, \mathbf{\Omega}_1, \mathbf{\Omega}_2) = \sum_{mnl\mu\nu} f_m f_n \hat{c}^{mnl}_{\mu\nu}(k) \sum_{\mu'\nu'\lambda'} \begin{pmatrix} m & n & l \\ \mu' & \nu' & \lambda' \end{pmatrix} R^m_{\mu'\mu}(\mathbf{\Omega}_1) R^n_{\nu'\nu}(\mathbf{\Omega}_2) R^l_{\lambda'0}(\hat{\mathbf{k}}) \tag{7.4}$$

As GSHs possess orthogonality eq. (H.21) and symmetry eq. (H.15), eq. (6.1) can be rewritten by (7.2, 7.3, 7.4), which gives (here we omit the detailed demonstration for simplicity, which is put in appendix D):

$$\hat{\gamma}^m_{\mu'\mu}(\mathbf{k}) = \sum_{nl\nu} \hat{c}^{mnl}_{\mu\nu}(k) \sum_{\nu'\lambda'} (-)^{\nu'+\nu} \Delta\hat{\rho}^n_{\underline{\nu'\nu}}(\mathbf{k}) \begin{pmatrix} m & n & l \\ \mu' & \nu' & \lambda' \end{pmatrix} R^l_{\lambda'0}(\hat{\mathbf{k}}) \tag{7.5}$$

thus the OZ equation is expanded on GSHs and rotational invariants.

Note that eq. (7.5) is reducible. Blum's χ-transform [17] defines:

$$\hat{c'}^{mn}_{\mu\nu,\chi}(k) = \sum_{l=|m-n|}^{m+n} \begin{pmatrix} m & n & l \\ \chi & -\chi & 0 \end{pmatrix} \hat{c}^{mnl}_{\mu\nu}(k) \tag{7.6}$$

$$\hat{c}^{mnl}_{\mu\nu}(k) = (2l+1) \sum_{\chi=-\min(m,n)}^{\min(m,n)} \begin{pmatrix} m & n & l \\ \chi & -\chi & 0 \end{pmatrix} \hat{c'}^{mn}_{\mu\nu,\chi}(k) \tag{7.7}$$

Invariants of form $\hat{F'}^{mn}_{\mu\nu,\chi}(k)$ have a very simple relation with their combined function $F(k, \boldsymbol{\omega_1}, \boldsymbol{\omega_2})$ in the intermolecular coordinate system (see appendix F, eq. (F.26, F.27)); that is how the OZ equation can be reduced. In MDFT, we can also take advantage of this quantity by defining the projections of $\hat{\gamma}$ and $\hat{\rho}$ in the local frame ($\boldsymbol{\omega}_i = \hat{\mathbf{k}}^{-1}\boldsymbol{\Omega}_i$):

$$\hat{\gamma}(\mathbf{k}, \boldsymbol{\omega}_1) = \sum_{m\chi\mu} f_m \hat{\gamma'}^{m}_{\chi\mu}(\mathbf{k}) R^{m}_{\chi\mu}(\boldsymbol{\omega}_1) \tag{7.8}$$

$$\Delta\hat{\rho}(\mathbf{k}, \boldsymbol{\omega}_2) = \sum_{n\chi\nu} f_n \Delta\hat{\rho'}^{n}_{\chi\nu}(\mathbf{k}) R^{n}_{\chi\nu}(\boldsymbol{\omega}_2) \tag{7.9}$$

and with the rotation formula of GSH (eq. (H.23)), we have

$$\hat{\gamma'}^{m}_{\chi\mu}(\mathbf{k}) = \sum_{\mu'} \hat{\gamma}^{m}_{\mu'\mu}(\mathbf{k}) R^{m}_{\mu'\chi}(\hat{\mathbf{k}}) \tag{7.10}$$

$$\Delta\hat{\rho}^{n}_{\underline{\nu'}\nu}(\mathbf{k}) = \sum_{\chi} \Delta\hat{\rho'}^{n}_{\chi\underline{\nu}}(\mathbf{k}) R^{n*}_{\underline{\nu'}\chi}(\hat{\mathbf{k}}) = \sum_{\chi} \Delta\hat{\rho'}^{n}_{\chi\underline{\nu}}(\mathbf{k}) \, (-)^{\,\chi+\nu'} R^{n}_{\nu'\underline{\chi}}(\hat{\mathbf{k}}) \tag{7.11}$$

Using eq. (7.5), (7.7), (7.10), (7.11) and GSH products relation eq. (H.24) and 3j-symbol orthogonality eq. (H.7), we deduce that:

$$\hat{\gamma'}^{m}_{\chi\mu}(\mathbf{k}) = \sum_{n\nu} (-)^{\,\chi+\nu} \hat{c'}^{mn}_{\mu\nu,\chi}(k) \Delta\hat{\rho'}^{n}_{\chi\underline{\nu}}(\mathbf{k}) \tag{7.12}$$

This OZ equation formalism is the main result of the new theory. A step-by-step operational way to make use of this equation for γ evaluation is shown in §7.3.

Eq. (7.12) is essential to the new algorithm. It states that, for the terms with the same index χ, the OZ equation is a simple product of matrix:

$$\tilde{\gamma'}_{\chi} = \left[(-)^{\,\chi+\nu} \tilde{c'}_{\chi}\right] \Delta\tilde{\rho'}_{\chi} \tag{7.13}$$

The index χ shares the same role with $\mathbf{k}$ in the treatment of spatial convolution, where the recombination of projections on the exponential orthogonal bases gives, for each $\mathbf{k}$, a simple product form of the OZ equation.

If we consider the solute is the same as the solvent, and take $\hat{c'}^{nm}_{\nu\mu,\underline{\chi}}(k)$ in the place of $\hat{c'}^{mn}_{\mu\nu,\chi}(k)$, eq. (7.12) is mathematically identical to eq. (7.1), as:

$$\hat{\gamma'}^{m}_{\chi\mu}(\mathbf{k}) = \sum_{l\lambda} f^{l} \hat{\gamma'}^{lm}_{\lambda\mu,\underline{\chi}}(k) R^{l}_{\underline{\chi}\lambda}(\hat{\mathbf{k}}) \tag{7.14}$$

$$\hat{\rho'}^{n}_{\chi\underline{\nu}}(\mathbf{k}) = \sum_{l\lambda} f^{l} \Delta\hat{\rho'}^{ln}_{\lambda\underline{\nu},\underline{\chi}}(k) R^{l}_{\underline{\chi}\lambda}(\hat{\mathbf{k}}) \tag{7.15}$$

according to the rotational invariant transform in eq. (F.26). In fact, it can be proven (with §F.5) that:

$$\hat{c'}^{nm}_{\nu\mu,\underline{\chi}}(k) = \hat{c'}^{mn*}_{\mu\nu,\chi}(k) \tag{7.16}$$

The incompatibility in the conjugate is yet to be explained. In the code, when we use the $\hat{c'}^{mn}_{\mu\nu,\chi}(k)$ issued from IET, we also need to take its conjugate to obtain the same result as IET. Note that the demonstration from eq. (7.2) to eq. (7.12) does not contain any

$m_{\max}$	0	1	2	3	4	5
N_Θ	1	2	3	4	5	6
N_{ang} (Gauss-Legendre)	1 (1)	18 (6)	75 (45)	196 (84)	405 (225)	726 (330)
N_{ang} (Lebedev×ψ)	1 (1)	18 (6)	70 (42)	182 (78)	342 (190)	550 (250)
N_{proj}	1 (1)	10 (4)	35 (19)	84 (40)	165 (85)	286 (140)
FE for eq. (6.1)	1 (1)	324 (36)	5625 (2025)	38416 (7056)	164025 (50625)	527076 (108900)
FE for eq. (7.5)	1 (1)	262 (34)	4787 (1459)	36588 (8116)	175989 (47221)	633490 (150566)
FE for eq. (7.12)	1 (1)	34 (6)	259 (75)	1092 (252)	3333 (877)	8294 (2002)

Table 7.1: Number of FE needed by OZ equation of different form for arbitrary solvent (outside the parentheses) and solvent possessing C_{2v} symmetry (inside the parentheses)

incompatibility; it only occurs in comparison with the IET formalism for homogeneous liquids.

With the approach described above, the integral of the angular part in eq. (6.1) can be reduced to a sum of a few terms. Table 7.1 shows some parameters linking to computing cost of different algorithms. It shows that the expansion on GSHs (eq. (7.5)) does not give any reduction of FE compared to its 6D function form (eq. (6.1))*; but after Blum's χ-transform, the OZ equation is largely reduced. The fact is that as the treatment of spatial convolution takes advantage of the transitional invariance r_{12}, the χ-transform makes use of the rotational invariance.

*Only if we do not need to calculate $\hat{c}(\mathbf{k}, \mathbf{\Omega}_1, \mathbf{\Omega}_2)$.

7.2 FAST GENERALIZED SPHERICAL HARMONIC TRANSFORM

The algorithm above for angular convolution takes advantage of the orthogonality and symmetries of GSHs. To use this algorithm as analogous to the treatment of the convolution with FFT for spatial grids, the transform described in eq. (7.2) and (7.3), here defined as the generalized spherical harmonic transform (GSHT), *a priori* should be fast. This is possible owing to the exponential components in the definition of GSH, that will be discussed later as the fast generalized spherical harmonic transform (FGSHT).

GSHT provides a forward-backward transform between a general angular function $F(\mathbf{\Omega}) \equiv F(\cos\Theta, \Phi, \Psi)$ and its projections $F^m_{\mu'\mu}$ ($|\mu'|, |\mu| \leq m$):

$$F^m_{\mu'\mu} = \frac{f_m}{8\pi^2} \int \mathrm{d}\mathbf{\Omega} F(\mathbf{\Omega}) R^{m*}_{\mu'\mu}(\mathbf{\Omega}) \quad \text{(forward)} \tag{7.17}$$

$$F(\mathbf{\Omega}) = \sum_{m,\mu',\mu} f_m F^m_{\mu'\mu} R^m_{\mu'\mu}(\mathbf{\Omega}) \quad \text{(backward)} \tag{7.18}$$

where $\left\{R^m_{\mu'\mu}(\mathbf{\Omega})\right\}$ are the Wigner generalized spherical harmonics (Appendix H), which form a complete orthogonal set, being defined as:

$$R^m_{\mu'\mu}(\mathbf{\Omega}) = r^m_{\mu'\mu}(\Theta) e^{-i(\mu'\Phi + \mu\Psi)} \tag{7.19}$$

7.2.1 *Equivalence of order in angular quadratures and projections*

Suppose that $F(\mathbf{\Omega})$ is a polynomial of both $\cos\Theta$, $\cos\Phi$ and $\cos\Psi$ of order n, $(n+1$ polynomial terms). To completely expand this function as shown in equation (7.18), at least $m_{\max} = n$ is needed, where $m_{\max}$ is the highest order of projections $F^m_{\mu'\mu}$ in the expansion. Note that $m_{\max} = n$ is not always sufficient to completely expand $F(\mathbf{\Omega})$, while a discussion of this issue will be given in §10.2.

To evaluate exactly the integration in equation (7.17), at least $n+1$ for $\cos\Theta$ (Gauss-Legendre grid), $2n+1$ for Φ (equal-spaced grid), $2n+1$ for Ψ (equal-spaced grid) points of angular grid are needed (c.f. appendix E). In the case of water which possesses a C_2 symmetry $F(\Psi+\pi)=F(\Psi)$, only projections of even μ are nonzero:

$$\begin{aligned} F_\mu &= \int \mathrm{d}\Psi F(\Psi)e^{i\mu\Psi} = \int \mathrm{d}(\Psi+\pi)F(\Psi+\pi)e^{i\mu(\Psi+\pi)} \\ &= e^{i\mu\pi}\int \mathrm{d}\Psi F(\Psi)e^{i\mu\Psi} = e^{i\mu\pi}F_\mu \end{aligned} \tag{7.20}$$

$$F_\mu = \begin{cases} 0 & \mu = 2n+1, n\in\mathbb{Z} \\ F_\mu & \mu = 2n, n\in\mathbb{Z} \end{cases} \tag{7.21}$$

Therefore the function

$$F(\Psi) = \sum_\mu F_\mu e^{-i\mu\Psi} \tag{7.22}$$

can be rewritten as:

$$F(\Psi_2/2\equiv\Psi) = \sum_{\mu_2\equiv\mu/2} F_{2\mu_2}e^{-i\mu_2\Psi_2} \tag{7.23}$$

As $|\mu_2|\le n/2$, $F(\Psi_2/2\equiv\Psi)$ is a polynomial of $\cos\Psi_2$ of order $\mathrm{floor}(n/2)\equiv\lfloor n/2\rfloor$, in the forward transform

$$F_{2\mu_2\equiv\mu} = \int \mathrm{d}\Psi F(\Psi)e^{i\mu\Psi} = \frac{1}{2}\int \mathrm{d}\Psi_2 F(\Psi_2/2\equiv\Psi)e^{i\mu_2\Psi_2} \tag{7.24}$$

the total degree $\cos\Psi_2$ polynomial in the integrand is $2\lfloor n/2\rfloor$, then $2\lfloor n/2\rfloor+1$ points of Ψ_2 (or Ψ) are needed.

For further implementation, we take these conclusions, but distinguish the order of quadrature $m_{\max}$ (linked to the angular grid) and the order of projection $n_{\max}$ (linked to the GSH transform) for numerical reason.

7.2.2 *Integration of Φ, Ψ using FFT*

Here we write eq. (7.17, 7.18) in an explicit way:

$$F^m_{\mu'\mu} = \frac{f_m}{8\pi^2}\sum_{i=0}^{m_{\max}} w_i \sum_{j=0}^{2m_{\max}} \sum_{k=0}^{2\lfloor m_{\max}/s\rfloor} F(\Theta_i,\Phi_j,\Psi_k)R^{m*}_{\mu'\mu}(\Theta_i,\Phi_j,\Psi_k) \tag{7.25}$$

$$F(\Theta_i,\Phi_j,\Psi_k) = \sum_{m=0}^{n_{\max}} f_m \sum_{\mu'=-m}^{m} \sum_{\substack{\mu=-m \\ \mathrm{mod}\ (\mu,s)=0}}^{m} F^m_{\mu'\mu}R^m_{\mu'\mu}(\Theta_i,\Phi_j,\Psi_k) \tag{7.26}$$

where w_i is the weight of Gauss-Legendre quadrature ($m_{\max}+1$ points of Θ_i), normalized to the total angular integration; and s is the molecule rotation symmetry order (MRSO), $s=1$ or 2 according to the symmetry C_s of solvent.

To integrate eq. (7.25) in a direct way, $(m_{\max}+1)(2m_{\max}+1)(2\lfloor m_{\max}/s\rfloor+1) = N_\Theta N_{\Phi\Psi} = N$ FE are needed for each $F^m_{\mu'\mu}$, an overall $O(N^2_{FE})$ process is needed and *vice versa*. Therefore, a faster algorithm proposed by Numerical Recipes [62] proposes to reduce this cost to $O(N^2_\Theta N_{\Phi\Psi}\ln N_{\Phi\Psi}\simeq N^{4/3})$ by FFT.

Following this idea, eq. (7.25) can be rewritten as:

$$F^m_{\mu'\mu} = \frac{f_m}{8\pi^2}\sum_{i=0}^{m_{\max}} w_i r^m_{\mu'\mu}(\Theta_i)F_{\mu'\mu}(\Theta_i) \tag{7.27}$$

where $F_{\mu'\mu}(\Theta_i)$ is the Φ, Ψ integration evaluated using trapezoid (or Gauss-Chebyshef) quadrature:

$$\begin{aligned} F_{\mu'\mu}(\Theta_i) &= \sum_{j=0}^{2m_{\max}} \sum_{k=0}^{2\lfloor m_{\max}/s \rfloor} F(\Theta_i, \Phi_j, \Psi_k) e^{i(\mu'\Phi_j + \mu\Psi_k)} \\ &= \sum_{j=0}^{2m_{\max}} \sum_{k=0}^{2\lfloor m_{\max}/s \rfloor} F(\Theta_i, \Phi_j, \Psi_k) e^{2\pi i \mu' j/(2m_{\max}+1)} e^{2\pi i \mu k/(2\lfloor m_{\max}/s \rfloor + 1)} \end{aligned} \tag{7.28}$$

that shares the same formula with an FFT-2D process of $(2m_{\max}+1)\,(2\lfloor m_{\max}/s \rfloor + 1)$ elements.

Similarly, the backward process (7.18) can be rewritten as:

$$\begin{aligned} F(\Theta_i, \Phi_j, \Psi_k) &= \sum_{m=0}^{n_{\max}} f_m \sum_{\mu'=-m}^{m} \sum_{\substack{\mu=-m \\ \text{mod }(\mu,s)=0}}^{m} F^m_{\mu'\mu} R^m_{\mu'\mu}(\Theta_i, \Phi_j, \Psi_k) \\ &= \sum_{\mu'=-n_{\max}}^{n_{\max}} \sum_{\substack{\mu=-n_{\max} \\ \text{mod }(\mu,s)=0}}^{n_{\max}} \sum_{m=\max(|\mu'|,|\mu|)}^{n_{\max}} f_m F^m_{\mu'\mu} R^m_{\mu'\mu}(\Theta_i, \Phi_j, \Psi_k) \\ &= \sum_{\mu'=-n_{\max}}^{n_{\max}} \sum_{\substack{\mu=-n_{\max} \\ \text{mod }(\mu,s)=0}}^{n_{\max}} F_{\mu'\mu}(\Theta_i) e^{2\pi i \mu' j/(2m_{\max}+1)} e^{2\pi i \mu k/(2\lfloor m_{\max}/s \rfloor + 1)} \end{aligned} \tag{7.29}$$

with

$$F_{\mu'\mu}(\Theta_i) = \sum_{m=\max(|\mu'|,|\mu|)}^{n_{\max}} f_m F^m_{\mu'\mu} r^m_{\mu'\mu}(\Theta_i) \tag{7.30}$$

Note that the GSHT is able to treat the case $n_{\max} > m_{\max}$.

When $n_{\max} \leq m_{\max}$, the double sum in eq. (7.29) is included in the FFT-2D process of $(2m_{\max}+1)\,(2\lfloor m_{\max}/s \rfloor + 1)$ elements. However, if $n_{\max} > m_{\max}$, the FFT-2D process only gives a partial sum of $|\mu'|, |\mu| \leq m_{\max}$, the other terms in eq. (7.29) can only be calculated by a GSHT process, as $F_{\mu'\mu}(\Theta_i)$ is not periodic for μ' and μ. There can be further approximations to treat this problem, but for practical usage, we only consider the case of $n_{\max} \leq m_{\max}$.

As the angular function $F(\mathbf{\Omega})$ is real, and the GSHs possess symmetry of eq. (H.15):

$$R^m_{\underline{\mu'\mu}}(\mathbf{\Omega}) = (-1)^{\mu'+\mu} R^{m*}_{\mu'\mu}(\mathbf{\Omega}) \tag{7.31}$$

the symmetry relation between the projections are

$$F^m_{\underline{\mu'\mu}} = (-1)^{\mu'+\mu} F^{m*}_{\mu'\mu} \tag{7.32}$$

Therefore only the projections of $\mu \geq 0$ need to be stocked, which can be calculated with only these FFTW3 output elements reduced by the Hermitian symmetry (5.9). The full process of FFTW3-2D real to real transform is illustrated in figure 7.1.

As the output array of FFTW3 is periodic,

$$e^{2\pi i \mu k/n} = e^{2\pi i(\mu-n)k/n} e^{2\pi i k} = e^{2\pi i(\mu-n)k/n} \tag{7.33}$$

the indices $\mu = m_{\max}+1, \ldots, 2m_{\max}$ actually correspond to $\mu = -m_{\max}, \ldots, -1$. Note that eq. (7.28) and (7.29) do not possess the periodicity of eq. (7.33), only in the domain of definition of μ' and μ some intermediary functions share the same formula with FFT.

Moreover, from eq. (7.28), (7.30) and (7.32), we can verify that

$$F_{\mu'\mu}(\Theta) = F^*_{\underline{\mu'\mu}}(\Theta) \tag{7.34}$$

The latter is used in the code since, according to the definition in eq. (5.7) and (5.8), $F_{\underline{\mu'\mu}}(\Theta)$ is calculated instead of $F_{\mu'\mu}(\Theta)$.

dim 1 in_forward / out_backward (real) | in_backward / out_forward (complex)

array index	1	2	3	...	m'+1	m'+2	...	2m'	2m'+1	1	2	3	...	m'+1
real index	0	1	2	...	m'	m'+1	...	2m'-1	2m'	0	1	2	...	m'
$k \leftrightarrow \mu$	1	2	3	...	m'+1	m'+2	...	2m'	2m'+1	0	1	2	...	m'

dim 2 in_forward / out_backward (complex) | in_backward / out_forward (complex)

array index	1	2	3	...	m+1	m+2	...	2m	2m+1	1	2	3	...	m+1	m+2	...	2m	2m+1
real index	0	1	2	...	m	m+1	...	2m-1	2m	0	1	2	...	m	m+1	...	2m-1	2m
$j \leftrightarrow \mu'$	1	2	3	...	m+1	m+2	...	2m	2m+1	0	1	2	...	m	-m	-m+1	...	-1

Figure 7.1: Indices arrangement in a complete forward-backward FFT-2D process of m'×m elements. The DFT of dim 1 (k to μ) and dim 2 (j to μ') are done sequentially and *vice versa*. Array index is the one used by Fortran array, real index is the one shown in eq. (5.7) and (5.8), k and j indices shown in the left as well as μ and μ' in the right are those in eq. (7.28) and (7.29). Here $\mathrm{m} = m_{\max}$ and $\mathrm{m}' = \lfloor m_{\max}/s \rfloor$.

7.3 OPERATIONAL ALGORITHM

As described above, the whole process of γ and $\mathcal{F}_{\text{exc}}$ functional evaluation proposed by this algorithm can be concluded as 8 operations:

1. Firstly, the Fourier transform of the density is computed:

$$\Delta\hat{\rho}(\mathbf{k}, \mathbf{\Omega}) = \int \mathrm{d}\mathbf{r} \Delta\rho(\mathbf{r}, \mathbf{\Omega}) e^{-i\mathbf{k}\cdot\mathbf{r}} \tag{7.35}$$

2. Then $\Delta\hat{\rho}(\mathbf{k}, \mathbf{\Omega})$ is expanded on GSHs:

$$\Delta\hat{\rho}^m_{\mu'\mu}(\mathbf{k}) = \frac{f_m}{8\pi^2} \int \mathrm{d}\mathbf{\Omega} \Delta\hat{\rho}(\mathbf{k}, \mathbf{\Omega}) R^{m*}_{\mu'\mu}(\mathbf{\Omega}) \tag{7.36}$$

   Note that these two steps, as with their backward transform, are commutable, which will be discussed later.

3. Afterwards the projections in k-frame are then rotated into the local coordinate system along the unit vector $\hat{\mathbf{k}}$:

$$\Delta\hat{\rho}'^m_{\chi\mu}(\mathbf{k}) = \sum_{\mu'} \Delta\hat{\rho}^m_{\mu'\mu}(\mathbf{k}) R^m_{\mu'\chi}(\hat{\mathbf{k}}) \tag{7.37}$$

   where the rotation matrix elements $R^m_{\mu'\chi}(\hat{\mathbf{k}})$ should be calculated directly because of the huge memory required by its storage. The algorithm by recurrence used to evaluate $R^m_{\mu'\chi}(\hat{\mathbf{k}})$ in this thesis is detailed in appendix G.

4. Next, computing the OZ equation with Blum's reduction:

$$\hat{\gamma}'^m_{\chi\mu}(\mathbf{k}) = \sum_{n,\nu} (-1)^{\chi+\nu} \hat{c}'^{mn}_{\mu\nu,\chi}(\mathbf{k}) \Delta\hat{\rho}'^n_{\chi\underline{\nu}}(\mathbf{k}) \tag{7.38}$$

5. The γ projections are then transformed back to global coordinates system:

$$\hat{\gamma}^m_{\mu'\mu}(\mathbf{k}) = \sum_{\chi} \hat{\gamma}'^m_{\chi\mu}(\mathbf{k}) R^{m*}_{\mu'\chi}(\hat{\mathbf{k}}) \tag{7.39}$$

6. From here the function in angular frame can thus be rebuilt:

$$\hat{\gamma}(\mathbf{k},\mathbf{\Omega}) = \sum_{m,\mu',\mu} f_m \hat{\gamma}^m_{\mu'\mu}(\mathbf{k}) R^m_{\mu'\mu}(\mathbf{\Omega}) \tag{7.40}$$

7. Then the inverse Fourier transform of these projections is:

$$\gamma(\mathbf{r},\mathbf{\Omega}) = \int \mathrm{d}\mathbf{k} \hat{\gamma}(\mathbf{k},\mathbf{\Omega}) e^{i\mathbf{r}\cdot\mathbf{k}} \tag{7.41}$$

8. Finally, the functional $\mathcal{F}_{\mathrm{exc}}$ is computed by:

$$\mathcal{F}_{\mathrm{exc}} = -\frac{k_{\mathrm{B}}T}{2} \int \mathrm{d}\mathbf{r}\mathrm{d}\mathbf{\Omega} \Delta\rho(\mathbf{r},\mathbf{\Omega}) \gamma(\mathbf{r},\mathbf{\Omega}) \tag{7.42}$$

7.3.1 *Commutativity between operations*

As mentioned in the operational algorithm, three types of operations are being done before and after the OZ equation. They are:

1. Fast Fourier transform for 3-dimensional spatial grid (FFT3D): implemented by package FFTW3 [59], mathematically leading to no accuracy loss;

2. Fast generalized spherical harmonics transform (FGSHT): has real or complex input, is exact if $F(\mathbf{\Omega})$ can be given as an expansion of GSHs of order at most $m_{\max}$;

3. Rotation between laboratory coordinate system and local system linked to vector $\mathbf{k}$ (RotS): can be done for both function and projections. It introduces a minus error in accuracy at origin and border of the box, which will be discussed in §10.3.3.

Their commutativity is shown in figure 7.2.

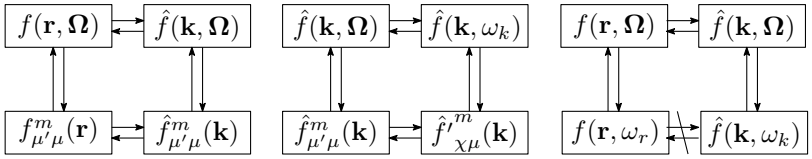

Figure 7.2: Commutativity of operations. (a) FFT3D and FGSHT; (b) RotS and FGSHT; (c) FFT3D and RotS.

As shown in figure 7.2, the FFT3D does not depend on the angular part of the function, and the FGSHT does not depend on the spatial part of the function. The two operations are commutative.

It can be also proven that the passage from the function $\hat{f}$ in laboratory frame $\hat{f}(\mathbf{k},\mathbf{\Omega})$ to the projections in local frame $f'^m_{\chi\mu}(\mathbf{k})$ can be achieved either by a rotation to the function $\hat{f}(\mathbf{k},\boldsymbol{\omega}_k)$ in intermolecular frame followed by an GSH expansion as eq. (7.8), or an GSH expansion that gives the projections $f^m_{\mu'\mu}(\mathbf{k})$ following by a rotation as eq. (7.10).

However, the rotation from $f(\mathbf{r},\mathbf{\Omega})$ to $f(\mathbf{r},\boldsymbol{\omega})$ depends on the vector $\mathbf{r}$, of which the information is totally lost after FFT3D. The rotation from $f(\mathbf{k},\mathbf{\Omega})$ to $f(\mathbf{k},\boldsymbol{\omega})$ can only depend on the vector $\mathbf{k}$; they are not the same rotation, therefore non-commutative.

7.3.2 *Reduction by symmetry*

A further reduction of computing cost can be made by performing about only half of the operations, thanks to the symmetric relations between the projections.

In eq. (7.36), $\Delta\rho(\mathbf{r},\mathbf{\Omega})$ is real. With the property of GSH (eq. (H.15)):

$$R^m_{\mu'\mu}(\mathbf{\Omega}) = (-)^{\mu'+\mu} R^{m*}_{\underline{\mu'\mu}}(\mathbf{\Omega}) \tag{7.43}$$

we find

$$\Delta\rho^m_{\mu'\mu}(\mathbf{r}) = (-)^{\mu'+\mu} \Delta\rho^{m*}_{\underline{\mu'\mu}}(\mathbf{r}) \tag{7.44}$$

Therefore only the projections of $\mu' \geq 0$ or $\mu \geq 0$ are needed to generate all information.

When $\Delta\hat{\rho}^m_{\mu'\mu}(\mathbf{r})$ is transformed into k-space, replacing

$$\Delta\hat{\rho}^m_{\mu'\mu}(\mathbf{k}) = \int \mathrm{d}\mathbf{r} \Delta\rho^m_{\mu'\mu}(\mathbf{r}) e^{-i\mathbf{r}\cdot\mathbf{k}} \tag{7.45}$$

with eq. (7.44) gives

$$\Delta\hat{\rho}^m_{\mu'\mu}(\mathbf{k}) = (-)^{\mu'+\mu} \Delta\hat{\rho}^{m*}_{\underline{\mu'\mu}}(-\mathbf{k}) \tag{7.46}$$

Therefore only the projections of $\mu' \geq 0$, $\mu \geq 0$, or half of $\mathbf{k}$ where one of the dimensions $k_i \geq 0$ are independent.

In the implementation, it is a natural choice to keep only half of the projections $\Delta\hat{\rho}^m_{\mu'\mu}(\mathbf{k})$, as either the real-to-complex FFT3D ($k_3 \geq 0$) or the real-to-complex FGSHT ($\mu \geq 0$) gives implicitly half of the information. As the OZ equation (7.12) is separable for each $\mathbf{k}$, but not on μ (ν in equation), it is more natural to compute half of $\mathbf{k}$, which is actually the choice in our code. All the rest we should prove is that the $\hat{\gamma}^m_{\mu'\mu}(\mathbf{k})$ calculated from this half of known density is still able to generate all the informations.

The relation deduced from the symmetries of GSH (appendix H):

$$r^m_{\mu'\mu}(\theta) = (-)^{m+\mu'} r^m_{\mu'\underline{\mu}}(\pi-\theta) \tag{7.47}$$

$$\begin{aligned} R^m_{\mu'\mu}(\phi\theta\psi) &= (-)^{m+\mu'} e^{i\mu'\pi} R^m_{\mu'\underline{\mu}}(\pi+\phi, \pi-\theta, -\psi) && (7.48)\\ &= (-)^m R^m_{\mu'\underline{\mu}}(\pi+\phi, \pi-\theta, -\psi) && (7.49) \end{aligned}$$

gives that

$$R^l_{\lambda'0}(\hat{\mathbf{k}}) = (-)^l R^l_{\lambda'0}(-\hat{\mathbf{k}}) = (-)^{l+\lambda'} R^{l*}_{\underline{\lambda'}0}(-\hat{\mathbf{k}}) \tag{7.50}$$

If we replace eq. (7.5) by eq. (7.46) and (7.50), with symmetry of 3j-symbol (H.6) and symmetry of $\hat{c}$ [16]:

$$\hat{c}^{mnl}_{\mu\nu}(k) = (-)^{m+n+\mu+\nu}\, \hat{c}^{mnl*}_{\underline{\mu\nu}}(k) \tag{7.51}$$

we have the same symmetry property for $\hat{\gamma}$ as for $\Delta\hat{\rho}$:

$$\hat{\gamma}^m_{\mu'\mu}(\mathbf{k}) = (-)^{\mu'+\mu}\, \hat{\gamma}^{m*}_{\underline{\mu'\mu}}(-\mathbf{k}) \tag{7.52}$$

which means the half $\hat{\gamma}^m_{\mu'\mu}(\mathbf{k})$ is sufficient to generate $\hat{\gamma}(\mathbf{k},\mathbf{\Omega})$ or $\gamma(\mathbf{r},\mathbf{\Omega})$. Thus the OZ equation can be safely reduced by a factor of two.

We can also find

$$R^m_{\mu'\chi}(\hat{\mathbf{k}}) = (-)^m R^m_{\mu'\underline{\chi}}(-\hat{\mathbf{k}}) = (-)^{m+\mu'+\chi} R^m_{\underline{\mu'}\chi}(-\hat{\mathbf{k}}) \tag{7.53}$$

which gives

$$\Delta\hat{\rho}'^m_{\chi\mu}(\mathbf{k}) = (-)^{m+\mu+\chi} \Delta\hat{\rho}'^{m*}_{\chi\underline{\mu}}(-\mathbf{k}) \tag{7.54}$$

$$\hat{\gamma'}^{m}_{\chi\mu}(\mathbf{k}) = (-)^{m+\mu+\chi}\hat{\gamma'}^{m*}_{\chi\underline{\mu}}(-\mathbf{k}) \tag{7.55}$$

If we replaced the OZ equation by these two equations, we can find the symmetries of $\hat{c'}^{mn}_{\mu\nu,\chi}(k)$ in eq. (F.51):

$$\hat{c'}^{mn}_{\mu\nu,\chi}(k) = (-)^{m+n+\mu+\nu}\,\hat{c'}^{mn*}_{\underline{\mu\nu},\chi}(k) \tag{7.56}$$

It should be noted that not exactly half of the points are calculated. If we choose to calculate half of $\mathbf{k}$, as shown in figure 7.3, where the 2D plan corresponds to two of the three dimensions in k-space grid, the green points can be generated from the black points by the symmetries of eq. (7.46), but the red points should be all calculated, of which the corresponding points are also a red point or even itself. This ever caused a huge problem in the implementation, as we put $\Delta\hat{\rho}^{m}_{\mu'\mu}(\mathbf{k})$ and $\hat{\gamma}^{m}_{\mu'\mu}(\mathbf{k})$ in the same array for purposes of memory. It should be assured that these points are calculated only once.

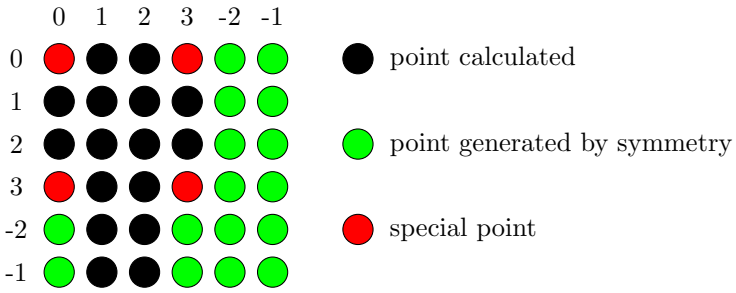

Figure 7.3: Distribution of points to be calculated according to symmetry in a 2D plan

8

Solvation Properties

The solvation free energy and solvent structure are the most important properties that we seek; as shown in previous sections, they can both be obtained by the minimization of the free energy functional $\mathcal{F}[\rho]$. Here is a discussion about some corrections needed for charged solutes and some profiles of structures deduced from the solvent density.

8.1 Free energy correction for single ions

In the calculation of external potential as well as the total solvation free energy, the use of different conventions can lead to a charge-independent offset, which introduces error for charged solutes [63–65]. This offset is mainly caused by two sources: (1) resulting from the use of a finite system size; in our case, it is a system with cubic periodic boundary conditions, which presents artificial interactions between the ion and its own periodic copies, as well as between the solvent and the periodic copies of the ion (Type-B); (2) resulting from the choice of convention for summing up the contributions of solvent charges to the electrostatic potential in the sample system (Type-C).

8.1.1 *Correction of type B*

Type B correction should be added for systems with finite size or periodic boundary conditions, accounting for the error in the solvent polarization:

$$\Delta G_B = \frac{1}{8\pi\varepsilon_0}\left(1-\varepsilon^{-1}\right)\frac{q^2}{L}\left[\xi + \frac{4\pi}{3}\left(\frac{R_\mathrm{I}}{L}\right)^2 - \frac{16\pi}{45}\left(\frac{R_\mathrm{I}}{L}\right)^5\right] \tag{8.1}$$

Another way to evaluate this error is to make a numerical extrapolation of the inverse of the box size $(1/L)$; it is more accurate, but demands much more calculation.

where

- ε_0 is the vacuum permittivity;
- ε is the solvent permittivity (dielectric constant), here $\varepsilon = 71$ for water [47, 66];
- q is the solute charge;
- L is the box length;
- R_I is the ionic radius;
- ξ is the energy per particle in a simple cubic lattice, $\xi \simeq -2.837297$ [67].

As R_I is significantly smaller than the size of the computational box, i.e. $R_\mathrm{I} \ll L$, its quadratic as well as higher order of (R_I/L) is considered negligible, thus eq. (8.1) becomes:

$$\Delta G_\mathrm{B} = \frac{\xi}{8\pi\varepsilon_0}\left(1-\varepsilon^{-1}\right)\frac{q^2}{L} \tag{8.2}$$

which has the same form as the Born model in eq. (2.10).

8.1.2 *Correction of type C*

Type-C corrections are needed when the systems to be compared use different electrostatic summation schemes: on the basis of point charges within entire solvent molecules (M scheme) or on the basis of individual point charges (P scheme), shown in figure 8.1 (c) and (d), which brings a fixed free energy difference at the boundary.

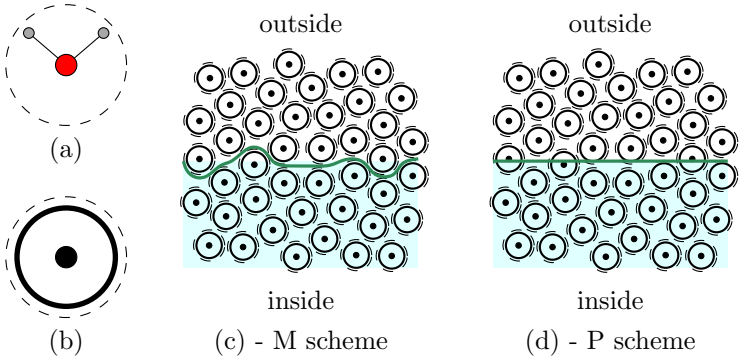

Figure 8.1: IQ model and summation scheme. (a) The solvent molecule. (b) The equivalent isotropic quadrupole (IQ) fluid model. (c) In the M scheme, one evaluates the Coulombic potential generated by the solvent charges belonging to all molecules within the boundary. (d) In the P scheme, one evaluates the Coulombic potential generated by all solvent charges within the boundary.

It can be deduced analytically by considering the solvent as a canonical ensemble under the orientational disorder limit (ODL) [63], which becomes an isotropic quadrupole (IQ) fluid, whose solvent molecule (figure 8.1 (b)) possesses the same quadrupole trace

γ is elsewhere referred to as the spheropole moment [68, 69], which is the spherical component of the quadrupole moment, and is invariant with respect to rotations.

$$\gamma = \mathrm{tr}(\mathcal{Q}) = \mathcal{Q}_{xx} + \mathcal{Q}_{yy} + \mathcal{Q}_{zz} \tag{8.3}$$

where the quadrupole moment of the solvent molecule can be calculated by its definition [70]

$$\mathcal{Q}_{ij} = \int_V r_i r_j \rho(\mathbf{r}) \mathrm{d}v = \sum_{\alpha=1}^{N} q^{(\alpha)} r_i^{(\alpha)} r_j^{(\alpha)} \tag{8.4}$$

It can be shown that the charge density of the solvent located within the boundary of the sample system vanishes everywhere, except at the boundary in the M scheme, which results in a uniform normal surface polarization. The correction needed is:

$$\Delta G_{\mathrm{C}} = -q \left(1 - \frac{4\pi R_{\mathrm{I}}^3}{3L^3}\right) \Delta\Phi_{\mathrm{ODL}} \tag{8.5}$$

where $\Delta\Phi_{\mathrm{ODL}} = (6\varepsilon_0)^{-1} \eta\gamma$, η being the solvent number density.

In the same way, when we consider $R_{\mathrm{I}} \ll L$, eq. (8.5) becomes

$$\Delta G_{\mathrm{C}} = -(6\varepsilon_0)^{-1} \eta\gamma q \tag{8.6}$$

8.2 SOLVATION STRUCTURE

In MDFT, all the information about solvation structure can be deduced from the solvent density $\rho(\mathbf{r}, \mathbf{\Omega})$. Here we present some examples of structure which are used in later chapters.

8.2.1 *Radial and site-site distribution function*

When the solvent is homogeneous, the PDF can be reduced to $g(r_{12})$, which is sometimes referred to as the radial distribution function (RDF). However, it can be also used as a key character of the structure for inhomogeneous fluids, which can be calculated equivalently as:

$$g(r) = \langle \rho(r, \hat{\mathbf{r}}) \rangle / \rho_0 = \frac{\int \rho(r, \hat{\mathbf{r}}) \mathrm{d}s_r}{\rho_0 \int \mathrm{d}s_r} \tag{8.7}$$

To do this integration, it is required to transform $\rho(\mathbf{r}, \mathbf{\Omega})$ into spherical coordinates. But as $\rho(\mathbf{r}, \mathbf{\Omega})$ in the code is a N-point discrete space grid:

$$\rho(\mathbf{r}) = \int \mathrm{d}\mathbf{\Omega} \rho(\mathbf{r}, \mathbf{\Omega}) / \rho_0 = \sum_{i=1}^{N} \rho_i \delta(\mathbf{r} - \mathbf{r}_i) \tag{8.8}$$

The best way to do the integration is to use a histogram approach.

The grid points are assumed to be homogenous in space, such that the number of points entering in an arbitrary volume v is proportional to this volume. Obviously the grid of $\rho(\mathbf{r}, \mathbf{\Omega})$ satisfies this assumption.

The average value of $g(r)$ between an interval δr is

$$g(r_i) = \langle g(r) \rangle_r^{r+\delta r} = \frac{\int_r^{r+\delta r} g(r) \mathrm{d}r}{\delta r} \tag{8.9}$$

Thus

$$g(r_i) = \frac{1}{\delta v_i} \int_r^{r+\delta r} \int_s \rho(r, \hat{\mathbf{r}}) \mathrm{d}r \mathrm{d}s_r = \frac{1}{\delta v_i} \int_{v_i} \sum_{i=1}^{N} \rho_i \delta(\mathbf{r} - \mathbf{r}_i) \mathrm{d}v_i \tag{8.10}$$

where $\delta v_i = \delta r \cdot s_{r_i} = \int_{v_i} \delta(\mathbf{r} - \mathbf{r}_i) \mathrm{d}v_i$ (as the points are homogeneous).

The total function is

$$g(r_i) = \frac{\int_{v_i} \sum_{i=1}^{N} \rho_i \delta(\mathbf{r} - \mathbf{r}_i) \mathrm{d}v_i}{\int_{v_i} \delta(\mathbf{r} - \mathbf{r}_i) \mathrm{d}v_i} \tag{8.11}$$

and it becomes necessary to sum up the point values ρ_i in the interval $\delta v = \delta r \cdot S_r$, and divide it by the number of points in this interval.

A site-site distribution function is the same type as RDF, but the origin for the calculation of $\mathbf{r}$ is no longer at the center of the solute; instead it is now at the site coordinate $\mathbf{r}_u$, such that the new coordinates are calculated as $\mathbf{r}' = \mathbf{r} - \mathbf{r}_u$. Calculation of solvent site outside the solvent center requires more complicated calculations, involving the rotation of solvent coordinate to $\mathbf{\Omega}$-frame. It has equivalent information of the structure to the rotational invariant projections of higher order, the implementation of which we have not done here.

8.2.2 *Radial polarization function*

Radial polarization function (RPF) is defined as

$$p(r) = \langle \mathbf{P}(\mathbf{r}) \cdot \hat{\mathbf{r}} \rangle / \rho_0 \tag{8.12}$$

where $\mathbf{P}(\mathbf{r})$ is the polarization $\mathbf{P}(\mathbf{r}) = \int \mathrm{d}\mathbf{\Omega}\mathbf{\Omega} \cdot \rho(\mathbf{r}, \mathbf{\Omega}) / \rho_0$. It can be calculated in the same way as $g(r)$.

8.2.3 *Rotational invariant expansion*

If the solute is simple, like a spherical ion or little molecule, it is convenient to expand the density on rotational invariants which possess numerous symmetries:

$$\rho(\mathbf{r},\mathbf{\Omega})/\rho_0 = \sum_{mnl\mu\nu} \rho_{\mu\nu}^{mnl}(r)\Phi_{\mu\nu}^{mnl}(0,\mathbf{\Omega},\hat{\mathbf{r}}) \tag{8.13}$$

$$= \sum_{mnl\mu\nu} \rho_{\mu\nu}^{mnl}(r) f^m f^n \sum_{\eta} \begin{pmatrix} m & n & l \\ \mu & \eta & -\mu-\eta \end{pmatrix} R_{\eta\nu}^{n}(\mathbf{\Omega}) R_{-\mu-\eta,0}^{l}(\hat{\mathbf{r}}) \tag{8.14}$$

Here the form of $\Phi_{\mu\nu}^{mnl}(0,\mathbf{\Omega},\hat{\mathbf{r}})$ is reduced for the laboratory coordinate system.

The forward transform to obtain the projections is:

$$\rho_{\mu\nu}^{mnl}(r) = f^m f^n \sum_{\eta} \begin{pmatrix} m & n & l \\ \mu & \eta & -\mu-\eta \end{pmatrix} \int \mathrm{d}\hat{\mathbf{r}} R_{-\mu-\eta,0}^{l*}(\hat{\mathbf{r}}) \int \mathrm{d}\mathbf{\Omega} \rho(r,\hat{\mathbf{r}},\mathbf{\Omega}) R_{\eta,\nu}^{n*}(\mathbf{\Omega})/\rho_0 \tag{8.15}$$

Like the RDF and PDF, histogram approach is used in this process to evaluate the integration $\int \mathrm{d}\hat{\mathbf{r}}$ to take advantage of the $R_{\lambda 0}^{l*}(\hat{\mathbf{r}})$ in regular spatial space calculated by recurrence (appendix G). A detailed deduction for these generalized formulae is in appendix F.

Note that if the solvent is water, that processes a symmetry axis C_{2v}, the projections $\rho_{\mu\nu}^{mnl}(r)$ are purely real.

8.2.4 *Equivalence between the curves*

The relation between these profiles of structure can be proven mathematically.

Firstly, as

$$\Phi_{00}^{000}(\mathbf{r},\mathbf{\Omega}) = 1 \tag{8.16}$$

there is only one expansion term in eq. (8.13). The projection is thus

$$\rho_{00}^{000}(r) = \int \mathrm{d}\hat{\mathbf{r}}\mathrm{d}\mathbf{\Omega}\rho(\mathbf{r},\mathbf{\Omega})/\rho_0 = g(r) \tag{8.17}$$

Then, according to appendix F we can calculate

$$\Phi_{00}^{011}(\mathbf{r},\mathbf{\Omega}) = -\mathbf{\Omega}\cdot\hat{\mathbf{r}} \tag{8.18}$$

such that:

$$\rho_{00}^{011}(r) = \int \mathrm{d}\hat{\mathbf{r}}\mathrm{d}\mathbf{\Omega}\rho(\mathbf{r},\mathbf{\Omega})\Phi_{00}^{011*}(\mathbf{r},\mathbf{\Omega})/\rho_0 = -\frac{\int \mathrm{d}\hat{\mathbf{r}}\mathbf{P}(\mathbf{r})\cdot\hat{\mathbf{r}}}{\int \mathrm{d}\hat{\mathbf{r}}\mathrm{d}\mathbf{\Omega}\left\|\Phi_{00}^{011}(\mathbf{r},\mathbf{\Omega})\right\|^2} \tag{8.19}$$

Note that the orthogonality in eq. (F.6) gives $\int \mathrm{d}\hat{\mathbf{r}}\mathrm{d}\mathbf{\Omega}\left\|\Phi_{00}^{011}(\mathbf{r},\mathbf{\Omega})\right\|^2 = (2l+1)^{-1} = \frac{1}{3}$; we can find:

$$\rho_{00}^{011}(r) = -3p(r) \tag{8.20}$$

Chapter III

Implementation

The code MDFT developed in this thesis is based on the master branch of Git project MDFT (`https://github.com/maxlevesque/MDFT/`), version [Fri Jun 20 19:05:52 2014 +0200]. All the tests of computing performance are run on **POINCARE** machines of IDRIS, which involve nodes of kind:

poincare[001-092]: 2 processors Sandy Bridge E5-2670 (2.60GHz, 8 cores per processor, with 16 cores per node); 32 GB of memory per node.

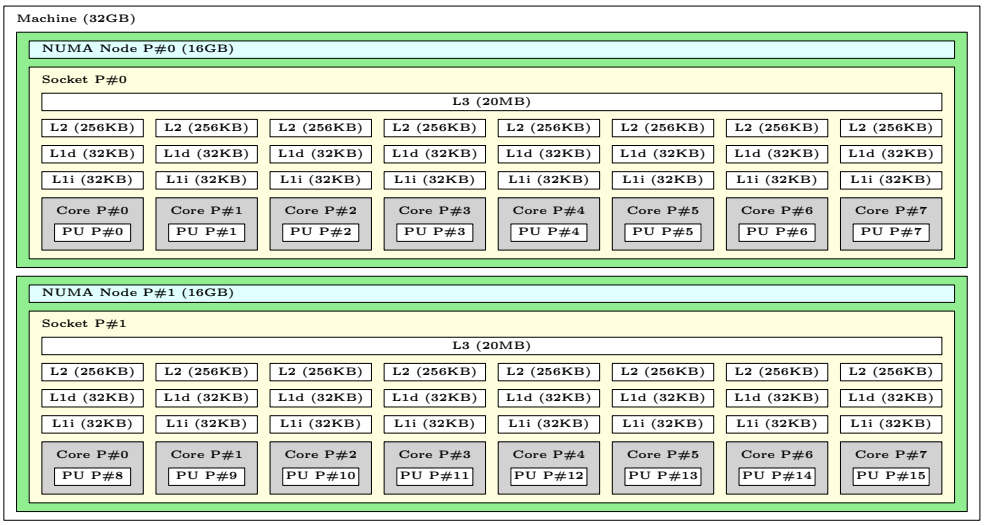

This chapter presents the implementation results of the theories established in chapter II. Firstly in section 9, we summarize all the possible algorithms to evaluate $\gamma(\mathbf{r}, \mathbf{\Omega})$ from $\Delta\rho(\mathbf{r}, \mathbf{\Omega})$, and name a selection of branches in order to facilitate further discussions. In the following sections, the results are regrouped into two aspects, the accuracy and performance:

Section 10 examines all the possible accuracy loss in the implementation compared to the theoretical model, which is in a general sense continuous and infinite. The accuracy loss is mainly due to the discretization of the system: the finite expansion of GSHT, the effects linking to a discretized grid, as well as finite size of sample box. The factors linked to these effects are thus analyzed in order to determine their acceptable minimum number to give a reasonable result.

Section 11 discusses the computing performance of the code, from subroutines to entire algorithms. The goal is to show that the new algorithms are much faster than the old ones, according to the theory, but also to give a detailed evaluation of timing of all algorithms for further code development.

9

Algorithms and Branches

As discussed in section 5, in code MDFT, we evaluate the functional $\mathcal{F}[\varphi]$ and its gradient $\delta\mathcal{F}[\varphi]/\delta\varphi$ in each iteration. Figure 9.1 shows a detailed portion of the total MDFT flow chart in figure 5.1, including the functional evaluation and minimization.

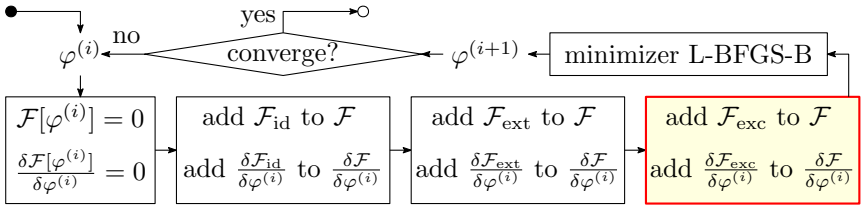

Figure 9.1: Process "find equilibrium density" in MDFT. After the "initiation" process, the flow chart begins at the black point. The three terms of functional and their gradients are then accumulated in order. The process ends at the white point, which then goes through the "output" process.

As shown in figure 9.1, the three functional terms and their gradients can be both calculated separately. With the first two terms well presented in section 5, this section aims to summarize all the algorithms to evaluate the excess functional gradient $\gamma(\mathbf{r},\boldsymbol{\Omega})$ from $\Delta\rho(\mathbf{r},\boldsymbol{\Omega})$, knowing that

$$\rho(\mathbf{r},\boldsymbol{\Omega}) = \rho_0\varphi^2(\mathbf{r},\boldsymbol{\Omega}) \tag{9.1}$$

$$\frac{\delta\mathcal{F}_{\text{exc}}}{\delta\varphi} = -k_{\text{B}}T\rho_0\varphi(\mathbf{r},\boldsymbol{\Omega})\gamma(\mathbf{r},\boldsymbol{\Omega}) \tag{9.2}$$

and the functional $\mathcal{F}_{\text{exc}}$ can be calculated as:

$$\mathcal{F}_{\text{exc}} = -\frac{k_{\text{B}}T}{2}\int \text{d}\mathbf{r}\text{d}\boldsymbol{\Omega}\Delta\rho(\mathbf{r},\boldsymbol{\Omega})\gamma(\mathbf{r},\boldsymbol{\Omega}) \tag{9.3}$$

According to the commutativity of operations (see §7.3.1), the only possible algorithms to evaluate $\gamma(\mathbf{r},\boldsymbol{\Omega})$ from $\Delta\rho(\mathbf{r},\boldsymbol{\Omega})$ are shown in the figure 9.2. We recall here that $\boldsymbol{\Omega}$ and $f^m_{\mu'\mu}$ refer to orientations in the laboratory frame whereas $\boldsymbol{\omega}$ and $f'^m_{\chi\mu}$ refer to orientations in the intermolecular frame (axis $\overrightarrow{Oz}$ in the direction of $\mathbf{k}$).

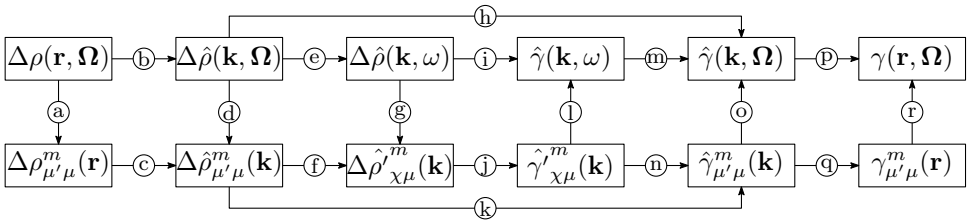

Figure 9.2: Possible algorithms for γ evaluation

Several branches are built to test and compare between algorithms, which are shown below in table 9.1. These branches should give numerically the same result in certain conditions, that will be discussed in later sections.

METHOD	SUB-METHOD	DESCRIPTION	THEORY
reference	dipole	calculate $n(\mathbf{r})$ and $\mathbf{P}(\mathbf{r})$ separately	Ref [32]
naive	standard	use $\hat{c}^{mn}_{\mu\nu,\chi}(k)$ as input DCF	§6.2.2
	zero-order	use $\hat{c}(k,\boldsymbol{\omega_1},\boldsymbol{\omega_2})$ and take the nearest point	§6.1.1
	interpolation	use $\hat{c}(k,\boldsymbol{\omega_1},\boldsymbol{\omega_2})$ with linear interpolation	§6.1.2
	dipole	use $\hat{c}_S$, $\hat{c}_\Delta$, $\hat{c}_D$ issued from [71]	§6.2.1
	nmax1	use $\hat{c}_S$, $\hat{c}_\Delta$, $\hat{c}_D$, $\hat{c}^{011}$ issued from [72]	§6.2.1
convolution	standard	algorithm with symmetry reduction	§7.3.2
	asymm	algorithm without symmetry reduction	§7.3.2
	pure_angular	swap FFT and FGSHT	§9

Table 9.1: Branch option in MDFT

9.1 BRANCHES "NAIVE"

Branches **`naive`** are the algorithms mentioned in section 6, which go through the path

$$(b) \to (h) \to (p)$$

in figure 9.2, calculating directly $\hat{\gamma}(\mathbf{k},\boldsymbol{\Omega})$ from $\Delta\hat{\rho}(\mathbf{k},\boldsymbol{\Omega})$ with

$$\hat{\gamma}(\mathbf{k},\boldsymbol{\Omega}_1) = \int \mathrm{d}\boldsymbol{\Omega}_2 \Delta\hat{\rho}(\mathbf{k},\boldsymbol{\Omega}_2)\hat{c}(\mathbf{k},\boldsymbol{\Omega}_1,\boldsymbol{\Omega}_2) \tag{9.4}$$

The DCF in laboratory frame, $\hat{c}(\mathbf{k},\boldsymbol{\Omega}_1,\boldsymbol{\Omega}_2)$, is reconstructed from the intermolecular DCF, $\hat{c}(k,\boldsymbol{\omega}_1,\boldsymbol{\omega}_2)$, by a pre-established relation $\boldsymbol{\omega}(\boldsymbol{\Omega}_1,\boldsymbol{\Omega}_2)$. The difference between branches is the method to calculate $\hat{c}(k,\boldsymbol{\omega}_1,\boldsymbol{\omega}_2)$. Branch **`naive_standard`** uses $\hat{c}^{mn}_{\mu\nu,\chi}(k)$ as input DCF, and calculates $\hat{c}(k,\boldsymbol{\omega}_1,\boldsymbol{\omega}_2)$ directly (eq. (6.15)) during the evaluation of eq. (9.4) with these coefficients. Branch **`naive_zero-order`** and **`naive_interpolation`** use a pre-tabulated $\hat{c}(k,\boldsymbol{\omega}_1,\boldsymbol{\omega}_2)$ as input, either calculated from $\hat{c}^{mn}_{\mu\nu,\chi}(k)$ or in another way. Branch **`naive_zero-order`** takes the neatest point of $\hat{c}(k,\boldsymbol{\omega}_1,\boldsymbol{\omega}_2)$ according to the pre-established correspondence $\boldsymbol{\omega}(\boldsymbol{\Omega}_1,\boldsymbol{\Omega}_2)$, while **`naive_interpolation`** gives a linear interpolation on $\boldsymbol{\omega}$. The former is rejected in the implementation due to a lack of precision (appendix C), thus only **`naive_standard`** and **`naive_interpolation`** are practically in use, apart from the $n_{\max} = 1$ cases discussed later. For all **`naive`** methods, we always take the nearest point of $\|\mathbf{k}\|$ in $\hat{c}^{mn}_{\mu\nu,\chi}(k)$ or in $\hat{c}(k,\boldsymbol{\omega}_1,\boldsymbol{\omega}_2)$, i.e. zeroth order interpolation for k.

It should be noted that although the intermolecular form of DCF (function or projections) is used in every branch **`naive`**, the DCF in laboratory form $\hat{c}(\mathbf{k},\boldsymbol{\Omega}_1,\boldsymbol{\Omega}_2)$ needs to be calculated. To exactly take the path

$$(b) \to (e) \to (i) \to (m) \to (p)$$

with $(k,\boldsymbol{\omega}_1,\boldsymbol{\omega}_2)$ numbers of FE for OZ equation, the density variable $\Delta\hat{\rho}(\mathbf{k},\boldsymbol{\Omega})$ should be interpolated on $\Delta\hat{\rho}(\mathbf{k},\boldsymbol{\omega})$, which seems not to be a wise choice.

9.2 BRANCHES "CONVOLUTION"

The methods **convolution**, which are developed in the objective of this thesis and detailed theoretically in section 7, contains three branches.

Branches **convolution_asymm** and **convolution_standard** go through the path

$$(a) \to (c) \to (f) \to (j) \to (n) \to (q) \to (r)$$

with **convolution_asymm** using the original algorithm (§7.3) without symmetry reduction (§7.3.2), i.e. artificially generating all the projections $\Delta\rho^m_{\mu'\mu}(\mathbf{r})$ from the projections of $\mu \geq 0$ given implicitly by the real-to-complex FGSHT process; while **convolution_standard** takes only the projections $\mu \geq 0$, and calculates the projections in local frame (eq. (7.37))

$$\Delta\hat{\rho}'^m_{\chi\mu}(\mathbf{k}) = \sum_{\mu'} \Delta\hat{\rho}^m_{\mu'\mu}(\mathbf{k}) R^m_{\mu'\chi}(\hat{\mathbf{k}}) \tag{9.5}$$

for all μ and $k_3 \geq 0$, with the symmetry relation (eq. (7.46))

$$\Delta\hat{\rho}^m_{\mu'\mu}(\mathbf{k}) = (-)^{\mu'+\mu} \Delta\hat{\rho}^{m*}_{\underline{\mu'\mu}}(-\mathbf{k}) \tag{9.6}$$

Branch **convolution_pure_angular** goes through the path

$$(b) \to (d) \to (f) \to (j) \to (n) \to (o) \to (p)$$

which swaps the FFT and FGSHT processes. It takes implicitly $k_3 \geq 0$ from the real-to-complex FFT process, thus implementing the same number of FE for the OZ equation as **convolution_standard**.

Theoretically, **convolution_standard** should be the fastest **convolution** method as its number of FE for FFT process depends on the number of projections $\Delta\rho^m_{\mu'\mu}$, which is smaller than the number of FE for **convolution_pure_angular** depending on the number of angles (Θ, Φ, Ψ).

9.3 TESTING BRANCHES FOR $n_{\max} = 1$

To show the mathematical equivalence between the branches, several testing branches for $n_{\max} = 1$ are built.

Branches **naive_dipole** and **naive_nmax1** go through the path $(b) \to (h) \to (p)$, calculating $\hat{c}(\mathbf{k}, \mathbf{\Omega}_1, \mathbf{\Omega}_2)$ directly with the projections $\hat{c}^{mnl}(k)$ as shown in §6.2.1, with separately the DCF of the references [71] and [72], whose slight difference is shown in §B.3.

Branch **reference_dipole** uses DCF in [71], which is the original method in MDFT to calculate $\mathcal{F}_{\text{exc}}$ via multipole expansion, and is mathematically equivalent to **naive_dipole**. In addition with branch **convolution_standard** that can also use the two DCFs mentioned above, a test of validation can be performed, which should in any case be exactly the same numerically if the same DCF is used.

9.4 OTHER PATHS

Considering the necessity, other paths such as those passing by (k) are only built for local test usage (c.f. §10.3.2 and §11.3).

10 Numerical Accuracy

Theoretically, if a process is mathematical equivalent to another one (for instance the different algorithms for $\mathcal{F}_{\text{exc}}$ evaluation mentioned previously), the numerical differences should be always zero, in the perfect condition that all the quantities are continuous (with infinite points of grid), the basis sets of FFT and FGSHT are complete (infinite number of $\mathbf{k}$ or order of expansion $n_{\max}$), and the system is border-free (infinite length of box). However, this is obviously impossible, and the errors due to such effects can be far from imperceptible within the level of discretization allowed by the computing capacity nowadays. This section works on all the possible effects and parameters that have an influence on the accuracy, e.g. the usage of different algorithms, or different discretizing parameters or convergence criteria. The goal of this study is to determine in which conditions the errors can be regarded as negligible; it thus gives a global view of the credibility for the results given by this code.

10.1 Significant digits and curve resolution

Before we examine the effects of discretization and limited orders, let us first have a discussion concerning precision that the code can achieve. The implementation can always give numbers at machine precision (approximatively 10^{-13}), but not all the digits that the machine gives have a physical meaning. For example, if the input DCF is at simple precision (10^{-7}), it is not necessary to look at numbers after the 7th decimal in the functional.

During the minimization of the functional, the convergence of final free energy is controlled by imposed criteria. Two criteria are used in code MDFT: $\varepsilon_{\mathcal{F}}$ is the difference between the free energies of the last two iterations, and $\|\text{proj}\mathbf{g}\|_\infty$ is the norm of the projected gradient in L-BFGS-B [57, 58]. The minimization is thought to converge if one of the criteria is met. We use the code implementation to measure how much significant digits we can obtain with such criteria. As shown in table 10.1, the normal convergence criteria (well converged) that we use in this thesis can give a free energy at two decimals. In case of convergence difficulty, as for some molecular solutes, looser criteria can be used.

Criteria, Functional	Well Converged	Converged (Chem. Accuracy)	Loose Convergence	Very Strict Criteria
$\varepsilon_{\mathcal{F}}$	< 0.00001	< 0.001	< 0.01	< 0.00000001
$\|\text{proj}\mathbf{g}\|_\infty$	< 0.00001	< 0.0001	< 0.001	< 0.000000001
$\mathcal{F}^{\text{nmax3}}(CH_4)$	27.24(-0.02)	28(-1)	60(-33)	27.21916
$\mathcal{F}^{\text{nmax3}}\left(CH_4^{+0.33}\right)$	20.560(-0.004)	22(-1)	40(-19)	20.55578
$\mathcal{F}^{\text{nmax3}}\left(CH_4^{+}\right)$	-129.050(-0.002)	128.8(-0.3)	-118(-11)	-129.05278
$\mathcal{F}^{\text{dipole}}(H_2O)$	-70.601(-0.003)	-70.4(-0.2)	-68(-3)	-70.60436
$\mathcal{F}^{\text{nmax3}}(O_2)$	21.90(-0.02)	23(-1)	49(-27)	21.88995

Table 10.1: Minimized free energy $\mathcal{F}$ ($\text{kJ}\cdot\text{mol}^{-1}$) given by different convergence criteria, comparing to those converged with very strict criteria. Test of water SPC/E uses Lebedev quadrature of $m_{\max} = 1$, with dipole DCF; and others use Gauss-Legendre quadrature with DCF of $n_{\max} = 3$. All tests are done in a box of $L = 24$ Å, nfft = 72.

Note that although the convergence criteria allow several decimals, if the result is for chemical usage, it is better to take no decimal or at most only one, as the error of normal simulations of chemical system is already at 1 to 2 kJ/mol.

The output curves (RDF, RPF, etc.) with respect to r that this code provides, always pass through a histogram process (§8.2). Therefore, the number of bins (n_{bin}) of the histogram (which determines δr) can have an influence on the shown results. Implicitly (without specification) the number of bins is determined by the Rice rule:

$$n_{\text{bin}} = 2n^{\frac{1}{3}} \tag{10.1}$$

where n is the total number of grid points to be counted. The curves obtained with this setting are smooth enough for LJ centers and ions, but for non-spherical solutes, n_{bin} seems to be too large in view of the fluctuations of the sample. In figure 10.1, we give an example of RDF with different resolution parameters for the site O of the O_2 molecule. It is shown that the curves do not vary too much within n_{bin} to $\frac{1}{8}n_{\text{bin}}$, and from $\frac{1}{3}n_{\text{bin}}$, the noise is well avoided.

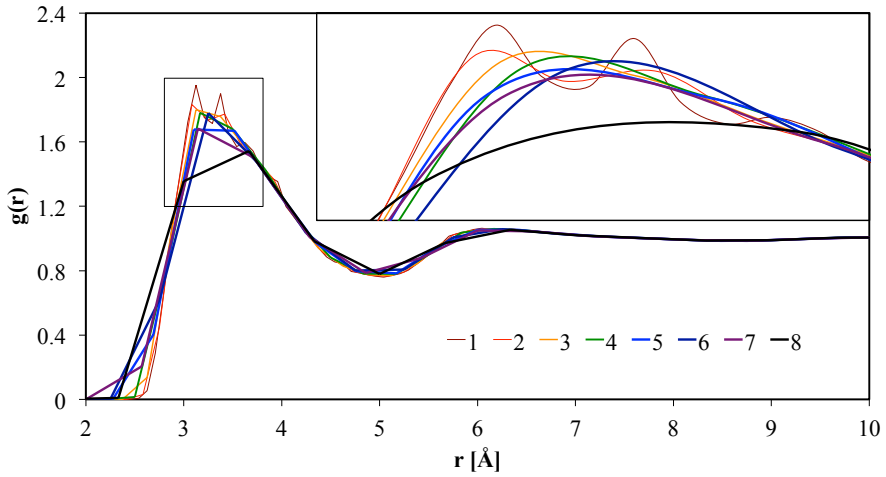

Figure 10.1: RDF of site O in O_2 molecule ($n_{\max} = 4$, $L = 24$ Å, nfft $= 72$) with different resolution parameter. The curves take $\frac{1}{N}n_{\text{bin}}$ as number of bins, with n_{bin} determined by the Rice rule, N varying from 1 to 8. The square box on the left is zoomed and smoothed (with Catmull-Rom spline implicitly used by Excel) in the right box.

10.2 GENERALIZED SPHERICAL HARMONICS TRANSFORM

As discussed in §7.2, a discretized function $F(\Theta, \Phi, \Psi)$ after a forward-backward GSHT process (eq. (7.25-7.26))

$$F^m_{\mu'\mu} = \frac{f_m}{8\pi^2} \sum_{i=0}^{m_{\max}} w_i \sum_{j=0}^{2m_{\max}} \sum_{k=0}^{2\lfloor m_{\max}/s \rfloor} F(\Theta_i, \Phi_j, \Psi_k) R^{m*}_{\mu'\mu}(\Theta_i, \Phi_j, \Psi_k) \tag{10.2}$$

$$F(\Theta_i, \Phi_j, \Psi_k) = \sum_{m=0}^{n_{\max}} f_m \sum_{\mu'=-m}^{m} \sum_{\substack{\mu=-m \\ \text{mod } (\mu,s)=0}}^{m} F^m_{\mu'\mu} R^m_{\mu'\mu}(\Theta_i, \Phi_j, \Psi_k) \tag{10.3}$$

only remains the same when:

1. F can be expanded on GSHs of order at most $n_{\max}$ in eq. (10.3), thus it is always the case that F is a polynomial of both $\cos\Theta$, $\cos\Phi$ and $\cos\Psi$ of order n, where $n \leq n_{\max}$;

2. The order of quadrature $m_{\max}$ used in the GSH expansion in eq. (10.2) should be larger than the order of the polynomial F, which means $n \leq m_{\max}$;

The two rules are quite evident. It should be also noted that as we do first a forward then a backward transform, when $m_{\max} < n_{\max}$, even the input function is of order at most $m_{\max}$; the output function is of order $n_{\max}$ in the presence of $R^m_{\mu'\mu}$ which is of order $n_{\max}$. That means F is no longer the same. Therefore, the forward-backward error is also controlled by the relation between the two discretizing parameters:

3. $m_{\max} \geq n_{\max}$ is needed to ensure the absence of accuracy loss.

In reality, the density variable $\rho(\mathbf{r}, \mathbf{\Omega})$ and the gradient $\gamma(\mathbf{r}, \mathbf{\Omega})$ that should be expanded via FGSHT are never a simple polynomial. It is important to understand how much the choice of $m_{\max}$ and $n_{\max}$ will affect the accuracy, as they are tightly linked to the performance. Therefore we chose some simple functions below to see what happens when the function does not meet the three conditions. Note that the FFT process leads to strictly no accuracy loss (at machine precision, approximatively 10^{-13}), which means the FGSHT process will have strictly the same result with the GSHT process. Here we do not need to distinguish the two.

10.2.1 $m_{\max}$ *and* $n_{\max}$ *of projections*

The numerical error tests of a forward-backward GSHT process with different order $n_{\max}$ of GSH and $m_{\max}$ of quadrature are shown in table 10.2 for various polynomials; the absolute error

$$E_{\mathrm{a}}(\mathbf{\Omega}) = \left| f^{\mathrm{before}}(\mathbf{\Omega}) - f^{\mathrm{after}}(\mathbf{\Omega}) \right| \tag{10.4}$$

being defined as the norm of difference in function $f(\mathbf{\Omega})$ after a forward-backward GSHT process. The maximum absolute error $E_a^{\max}$ is the maximum value in $E_{\mathrm{a}}(\mathbf{\Omega})$.

From table 10.2 we can see that for function $f(\mathbf{\Omega}) = 1 = R^0_{00}$, $m_{\max} \geq 0$, $n_{\max} \geq 0$ and $m_{\max} \geq n_{\max}$ give a null difference. Similarly, function $f(\mathbf{\Omega}) = \cos 3\Theta = 4\cos^3\Theta - 3\cos\Theta$ is a polynomial of $\cos\Theta$ of order 3, which can be expanded on R^3_{00} and R^1_{00} terms; it should satisfy $m_{\max} \geq n_{\max} \geq 3$. $f(\mathbf{\Omega}) = \cos 3\Phi$ is a polynomial of $\cos\Phi$ of order 3, but it cannot be expanded on GSHs. In fact, all the functions in which the order of $\cos\Phi$ and $\cos\Psi$ is greater than $\cos\Theta$ cannot be expanded on a finite number of GSHs. R^3_{30} can be expanded on itself, and indeed a polynomial of order 3 requiring $m_{\max} \geq n_{\max} \geq 3$.

We can see that all the $E_a^{\max}$ where $m_{\max} < n_{\max}$ is are rather large, and fortunately we use only $m_{\max} \geq n_{\max}$ in FGSHT for numerical reasons. Yet the $E_a^{\max}$ for $m_{\max} \geq n_{\max}$ may not be negligible either, knowing that the values of trigonometric functions are in between $[-1, 1]$. However, if the greatest portion of the function is a polynomial within the required order, the extra part does not play a great role, and the total mean error will not be as significant as seen now.

10.2.2 *From* ρ *to* γ

In the same way, the maximum absolute error of the density variable $\rho(\mathbf{r}, \mathbf{\Omega})$, which is not a combination of GSHs, can be huge. It even gives the appearance of unphysical density $\rho(\mathbf{r}, \mathbf{\Omega}) < 0$ (i.e. $\Delta\rho(\mathbf{r}, \mathbf{\Omega})/\rho_0 < -1$) at certain points after a forward-backward GSHT process, as shown in figure 10.2.

Theoretically, we expect this minimum value to approach zero when increasing $m_{\max}$ or $n_{\max}$. This is not exactly the case. That means the order of expansion within the computing capacity ($n_{\max} \leq 5$) is still far from finding a tendency. If we look at the

$m\backslash n$	0	1	2	3	4	5
0	**0.00 (0.00)**	9.00 (3.00)	34.00 (18.00)	83.00 (39.00)	164.00 (84.00)	285.00 (139.00)
1	**0.00 (0.00)**	**0.00 (0.00)**	0.00 (1.67)	4.34 (6.07)	7.06 (13.63)	14.88 (17.30)
2	**0.00 (0.00)**	**0.00 (0.00)**	**0.00 (0.00)**	0.00 (0.00)	0.00 (0.00)	5.65 (2.71)
3	**0.00 (0.00)**	**0.00 (0.00)**	**0.00 (0.00)**	**0.00 (0.00)**	0.00 (0.00)	0.00 (0.00)
4	**0.00 (0.00)**	**0.00 (0.00)**	**0.00 (0.00)**	**0.00 (0.00)**	**0.00 (0.00)**	0.00 (0.00)
5	**0.00 (0.00)**	**0.00 (0.00)**	**0.00 (0.00)**	**0.00 (0.00)**	**0.00 (0.00)**	**0.00 (0.00)**

(a) $f(\mathbf{\Omega}) = 1$

$m\backslash n$	0	1	2	3	4	5
0	0.00 (0.00)	0.00 (0.00)	0.00 (0.00)	0.00 (0.00)	0.00 (0.00)	0.00 (0.00)
1	0.96 (0.96)	0.00 (0.00)	0.00 (0.00)	2.56 (6.99)	10.76 (14.15)	13.83 (21.21)
2	0.46 (0.46)	0.00 (0.00)	0.00 (0.00)	0.00 (0.00)	0.00 (0.00)	1.36 (0.50)
3	0.86 (0.86)	0.66 (0.66)	0.66 (0.66)	**0.00 (0.00)**	0.00 (0.00)	0.66 (0.66)
4	0.99 (0.99)	0.80 (0.80)	0.80 (0.80)	**0.00 (0.00)**	**0.00 (0.00)**	0.00 (0.00)
5	0.83 (0.83)	1.01 (1.01)	1.01 (1.01)	**0.00 (0.00)**	**0.00 (0.00)**	**0.00 (0.00)**

(b) $f(\mathbf{\Omega}) = \cos 3\Theta$

$m\backslash n$	0	1	2	3	4	5
0	0.00 (0.00)	9.00 (3.00)	34.00 (18.00)	83.00 (39.00)	164.00 (84.00)	285.00 (139.00)
1	0.00 (0.00)	0.00 (0.00)	0.00 (1.67)	4.34 (6.07)	7.06 (13.63)	14.88 (17.30)
2	1.00 (1.00)	1.00 (1.00)	0.50 (0.50)	1.53 (1.53)	1.15 (1.15)	3.65 (0.89)
3	1.00 (1.00)	1.00 (1.00)	1.00 (1.00)	0.83 (0.83)	1.10 (1.10)	1.11 (1.11)
4	1.00 (1.00)	1.00 (1.00)	1.00 (1.00)	0.90 (0.90)	0.90 (0.90)	0.69 (0.69)
5	1.00 (1.00)	1.00 (1.00)	1.00 (1.00)	0.94 (0.94)	0.94 (0.94)	0.80 (0.80)

(c) $f(\mathbf{\Omega}) = \cos 3\Phi$

$m\backslash n$	0	1	2	3	4	5
0	0.00 (0.00)	5.03 (1.68)	19.01 (10.06)	46.40 (21.80)	91.68 (46.96)	- (77.70)
1	0.00 (0.00)	0.00 (0.00)	0.00 (0.51)	1.32 (1.85)	2.15 (4.15)	4.53 (5.26)
2	0.56 (0.56)	0.56 (0.56)	0.07 (0.07)	0.55 (0.55)	0.76 (0.76)	2.05 (1.00)
3	0.47 (0.47)	0.47 (0.47)	0.47 (0.47)	**0.00 (0.00)**	0.46 (0.46)	0.46 (0.46)
4	0.56 (0.56)	0.56 (0.56)	0.56 (0.56)	**0.00 (0.00)**	**0.00 (0.00)**	0.00 (0.00)
5	0.51 (0.51)	0.51 (0.51)	0.51 (0.51)	**0.00 (0.00)**	**0.00 (0.00)**	**0.00 (0.00)**

(d) $f(\mathbf{\Omega}) = R^3_{30}(\mathbf{\Omega})$

Table 10.2: Maximum absolute error $E_a^{\max}$ of some function $f(\mathbf{\Omega})$ introduced by a forward-backward GSHT process, with $s = 1$ outside the parentheses and $s = 2$ inside the parentheses; s being the MRSO defined in §7.2 concerning the C_{2v} symmetry. Differences that should be theoretically null (at machine precision) are shown in bold character and double underlined; which are null in fact at machine precision and here presented with 2 decimals for simpleness.

rotational invariant expansion of $\rho(\mathbf{r}, \mathbf{\Omega})$, which gives the projections $\rho_{0\nu}^{0nl}(r)$ (0 as the solute is spherical) shown in figure 10.3a, we observe that the first peaks of higher order projections are still non-negligible. That gives the tendency in figure 10.2. The first projection $\rho_{00}^{000}(r)$ is purely positive, such that the minimum of ρ is zero; when the more negative projections are added on to the combined function, this error will go to negative. The minimum will have a tendency to converge only if the order of projections are above the current order 5.

It is normal that the curves in figure 10.3a and 10.3b are a little noised (with n_{bin}) as discussed above.

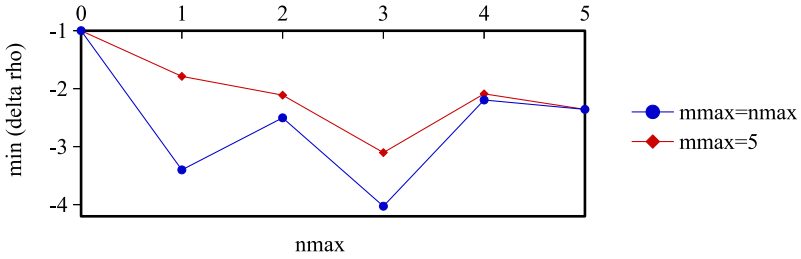

Figure 10.2: The minimum value of $\Delta\rho(\mathbf{r},\mathbf{\Omega})/\rho_0$ after a forward-backward GSHT process with respect to $n_{\max}$. Computed for a 45^3 grid ($L = 25$) for a converged density of an artificial charged LJ center $CH_4^{+0.4}$.

That means within the computing capacity, we cannot correctly expand the density ρ on GSHs. However, in the code MDFT, the density ρ is generated by the minimization process determined by the gradient of energy γ. Note that $\hat{\gamma}(\mathbf{k},\mathbf{\Omega})$ is a convolution product, where $\Delta\hat{\rho}(\mathbf{k},\mathbf{\Omega})$ and the DCF $\hat{c}(k,\mathbf{\Omega}_1,\mathbf{\Omega}_2)$ can be both expanded on GSHs and rotational invariants. Therefore, the higher order terms vanish more easily in $\hat{\gamma}$, as they are the product of higher order terms of $\Delta\hat{\rho}(\mathbf{k},\mathbf{\Omega})$ and $\hat{c}(k,\mathbf{\Omega}_1,\mathbf{\Omega}_2)$. We see in figure 10.3b that the first terms of γ are much stronger than the terms of $n = 3,4,5$. Therefore we can consider that the expansion of γ already converges within $n_{\max} \leq 5$, even $n_{\max} \leq 3$.

Note that the projections $f_{\mu\nu}^{mnl}$ are purely real if f is real and μ, ν are even numbers.

10.3 COMPARISON BETWEEN BRANCHES

The algorithms mentioned in section 9 should give the same result if the same DCF is used, on the condition that the error due to discretization is not fatal. The most direct comparison can be done with the free energy and structure obtained at the end of minimization. To be more strict, it is also worthwhile to study only the $\mathcal{F}_{\text{exc}}$ functional evaluation during one iteration without minimization, i.e. the process shown in figure 9.2. In this scope, $\gamma(\mathbf{r},\mathbf{\Omega})$ becomes a better detailed criteria than $\mathcal{F}_{\text{exc}}$ to be compared.

METHOD	$n_{\max}$	DCF	FREE ENERGY (kJ/mol)
`dipole`	1	[71]	13.965
`naive_dipole`	1	[71]	13.965
`convolution_standard`	1	[71]	13.965
`naive_standard`	1	[72]	19.224
`naive_interpolation`	1	[72]	19.434
`naive_nmax1`	1	[72]	19.225
`convolution_standard`	1	[72]	19.225
`convolution_asymm`	1	[72]	19.225
`convolution_pure_angular`	1	[72]	19.225
`naive_standard`	3	[72]	26.105
`naive_interpolation`	3	[72]	26.971
`convolution_standard`	3	[72]	26.105
`convolution_asymm`	3	[72]	26.105
`convolution_pure_angular`	3	[72]	26.105

Table 10.3: Minimized free energy via different branches MDFT of a charged $CH_4^{+0.33}$ LJ center calculated for a 33^3 ($L = 20$Å) grid. Gauss-Legendre quadrature is used as Θ angle grid, with $m_{\max} = n_{\max}$.

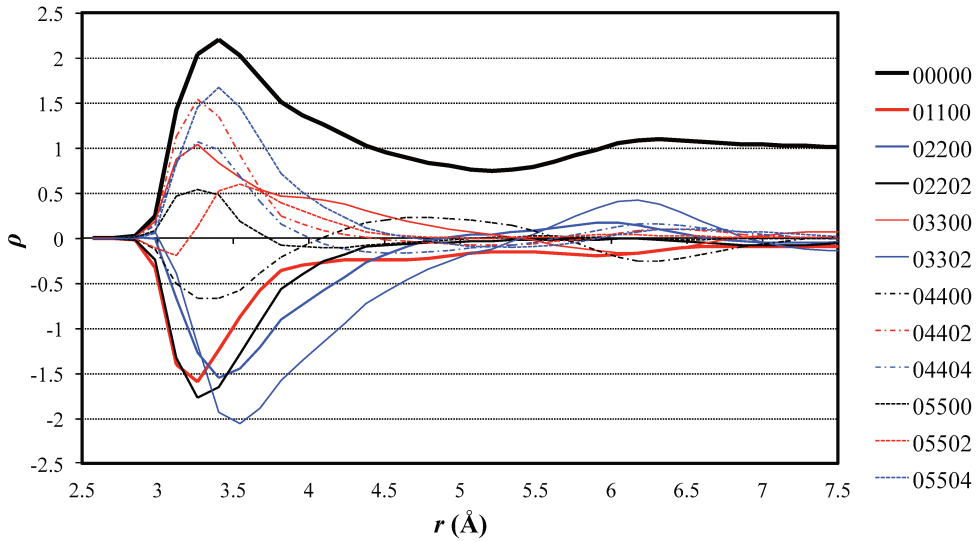

(a) $\rho_{0\nu}^{0nl}(r)$

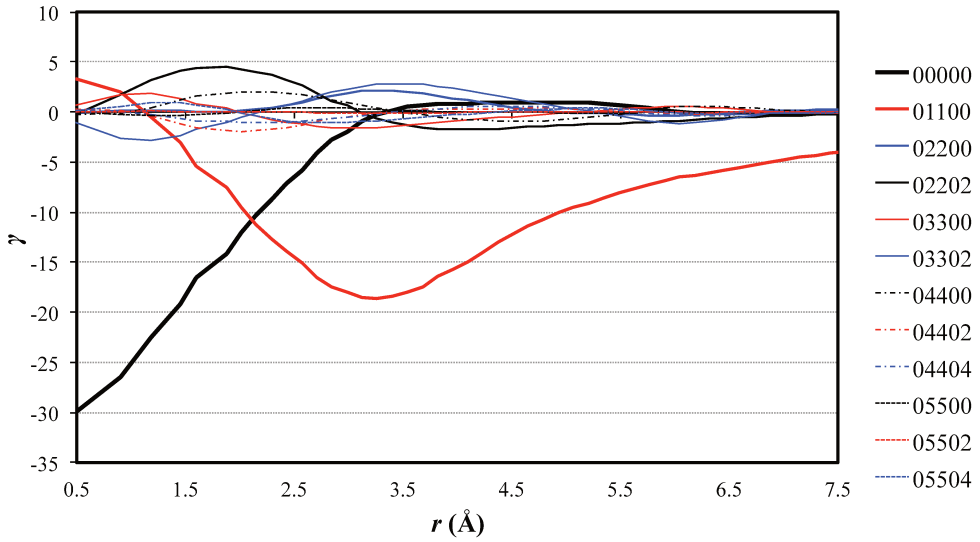

(b) $\gamma_{0\nu}^{0nl}(r)$

Figure 10.3: The projections $\rho_{0\nu}^{0nl}(r)$ and $\gamma_{0\nu}^{0nl}(r)$ computed for a 45^3 grid ($L = 25$) for a converged density of an artificial charged LJ center $CH_4^{+0.4}$

10.3.1 *Difference in energy evaluation*

Illustrated in table 10.3, the different methods listed in table 9.1 and using the same DCF give nearly the same total free energy at the end of minimization.

In table 10.3, we can see that apart from **`naive_interpolation`**, all branches give the same result if other parameters are fixed. The slight difference due to the interpolation error is also acceptable (in this case); and the error due to the GSH expansion (difference between, for instance, **`naive_standard`** and **`convolution_standard`**) seems to be well compensated during the minimization. This also supports the conclusion above that in fact we just need a lower expansion of GSH for γ than for $\Delta\rho$.

10.3.2 *A single k-kernel*

If we want to compare within one evaluation of $\mathcal{F}_{\text{exc}}$ as shown in figure 9.2, we can first examine the local paths from $\Delta\hat{\rho}^m_{\mu'\mu}(\mathbf{k})$ to $\hat{\gamma}^m_{\mu'\mu}(\mathbf{k})$ that can be tested independently for a given $\mathbf{k}$. Referring to figure 10.4, four algorithms are available for such a purpose:

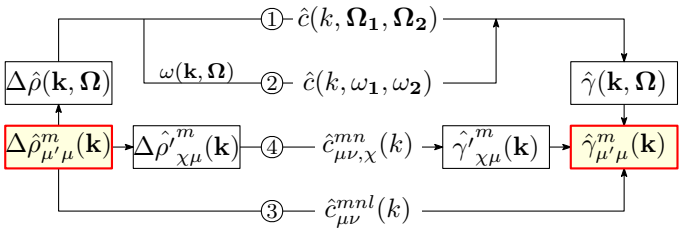

Figure 10.4: A k-kernel

A program to compare each element of $\hat{\gamma}^m_{\mu'\mu}(\mathbf{k})$ issued from these four algorithms for a given $\Delta\hat{\rho}^m_{\mu'\mu}(\mathbf{k})$ shows that the $\hat{\gamma}^m_{\mu'\mu}(\mathbf{k})$ for the four algorithms are strictly identical, i.e. the maximum error is at machine precision. This means the final result of energy and structure is independent to the choice of path inside a k-kernel, if $\Delta\hat{\rho}(\mathbf{k}, \mathbf{\Omega})$ can be fully expanded on GSHs.

10.3.3 *k-border effect*

The next step is to test the whole process shown in figure 9.2. Theoretically, if $\Delta\rho(\mathbf{r}, \mathbf{\Omega})$ is generated from a recombination of GSH projections $\Delta\rho^m_{\mu'\mu}(\mathbf{r})$, all the branches should give mathematically the same gradient $\gamma(\mathbf{r}, \mathbf{\Omega})$.

The detailed error value of γ here has not been noted, as it was regarded as a bug in the code at that time, then the code has since been modified. But in fact, the choice to add corrections or not on the even number grid is not a matter of right and wrong.

Firstly, we compare the three **`convolution`** algorithms passing by GSH expansion. For a 64^3 grid, $n_{\max} = 3$, the three algorithms **`convolution_standard`**, **`convolution_asymm`**, and **`convolution_pure_angular`** give the same $\mathcal{F}_{\text{exc}}$ at first sight, but somewhat different results when comparing each element of $\gamma(\mathbf{r}, \mathbf{\Omega})$. The perceived difference seems to decrease when increasing the number of grid points. Moreover, $\gamma(\mathbf{r}, \mathbf{\Omega})$ recombined from projections $\gamma^m_{\mu'\mu}(\mathbf{r})$, which should be purely real as explained in §7.3.2, have a slight imaginary part. Surprisingly, for a 65^3 grid, it gives numerically the same $\gamma(\mathbf{r}, \mathbf{\Omega})$ for all three algorithms at machine precision. The theory behind this behavior is found to be a special k-border effect linking to an even number of nodes in any dimension of the grid.

As the symmetry

$$\Delta\hat{\rho'}^m_{\chi\mu}(\mathbf{k}) = (-)^{m+\mu+\chi}\Delta\hat{\rho'}^{m*}_{\chi\underline{\mu}}(-\mathbf{k}) \tag{10.5}$$

is generated by two symmetries

$$\Delta\hat{\rho}^m_{\mu'\mu}(\mathbf{k}) = (-)^{\mu'+\mu}\Delta\hat{\rho}^{m*}_{\underline{\mu'}\underline{\mu}}(-\mathbf{k}) \tag{10.6}$$

$$R^m_{\mu'\chi}(\hat{\mathbf{k}}) = (-)^{m+\mu'+\chi}R^m_{\underline{\mu'}\chi}(-\hat{\mathbf{k}}) \tag{10.7}$$

For the k points "at border", i.e. after the FFT where the point having $\pm k_i = k_i^{\max}$, $i = 1, 2, 3$, for example for k_1,

$$\Delta\hat{\rho}^m_{\mu'\mu}(\pm k_1, k_2, k_3) = \Delta\hat{\rho}^m_{\mu'\mu}(k_1^{\max}, k_2, k_3) \tag{10.8}$$

is naturally put in the same array by FFT for the grids of an even number, as shown in figure 10.5.

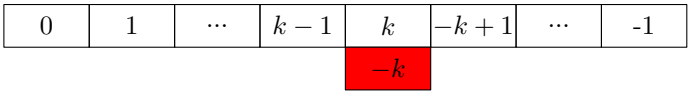

Figure 10.5: k-border effect

For example, for a grid 1D, the FFT having 6 points gives the values for indices 0,1,2,3,-2,-1, and the FFT having 7 points gives the values for 0,1,2,3,-3,-2,-1.

As FFT possesses periodicity, the symmetry (10.6) can always be respected at the border. However, as

$$R^m_{\underline{\mu'}\chi}(-\hat{k} \equiv (-k_1, -k_2, -k_3)) \neq R^m_{\mu'\chi}(k_1^{\max}, -k_2, -k_3) \tag{10.9}$$

the symmetries (10.7) and (10.5) are not respected for these points. In the backward process, if we account for all the $\gamma^m_{\mu'\mu}(\mathbf{k})$, as

$$\gamma^m_{\mu'\mu}(-\hat{k} \equiv (-k_1, -k_2, -k_3)) \neq \gamma^m_{\mu'\mu}(k_1^{\max}, -k_2, -k_3) \tag{10.10}$$

the symmetry

$$\gamma^m_{\mu'\mu}(\mathbf{k}) = (-)^{\mu'+\mu}\gamma^{m*}_{\underline{\mu'\mu}}(-\mathbf{k}) \tag{10.11}$$

is not totally respected, and this imposes that $\gamma^m_{\mu'\mu}(\mathbf{r})$ has an imaginary part. This imaginary part has been omitted implicitly in the "real to complex" FFT process used in, for example, FGSHT in **`convolution_standard`**, or FFT3D in **`convolution_pure_angular`**. That is to say, we keep only the part of nonnegative $\mathbf{k}$ or nonnegative μ, supposing that the part we omit respects the symmetry.

For the purpose that the three algorithm gives the same result, we can artificially impose at the border:

$$R^m_{\mu'\chi}(k_i^{\max}) = \frac{1}{2}\left[R^m_{\mu'\chi}(k_i) + R^m_{\mu'\chi}(-k_i)\right] \tag{10.12}$$

where i is the conflict index in figure 10.5. If more than one dimension is in conflict, this process can be done twice (4 terms for "edges" of the cube) or three times (8 terms for "vertices"). The point $\mathbf{k} = \hat{0}$ is different; as it is defined along the z-axes to avoid underdetermination, it does not respect eq. (10.7) or (10.5), neither. However, this point is proven to be negligible compared to the hundreds of thousands of total points.

10.3.4 *Difference in γ for "naive" and "convolution" methods*

In the same way, we compare the $\mathcal{F}_{\text{exc}}$ and $\gamma(\mathbf{r}, \mathbf{\Omega})$ given by branches **`naive_standard`** and **`convolution_standard`**. The $\mathcal{F}_{\text{exc}}$ of these two branches are identical for a 65^3 and $n_{\max} = 3$ grid, but the elements of $\gamma(\mathbf{r}, \mathbf{\Omega})$ have a difference at order of 10^{-2} to 10^{-3} which seems to be random. A test redone for a 45^3 grid is shown in figure 10.6.

According to figure 10.6, we can hypothesize that this error depends on the angular quadrature $m_{\max}$. The dependence is natural, as the difference between algorithms **`naive`** and **`convolution`** is the treatment of the angular part. There is also a dependence on L in the k-space, but after FFT it is mixed. The increase of error in the $n_{\max}$ chart is unnatural, implying there is still something theoretical that we have missed, or a bug in the code.

In short, this troublesome difference cannot be yet explained, as the **`naive`** methods do not have a k-border effect linked to symmetry, and in fact we used an odd grid. The projections $\gamma^{mnl}_{\mu\nu}(r)$ of these two algorithms seem to be identical (figure 10.7), which is to say that the global profile of the two should be almost the same, and thus the error would not be very decisive. Knowing that the difference is even further compensated with many iterations as shown in table 10.3, we can consider that this slight difference has no consequence to the final result.

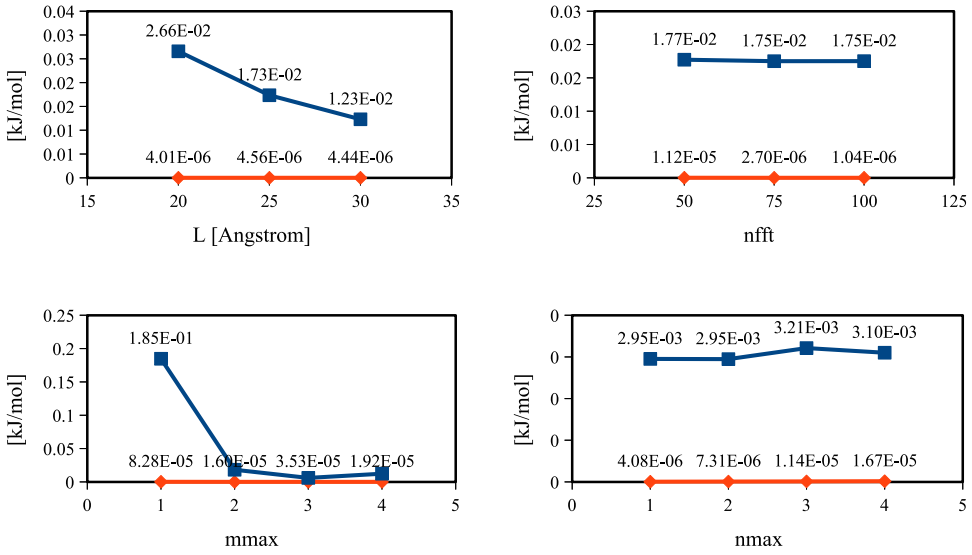

(a) $\delta\left[k_{\mathrm{B}}T\rho_0\hat{\gamma}(\mathbf{k},\mathbf{\Omega})\right]$

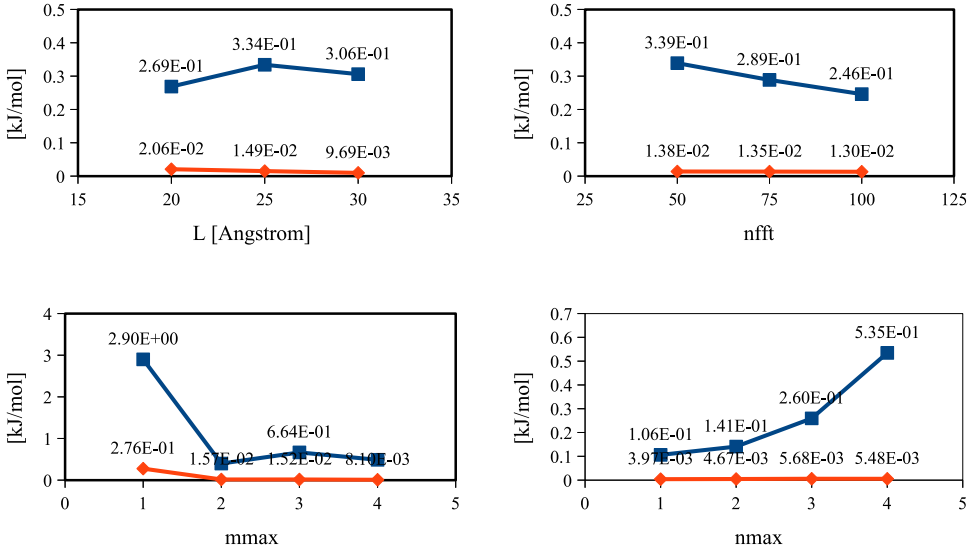

(b) $\delta\left[k_{\mathrm{B}}T\rho_0\gamma(\mathbf{r},\mathbf{\Omega})\right]$

Figure 10.6: Maximum (blue) and average (red) absolute difference in $\hat{\gamma}(\mathbf{k},\mathbf{\Omega})$ and $\gamma(\mathbf{r},\mathbf{\Omega})$ (normalized with $k_{\mathrm{B}}T\rho_0$), for tests of: (1) different box length L, with nfft $= 65$, $m_{\max} = n_{\max} = 2$; (2) different number of grid nfft^3, with $L = 25$ Å, $m_{\max} = n_{\max} = 2$; (3) $n_{\max} = 1$ to 4 for $m_{\max} = n_{\max}$ with 45^3 grid ($L = 25$ Å); (4) $n_{\max} = 1$ to 4 for $m_{\max} = 5$ with 45^3 grid ($L = 25$ Å). The test of $m_{\max} = n_{\max} = 5$ with 45^3 grid ($L = 25$ Å) is dropped as it takes too long. All the tests uses a converged density $\rho(\mathbf{r},\mathbf{\Omega})$ of an artificial charged LJ center $CH_4^{+0.4}$, recombined from GSH projections of corresponding order $m_{\max}$ and $n_{\max}$.

10.4 INTRINSIC VARIATION OF FREE ENERGY

The comparison between branches shows that there is no significant difference between the branches, if other parameters are all fixed. Therefore we are free to study the dependence on discretizing parameters with one or another algorithm.

Before studying the dependence on expansion order $m_{\max}$ and $n_{\max}$, we are interested in the spatial grid dependance, as well as the Ψ grid dependance if it is not automatically fixed by $m_{\max}$ (figure 10.8), which can have an influence on the tests later.

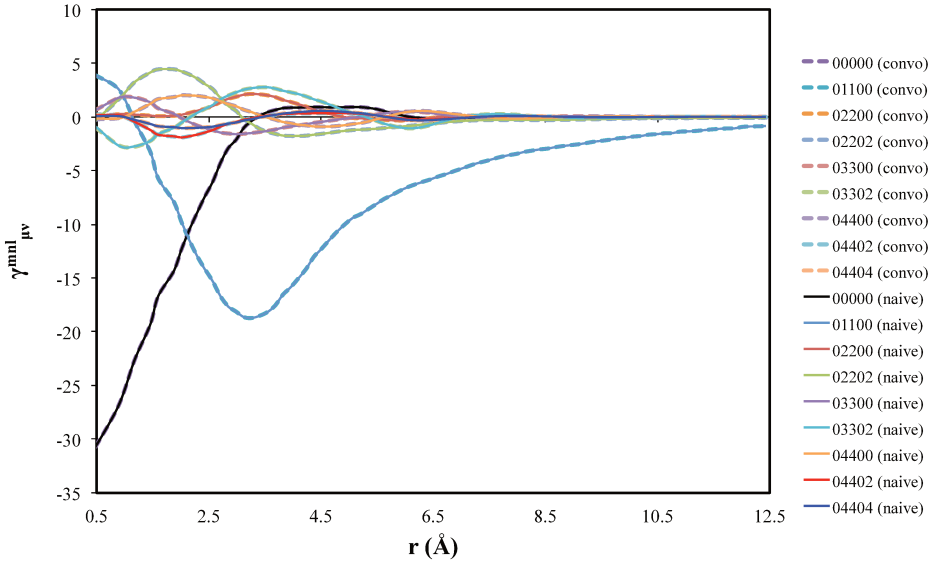

Figure 10.7: Comparison of projections $\gamma^{0nl}_{0\nu}(r)$ for branches "naive_standard" and "convolution_standard", computed with a 45^3 grid ($L = 25$) for a converged density of an artificial charged LJ center $CH_4^{+0.4}$.

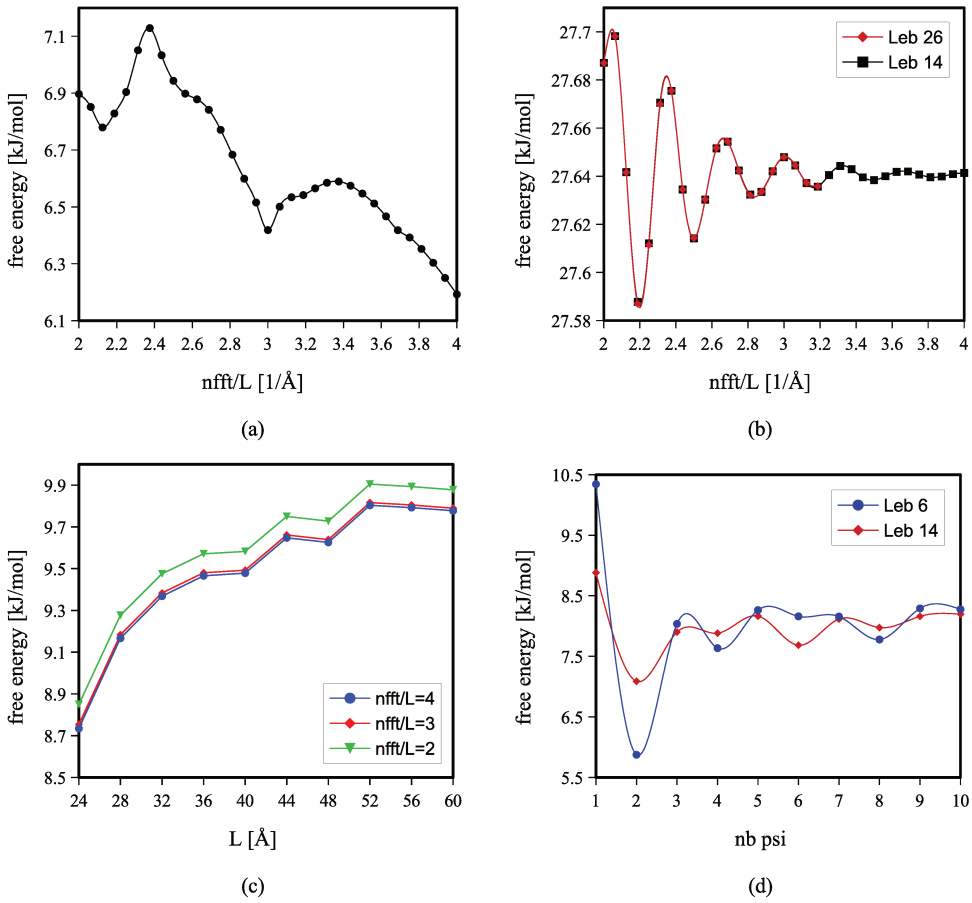

Figure 10.8: Space-grid and Ψ dependence of code MDFT. (a) $CH_4^{+0.33}$ using dipole DCF with $n_{\max} = 1$, $L = 32$ Å; (b) CH_4 using DCF of $n_{\max} = 5$, $L = 32$ Å, Lebedev quadrature of order 2 or 3; (c) acetone using dipole DCF, Lebedev quadrature 1 and 1Ψ angles, $\text{nfft}/L = 2, 3, 4$, using direct summation; (d) acetone using dipole DCF and Lebedev quadrature 1 or 2, varying Ψ, $L = 32$ Å, nfft = 96.

Looking at figure 10.8 (a) and (b), we show that the resolution of the spatial grid has an effect on the calculated free energy. For the charged solute $CH_4^{+0.33}$, the energy has a tendency to decrease when increasing the resolution of grid (nfft). This decrease does not link to the border correction mentioned in §8.1, as both the box length and the charge remain the same for the whole set of tests. From (b) we consider that at least a 3-points grid in 1 dimension (each direction) per Angstrom is needed to reduce the uncertainty due to grid resolution. The molecule in Figure (c) is neutral (although dipolar), i.e. it does not need any border correction neither. We see that the energy also varies with respect to the box length (with direct summation this time), and has the same tendency for different resolutions nfft/L. The curves of nfft/$L = 3$ and nfft/$L = 4$ do not give too much difference. Figure (d) fixed the Lebedev quadrature for Θ and Φ, but left varying the Ψ. We can also see a dependence on Ψ which does not completely vanish when increasing the resolution of angular grid. Since throughout the whole thesis the Ψ is theoretically fixed by the order of the quadrature in Θ and Φ, this remains an issue requiring further verification. We can roughly conclude that an error around 1-2 kJ/mol is common for this code. The spatial grid dependence will not be treated in this thesis as it may come from other terms of the functional.

10.5 SERIES OF CHARGED LJ CENTERS

To validate the method by comparing with IET, as well as to study the dependance on $m_{\max}$ and $n_{\max}$, we firstly chose a series of charged LJ centers, which possess the LJ parameters of CH_4 [73], and have a variable charge from -1.0 to 1.0 (table 10.4).

For both IET and DM results in this thesis, 298K is used according to habitude instead of 303K recommended in reference [47]. For MDFT, 300K and 298K are used.

SOLUTE	$\mathfrak{q}$	σ [Å]	ϵ [kJ · mol^{-1}]
CH_4	-1.0 to 1.0	3.73	1.23

Table 10.4: Parameters of charged CH_4 LJ centers for test usage

10.5.1 *Box length dependance and charge dependance of free energy*

As discussed in section 8.1, for single ions, two types of corrections need to be added on the free energy, which depend on the box length and charge of the ion. To verify these dependencies, we implement a systematic calculation with variable charge and box length using 3 different methods, the parameters of which are shown in table 10.5. It should be noted that the **`naive_interpolation`** only used 14 Lebedev and 3 Ψ angles to converge, which gives exactly the same result with 26 Lebedev and 4 Ψ angles. That means the **`naive`** methods do not need an order of quadrature $m_{\max}$ to be greater than the order of DCF $n_{\max}$.

Some points of negative charge diverged; (in IET, the negative charges also have difficulty converging), and all the converged results are presented.

METHOD	SURNAME	L	nfft/L	$m_{\max}$	$n_{\max}$
`naive_nmax1`	nmax1_lmn	24 to 60	3	1 (Leb), 3 angles for Ψ	1
`naive_interpolation`	nmax5_inter	24 to 60	3	2 (Leb), 3 angles for Ψ	5
`convolution_standard`	nmax1_convo	24 to 60	3	1	1

Table 10.5: Methods and parameters for charged CH_4 series test. Leb is Lebedev quadrature (6 angles of Θ and Φ for $m_{\max} = 1$ and 14 for $m_{\max} = 2$), which is mathematically equivalent to Gauss-Legendre quadrature but requires only ~2/3 angles.

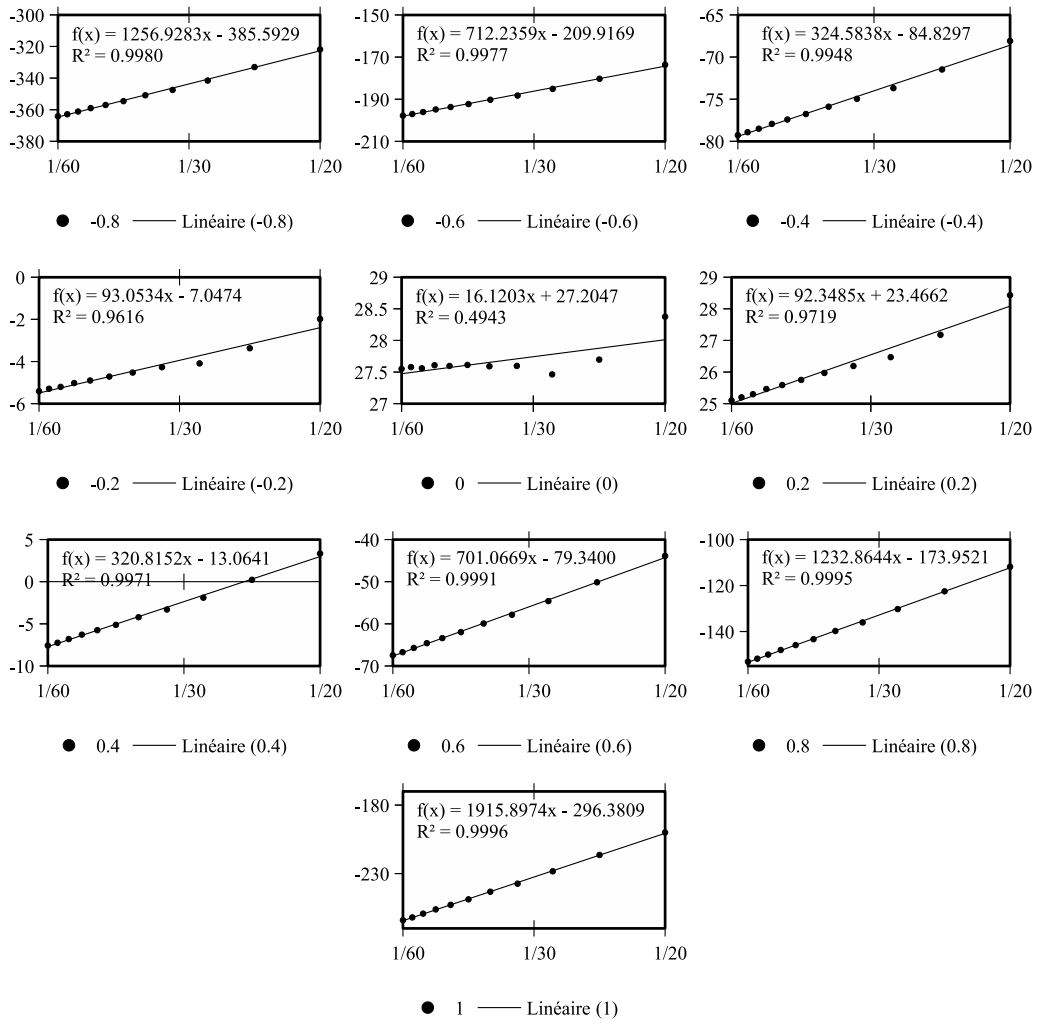

Figure 10.9: Free energy (without correction) of charged CH_4 center (-1.0 to 1.0) with respect to the box length, for **`naive_nmax1`** method, with 6 angles of Lebedev quadrature angles for Θ and Φ, 3 for Ψ, DCF of $n_{\max} = 1$, at 300K.

The collections of the raw results issued directly from the code MDFT are shown in figure 10.9, 10.10 and 10.11. We can see that the dependence of box length for each charge is almost linear, except for the charge between $[-0.2, 0.2]$ (where grid dependence dominated compared to other effects). This means the influence of box length is much greater than the intrinsic variation of result mentioned in 10.4. The charge dependency of the slopes in these figures is traced in figure 10.12 with respect to $\mathfrak{q}^2$, square of the corresponding number charge. A linear regression is done to give the slope in figure 10.12 at 1937.8 $\mathrm{kJ \cdot mol^{-1} \cdot Å}$. This slope corresponds to the correction of type-B:

$$\frac{f_Q \xi}{2}\left(1 - \frac{1}{\varepsilon}\right) = 1943.2\,\mathrm{kJ \cdot mol^{-1} \cdot Å} \tag{10.13}$$

where $f_Q = q_e^2 10^{-3} N_\mathrm{A}/(4\pi\varepsilon_0 10^{-10})$ is the electrostatic potential unit so that $f_Q \cdot \mathfrak{q}^2/r$ is in $[\mathrm{kJ \cdot mol^{-1}}]$.

The intercept values in each of figures 10.9 to 10.11 correspond to the free energy of an infinite box. The IET results to be compared were obtained using the 1D-HNC formalism (1 distance, 5 angles) developed by Belloni and collaborators [74]. The calculations were done with a cut-off distance of $R_{\max} = 102.4$Å and an additional Born-like correction of $-2.556 k_\mathrm{B} T$ to obtain the free energy in the infinite system. The difference in free

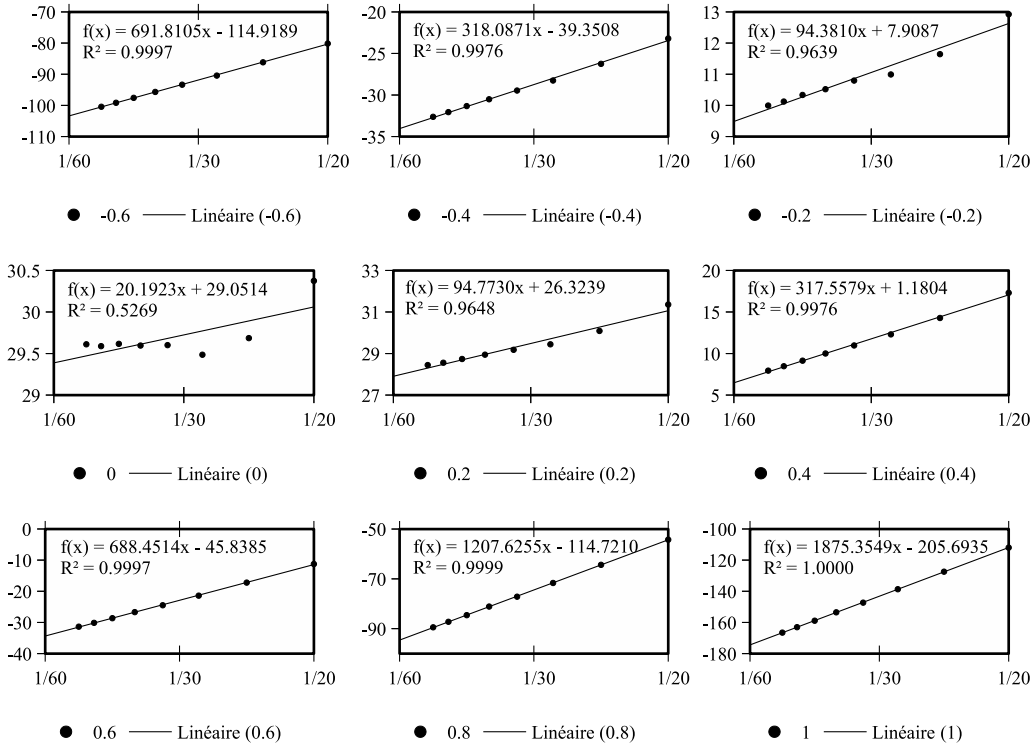

Figure 10.10: Free energy (without correction) of charged CH_4 center (-1.0 to 1.0) with respect to the box length, for **`naive_interpolation`** method, with 14 angles of Lebedev quadrature angles for Θ and Φ, 3 for Ψ, DCF of $n_{\max} = 5$, at 300K.

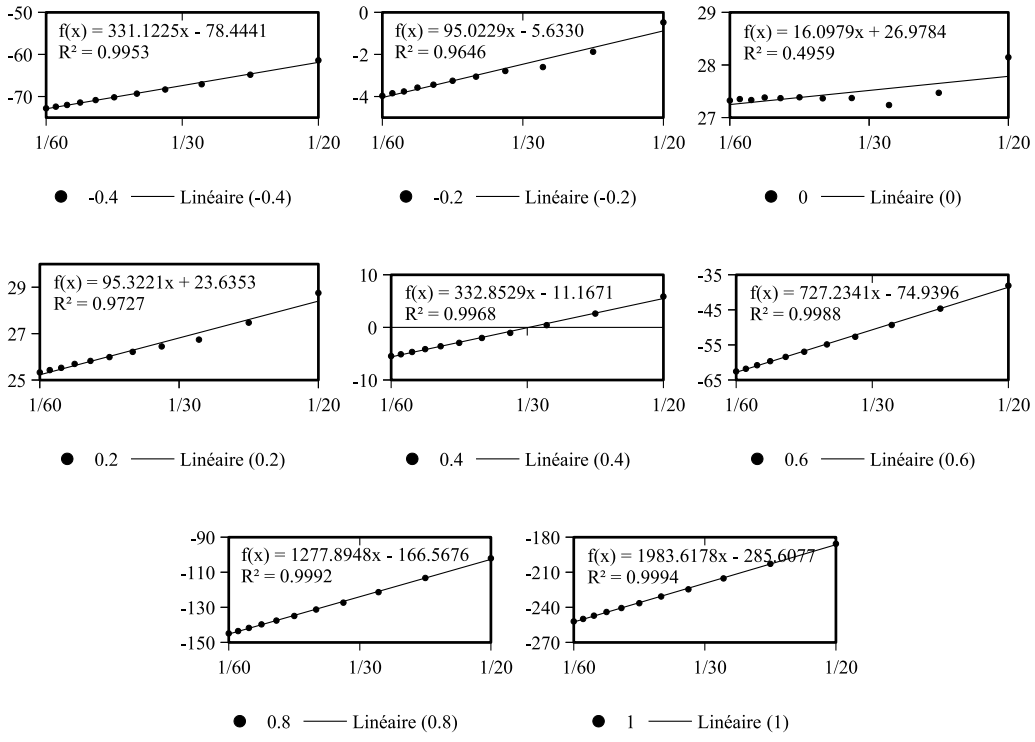

Figure 10.11: Free energy (without correction) of charged CH_4 center (-1.0 to 1.0) with respect to the box length, for **`convolution_standard`** method, with $m_{\max} = n_{\max} = 1$, at 298.15K.

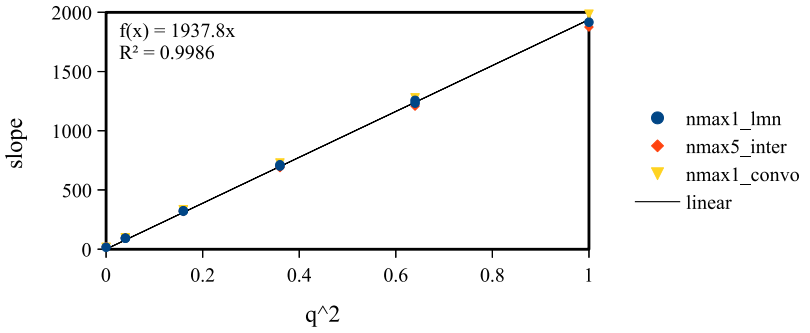

Figure 10.12: Quadratic charge dependence of free energy in CH_4^q series

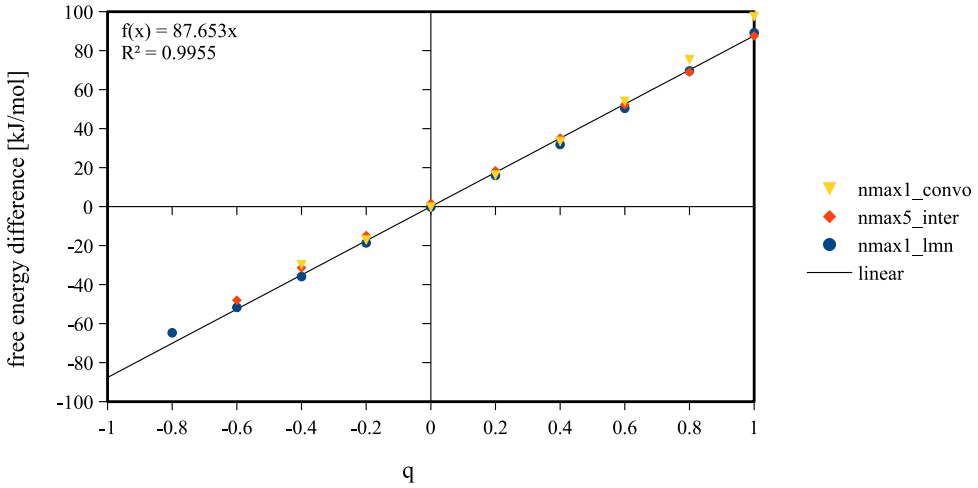

Figure 10.13: Free energy (extrapolated to infinite box length) of charged CH_4 compared to IET, without P-scheme correction

energy between MDFT and IET of the infinite system are given in figure 10.13. The linear regression is done with all existing points in this figure, and its slope 87.653 kJ · mol^{-1} corresponds to the correction of type-C:

$$\frac{2\pi}{3} f_Q \eta\gamma = 82.104 \text{kJ} \cdot \text{mol}^{-1} \tag{10.14}$$

The measured number and the theoretical one are a little different, which can be principally due to the lack of point at the -1 charge side.

10.5.2 *Comparison with IET after corrections*

The points in figure 10.13 after correction with eq. (10.14), as well as the difference between results of $m_{\max} = n_{\max} = 5$ given by **`convolution_standard`** (with $L = 24$ Å, nfft = 72) using theoretical corrections and IET with infinite corrections (nmax5_convo) are shown in figure 10.14. Note that the curves for the same DCF are not perfectly in agreement with each other, despite what is shown in table 10.3. The fact is that in "nmax1_lmn", Lebedev quadrature is used, and in "nmax1_convo", Gauss-Legendre quadrature is used, as we know the different angular grid can have an effect on the energy; and for $n_{\max} = 5$, as we have taken by chance the +0.4 as charge in table 10.3, the difference between the **`naive_interpolation`** and **`convolution_standard`** results are accidentally small. The troublesome energy shift of about 2 kJ · mol^{-1} between "nmax5_inter" and IET result is yet to be understood, as well as the dependence on q for "nmax5_convo" after correction. But if we look at the free energies without comparing them in figure

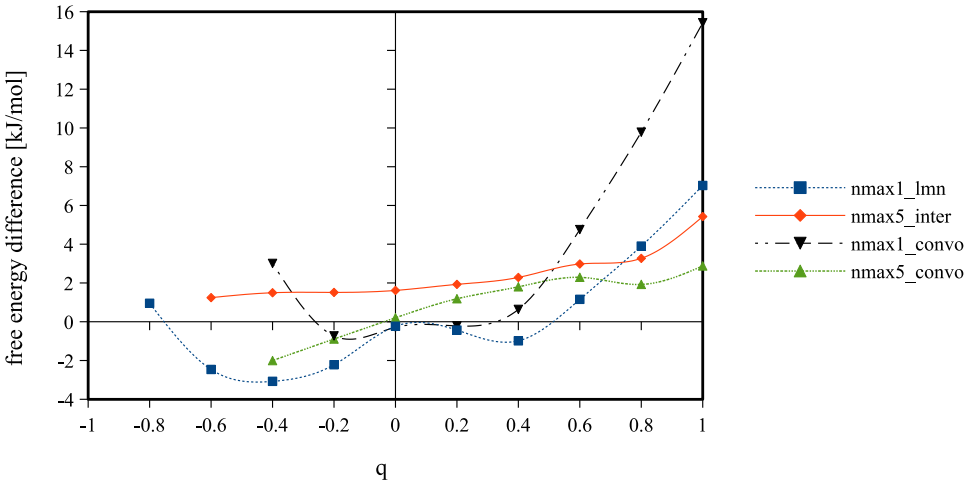

Figure 10.14: Free energy difference of CH_4^q series compared to IET, with all corrections

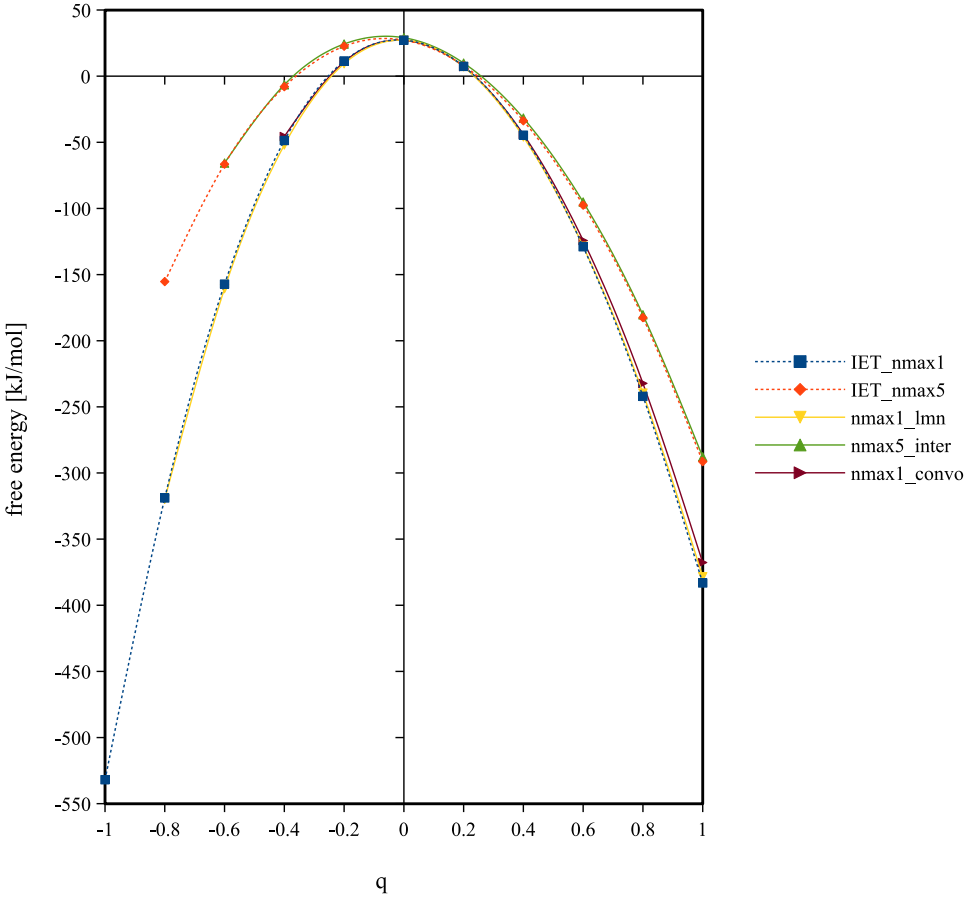

Figure 10.15: Free energy of CH_4^q series, with all corrections

10.15, we can see that these differences are almost negligible compared to the total energy they possess, and the curves only differ with different DCFs.

10.5.3 *Dependence on $m_{\max}$ and $n_{\max}$*

As we see, the free energy of charged CH_4^q series depends a lot on the order of DCF, $n_{\max}$. To study systematically the influence of $m_{\max}$ and $n_{\max}$, we chose a series of tests

CHARGE		-0.6			0			1	
$n_{\max}\backslash m_{\max}$	IET	$= n_{\max}$	$= 5$	IET	$= n_{\max}$	$= 5$	IET	$= n_{\max}$	$= 5$
1	-157.48	diverge	-163.35	27.33	27.47	27.97	-382.34	-365.89	-379.01
2	-84.32	-87.56	-87.71	27.82	27.94	28.12	-301.74	-298.95	-298.67
3	-66.25	-69.58	-69.70	27.16	27.24	27.50	-294.77	-292.12	-291.87
4	no data	-69.41	-69.50	no data	27.85	27.91	no data	-289.19	-289.04
5	-66.50	diverge	diverge	27.25	27.47	27.47	-291.60	-288.54	-288.54

Table 10.6: Free energy of CH_4^q series (with corrections) for IET, $m_{\max} = n_{\max}$ and $m_{\max} = 5$, using **convolution_standard**, with $L = 24$ Å, nfft $= 72$.

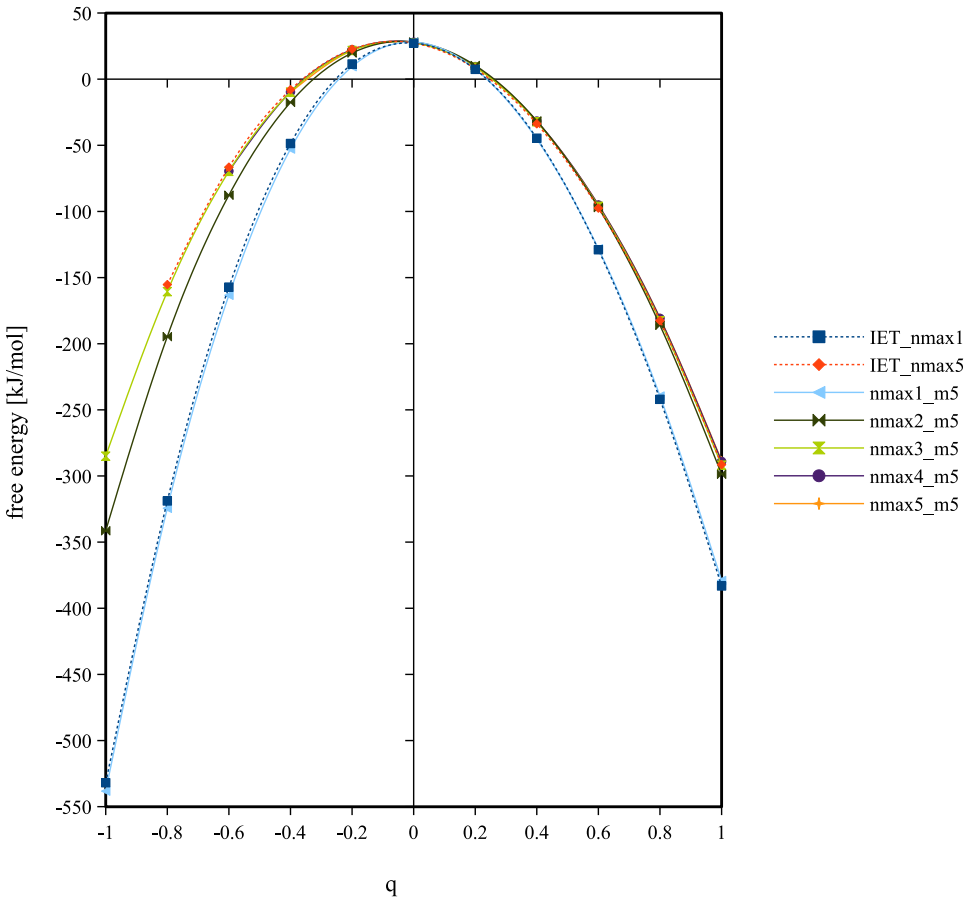

Figure 10.16: Free energy of CH_4^q series, with all corrections of IET results and MDFT $m_{\max} = 5$, $n_{\max} = 0, \ldots, 5$.

with three charges: -0.6, 0, and +1, using **convolution_standard**, as shown in table 10.6. Three types of energy are listed: the results issued from IET, and the case when $m_{\max} = n_{\max}$ and $m_{\max} = 5$. As we said previously the gradient γ is smoother than ρ; it is worthwhile to study the case when the order of quadrature $m_{\max}$ for the expansion of ρ is larger than the order of DCF $n_{\max}$ used in equation OZ to solve γ, in order to save computing cost.

From table 10.6 we can see that the free energy becomes stable in any case when $n_{\max} \geq 3$; the free energies are quite in agreement with IET results; and there is almost no difference between $m_{\max} = n_{\max}$ and $m_{\max} = 5$. That means, the quadrature of ρ has no influence on the final energy, which is yet comprehensible, as the extra order of

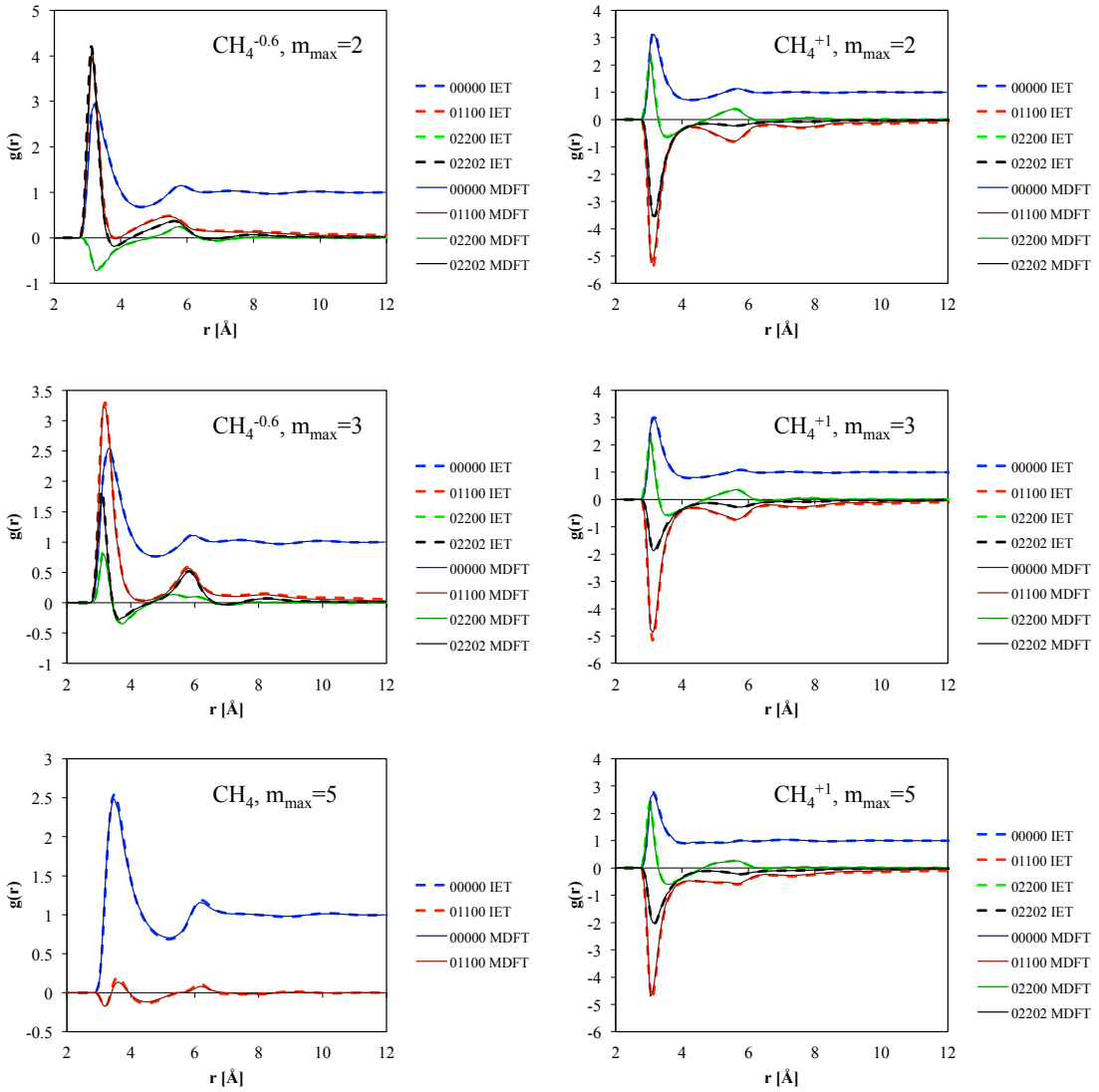

Figure 10.17: The projections $\rho_{0\nu}^{0nl}(r)$ of some selected charges of CH_4^q series comparing to IET, with $m_{\max} = n_{\max}$.

quadrature gives no influence on the functional gradient, and the ρ used to evaluate the functional is given by minimization, i.e. without expansion on GSHs.

A scheme of free energy evaluation with respect to $n_{\max}$ ($m_{\max} = 5$, as some of the points of $m_{\max} = n_{\max}$ have difficulty converging and if convergence is achieved they usually give the same result) is made in figure 10.16. We see that from $n_{\max} = 3$ to higher order, the curves do not vary a lot. We can conclude that within $n_{\max} \geq 3$ to $n_{\max} = 5$, the error in free energy is acceptable.

We take solute-solvent formalism for MDFT, and IET takes the solvent-solute formalism. Thus in MDFT the $g_{\mu\nu}^{mnl}$ corresponds to the $g_{\nu\mu}^{nml}$ in IET. In figure 10.17 it is converted to give better understanding.

Some selected projections $\rho_{0\nu}^{0nl}(r)$ (0 as solute is spherical) are compared to IET in figure 10.17. We can see that they are well in agreement.

If we compare one charge in one graph with all the $n_{\max}$, we can determine which $n_{\max}$ is sufficient to have a good structure of the density ρ. Figure 10.18 gives the RDFs and RPFs for the three charges, as well as their zoomed parts, in order to have a clear view of the differences. Firstly we can see that in most cases, apart from uncharged CH_4 and some $n_{\max} = 1$, the curves of $m_{\max} = 5$ and $m_{\max} = n_{\max}$ are superposed. That means even for structures of single ions, extra order of $m_{\max}$ is useless. For -0.6, the curves converge from $n_{\max} = 3$, and for +1, $n_{\max} = 4$. For CH_4 it seems to be a mess, but looking at the scale of the schema, we consider that it converges from $n_{\max} = 4$. To conclude, for

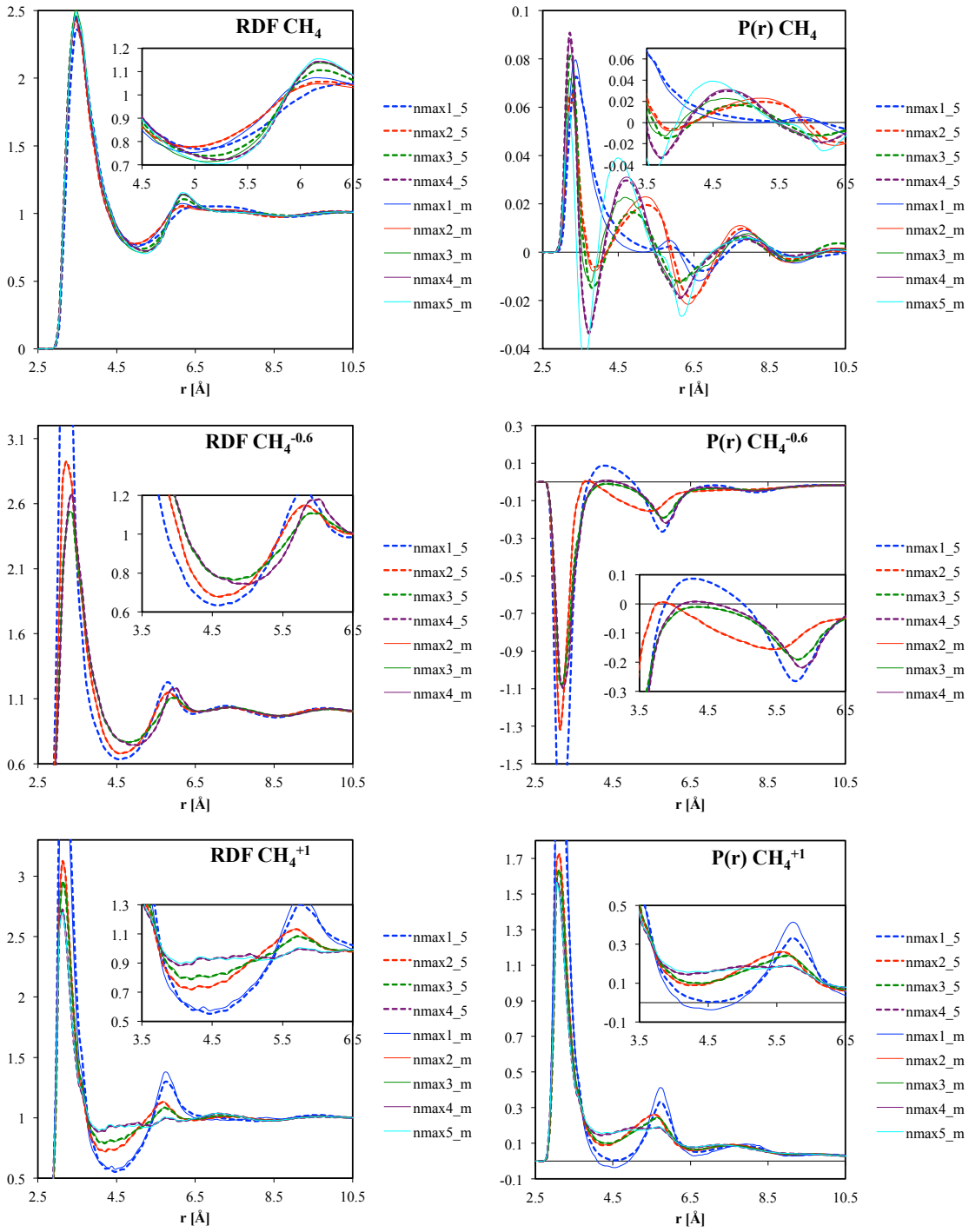

Figure 10.18: RDF and RPF of some selected charges of CH_4^q series with different $m_{\max}$ and $n_{\max}$

CH_4^q series, we think $n_{\max} = 3$ is sufficient for energy, and $n_{\max} = 4$ is sufficient for the structure to converge (without considering higher order projections).

10.6 UNCHARGED LJ CENTERS

As there is an energy shift between **`naive_interpolation`** and IET results even for uncharged CH_4 (figure 10.14), we have calculated some other uncharged LJ centers. Results

SOLUTE	σ	ϵ	dipole	1	2	3	4	5	inter	IET
Neon	3.035	0.15432	18.61	18.79	19.03	18.56	18.99	18.86	20.04	18.82
Argon	3.415	1.03931	22.16	22.47	22.86	22.15	22.72	22.39	24.24	22.27
Krypton	3.675	1.4051	25.36	25.76	26.23	25.48	26.14	25.73	27.82	25.49
Xenon	3.975	1.7851	29.68	30.24	30.77	30.13	30.74	30.25	32.66	29.92

Table 10.7: Free energy $[\mathrm{kJ \cdot mol^{-1}}]$ of rare gases, for respectively **`reference_dipole`**, **`convolution_standard`** with $m_{\max} = n_{\max} = 1, \ldots, 5$, and **`naive_interpolation`** with DCF of $n_{\max} = 5$; σ in [Å], ϵ in $[\mathrm{kJ \cdot mol^{-1}}]$, with $L = 24$ Å, nfft $= 72$.

in table 10.7 show that this energy shift is common in any uncharged LJ centers; and in these cases, even $n_{\max} = 1$ can satisfy the requirement of chemical precision.

10.7 LINEAR SOLUTES

To complete the story of $m_{\max}$ and $n_{\max}$ convergence, we choose some linear solutes shown in figure 10.19 and table 10.8. The direct summation method (§4.1.2) is used for $\mathcal{F}_{\mathrm{ext}}$ evaluation, as O_2 always diverges with the Poisson method. We can make a hypothesis that this is because the distance between the charges is too short, as shown in figure 10.19; therefore the interpolation in $\mathcal{F}_{\mathrm{ext}}$ evaluation can cause divergence. There is a better version of Poisson solver that is developed in parallel of this code, which has been reported to have better convergency. We consider that this divergency problem does not come from the evaluation of $\mathcal{F}_{\mathrm{exc}}$.

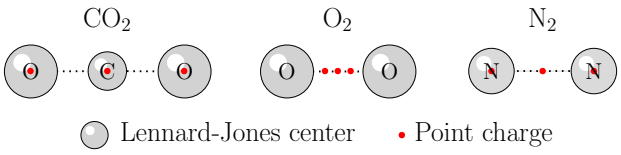

Figure 10.19: Test linear solutes

SOLUTE	SITE	q	σ [Å]	ϵ $[\mathrm{kJ \cdot mol^{-1}}]$	x [Å]
CO_2 [75]	1	0.6512	2.76	0.234	0.000
(20.48 $[\mathrm{kJ \cdot mol^{-1}}]$)	2	-0.3256	3.03	0.67	-1.149
	3	-0.3256	3.03	0.67	1.149
O_2 [76]	1	0.0	3.1062	0.36	-0.485
(22.05 $[\mathrm{kJ \cdot mol^{-1}}]$)	2	0.0	3.1062	0.36	0.485
	3	-2.1	0.00	0.00	-0.200
	4	-2.1	0.00	0.00	0.200
	5	4.2	0.00	0.00	0.000
N_2	1	-0.5075	3.30	0.30	-0.549
(26.75 $[\mathrm{kJ \cdot mol^{-1}}]$)	2	-0.5075	3.30	0.30	0.549
	3	1.0150	0.00	0.00	0.000

Table 10.8: Parameters of test solutes. Reference free energy by IET in parentheses.

Table 10.9 shows the free energy of solute with respect to $n_{\max}$. We also find that from $n_{\max} = 3$, the free energy seems to converge, and there is almost no difference between $m_{\max} = 5$ and $m_{\max} = n_{\max}$.

SOLUTE	CO_2 (20.48)		O_2 (22.05)		N_2 (26.75)	
$n_{\max}\backslash m_{\max}$	$m_{\max} = n_{\max}$	$m_{\max} = 5$	$m_{\max} = n_{\max}$	$m_{\max} = 5$	$m_{\max} = n_{\max}$	$m_{\max} = 5$
1	11.53	9.61	21.55	21.46	25.11	24.76
2	17.87	17.87	22.35	22.38	26.63	26.63
3	20.33	20.35	21.89	21.96	26.60	26.62
4	20.88	20.88	22.42	22.45	27.10	27.11
5	20.52	20.52	22.07	22.07	26.74	26.74

Table 10.9: Free energy of solutes. Reference free energy by IET in parentheses.

The solvent structures around the various solutes are also compared to IET results, as this of CO_2 shown in figure 10.20. For the projections of $m = 0$, they are well in agreement with IET results, but for the projections with $m = 2$, a factor of normalization at $\sqrt{3}$ appears, which seems to have no reason to exist, as the factor normally linked to m is $2m + 1$ or $\sqrt{2m + 1}$.

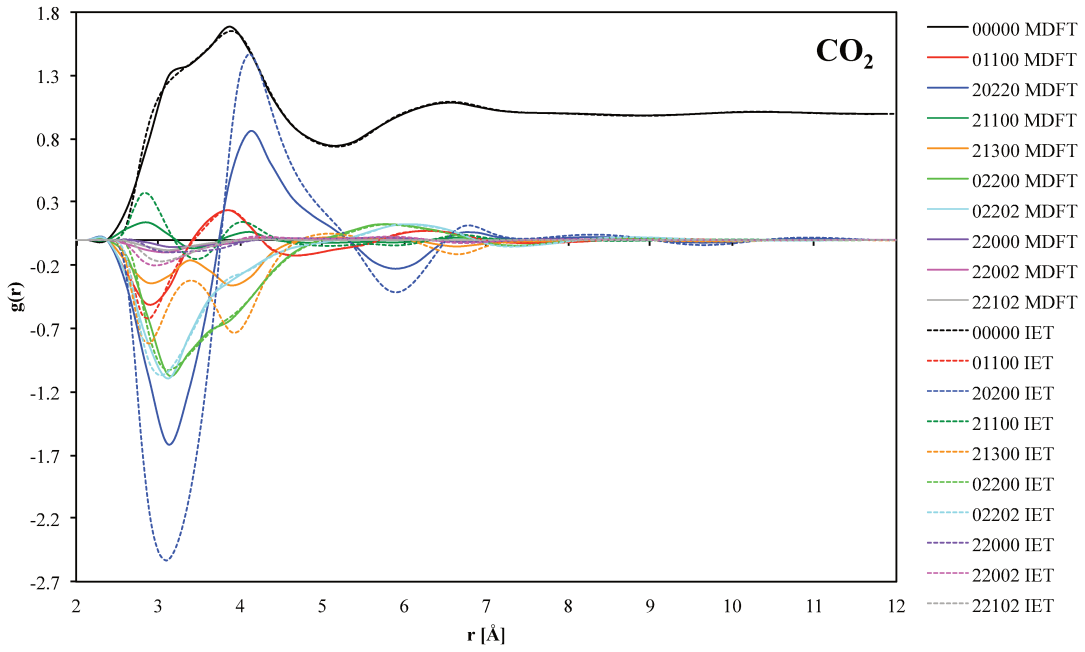

Figure 10.20: The projections $\rho_{\mu\nu}^{mnl}(r)$ of CO_2 comparing to IET, with $m_{\max} = n_{\max} = 5$, $L = 24$ Å, nfft = 72. $\frac{1}{3}n_{\text{bin}}$ is used in order to avoid noise.

10.8 FIRST CONCLUSION

From the above results, the following initial conclusions may be drawn:

- MDFT is capable of producing the solvation free energy at chemical precision with normal convergence criteria (which gives 2 decimals for a specific spatial and angular grid), which is nearly the same compared to mathematical equivalent IET results for LJ centers, single ions and linear solutes. The variance of free energy due to discretization parameters is at chemical precision, i.e. 1 to 2 kJ/mol. To keep this precision, at least $n_{\max} = 3$ is needed, and the order of quadrature $m_{\max}$ has no influence on the energy and structure if it is larger than $n_{\max}$. This $n_{\max}$ is far from sufficient to describe the solvent density ρ, but sufficient for γ. As ρ is produced by

the minimization, its expansion has no influence on the final result. The different branches produce almost the same result with the same DCF, compared to the error introduced by spatial grid dependence; while **`naive_interpolation`** seems to be a bit more stable compared to **`convolution`** methods in terms of convergence for negative molecules, but exhibits a small energy shift about 2 kJ/mol for neutral LJ centers. For charged solutes, the two types of free energy corrections mentioned in this thesis are needed.

- As for structure, MDFT can also produce the same result as IET. It requires about $n_{\max} = 4$ to have a converged curve of $g(r)$ projections. For solutes, we are obliged to use a looser sampling rate to have a smooth curve; as the spatial grid is cubic, but not in spherical coordinates as IET. Indeed MDFT has the great advantage to be generalizable to produce 3D solvent structures for complicated molecules, but IET is ideal, and much more efficient when giving information about small symmetric molecules using functions with respect to r.

11

Computing Performance

This section evaluates the computing performance (timing) of the code. Our goal is to show that the new algorithm of angular convolution is much faster than the old naive one; the huge amount of simulation during this thesis has proven that it is indeed the case. The purpose of this section is to substantiate this statement by a proper and systematic performance evaluation.

In this section, we will evaluate the performance only concerning the $\mathcal{F}_{\text{exc}}$ term, knowing that the two other terms of the functional, the $\mathcal{F}_{\text{id}}$ and $\mathcal{F}_{\text{ext}}$ contribution, require a computer time of the same magnitude as the new algorithms for $\mathcal{F}_{\text{exc}}$ part. The spatial and angular grid dependence of the various branches are discussed.

11.1 FFT

The FFT, which is used by the spatial convolution and the FGSHT process, play an important role in the implementation.

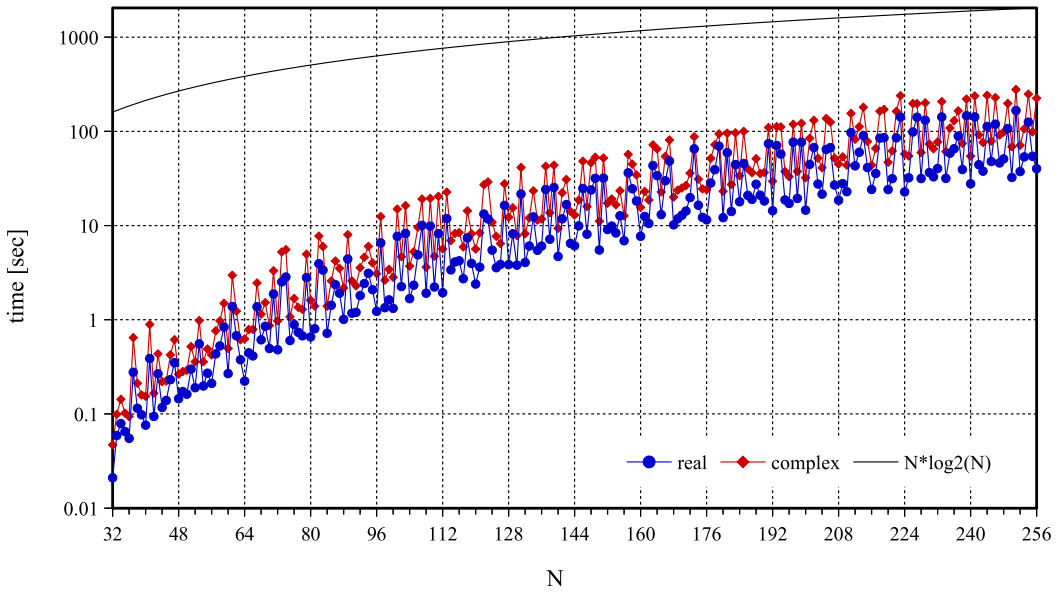

Figure 11.1: Timing of FFT for real-to-complex and complex-to-complex processes with respect to grid number N

Referring to figure 11.1, the expected dependance on $O(N \log_2 N)$ [62] does not totally exist, but it appears to be of the same form, depending on the algorithm of FFT [77]. It should be noted that a grid of prime number is always at one of the peaks in the figure, which means it can be twice or more times slower than that of a nearby composite number. Therefore it is better to use an even number grid, for which the k-border correction in §10.3.3 should absolutely be accounted for. Apart from this, to compare the algorithms for angular integration involved in this thesis, we are not really interested in computing performance with respect to the number of spatial grid. However, the ratio of real and complex FFT timing is important, as illustrated in figure 11.2, where the ratio between

real-to-complex and complex-to-complex FFT processes is measured as 0.54, near the theoretical ratio 0.5. For example, we may process n_{angle} real to complex FFT, then $n_{\text{spatial}}/2$ complex to complex FGSHT. Or we may process n_{spatial} real to complex FGSHT, then $n_{\text{proj}}/2$ complex to complex FFT. This should not give a significant difference if $n_{\text{angle}} \sim n_{\text{proj}}$ for small $n_{\max}$. If the ratio is not 1:2, it will have an influence on the choice of algorithm.

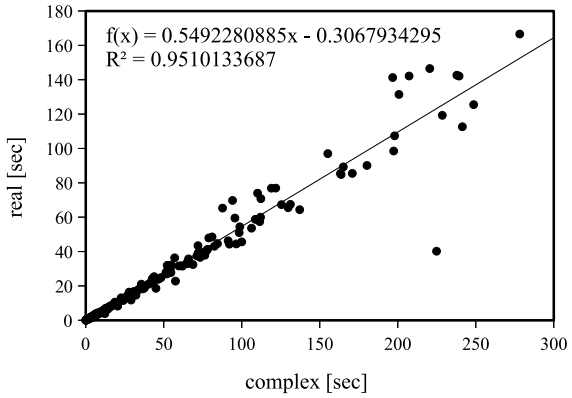

Figure 11.2: Timing of real-to-complex FFT processes with respect to its complex-to-complex process of the same grid number N

11.2 FGSHT

The computing times of GSHT and FGSHT are shown in figure 11.3. There is no reason to view in detail how much FFT has accelerated the GSHT process, but clearly FGSHT can be 100 times faster than GSHT. Besides, looking at the influence of the symmetry in Ψ on GSHT, $s = 1$ is on average 5 times longer than $s = 2$ (s being the MRSO defined in §7.2). As accuracy tests show that GSHT and FGSHT give exactly the same result, and as the case $m_{\max} < n_{\max}$ is never needed, it is possible to utilize FGSHT in all the cases to have a faster performance.

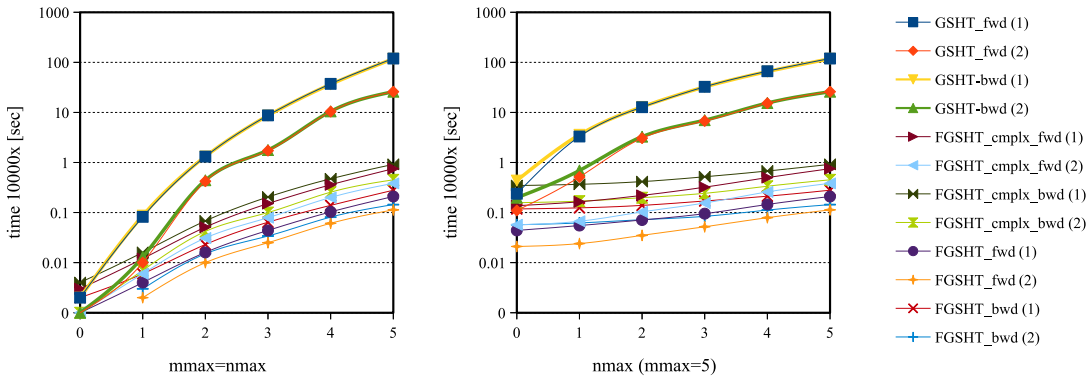

Figure 11.3: Computing time of GSHT and FGSHT (per 10000 times), between parentheses is the order of symmetry axes s

However, it is important to know the ratio between real and complex FGSHT processes for the same reason as FFT. It is demonstrated that this number is 0.3 in all cases, and

it does not depend on $m_{\max}$, $n_{\max}$ or s. The difference between these two is that the real one performs real-to-complex FFT for the Φ, Ψ grid and calculates only slightly more than half of projections ($\mu \geq 0$) than the complex one. Theoretically, the ratio should be greater than 0.5. This could mean there may be an extra process in the complex one, or it is controlled by the memory. Ultimately, the final result 0.3 means that doing n_{spatial} real to complex FGSHT should take only 0.6 the time of doing $n_{\text{spatial}}/2$ complex to complex FGSHT, which means in **`convolution_standard`** we should use less time to compute FGSHT than in **`convolution_pure_angular`**; which is in fact not observed in the following tests.

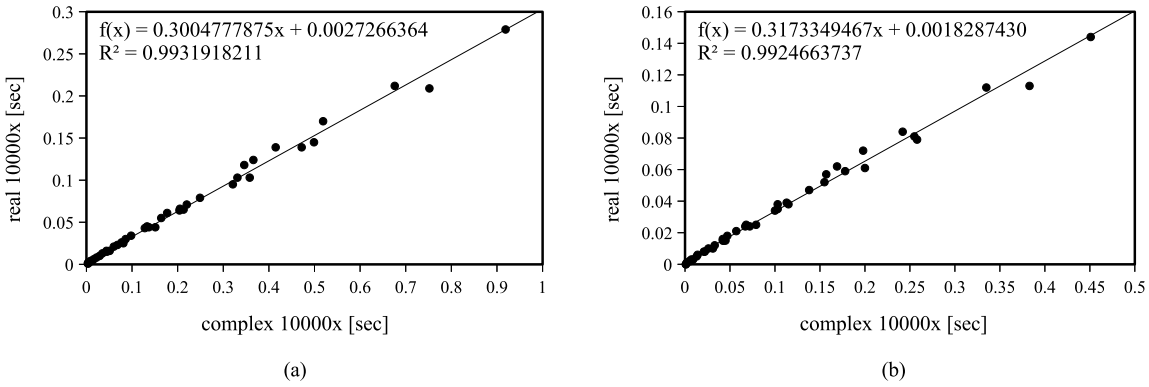

Figure 11.4: Timing of real-to-complex FGSHT processes with respect to its complex-to-complex process of the same $m_{\max}$ and $n_{\max}$, for $s = 1$ and $s = 2$

11.3 k-KERNEL

As discussed in the previous section, the final result of energy and structure is independent of the choice of path inside a k-kernel. That means we are free to choose the fastest path. Path (1) passing directly by $\hat{c}(k, \mathbf{\Omega}_1, \mathbf{\Omega}_2)$ in figure 10.4 has no interest in timing, as the memory limit does not support such a direct algorithm for the entire k-space. Here we only compare the paths (2), (3) and (4), which correspond to eq. (6.1), (7.5) and (7.12).

The theoretical predictions for the computing time of OZ equation with $m_{\max} = n_{\max}$ are listed in table 7.1. If the OZ equation is the most time-consuming part, the observed result should have the same tendency. Figure 11.5 shows the experimental timing of the three paths, where path (3) is 100 times longer than (4), corresponding well to the theoretical value. Path (2) is much longer than path (3) because apart from the OZ equation, the reading in memory and calculation of the DCF mentioned in §6 also takes time.

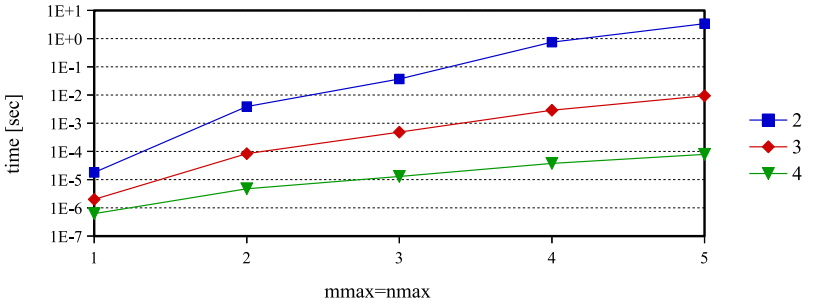

Figure 11.5: Timing of a k-kernel (log scale)

11.4 ENTIRE ITERATION OF $\mathcal{F}_{\text{exc}}$ EVALUATION

Apart from all the **naive** methods that will be discussed in §11.4.1, figure 11.6 shows all the comparable **convolution** timing data. We can see that **convolution_standard** is the fastest algorithm, and OZ equation is not the longest part in the iteration. All the tests are performed for a $L = 24$, nfft $= 72$ grid with 4 series: the three **convolution** methods with $m_{\max} = n_{\max}$, and **convolution_standard** with $m_{\max} = 5$, varying $n_{\max}$.

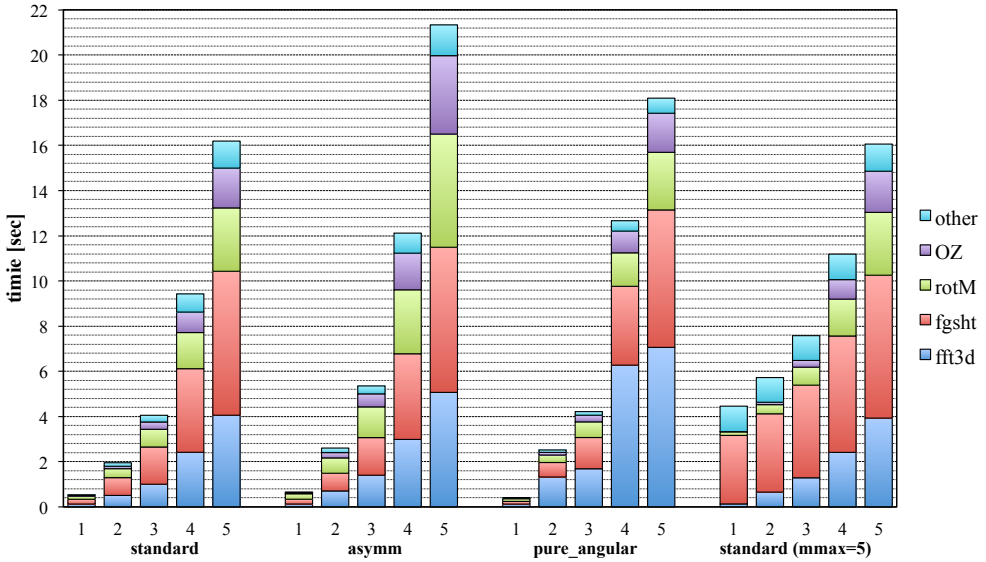

Figure 11.6: Entire iteration of $\mathcal{F}_{\text{exc}}$ evaluation: timing overall / decomposition of timing for 1 iteration evaluation

11.4.1 *"naive" methods and "convolution_pure_angular"*

The **naive_standard**, **naive_interpolation**, and **convolution_pure_angular** methods share the same processes out of the k-kernel. Table 11.1 shows the timing of loop k of these three methods. It indicates that **convolution_pure_angular** takes far less time than the other two methods, of which the loop k takes time on the same order of magnitude as the rest of the iteration. And once $m_{\max} \geq 2$, **naive_interpolation** is faster than **naive_standard**. Note that order 2 of **naive_interpolation** can give good results for a DCF of $n_{\max} = 5$. So in every case of **naive** methods, **naive_interpolation** should be used. This verifies the conclusion of k-kernel test in that the path (4) in figure 10.4 is the fastest.

$m_{\max}$	**naive_standard**	**naive_interpolation**	**convo_pure_angular**	OTHER
1	2.34	4.42	0.26	0.15
2	365.95	209.12	1.09	1.43
3	3295.00	752.70	2.37	1.85
4	too long	too long	5.93	6.73
5	too long	too long	10.36	7.73

Table 11.1: Timing [sec] of loop k of "naive_standard", "naive_interpolation" and "convolution_pure_angular", and the rest of iteration

11.4.2 *"convolution_standard" and "convolution_pure_angular"*

The comparison of **convolution_standard** and **convolution_pure_angular** appears in figure 11.7. Their difference lies in the inversion of FFT and FGSHT. We can see the other parts are almost identical, but the implementation of FFT is different in terms of time, because in **convolution_standard** the number of FE we need for FFT is the number of projections, and in **convolution_pure_angular** it is the number of angular grid nodes. As there are fewer projections than angular nodes, **convolution_standard** reasonably takes less time. The stepwise form of the **pure_angular** curve is due to the grid in Ψ, which requires $\lfloor m_{\max}/2 \rfloor$ points in the case of C_{2v} symmetry. Projections are less sensitive to this effect.

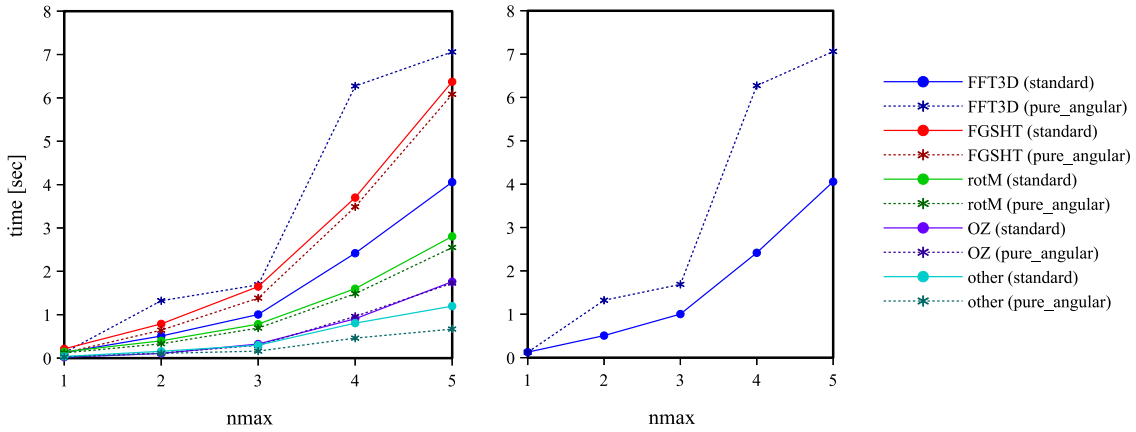

Figure 11.7: Performance **convolution_standard** vs **convolution_pure_angular**

11.4.3 *"convolution_standard" and "convolution_asymm"*

We compare **convolution_standard** and **convolution_asymm** in figure 11.8. The difference is that **standard** calculates half of the k's in the k-loop and **asymm** calculates all k's in the k-loop. They share the same process of FGSHT, while for the processes in a k-loop (rotM, OZ) **asymm** always takes longer. Since in **asymm** we calculate the FFT for all the projections and in **standard** we calculate only a half projections with $\mu \geq 0$, the time consumed by FFT is also different.

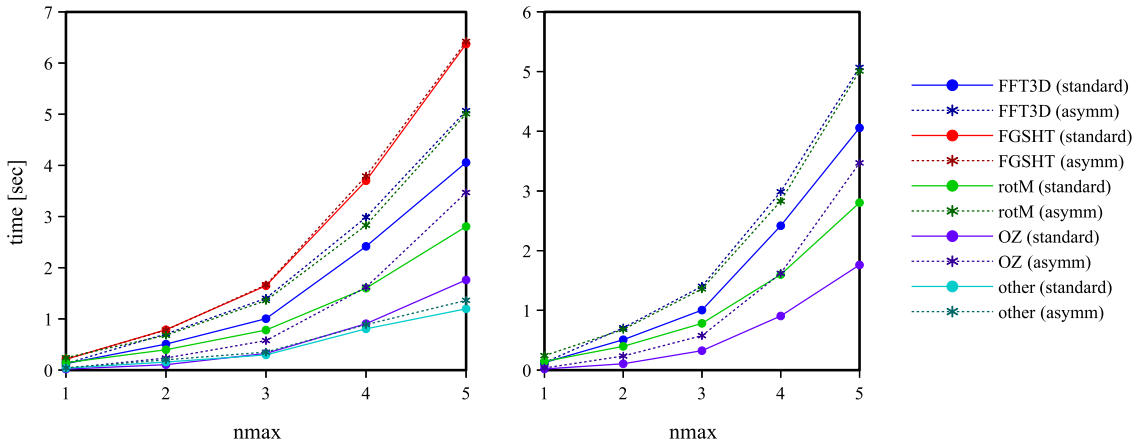

Figure 11.8: Performance **convolution_standard** vs **convolution_asymm**

11.4.4 *Distinction of $m_{\max}$ and $n_{\max}$*

The comparison of $m_{\max} = n_{\max}$ and $m_{\max} = 5$ for **convolution_standard** is shown in figure 11.9. We see that the choice of quadrature order $m_{\max}$ only affects the FGSHT process and the reading/storage of density variable (other). The time taken by extra order $m_{\max}$ is not cost-free, so as discussed in the last section, it is fully recommended to use $m_{\max} = n_{\max}$.

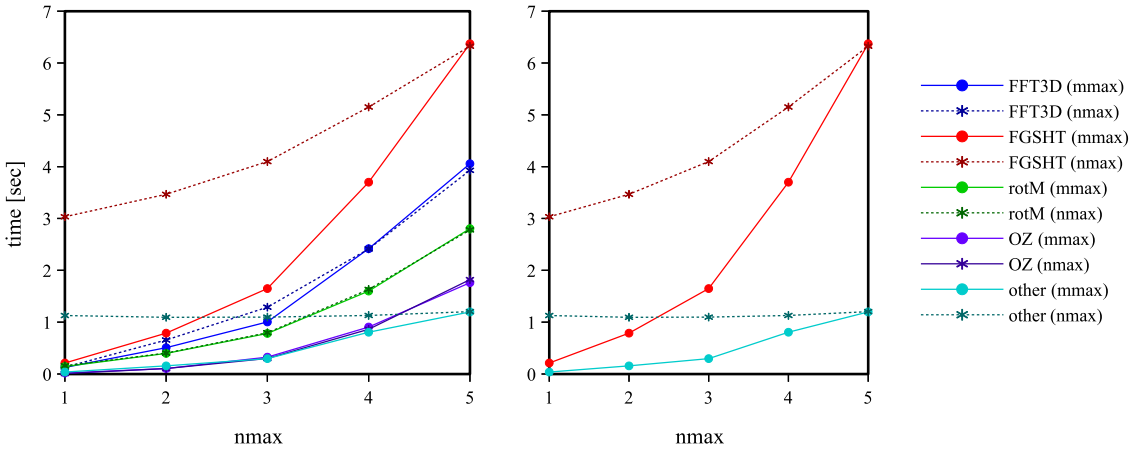

Figure 11.9: Performance **convolution_standard** for $m_{\max} = n_{\max}$ and $m_{\max} = 5$

11.5 GLOBAL VIEW OF THE CODE PERFORMANCE

Figure 11.10 gives the timing of the whole $\mathcal{F}$ iteration. We can see that the evaluation of $\mathcal{F}_{\text{exc}}$ is at the same order of magnitude as the other two terms and the same dependency on angular grid. That means that considering the priority of code optimization, the $\mathcal{F}_{\text{exc}}$ is no longer an absolute bottleneck to the whole process, owing to the new algorithm.

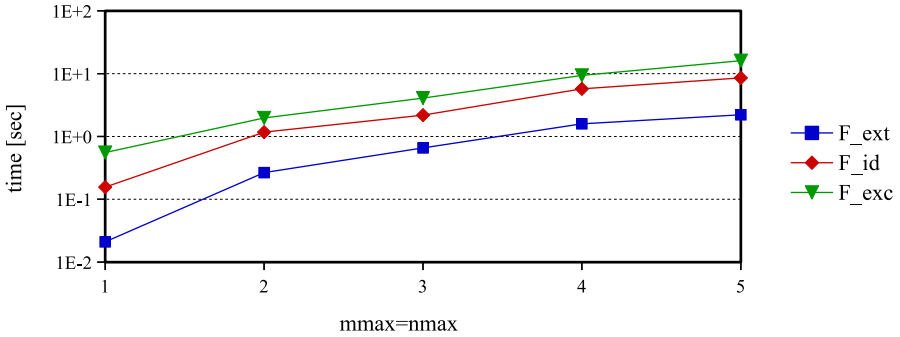

Figure 11.10: Timing of the whole $\mathcal{F}$ iteration with nfft/L = 72/24 grid (log scale), using **convolution_standard** algorithm

In conclusion, we stress that:

- **convolution_standard** is the fastest algorithm among those that we have tested. The **convolution** methods are orders of magnitude faster than **naive** methods. It means that we have been able to reduce a complex spatial and angular convolution process to roughly the same computer cost as a local calculation in both space and angles, which can be seen as the major accomplishment of this thesis.
- The attempt to fix $m_{\max}$ considerably damages the efficiency; in addition to the necessity, $m_{\max} = n_{\max}$ is absolutely recommended.

Chapter IV

Applications

In chapter III, we have studied the numerical accuracy of the code (through MDFT/HRF approximation) compared to IET. In this chapter, we are interested in the physical accuracy comparing to MD and experimental results. A few applications are made for this purpose in section 12, involving some LJ centers, ions and small molecules. The results are also compared to the dipolar reference method, which is the method corresponding to $n_{\max} = 1$ for linear or pseudo-linear molecules that was fully implemented so far, to show that this increase of computing cost has made an improvement on the results.

12 Comparison to MD simulation

In the last chapter, we proved that MDFT is capable of correctly predicting solvation properties of LJ centers, single ions and linear solutes compared to IET. In this section, we will compare them to MD and experimental results. All the solutes are optimized with the fast `convolution_standard` algorithm, with implicitly $L = 24$ Å, nfft $= 72$, $m_{\max} = n_{\max}$ unless otherwise specified. Comparison to the dipole method is also involved, as we should justify that the increase of computing cost when going from $n_{\max} = 1$ to $n_{\max} > 1$ is counterbalanced by the ability to produce better results.

12.1 LJ centers

The RDFs of rare gases calculated in §10.7 are compared to MD in figure 12.1 using $n_{\max} = 3$ to 5. The structures of different $n_{\max}$ is almost identical. Comparing to MD, it seems that there is no improvement over the dipole method in ref [32] or to calculation involving c_{00}^{000} only [78]. This kind of disagreement in curve shape is regarded as a known default of HNC (or HRF) approximation.

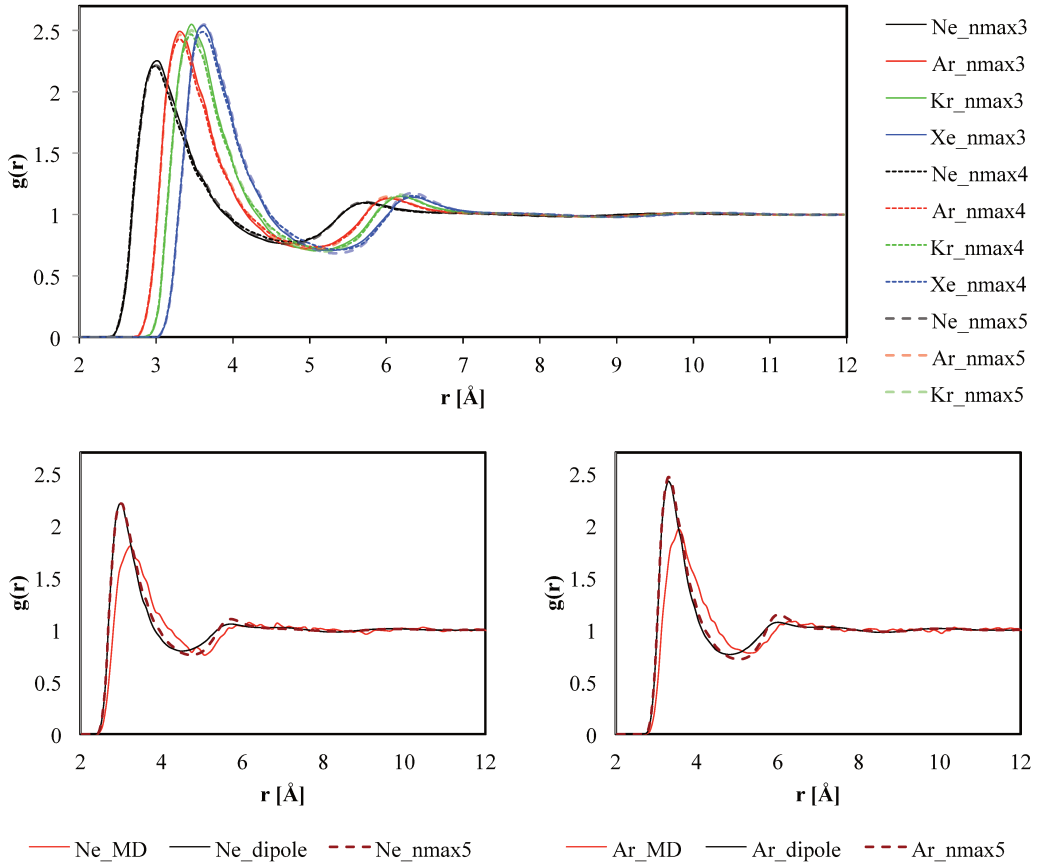

Figure 12.1: RDF of rare gases compared to MD result

12.2 CHARGED CH_4 SERIES

The comparison between the RDFs obtained from MDFT with MD results for charged CH_4 series are shown in figure 12.2. We can see that for positive charges, the complete $n_{\max} = 5$ gives much better results compared to the dipole method, which itself almost agrees with MD results. For negative charges, $n_{\max} = 5$ gives nearly the same result as dipole method, while the MD results are more smooth. Still the first peak of the MDFT results seems to be in the good position. We can conclude that the complete DCF gives a large improvement for positive charged ions.

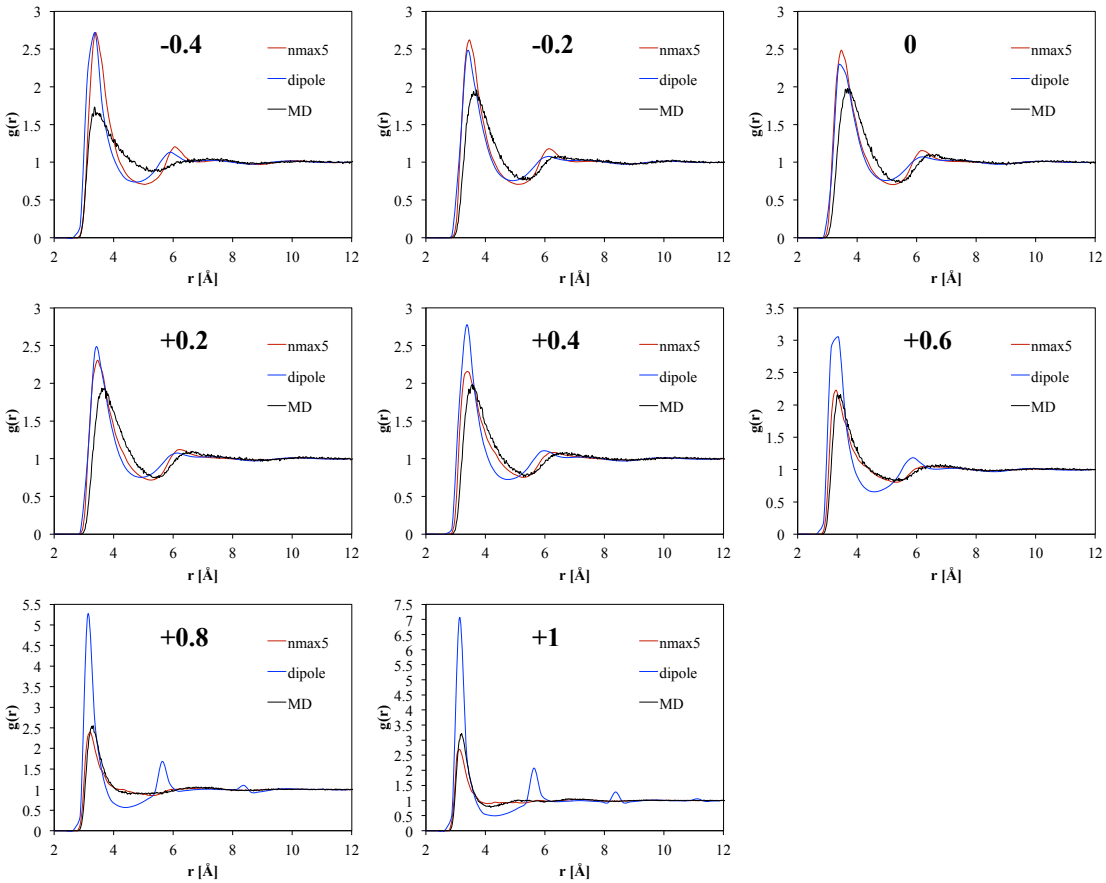

Figure 12.2: RDF of charged CH_4 series compared to MD result

12.3 SOLVATION FREE ENERGY OF SINGLE IONS

We consider that in a macroscopic system, the fluctuation of N and V are negligible, and all kinds of free energies become the same. [56]

From the previous paragraph we can see the RDF for positive ions are in good agreement with MD results. However, the free energy is more difficult to compare, as there are several finite-size corrections for single ions, depending on for example box length and charge; besides, the free energy depends largely on the input LJ parameters of the ions, which is independent to the method.

Table 12.1 gives from literatures some experimental and MD simulation results of solvation free energy as well as the positions of the first maximum of the RDF for alkali and halide ions. We can see that the experimental data themselves vary a lot. Furthermore the LJ parameters for ions in the literature are extremely dispersed. Therefore, we fo-

cused on a single series of force field parameters for halide anions and alkali cations taken from ref [79] based on SPC/E water, as shown in table 12.1 and 12.2.

Ion	$-\Delta G_{\text{solv}}^{\text{exp}}$(a)	$-\Delta F_{\text{solv}}^{\text{exp}}$(b)	$-\Delta G_{\text{solv}}^{\text{exp}}$(c)	R_1(d)	σ [Å](e)	ϵ [kJ · mol^{-1}](e)	$-\Delta G_{\text{solv}}^{\text{MD}}$(e)	R_1^{MD}(e)
F^-	465	374.5	428.8	2.08	3.434	0.465	430	2.74
Cl^-	340	318.4	304.2	2.36	4.394	0.416	306	3.23
Br^-	315	289.5	227.4	2.80	4.834	0.211	279	3.35
I^-	275	252.3	240.0	2.89	5.334	0.158	241	3.55
Li^+	475	511.0	529.4	3.14	2.874	0.000615	520	1.91
Na^+	365	411.5	423.8	2.63	3.814	0.000615	414	2.28
K^+	295	337.2	352.0	3.19	4.534	0.000615	347	2.54
Rb^+	275	316.0	329.3	3.37	no data	no data	no data	no data
Cs^+	250	283.8	no data	3.65	5.174	0.000615	300	2.79

Table 12.1: Free energy [kJ · mol^{-1}] and first maximum of ion-water oxygen RDF [Å] for alkali and halide ions from experimental and MD simulation result. (a). Ref [80]. (b). Ref [81]. (c) Ref [82]. (e) Ref [79] from MD simulation. (d) Ref [83].

Ion	σ [Å](e)	ϵ [kJ · mol^{-1}](e)	$\Delta G_{\text{solv}}^{\text{MD}}$	$\Delta\Omega_{\text{solv}}^{\text{dipole}}$	$\Delta\Omega_{\text{solv}}^{\text{nmax3}}$	R_1^{MD}	R_1^{dipole}	R_1^{nmax3}
F^-	3.434	0.465	-430	-805	-351	2.74	2.71	2.71
Cl^-	4.394	0.416	-306	-521	-233	3.23	3.21	3.21
Br^-	4.834	0.211	-279	-464	-205	3.35	3.37	3.37
I^-	5.334	0.158	-241	-388	-166	3.55	3.54	3.54
Li^+	2.874	0.000615	-520	-870	-480	1.91	2.13	2.13
Na^+	3.814	0.000615	-414	-742	-412	2.28	2.29	2.38
K^+	4.534	0.000615	-347	-623	-358	2.54	2.54	2.54
Cs^+	5.174	0.000615	-300	-528	-317	2.79	2.79	2.79
Li^+	1.374	1.538	-521	-889	-492	1.96	2.13	2.13
Na^+	2.134	1.538	-415	-749	-419	2.34	2.46	2.38
K^+	2.774	1.538	-345	-610	-360	2.68	2.71	2.71
Cs^+	3.334	1.538	-300	-512	-318	2.98	3.04	3.04
Li^+	1.474	0.65	-523	-891	-490	1.96	2.13	2.13
Na^+	2.234	0.65	-416	-753	-415	2.33	2.38	2.37
K^+	2.894	0.65	-344	-612	-358	2.65	2.63	2.71
Cs^+	3.434	0.65	-299	-517	-318	2.93	2.96	2.96

Table 12.2: Free energies [kJ · mol^{-1}] and first RDF maximum [Å] of single ions from MDFT results compared to MD results

The results shows in table 12.2 are calculated with $L = 32$ Å, nfft = 96; and $m_{\max} = 3$ to ensure that the $\mathcal{F}_{\text{id}}$ and $\mathcal{F}_{\text{ext}}$ terms calculated by using the DCF at $n_{\max} = 3$ or the dipole DCF are exactly the same. The free energies given by MDFT with $n_{\max} = 3$ are not perfect, but lie in the same order of magnitude as MD. For negative ions, there is always a shift at $\sim 80\,\text{kJ} \cdot \text{mol}^{-1}$ (knowing that the correction of type-C is at $82\,\text{kJ} \cdot \text{mol}^{-1}$ but we cannot tell what the shift is). For positive ions, the magnitude of free energy is slightly underestimated with small σ, and slightly overestimated for large σ. On the other hand, the free energies given by dipole DCF is too large in magnitude. In contrast, the position of the first solvation maximum for the three methods do not vary between them (apart from Li^+ which is very small). But if we look at the RDF of charged CH_4 series, we can see that $n_{\max} = 3$ still works better. We can conclude that the results in energy with a DCF at $n_{\max} = 3$ work better than the dipolar approximation, which is a positive sign for our developments.

12.4 SMALL MOLECULES

MDFT calculations involving some small molecular solutes were also generated to compare to MD; the chosen solutes are shown in figure 12.3 and defined in table 12.3. Note that a certain proportion of them have a non-linear, 3-dimensional geometry which could not be handled by the molecular IET; this shows the advantage of the general 3D-MDFT approach adopted in this thesis and the new algorithm that we have developed in this context.

Figure 12.4 gives the site-site RDFs (solute site to water O site) for $n_{\max} = 4$, the dipolar approximation ($n_{\max} = 1$), and MD for these test solutes. It is shown that in most of the cases, $n_{\max} = 4$ does give equivalent or better results than the dipolar order, apart from the cases of water, and especially SPC/E water. In methanol, the dipole method diverges. For most solutes, the comparison to MD is far from perfect but can be qualified as satisfactory in reproducing the - sometimes complex - shape of the RDFs and the main peaks positions. This statement is especially true for benzene and pyrimidine, for example. For hydrophobic molecules or molecules with hydrophobic sites (alkanes, oxygen, nitrogen, ...) one recovers the slight underestimation of the first peak position and the overestimation of peak height already remarked for rare gases; this is a clear defect of HNC. The case of molecules giving rise to hydrogen bonds to water (e.g. methanol, or water in water) is more problematic and subtle. Here the dipolar approximation gives a first peak for the water oxygen around the O-site that is too high but has the correct width, whereas $n_{\max} = 4$ shifts the first peak to higher values and makes it too wide (a sort of merge of the first and second peak, an effect even clearer for methanol). The H-O first peak, on the other hand, is at a correct position but underestimated, both for water and methanol. The tetrahedral order around a water solute is not correctly reproduced, although the correct balance to get the right structure is subtle and does not appear too far.

For the purpose of showing the ability of MDFT to calculate 3D solute structure, we display 3D solvent densities for specific solutes in figure 12.5 and 12.6. Figure 12.6 complements the discussion given just above concerning the expected tetrahedral structure around a water molecule in water. That structure can indeed be detected for SPC/E water and even more so for the TIP4P model. In SPC/E water, there is more density than expected on the north pole, and this piece of density disappears with the extra charge added on the TIP4P water.

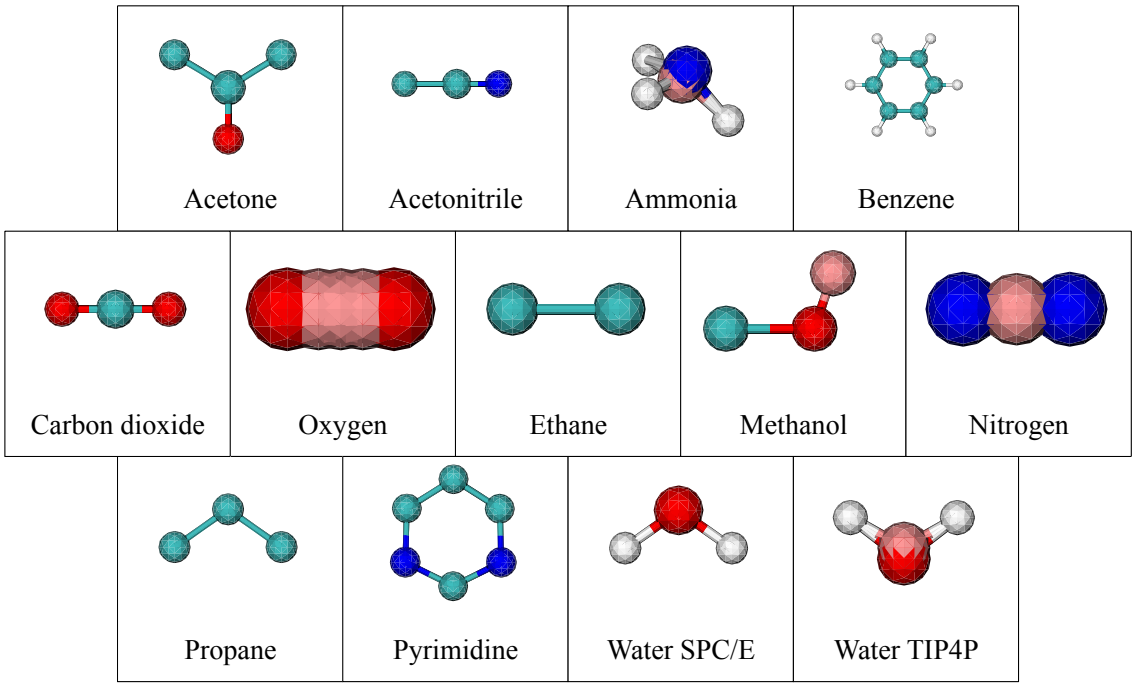

Figure 12.3: Test solutes

SOLUTE	SITE	q	σ [Å]	ϵ [kJ · mol^{-1}]	x [Å]	y [Å]	z [Å]
Acetone [84]	CH_3	0.062	3.91	0.6694	1.2810	0.7024	-0.0002
	C	0.300	3.75	0.4393	0.0101	-0.0872	0.0106
	O	-0.424	2.96	0.8796	0.0103	-1.3171	-0.0102
	CH_3	0.062	3.91	0.6694	-1.2813	0.7019	-0.0002
Acetonitrile	CH_3	0.269	3.6	1.590	0.0000	0.0000	-1.3254
	C	0.129	3.4	0.416	0.0000	0.0000	0.1346
	N	-0.398	3.3	0.416	0.0000	0.0000	1.3046
Ammonia [85]	N	0.000	3.4	1.164	0.000000	0.000000	0.000000
	X	-1.386	0.0	0.000	0.000000	0.000000	-0.156000
	H	0.462	0.0	0.000	-0.937790	0.000000	-0.381449
	H	0.462	0.0	0.000	0.468895	0.812150	-0.381449
	H	0.462	0.0	0.000	0.468895	-0.812150	-0.381449
Benzene [86]	C	-0.138	1.908	0.35980	1.386	0.000	0.000
(charged)	C	-0.138	1.908	0.35980	0.693	-1.200	0.000
	C	-0.138	1.908	0.35980	-0.693	-1.200	0.000
	C	-0.138	1.908	0.35980	-1.386	0.000	0.000
	C	-0.138	1.908	0.35980	-0.693	1.200	0.000
	C	-0.138	1.908	0.35980	0.693	1.200	0.000
	H	0.138	1.459	0.06276	2.462	0.000	0.000
	H	0.138	1.459	0.06276	1.231	-2.132	0.000
	H	0.138	1.459	0.06276	-1.231	-2.132	0.000
	H	0.138	1.459	0.06276	-2.462	0.000	0.000
	H	0.138	1.459	0.06276	-1.231	2.132	0.000
	H	0.138	1.459	0.06276	1.231	2.132	0.000
CO_2 [75]	C	0.6512	2.76	0.234	0.000	0.000	0.000
	O	-0.3256	3.03	0.67	-1.149	0.000	0.000
	O	-0.3256	3.03	0.67	1.149	0.000	0.000
O_2 [76]	O	0.0	3.1062	0.36	-0.485	0.000	0.000
	O	0.0	3.1062	0.36	0.485	0.000	0.000
	X	-2.1	0.00	0.00	-0.200	0.000	0.000
	X	-2.1	0.00	0.00	0.200	0.000	0.000
	X	4.2	0.00	0.00	0.000	0.000	0.000
Ethane [84]	CH_3	0.0	3.775	0.8661	-0.756	0.000	0.000
	CH_3	0.0	3.775	0.8661	0.756	0.000	0.000
Methanol [87]	CH_3	0.24746	3.7543	1.0027	-1.42460	0.000000	0.000000
	OH	-0.67874	3.0300	0.7307	0.00000	0.000000	0.000000
	X	0.43128	0.0000	0.0000	0.30035	0.896104	0.000000
N_2	N	-0.5075	3.30	0.30	-0.549	0.000	0.000
	N	-0.5075	3.30	0.30	0.549	0.000	0.000
	X	1.0150	0.00	0.00	0.000	0.000	0.000
Propane	CH_3	0.0	3.905	0.732	-1.25	-0.4417	0.0
	CH_2	0.0	3.905	0.494	0.0	0.4417	0.0
	CH_3	0.0	3.905	0.732	1.25	-0.4417	0.0
Pyrimidine [84]	N	-0.490	3.25	0.7113	1.2035	-0.6989	0.0000
	N	-0.490	3.25	0.7113	-1.2063	-0.6943	0.0000
	C^2H	0.410	3.75	0.4602	-0.0026	-1.2980	0.0001
	C^3H	0.245	3.75	0.4602	1.1692	0.6499	-0.0001
	C^4H	0.245	3.75	0.4602	-1.1666	0.6543	-0.0001
	C^5H	0.080	3.75	0.4602	0.0028	1.3870	0.0001
SPC/E [47]	O	-0.8476	3.165	0.65	0.000000	0.000000	0.0000000
	H	0.4238	0.000	0.00	0.816495	0.000000	0.5773525
	H	0.4238	0.000	0.00	-0.816495	0.000000	0.5773525
TIP4P [88]	O	0.0000	3.1589	0.775	0.00000	0.00000	0.00000
	H	0.5564	0.0000	0.000	0.75695	0.58588	0.00000
	H	0.5564	0.0000	0.000	-0.75695	0.58588	0.00000
	X	-1.1128	0.0000	0.000	0.00000	0.15460	0.00000

Table 12.3: Parameters of test solutes

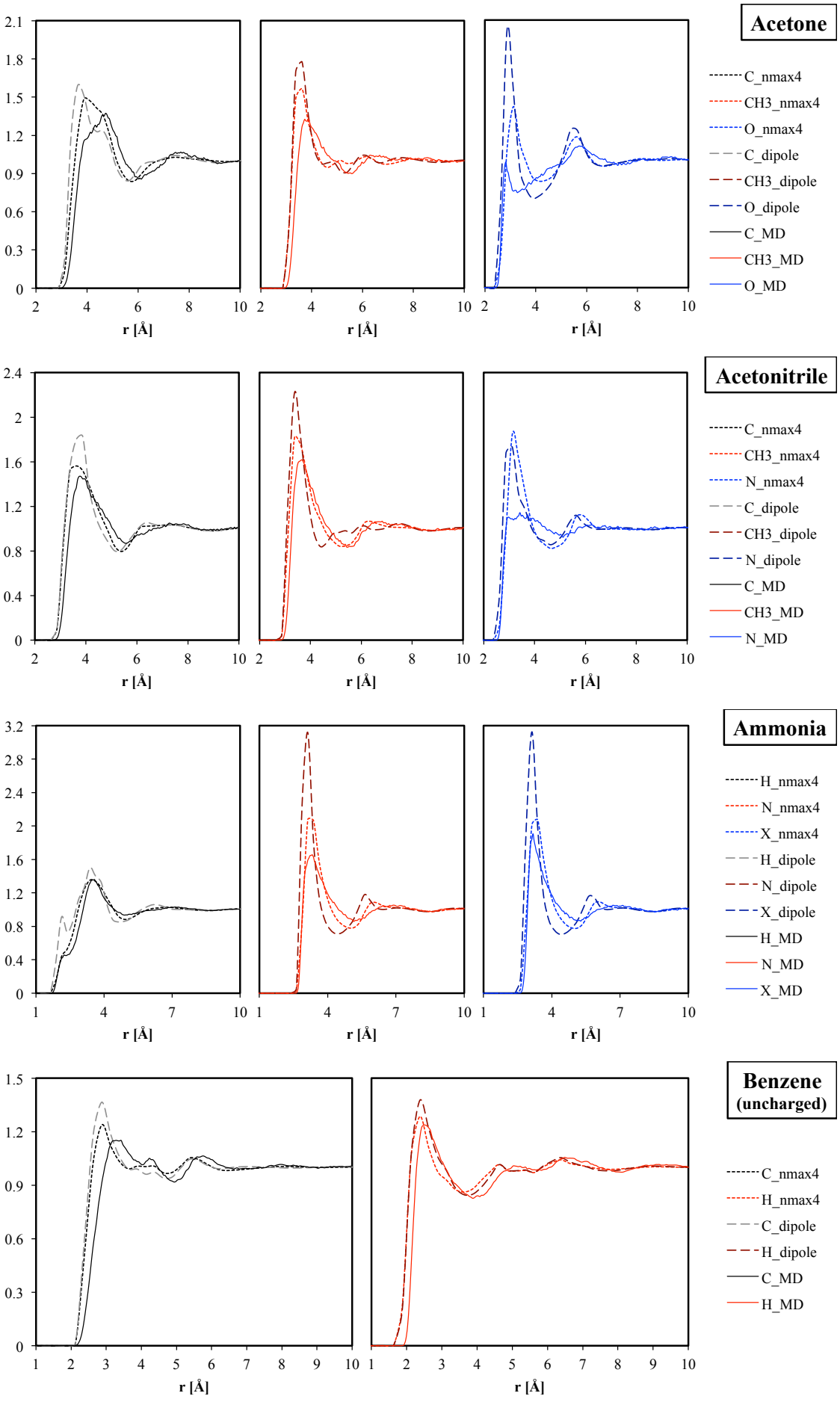

Figure 12.4: Site-O RDF of test solutes, with $m_{\max} = n_{\max} = 4$, $L = 24$ Å, nfft $= 72$. $\frac{1}{3}n_{\text{bin}}$ is used in order to avoid noise.

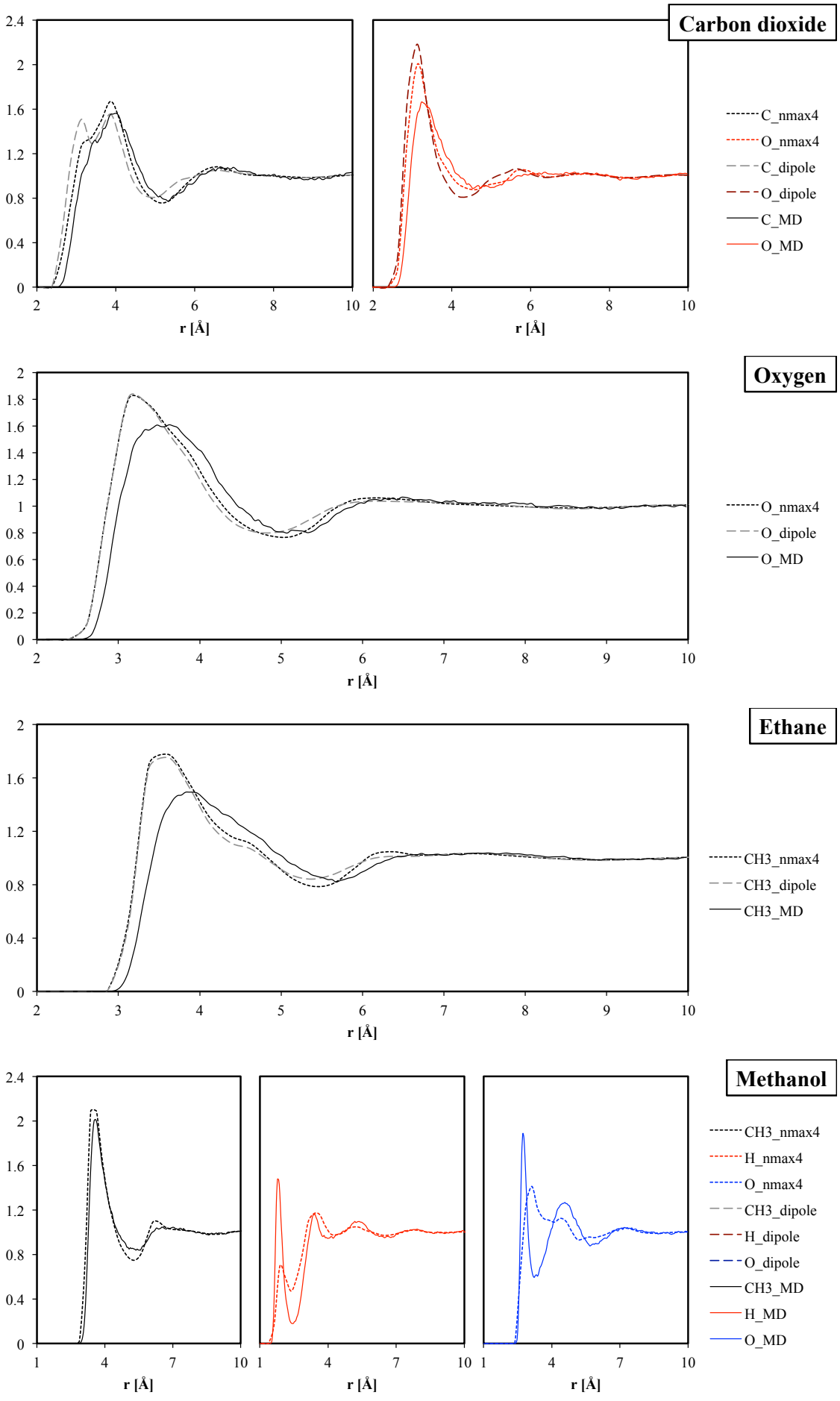

Figure 12.4: Site-O RDF of test solutes (continued)

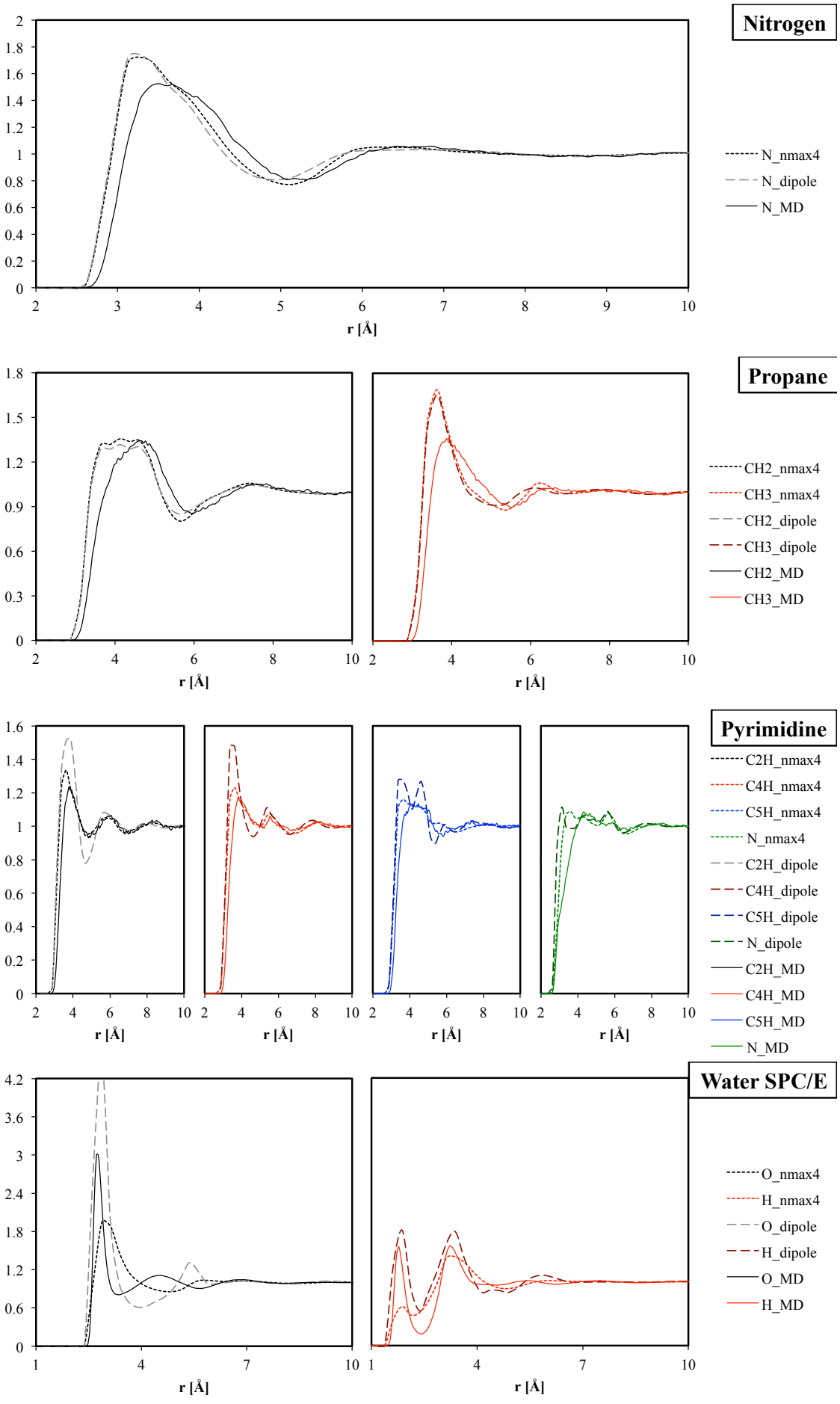

Figure 12.4: Site-O RDF of test solutes (continued)

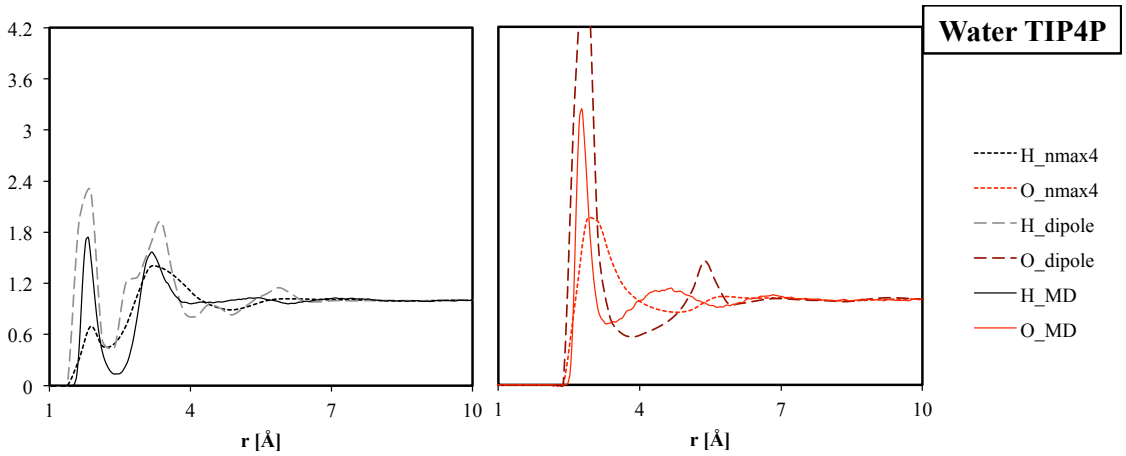

Figure 12.4: Site-O RDF of test solutes (continued)

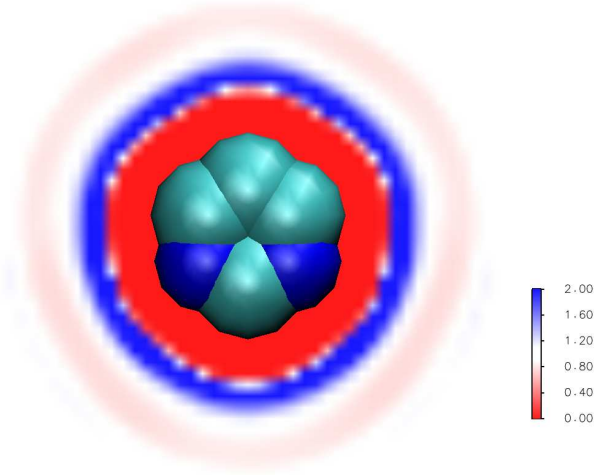

Figure 12.5: Volume slice of solvent number density $n(\mathbf{r})$ for pyrimidine

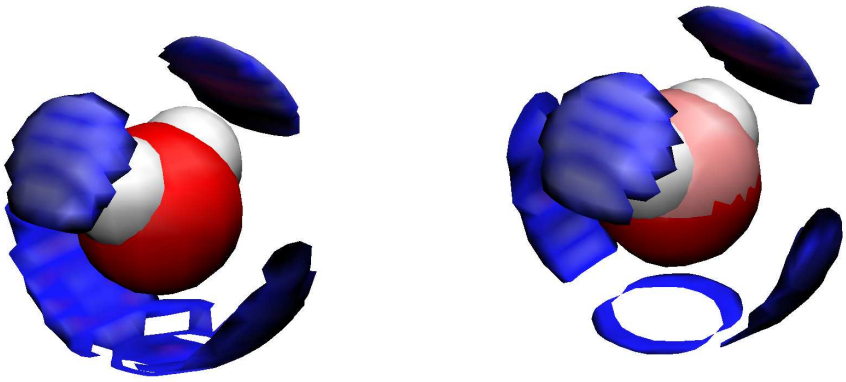

(a) SPC/E water (b) TIP4P water

Figure 12.6: Iso-surface of solvent number density $n(\mathbf{r}) = 2.4$ for test water molecules

Chapter V

Conclusion and Perspectives

In the framework of the molecular density functional theory (MDFT) theory, this thesis presents a complete study of the excess free energy functional evaluation under the homogeneous reference fluid (HRF) approximation (equivalent to the hypernetted-chain (HNC) approximation in integral equation language):

$$\mathcal{F}_{\text{exc}} = -\frac{k_{\text{B}}T}{2}\int \mathrm{d}\mathbf{r}_1\mathrm{d}\mathbf{r}_2\mathrm{d}\mathbf{\Omega}_1\mathrm{d}\mathbf{\Omega}_2\Delta\rho(\mathbf{r}_1,\mathbf{\Omega}_1)\Delta\rho(\mathbf{r}_2,\mathbf{\Omega}_2)c(\mathbf{r}_{12},\mathbf{\Omega}_1,\mathbf{\Omega}_2) \quad \text{(IV.1)}$$

where the orientations span the three Euler angles, $\mathbf{\Omega} \equiv (\Theta, \Phi, \Psi)$. It gives a new method to evaluate solvation properties (grand-canonical free energy and microscopic solvent density) within the framework of liquid-state theory. It is more complete and accurate compared within the development of molecular density functional theory (MDFT) presented so far. The approach is yet limited to rigid molecules and the neglect of three-body correlations.

To complete this work, we conclude all the achievements done in this thesis, and some unfinished work and related theories remaining due to the time limit.

13

Conclusion

In this thesis, we have firstly improved the original angular integration algorithm developed previously in the group, which uses FFT to deal with the spatial convolution, and a direct integration over angles. For practical reasons, this initial approach was limited to linear or pseudo-linear solvents in order to reduce the number of angular variables. In this work, it has been extended to deal with arbitrary 3D molecular solvents, which is mainly about writing out the expression of the more complicated rotation matrix which corresponds to the 3-Euler-angle case.

A new algorithm by generalized spherical harmonic (GSH) expansion, which aims to produce the same result as the algorithm mentioned above for molecular solvent but much faster, is then built for the treatment of the angular convolution part, inspired by Blum's χ-reduction of the MOZ equation. This algorithm takes advantage of the rotational invariance, separating the OZ equation in irreducible terms according to a series of χ values; those can be seen as an analogue of the **k**-vectors in FFT transform that takes advantage of translational invariance.

Theoretically and practically the new algorithm has been proven much faster than the previous one, with an acceptable accuracy lost.

The tests that have been performed show that the proposed methods are suitable for fast and accurate calculations of solvation free energies. The accuracy was assessed by comparing the results to a mathematical equivalent 1D-integral equation theory (IET) code for simple (spherical or linear) solutes. For the solvent structure, the relatively loose cubic spatial grid that has to be adopted in molecular density functional theory (MDFT) (3-4 points per Angstrom) prevents the theory to produce radial curves that are as smooth as those produced by IET for simple solutes. But indeed molecular density functional theory (MDFT) has much more capacity to deal with complex 3D solutes, and produce the 3D solvent structure on a regular grid.

Compared to MD and/or experimental results, it is shown that the new method works better in most cases than the previously implemented "dipolar-like" method. Concerning the solvent structure, the agreement with MD is far from perfect but can be qualified as satisfactory for solute molecules with limited hydrogen-bonding to the solvent. For small ions (in particular anions), or H-bonded molecules such as water itself or alcohols, the HRF/HNC theory has to be improved or corrected. Concerning thermodynamic properties such as solvation free energies, some small monovalent ions have been tested in this purpose. In this case we showed that it is very important to account for finite size effects through two types of corrections: a Madelung correction reminiscent of the Born correction for spherical systems, scaling as q^2/L, and a much less intuitive correction scaling as the ion charge q and accounting for the proper treatment of boundary charges in periodic systems. The tests need now to be extended to relevant databanks of organic molecules in order to fully assess the relevance of the method. One can anticipate that it will require the introduction of ad-hoc pressure corrections, or three-body correction terms in the functional, in order to compensate for the overly high pressure given by the HRF/HNC functional, a defect that has been pointed out previously.

In short, the new algorithm is now ready for chemical applications usage. However, there are still some minor problems needing to be addressed. Firstly, there are some

slight incompatibilities within the theory and through the implementation, notably the γ problem and the conjugate form of DCF which is explained as clearly as possible in the main text. There are also some sign and normalization factor issues of the projections $f_{\mu\nu}^{mnl}$. The grid dependence of free energy is somewhat worrying; it might be due to a slight deficiency in the calculation of the external potential, present in the initial version of the molecular density functional theory (MDFT) code used. Such an issue is not deepened as this thesis mainly treats the excess $\mathcal{F}_{\text{exc}}$ term of the functional.

14

Perspectives

Since no work is ever perfect, a great deal of unfinished work and theories linked to this thesis are presented here for consideration.

14.1 Reduce memory footprint in MDFT

The total CPU time to implement a MDFT minimization using the `convolution` algorithms is typically 1 to 30 minutes according to the resolution of grid. But the memory consumed for such a process is typically 1 to 20 GB of RAM. This is mainly due to the minimizer L-BFGS-B, which firstly needs to store several steps of information during the iterations, and secondly is in double precision. It is to say that the density variable $\rho(\mathbf{r}, \mathbf{\Omega})$ and the gradient also need to be stored in double precision, and if not, as tested, it leads to divergence. In addition, during the evaluation of the functional, the memory for at most 3 times $\rho(\mathbf{r}, \mathbf{\Omega})$ needs to be open simultaneously.

There are two ways to get over this memory limit, and both of them involve modifying the L-BFGS-B minimizer, which is a "blackbox", in Fortran 77. The simplest method is to change the double precision to single in the L-BFGS-B minimizer; this action can reduce the memory needed by a factor of 2. Another way to completely pass this limit is to parallelize the code to several nodes using MPI. This requires only to modify the FFT and L-BFGS-B process, where there is a mixing of variables $\rho(\mathbf{r}, \mathbf{\Omega})$. A third route would be to define a minimizer with much less memory requirements.

14.2 Site-based grid

The IET approach uses intermolecular spherical coordinates, and cannot describe large molecules. As for MDFT it uses a homogeneous spatial grid, which has the same resolution near and far from the solute. The caveat of MDFT is that the 3D grid needed should be relatively fine to produce satisfactory results (typically 3-4 points per Angstrom); for large solutes this may lead to a very huge number of grid points. A natural idea would be to use non-uniform grids. One way to think about the construction of the grid is like in 14.1, a set of spherical grids centered at each solute site. This could be understood as expanding the density into a set of "atomic-like orbitals", $\rho(\mathbf{r}) = \sum_\alpha c_\alpha \rho_\alpha(\mathbf{r})$. Each "'orbital" could be possibly expanded onto a local basis set, such as spherical harmonics, $\rho_\alpha(\mathbf{r}) = \sum_{l,m} \rho^m_{\alpha,l}(|\mathbf{r} - \mathbf{R_{ff}}|) Y^m_l(\theta, \phi)$.

14.3 Theories beyond the HRF approximation and other improvements

In terms of $\mathcal{F}_{\text{exc}}$, there can still be development beyond the HRF approximation, such as 3-body corrections.

Apart from the $\mathcal{F}_{\text{exc}}$ term, still many fields of study remains to be developed in MDFT. For example, the evaluation of the external potential V_{ext} still poses occasional problems

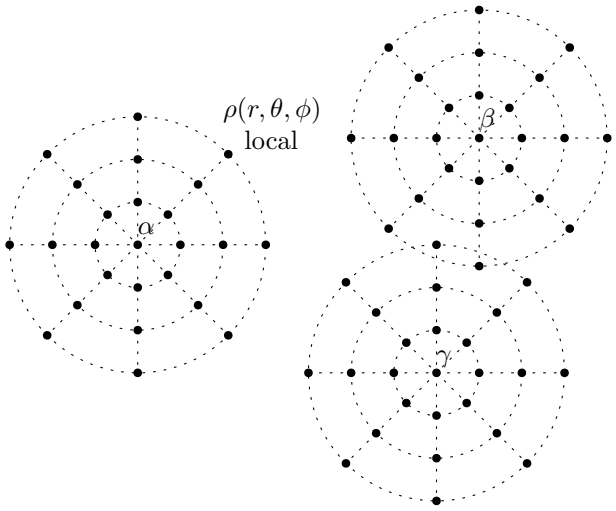

Figure 14.1: Site-site grid model

of convergence for molecular solutes and needs to be improved. Note also that the solute can be made polarizable, so that V_{ext} itself becomes a functional of the solvent density and varies during the minimization. The polarization can be introduced, for example, by an extra induced dipole on the solute center or on the solute sites.

14.4 MDFT VIEWER

This thesis originally contained a contribution on visualization. Due to time limitation, it had to be removed. The Viewer is an important part of the code development; it provides insightful visualization and easier analysis, and may help to popularize the code. GaussViewer is a good example.

14.5 APPLICATION TO REAL BIOLOGICAL SYSTEMS, AND ENTROPY

From this thesis we can see that MDFT is presently capable of dealing with small chemical systems, but it is still far from satisfying for common usage in the domain of bio-chemistry, or as a solvent model for QM. For example, for real applications, enthalpy and entropy are also important, as discussed in ref [1]. The properties of [1] cannot be repeated with QM calculations using simply a continuum model for solvent corrections (research subject of my university diploma), which cannot reproduce the correct tendency of entropy with respect to temperature (in DMSO). It is my intention to re-investigate this problem using the MDFT approach. It is not clear yet how (beyond the estimate by the $\mathcal{F}_{\text{id}}$ term), the solvation entropy rather than the free energy can be estimated from the MDFT calculations.

Chapter VI

Appendix

A

Basics of Algorithm Complexity

Algorithm complexity is one of the crucial criteria to evaluate the theoretical performance of the code, as defined below:

Let f and g be two functions defined over the natural numbers $\mathbb{N}$. We write

$$f = O(g) \tag{A.1}$$

if there is a strictly positive constant $c > 0$ such that from a certain number $n > n_0$ we always have $|f(n)| \leq c\,|g(n)|$. The O is also called the big-O notation [89], or order of growth. Figure A.1 shows the growth tendency of some frequent functions. We can see:

$$O(1) > O(\log_2 n) > O(n) > O(n \log_2 n) > O(n^2) > O(2^n) > O(n!) \tag{A.2}$$

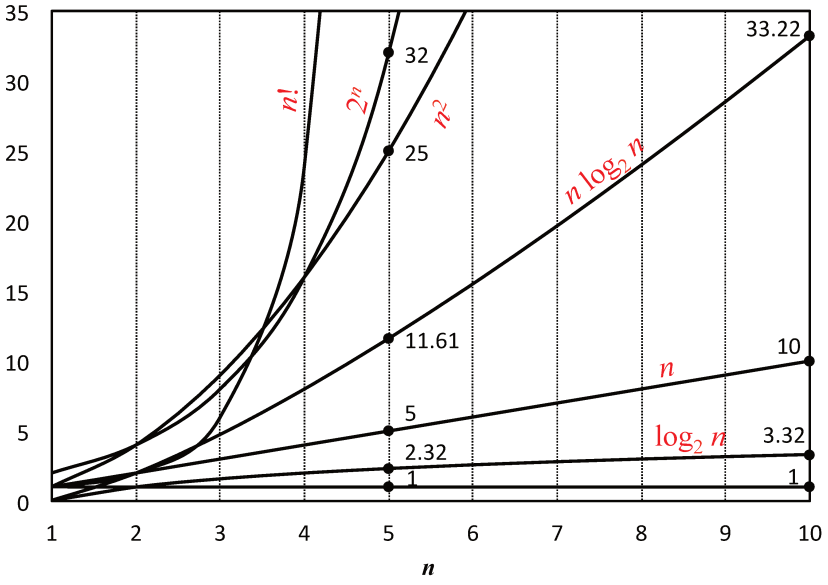

Figure A.1: Function growth

In this thesis, the big-O notation is used to measure algorithm complexity. Other notations can also be used for the same purpose, such as:

- $f = o(g)$ if $f(n)/g(n) \to 0$, $n \to \infty$
- The inverse of big-O notation $f = \Omega(g)$ if $g = O(f)$
- The notation $f = \Theta(g)$ means that both $f = O(g)$ and $g = O(f)$ hold, and we can also say they are of the same order.

In code development we always search for algorithms with a lower algorithm complexity. Ideally, the implementation of code matches the model and has the same growth tendency as its complexity. But in the practical case, overheads and memory delay can also limit the performance.

B

Direct Correlation Function of Water

The bulk DCF, which is an input for MDFT and does not depend on the solute, can be extracted from numerical simulations. In this thesis, the SPC/E water is used as a solvent. Two sources of bulk DCF are used:

1. The DCF at dipolar order ($\hat{c}_S^{000}$, $\hat{c}_\Delta^{110}$, $\hat{c}_D^{112}$) by Zhao *et al.* [71] using MD;
2. The complete DCF up to a given order, for instance $n_{\max} = 5$, by Puibasset *et al.* [72] using MC.

b.1 Dipole DCF from molecular dynamics simulation

The DCF produced by Zhao *et al.*, namely the dipole DCF, contains three primary rotational invariant projections that correspond to $n_{\max} = 1$. They are calculated with the angular dependent PCF in intermolecular frame, $h(r, \cos\theta_1, \cos\theta_2, \psi_1, \psi_2, \phi_{12})$, which is directly extracted from MD simulation.

As the primary projections do not depend on the ψ angles, the intermolecular frame DCF can be simplified as:

$$h(r, \boldsymbol{\omega}_1, \boldsymbol{\omega}_2) \equiv h(r, \cos\theta_1, \cos\theta_2, \phi_{12}) = \langle h(r, \cos\theta_1, \cos\theta_2, \psi_1, \psi_2, \phi_{12}) \rangle_{\psi_1, \psi_2} \tag{B.1}$$

and in k-space:

$$h(k, \boldsymbol{\Omega}_1, \boldsymbol{\Omega}_2) = \int \mathrm{d}r \mathrm{d}\cos\theta_r \mathrm{d}\phi_r e^{ikr\cos\theta_r} h(r, \boldsymbol{\omega}_1, \boldsymbol{\omega}_2) \tag{B.2}$$

where θ_r and ϕ_r are the orientations in spherical coordinates for $\mathbf{r}$ and $\boldsymbol{\Omega}$ is in laboratory coordinate system.

The correlation functions are then projected onto a basis of rotational invariants:

$$h^{nml}(k) = f^{nml} \left\langle h(k, \boldsymbol{\Omega}_1, \boldsymbol{\Omega}_2) \Phi^{nml} \right\rangle_{\boldsymbol{\Omega}_1, \boldsymbol{\Omega}_2} \tag{B.3}$$

with

$$\begin{aligned} \Phi^{000} &= 1 \\ \Phi^{110} &= \boldsymbol{\Omega}_1 \cdot \boldsymbol{\Omega}_2 \\ \Phi^{112} &= 3(\hat{\mathbf{k}} \cdot \boldsymbol{\Omega}_1)(\hat{\mathbf{k}} \cdot \boldsymbol{\Omega}_2) - \boldsymbol{\Omega}_1 \cdot \boldsymbol{\Omega}_2 \end{aligned} \tag{B.4}$$

and $f^{000} = 1$, $f^{110} = 3$, $f^{112} = 3/2$, according to the convention of Wertheim and Hansen.

To obtain the DCF, the OZ equation must be solved. It is shown that the isotropic ($n_{\max} = 0$) and dipolar ($n_{\max} = 1$) components are decoupled:

$$\hat{c}^{000}(k) = \frac{\hat{h}^{000}(k)}{1 + n_0 \hat{h}^{000}(k)} \tag{B.5}$$

$$\hat{c}_+(k) = \frac{\hat{h}_+(k)}{1 + \frac{2}{3} n_0 \hat{h}_+(k)} \tag{B.6}$$

$$\hat{c}_-(k) = \frac{\hat{h}_-(k)}{1 - \frac{1}{3}n_0\hat{h}_-(k)} \tag{B.7}$$

where

$$\hat{h}_+(k) = \hat{h}^{112}(k) + \frac{1}{2}\hat{h}^{110}(k) \tag{B.8}$$

$$\hat{h}_-(k) = \hat{h}^{112}(k) - \hat{h}^{110}(k) \tag{B.9}$$

and idem. for $\hat{c}$.

b.2 DCF PROJECTIONS FROM BULK MONTE CARLO SIMULATION

The complete DCF up to $n_{\max} = 5$, which is the default DCF used in this thesis, is calculated from the $g_{\mu\nu}^{mnl}(r)$ accumulated from MC simulation [72] by resolving the inverted MOZ equation

$$\ln y_\alpha(r) = \left\langle \ln \left[\sum_{\alpha'=1}^{\alpha_{\max}} g_{\alpha'}(r)\Phi_{\alpha'}(\tilde{\Omega}) \right] \Phi_\alpha^*(\tilde{\Omega}) \right\rangle + \beta v_\alpha(r) \tag{B.10}$$

with the closure

$$g_\alpha(r) = \begin{cases} g_\alpha^{\mathrm{MC}}(r), & r \le r_{\max}^{\mathrm{MC}} \\ \left\langle \exp\left[-\beta v(r,\tilde{\Omega}) + \sum_{\alpha'} \gamma_{\alpha'}(r)\Phi_{\alpha'}(\tilde{\Omega})\right] \Phi_\alpha^*(\tilde{\Omega}) \right\rangle, & r > r_{\max}^{\mathrm{MC}} \end{cases} \tag{B.11}$$

where $\ln y = \gamma + b$ is the cavity function (b the bridge function), α the projection number, and $r_{\max}^{\mathrm{MC}}$ is the maximum radius of the MC simulation. Beyond $r_{\max}^{\mathrm{MC}}$, g can be obtained by the usual HNC closure, and it is shown that the projections are continuous at $r_{\max}^{\mathrm{MC}}$, which means HNC closure is enough to cope with long range correlation functions. Note that the $\alpha_{\max}$'s for different $n_{\max}$'s lead to slightly different DCF results according to eq. (B.10,B.11).

The DCF in k-space is obtained by Hankel transform.

The convention of rotational invariants adapts those of Blum, which gives, for example, for $n_{\max} = 1$:

$$\begin{aligned} \Phi^{000} &= 1 \\ \Phi^{011} &= i\mathbf{k}\cdot\mathbf{\Omega}_1 \\ \Phi^{101} &= i\mathbf{k}\cdot\mathbf{\Omega}_2 \\ \Phi^{110} &= -\sqrt{3}\mathbf{\Omega}_1\cdot\mathbf{\Omega}_2 \\ \Phi^{112} &= \sqrt{\frac{3}{10}}\left[3(\mathbf{k}\cdot\mathbf{\Omega_1})(\mathbf{k}\cdot\mathbf{\Omega_2}) - \mathbf{\Omega}_1\cdot\mathbf{\Omega}_2\right] \end{aligned} \tag{B.12}$$

b.3 COMPARISON BETWEEN DCFS

The comparison between the primary projections of the DCFs is given in figure B.1.

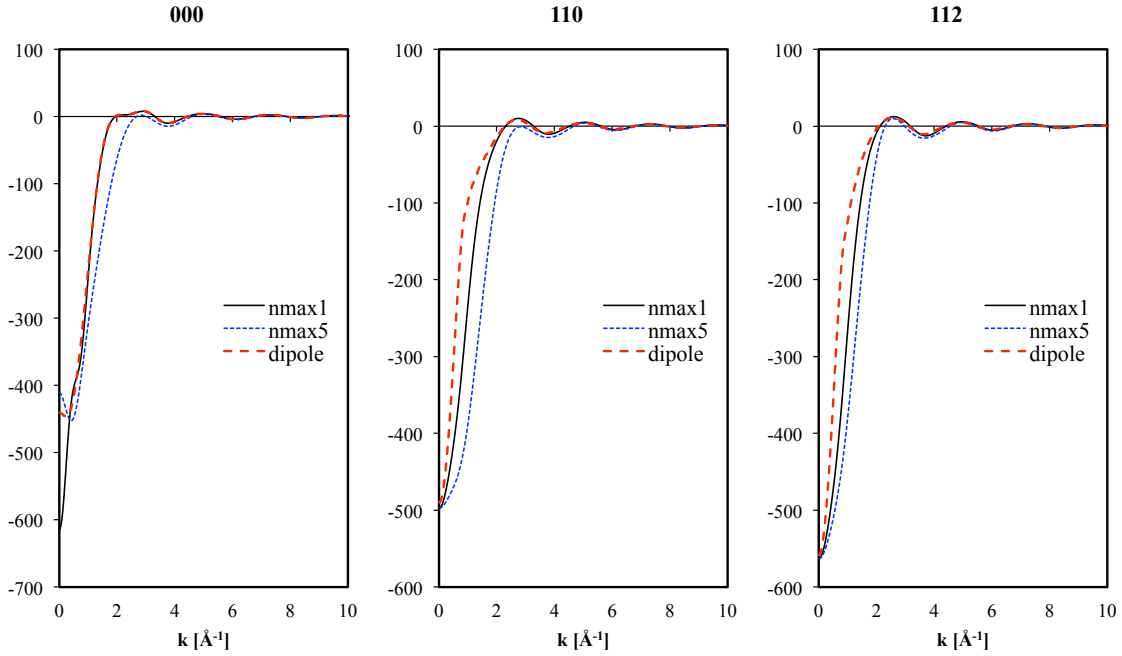

Figure B.1: Comparison between the DCF projections of $n_{\max} = 1$ (dipole) from ref [71] and $n_{\max} = 1, 5$ from ref [72] (in convention of Wertheim and Hansen)

C

Error evaluation of interpolation strategies for DCF in local frame

The error introduced by the two interpolation orders for a DCF of order $n_{\max} = 1$ (for which the exact DCF can be computed directly; see details later) is shown in figure C.1.

Absolute error is the histogram that counts the number of times that the calculated DCF gives the corresponding absolute error E_{a}^i with a resolution of 0.01, in range of $[0, 10]$:

$$E_{\mathrm{a}}^i = \left| c_k^i - c_k \right| \tag{C.1}$$

where c_k^i is any element of $\hat{c}(\mathbf{k}, \mathbf{\Omega_1}, \mathbf{\Omega_2})$ of unity Å^3 calculated as described and c_k is the one calculated directly as the reference.

Log absolute error is treated the same way as E_{a}^i, with E_{l}^i defined as:

$$E_{\mathrm{l}}^i = \log \left| c_k^i - c_k \right| \tag{C.2}$$

Relative error is defined as:

$$E_r^i = \left| c_k^i - c_k \right| / \left| c_k \right| \tag{C.3}$$

with resolution of 0.1%, in range of [0, 1].

In all three figures, the 4 curves given by zero-order interpolation do not diverge a great deal compared with the linear interpolation one. The result of MDFT also shows that zero-order interpolation gives large energy error with a DCF of $n_{\max} = 1$, and has convergence problems in certain cases. We conclude that the linear interpolation scheme is absolutely necessary. On the other hand, as seen in eq. (6.12), it is computationally much more expensive than the simple histogram scheme, as it requires $2^5 = 32$ times the number of operations.

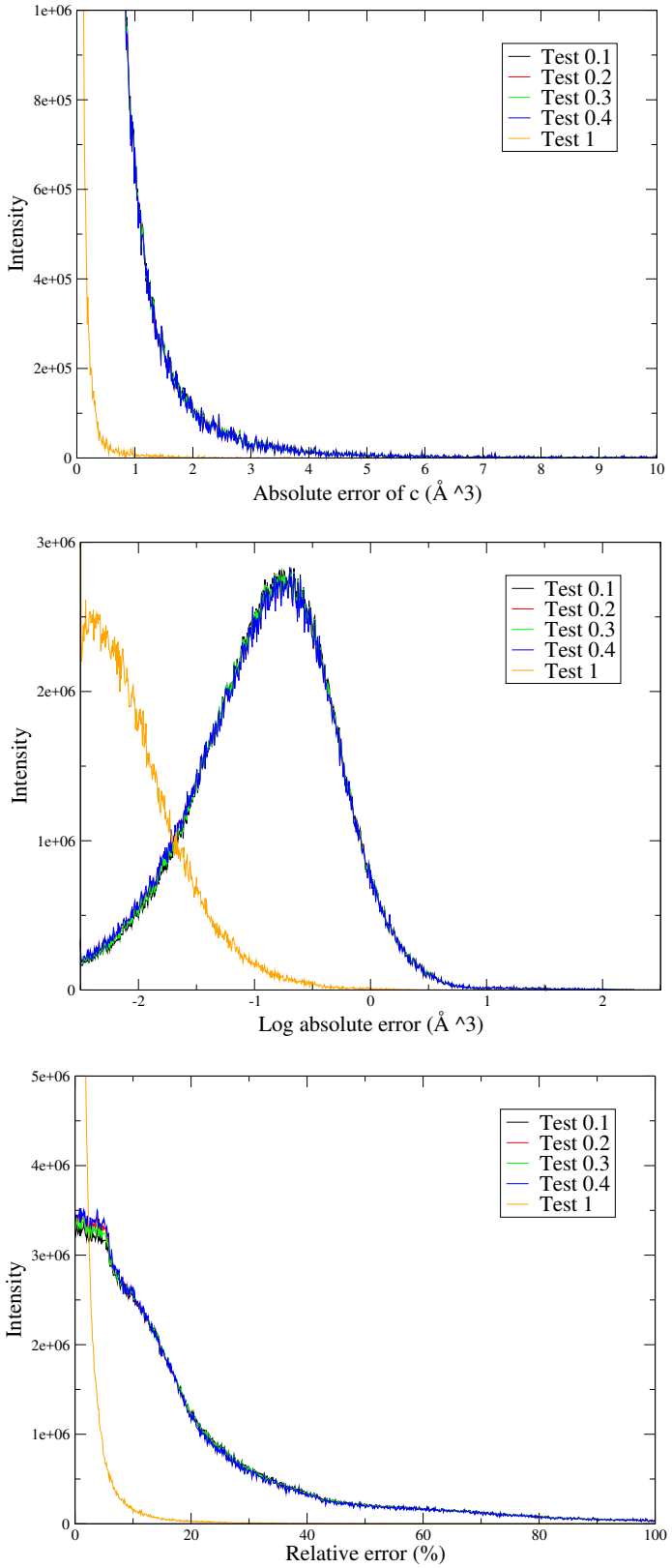

Figure C.1: Error of finding $\hat{c}(\mathbf{k}, \mathbf{\Omega}_1, \mathbf{\Omega}_2)$ by interpolation compared to direct calculation: Test 0.1-0.4 is zero-order interpolation with ϕ tabulated as in figure 6.4. Test 1 is linear interpolation.

D

Angular convolution using Blum's reduction

To make an analogue to the FFT treatment for the convolution of spatial part of the integral, a fast generalized spherical harmonics transform (FGSHT) treatment is proposed by developing $\hat{\gamma}$ and $\hat{\rho}$ in eq. (II.3)

$$\hat{\gamma}(\mathbf{k},\mathbf{\Omega}_1) = -\beta^{-1}\int \mathrm{d}\mathbf{\Omega}_2 \Delta\hat{\rho}(\mathbf{k},\mathbf{\Omega}_2)\hat{c}(k_{12},\mathbf{\Omega}_1,\mathbf{\Omega}_2) \tag{D.1}$$

on generalized spherical harmonics:

$$\hat{\gamma}(\mathbf{k},\mathbf{\Omega}_1) = \sum_{m\mu'\mu} f_m \hat{\gamma}^m_{\mu'\mu}(\mathbf{k}) R^m_{\mu'\mu}(\mathbf{\Omega}_1) \tag{D.2}$$

$$\Delta\hat{\rho}(\mathbf{k},\mathbf{\Omega}_2) = \sum_{n\nu'\nu} f_n \Delta\hat{\rho}^n_{\underline{\nu'\nu}}(\mathbf{k}) R^n_{\underline{\nu'\nu}}(\mathbf{\Omega}_2) \tag{D.3}$$

where $|\mu'|, |\mu| < m$ and $|\nu'|, |\nu| < n$; $f_m = (2m+1)^{\frac{1}{2}}$ is the normalization factor.

The DCF can also be expanded on rotational invariants [16], with the normalization factors according to Blum's definition:

$$\hat{c}(k,\mathbf{\Omega}_1,\mathbf{\Omega}_2) = \sum_{mnl\mu\nu} f_m f_n \hat{c}^{mnl}_{\mu\nu}(k) \sum_{\mu'\nu'\lambda'} \begin{pmatrix} m & n & l \\ \mu' & \nu' & \lambda' \end{pmatrix} R^m_{\mu'\mu}(\mathbf{\Omega}_1) R^n_{\nu'\nu}(\mathbf{\Omega}_2) R^l_{\lambda' 0}(\hat{\mathbf{k}}) \tag{D.4}$$

Replace eq. (D.1) by (D.2, D.3, D.4), as GSHs possess orthogonality [13, 61]

$$\int \frac{\mathrm{d}\mathbf{\Omega}_2}{8\pi^2} R^m_{\mu'\mu}(\mathbf{\Omega}_2) R^{n*}_{\nu'\nu}(\mathbf{\Omega}_2) = \frac{\delta_{m,n}\delta_{\mu',\nu'}\delta_{\mu,\nu}}{2n+1} \tag{D.5}$$

and symmetry

$$R^{n*}_{\nu'\nu}(\mathbf{\Omega}_2) = (-)^{\nu'+\nu} R^n_{\underline{\nu'\nu}}(\mathbf{\Omega}_2) \tag{D.6}$$

Eq. (D.1) becomes

$$\sum_{m\mu'\mu} \hat{\gamma}^m_{\mu'\mu}(\mathbf{k}) R^m_{\mu'\mu}(\mathbf{\Omega}_1) \tag{D.7}$$

$$= \sum_{mnl\mu\nu} \hat{c}^{mnl}_{\mu\nu}(k) \sum_{\mu'\nu'\lambda'} (-)^{\nu'+\nu} \Delta\hat{\rho}^n_{\underline{\nu'\nu}}(\mathbf{k}) \begin{pmatrix} m & n & l \\ \mu' & \nu' & \lambda' \end{pmatrix} R^m_{\mu'\mu}(\mathbf{\Omega}_1) R^l_{\lambda' 0}(\hat{\mathbf{k}})$$

As the basis sets are orthogonal,

$$\hat{\gamma}^m_{\mu'\mu}(\mathbf{k}) = \sum_{nl\nu} \hat{c}^{mnl}_{\mu\nu}(k) \sum_{\nu'\lambda'} (-)^{\nu'+\nu} \Delta\hat{\rho}^n_{\underline{\nu'\nu}}(\mathbf{k}) \begin{pmatrix} m & n & l \\ \mu' & \nu' & \lambda' \end{pmatrix} R^l_{\lambda' 0}(\hat{\mathbf{k}}) \tag{D.8}$$

According to Gubbins eq. (A.41-43) and Messiah eq. (C.76):

$$R^m_{\chi\mu}(\boldsymbol{\omega}) = \sum_{\mu'} R^{m*}_{\mu'\chi}(\hat{\mathbf{k}}) R^m_{\mu'\mu}(\mathbf{\Omega}) \tag{D.9}$$

$$R^m_{\mu'\mu}(\mathbf{\Omega}) = \sum_\chi R^{m*}_{\chi\mu'}(\hat{\mathbf{k}}^{-1}) R^m_{\chi\mu}(\boldsymbol{\omega}) = \sum_\chi R^m_{\mu'\chi}(\hat{\mathbf{k}}) R^m_{\chi\mu}(\boldsymbol{\omega}) \tag{D.10}$$

where $\boldsymbol{\omega} = \hat{\mathbf{k}}^{-1}\mathbf{\Omega}$. Suppose $\hat{\gamma}$ has rotational invariance, and

$$\hat{\gamma}(\mathbf{k}, \boldsymbol{\omega}_1) = \sum_{m\chi\mu} f_m \hat{\gamma'}^m_{\chi\mu}(\mathbf{k}) R^m_{\chi\mu}(\boldsymbol{\omega}_1) \tag{D.11}$$

Compared to (D.2), we have:

$$\hat{\gamma'}^m_{\chi\mu}(\mathbf{k}) = \sum_{\mu'} \hat{\gamma}^m_{\mu'\mu}(\mathbf{k}) R^m_{\mu'\chi}(\hat{\mathbf{k}}) \tag{D.12}$$

Idem.

$$\Delta\hat{\rho}^n_{\underline{\nu'}\nu}(\mathbf{k}) = \sum_\chi \Delta\hat{\rho'}^n_{\chi\underline{\nu}}(\mathbf{k}) R^{n*}_{\underline{\nu'}\chi}(\hat{\mathbf{k}}) = \sum_\chi \Delta\hat{\rho'}^n_{\chi\underline{\nu}}(\mathbf{k}) \, (-)^{\chi+\nu'} R^n_{\nu'\underline{\chi}}(\hat{\mathbf{k}}) \tag{D.13}$$

as the symmetry (D.6).

As there is an equivalence of OZ equation and the gradient γ, we can be inspired by Blum's reduction of the OZ equation [17] by proposing

$$\hat{c}^{mnl}_{\mu\nu}(k) = (2l+1) \sum_\chi \begin{pmatrix} m & n & l \\ \chi & -\chi & 0 \end{pmatrix} \hat{c'}^{mn}_{\mu\nu,\chi}(k) \tag{D.14}$$

Thus replacing (D.12) by (D.8), gives

$$\begin{aligned} & \hat{\gamma'}^m_{\chi\mu}(\mathbf{k}) \\ = & \sum_{\mu'} \left[\sum_{nl\nu} \hat{c}^{mnl}_{\mu\nu}(k) \sum_{\nu'\lambda'} (-)^{\nu'+\nu} \Delta\hat{\rho}^n_{\underline{\nu'}\nu}(\mathbf{k}) \begin{pmatrix} m & n & l \\ \mu' & \nu' & \lambda' \end{pmatrix} R^l_{\lambda' 0}(\hat{\mathbf{k}}) \right] R^m_{\mu'\chi}(\hat{\mathbf{k}}) \\ = & \sum_{nl\nu} \hat{c}^{mnl}_{\mu\nu}(k) \sum_{\mu'\nu'\lambda'} (-)^{\nu'+\nu} \Delta\hat{\rho}^n_{\underline{\nu'}\nu}(\mathbf{k}) \begin{pmatrix} m & n & l \\ \mu' & \nu' & \lambda' \end{pmatrix} R^l_{\lambda' 0}(\hat{\mathbf{k}}) R^m_{\mu'\chi}(\hat{\mathbf{k}}) \end{aligned} \tag{D.15}$$

then with eq. (D.13):

$$\begin{aligned} \hat{\gamma'}^m_{\chi\mu}(\mathbf{k}) = & \sum_{nl\nu} \hat{c}^{mnl}_{\mu\nu}(k) \sum_{\mu'\nu'\lambda'} \left[\sum_{\chi'} \Delta\hat{\rho'}^n_{\chi'\underline{\nu}}(\mathbf{k}) \, (-)^{\chi'+\nu} R^n_{\nu'\underline{\chi'}}(\hat{\mathbf{k}}) \right] \\ & \times \begin{pmatrix} m & n & l \\ \mu' & \nu' & \lambda' \end{pmatrix} R^l_{\lambda' 0}(\hat{\mathbf{k}}) R^m_{\mu'\chi}(\hat{\mathbf{k}}) \\ = & \sum_{nl\nu} \hat{c}^{mnl}_{\mu\nu}(k) \sum_{\chi'} \Delta\hat{\rho'}^n_{\chi'\underline{\nu}}(\mathbf{k}) \, (-)^{\chi'+\nu} \\ & \times \left[\sum_{\mu'\nu'\lambda'} \begin{pmatrix} m & n & l \\ \mu' & \nu' & \lambda' \end{pmatrix} R^l_{\lambda' 0}(\hat{\mathbf{k}}) R^m_{\mu'\chi}(\hat{\mathbf{k}}) R^n_{\nu'\underline{\chi'}}(\hat{\mathbf{k}}) \right] \end{aligned} \tag{D.16}$$

Gubbins eq. (A.91) gives the symmetry relation:

$$\sum_{\mu'\nu'\lambda'} \begin{pmatrix} m & n & l \\ \mu' & \nu' & \lambda' \end{pmatrix} R^m_{\mu'\chi}(\hat{\mathbf{k}}) R^n_{\nu'\underline{\chi'}}(\hat{\mathbf{k}}) R^l_{\lambda' 0}(\hat{\mathbf{k}}) = \begin{pmatrix} m & n & l \\ \chi & -\chi' & 0 \end{pmatrix} \tag{D.17}$$

Thus with eq. (D.14), eq. (D.16) becomes

$$\begin{aligned}\hat{\gamma'}^{m}_{\chi\mu}(\mathbf{k}) &= \sum_{nl\nu}(2l+1)\sum_{\chi'\chi''}(-)^{\chi'+\nu}\begin{pmatrix} m & n & l \\ \chi'' & -\chi'' & 0\end{pmatrix}\begin{pmatrix} m & n & l \\ \chi & -\chi' & 0\end{pmatrix} \qquad \text{(D.18)}\\ &\quad \times\hat{c'}^{mn}_{\mu\nu,\chi''}(k)\Delta\hat{\rho'}^{n}_{\chi'\underline{\nu}}(\mathbf{k})\\ &= \sum_{n\nu}(2l+1)\sum_{\chi'\chi''}(-)^{\chi'+\nu}\hat{c'}^{mn}_{\mu\nu,\chi''}(k)\Delta\hat{\rho'}^{n}_{\chi'\underline{\nu}}(\mathbf{k}) \qquad \text{(D.19)}\\ &\quad \times\left[\sum_{l}\begin{pmatrix} m & n & l \\ \chi'' & -\chi'' & 0\end{pmatrix}\begin{pmatrix} m & n & l \\ \chi & -\chi' & 0\end{pmatrix}\right]\end{aligned}$$

As the 3-j symbols possess the symmetry [61]

$$\sum_{l}\begin{pmatrix} m & n & l \\ \chi'' & -\chi'' & 0\end{pmatrix}\begin{pmatrix} m & n & l \\ \chi & -\chi' & 0\end{pmatrix} = (2l+1)^{-1}\,\delta_{\chi''\chi}\delta_{\chi''\chi'} \qquad \text{(D.20)}$$

Eq. (D.18) becomes

$$\hat{\gamma'}^{m}_{\chi\mu}(\mathbf{k}) = \sum_{n\nu}(-)^{\chi+\nu}\hat{c'}^{mn}_{\mu\nu,\chi}(k)\Delta\hat{\rho'}^{n}_{\chi\underline{\nu}}(\mathbf{k}) \qquad \text{(D.21)}$$

In this way, the integral of the angular part in eq. (D.1) is reduced to a sum of few terms.

E

Equivalence of Quadrature-Projection Order

e.1 gaussian quadrature

Theorem:

Let $P_n(x)$ be a nonzero polynomial of degree n, and $w(x)$ a positive weight function so that

$$\int_a^b x^k P_n(x) w(x) \mathrm{d}x = 0, (k = 0, \ldots, n-1) \tag{E.1}$$

If $\{x_i\}$ $(i = 1, \ldots n)$ are the zeros of $P_n(x)$, then

$$\int_a^b f(x) w(x) \mathrm{d}x \simeq \sum_{i=1}^{n} A_i f(x_i) \tag{E.2}$$

with

$$A_i = \int_a^b l_{i-1}(x) w(x) \mathrm{d}x \tag{E.3}$$

is exact for all polynomials $f(x)$ of degree at most $2n-1$, where $\{l_i\}$ are the usual Lagrange interpolating polynomials.

Proof:

Assume that $f(x)$ is a polynomial of degree at most $2n-1$. Using long division

$$f(x) = P_n(x) p(x) + r(x) \tag{E.4}$$

$p(x)$ and $r(x)$ are obtained as polynomials of degree at most $n-1$.

By taking $\{x_i\}$ as the zeros of $P_n(x)$, we can easily find $f(x_i) = r(x_i), (i = 1, \ldots n)$, then

$$\begin{aligned} \int_a^b f(x) w(x) \mathrm{d}x &= \int_a^b \left[P_n(x) p(x) + r(x) \right] w(x) \mathrm{d}x \\ &\simeq \overbrace{\sum_{i=1}^{n} P_n(x_i) p(x_i) w_i}^{=0} + \sum_{i=1}^{n} A_i r(x_i) \end{aligned} \tag{E.5}$$

is exact for $r(x)$ of degree at most $n-1$ (c.f. Numerical Recipes [62] p.118), and thus exact for $f(x)$ of degree at most $2n-1$.

e.2 angular integration in gsht

To expand a function onto GSHs, as in eq. (7.17), quadrature is needed. Assume that $F(\mathbf{\Omega})$ is a polynomial of $\cos\Theta$, $\cos\Phi$ and $\cos\Psi$ of order n. As $R^{m*}_{\mu'\mu}(\mathbf{\Omega})$ is also a polynomial

of order n, the total degree of integrand is $2n$. It should be noted that the surface area element is:

$$\mathrm{d}\mathbf{\Omega} = \sin\Theta \mathrm{d}\Theta \mathrm{d}\Phi \mathrm{d}\Psi = \mathrm{d}\cos\Theta \mathrm{d}\Phi \mathrm{d}\Psi \tag{E.6}$$

For $\cos\Theta$ integration, considering $w(x) = 1$ and $x = \cos\Theta$, Gauss-Legendre quadrature should be used. Thus $n+1$ points on x should be taken, with $\{x_i\}$ given by Legendre polynomials $P_{n+1}(x)$.

For Φ and Ψ integration, taking $w(x) = \left(1-x^2\right)^{-\frac{1}{2}}$, the abscissae are given by the $N = n+1$ roots of the Chebyshev polynomial of the first kind:

$$T_N(x) = \cos(N\cos x) \quad \Rightarrow \quad x_i = \cos\left[\tfrac{(2i-1)\pi}{2N}\right], \quad i \in 1, \ldots, N \tag{E.7}$$

with weight $w_i = \frac{\pi}{N}$, it corresponds to points in $\Phi \in [0, \pi]$ regularly distributed. However, for $\Phi \in [0, 2\pi]$, two times of function evaluation should be calculated:

$$\begin{aligned} &\int_{-1}^{1} f(\cos\Phi) \frac{1}{\sqrt{1-\cos^2\Phi}} \mathrm{d}\cos\Phi \\ &= \begin{cases} \int_{\pi}^{0} f(\cos\Phi)\mathrm{d}\Phi = -\int_{0}^{\pi} f(\cos(\Phi))\mathrm{d}\Phi & \Phi \in [0,\pi] \\ \int_{-\pi}^{0} f(\cos(\Phi))\mathrm{d}(\Phi) = \int_{0}^{\pi} f(\cos(-\Phi'))\mathrm{d}\Phi' & \Phi' \in [0,\pi] \end{cases} \end{aligned} \tag{E.8}$$

so that

$$\int_0^{2\pi} f(\cos\Phi)\mathrm{d}\Phi = \int_{-\pi}^{\pi} f(\cos\Phi)\mathrm{d}\Phi = \int_0^{\pi} \left[f(\cos(-\Phi)) - f(\cos\Phi)\right] \mathrm{d}\Phi \tag{E.9}$$

It corresponds to $2n+2$ points in $\Phi \in [0, 2\pi]$ regularly distributed. However, it's not the minimal number of points necessary to do the exact integration. Suppose that $\Phi_2 \equiv \Phi/2$,

$$\int_0^{2\pi} f(\cos\Phi)\mathrm{d}\Phi = \int_0^{\pi} f(\cos(2\Phi_2))\mathrm{d}\Phi_2 = \int_0^{\pi} \left[f(2\cos^2\Phi_2 - 1)\right] \mathrm{d}\Phi_2 \tag{E.10}$$

As $f(2\cos^2\Phi_2 - 1)$ is a polynomial of Φ of degree $2n$, it's a polynomial of Φ_2 of degree $4n$. Thus only $2n+1$ points are needed.

F

Rotational Invariant Expansion

If a function $F(\mathbf{X}_1, \mathbf{X}_2)$, $\mathbf{X}_i \equiv (\mathbf{r}_i, \mathbf{\Omega}_i)$ has transitional and rotational invariance [16], it can be expanded as

$$F(\mathbf{X}_1, \mathbf{X}_2) = \sum_{mnl\mu\nu} F^{mnl}_{\mu\nu}(\|\mathbf{r}_{12}\|)\Phi^{mnl}_{\mu\nu}(\mathbf{\Omega}_1, \mathbf{\Omega}_2, \hat{\mathbf{r}}_{12}) \tag{F.1}$$

where $\mathbf{r}_{12} \equiv \mathbf{r}_1 - \mathbf{r}_2$ according to the transitional invariance, and

$$\Phi^{mnl}_{\mu\nu}(\mathbf{\Omega}_1, \mathbf{\Omega}_2, \hat{\mathbf{r}}_{12}) = f^{mnl} \sum_{\mu'\nu'\lambda'} \begin{pmatrix} m & n & l \\ \mu' & \nu' & \lambda' \end{pmatrix} R^m_{\mu'\mu}(\mathbf{\Omega}_1) R^n_{\nu'\nu}(\mathbf{\Omega}_2) R^l_{\lambda' 0}(\hat{\mathbf{r}}_{12}) \tag{F.2}$$

where $R^m_{\mu'\mu}$ is the Wigner generalized spherical harmonics or Wigner D-symbol defined in the same convention as Messiah [61] (different than Edmonds [90]). f^{mnl} can be any arbitrary non-zero constant [19]. Here we keep the same definition as Blum, where $f^{mnl} = f^m f^n = \sqrt{2m+1}\sqrt{2n+1}$.

Two special cases are adopted in this thesis (as shown in figure 6.1):

1. $F(\mathbf{X}_1, \mathbf{X}_2)$ in laboratory coordinate system with particle 1 at origin (fixed frame);
2. $F(\mathbf{X}_1, \mathbf{X}_2)$ in intermolecular coordinate system (local frame).

Their formalism and symmetry properties will be given later.

f.1 orthogonality of Φ

The rotational invariants Φ in eq. (F.2) form an orthogonal basis set, as proven below:

$$\begin{aligned}
\langle \Phi \mid \Phi_2 \rangle &= \int \mathrm{d}\mathbf{\Omega}_1 \mathrm{d}\mathbf{\Omega}_2 \mathrm{d}\hat{\mathbf{r}} \Phi^{mnl}_{\mu\nu}(\mathbf{\Omega}_1, \mathbf{\Omega}_2, \hat{\mathbf{r}}_{12}) \Phi^{m_2 n_2 l_2 *}_{\mu_2\nu_2}(\mathbf{\Omega}_1, \mathbf{\Omega}_2, \hat{\mathbf{r}}_{12}) \\
&= f^m f^n f^{m_2} f^{n_2} \sum_{\mu'\nu'\lambda'} \begin{pmatrix} m & n & l \\ \mu' & \nu' & \lambda' \end{pmatrix} \sum_{\mu'_2\nu'_2\lambda'_2} \begin{pmatrix} m_2 & n_2 & l_2 \\ \mu'_2 & \nu'_2 & \lambda'_2 \end{pmatrix} \\
&\quad \times \{ \int \mathrm{d}\mathbf{\Omega}_1 R^m_{\mu'\mu}(\mathbf{\Omega}_1) R^{m_2 *}_{\mu'_2\mu_2}(\mathbf{\Omega}_1) \\
&\quad \left[\int \mathrm{d}\mathbf{\Omega}_2 R^n_{\nu'\nu}(\mathbf{\Omega}_2) R^{n_2 *}_{\nu'_2\nu_2}(\mathbf{\Omega}_2) \left(\int \mathrm{d}\hat{\mathbf{r}} R^l_{\lambda' 0}(\hat{\mathbf{r}}_{12}) R^{l_2 *}_{\lambda'_2 0}(\hat{\mathbf{r}}_{12}) \right) \right] \} \\
&= (2l+1)^{-1} \sum_{\mu'\nu'\lambda'} \begin{pmatrix} m & n & l \\ \mu' & \nu' & \lambda' \end{pmatrix} \sum_{\mu'_2\nu'_2\lambda'_2} \begin{pmatrix} m_2 & n_2 & l_2 \\ \mu'_2 & \nu'_2 & \lambda'_2 \end{pmatrix} \\
&\quad \times \delta_{m,m_2} \delta_{n,n_2} \delta_{l,l_2} \delta_{\mu,\mu_2} \delta_{\nu,\nu_2} \delta_{\mu',\mu'_2} \delta_{\nu',\nu'_2} \delta_{\lambda',\lambda'_2} \\
&= (2l+1)^{-1} \sum_{\mu'\nu'\lambda'} \begin{pmatrix} m & n & l \\ \mu' & \nu' & \lambda' \end{pmatrix} \begin{pmatrix} m & n & l \\ \mu' & \nu' & \lambda' \end{pmatrix} \qquad \text{(F.3)} \\
&\quad \times \delta_{m,m_2} \delta_{n,n_2} \delta_{l,l_2} \delta_{\mu,\mu_2} \delta_{\nu,\nu_2} \qquad \text{(F.4)}
\end{aligned}$$

and using the orthogonality of 3j-symbol [90]

$$\sum_{\mu'\nu'} \begin{pmatrix} m & n & l \\ \mu' & \nu' & \lambda' \end{pmatrix} \begin{pmatrix} m & n & l_2 \\ \mu' & \nu' & \lambda'_2 \end{pmatrix} = (2l+1)^{-1} \delta_{ll_2} \delta_{\lambda'_1 \lambda'_2} \tag{F.5}$$

it gives

$$\langle \Phi \mid \Phi_2 \rangle = (2l+1)^{-1} \times \delta_{m,m_2} \delta_{n,n_2} \delta_{l,l_2} \delta_{\mu,\mu_2} \delta_{\nu,\nu_2} \tag{F.6}$$

f.2 ROTATIONAL INVARIANCE OF Φ

In any coordinate system, the value of $\Phi^{mnl}_{\mu\nu}$ remains the same. Here is a partial demonstration with the fixed and local frame mentioned above, described in figure 6.1.

Let's use the definition in eq. (F.2):

$$\Phi^{mnl}_{\mu\nu}(\boldsymbol{\omega}_1, \boldsymbol{\omega}_2, 0) = f^{mnl} \sum_{\mu''\nu''\lambda''} \begin{pmatrix} m & n & l \\ \mu'' & \nu'' & \lambda'' \end{pmatrix} R^m_{\mu''\mu}(\boldsymbol{\omega}_1) R^n_{\nu''\nu}(\boldsymbol{\omega}_2) R^l_{\lambda''0}(0) \tag{F.7}$$

$$\Phi^{mnl}_{\mu\nu}(0, \boldsymbol{\Omega}, \hat{\mathbf{r}}) = f^{mnl} \sum_{\mu'\nu'\lambda'} \begin{pmatrix} m & n & l \\ \mu' & \nu' & \lambda' \end{pmatrix} R^m_{\mu'\mu}(0) R^n_{\nu'\nu}(\boldsymbol{\Omega}) R^l_{\lambda'0}(\hat{\mathbf{r}}) \tag{F.8}$$

The spherical harmonics have property [61, 90]

$$R^m_{\mu'\mu}(0) = \sum_{\mu''} R^m_{\mu'\mu''}(\hat{\mathbf{r}}) R^m_{\mu''\mu}(\boldsymbol{\omega}_1) \tag{F.9}$$

$$R^n_{\nu'\nu}(\boldsymbol{\Omega}) = \sum_{\nu''} R^n_{\nu'\nu''}(\hat{\mathbf{r}}) R^n_{\nu''\nu}(\boldsymbol{\omega}_2) \tag{F.10}$$

$$R^l_{\lambda'0}(\hat{\mathbf{r}}) = \sum_{\lambda''} R^l_{\lambda'\lambda''}(\hat{\mathbf{r}}) R^l_{\lambda''0}(0) \tag{F.11}$$

so

$$\begin{aligned} \Phi^{mnl}_{\mu\nu}(0, \boldsymbol{\Omega}, \hat{\mathbf{r}}) = f^{mnl} \sum_{\mu''\nu''\lambda''} & R^m_{\mu''\mu}(\boldsymbol{\omega}_1) R^n_{\nu''\nu}(\boldsymbol{\omega}_2) R^l_{\lambda''0}(0) \times \\ & \left[\sum_{\mu'\nu'\lambda'} \begin{pmatrix} m & n & l \\ \mu' & \nu' & \lambda' \end{pmatrix} R^m_{\mu'\mu''}(\hat{\mathbf{r}}) R^n_{\nu'\nu''}(\hat{\mathbf{r}}) R^l_{\lambda'\lambda''}(\hat{\mathbf{r}}) \right] \end{aligned} \tag{F.12}$$

According to eq. (4.3.3) in Edmonds [90] or (A.91) in Gray & Gubbins [13]

$$\sum_{\mu'\nu'\lambda'} \begin{pmatrix} m & n & l \\ \mu' & \nu' & \lambda' \end{pmatrix} R^{m*}_{\mu'\mu''}(\hat{\mathbf{r}}) R^{n*}_{\nu'\nu''}(\hat{\mathbf{r}}) R^{l*}_{\lambda'\lambda''}(\hat{\mathbf{r}}) = \begin{pmatrix} m & n & l \\ \mu'' & \nu'' & \lambda'' \end{pmatrix} \tag{F.13}$$

where we can also prove

$$\sum_{\mu'\nu'\lambda'} \begin{pmatrix} m & n & l \\ \mu' & \nu' & \lambda' \end{pmatrix} R^m_{\mu'\mu''}(\hat{\mathbf{r}}) R^n_{\nu'\nu''}(\hat{\mathbf{r}}) R^l_{\lambda'\lambda''}(\hat{\mathbf{r}}) = \begin{pmatrix} m & n & l \\ \mu'' & \nu'' & \lambda'' \end{pmatrix} \tag{F.14}$$

$\Phi^{mnl}_{\mu\nu}$ remains identical in the two cases

$$\begin{aligned} \Phi^{mnl}_{\mu\nu}(0, \boldsymbol{\Omega}, \hat{\mathbf{r}}) &= f^{mnl} \sum_{\mu''\nu''\lambda''} \begin{pmatrix} m & n & l \\ \mu'' & \nu'' & \lambda'' \end{pmatrix} R^m_{\mu''\mu}(\boldsymbol{\omega}_1) R^n_{\nu''\nu}(\boldsymbol{\omega}_2) R^l_{\lambda''0}(0) \\ &= \Phi^{mnl}_{\mu\nu}(\boldsymbol{\omega}_1, \boldsymbol{\omega}_2, 0) \end{aligned} \tag{F.15}$$

Therefore, the projections $F^{mnl}_{\mu\nu}(r)$ also remain rotational invariant in these two coordinate systems.

f.3 TRANSFORM IN LOCAL FRAME

In the intermolecular (local) coordinate system, the 2 molecules are both positioned along the z axis. Using the properties of generalized spherical harmonics [13, 61, 90]:

$$R^m_{\mu'\mu}(\Theta,\Phi,\Psi) = \delta_{\mu'\mu} \quad \text{if} \quad \Theta=\Phi=\Psi=0 \tag{F.16}$$

and of 3j-symbol

$$\begin{pmatrix} m & n & l \\ \mu' & \nu' & \lambda' \end{pmatrix} \neq 0 \quad \text{only if} \quad \mu'+\nu'+\lambda'=0 \tag{F.17}$$

$\Phi^{mnl}_{\mu\nu}(\boldsymbol{\Omega}_1,\boldsymbol{\Omega}_2,\hat{\mathbf{r}}_{12})$ in eq. (F.2) can be simplified to

$$\Phi^{mnl}_{\mu\nu}(\boldsymbol{\omega}_1,\boldsymbol{\omega}_2,0) = \sum_\chi \begin{pmatrix} m & n & l \\ \chi & -\chi & 0 \end{pmatrix} f^m f^n R^m_{\chi\mu}(\boldsymbol{\omega}_1) R^n_{\underline{\chi}\nu}(\boldsymbol{\omega}_2) \tag{F.18}$$

Thus eq. (F.1) becomes

$$\begin{aligned} F(\boldsymbol{\omega}_1,\boldsymbol{\omega}_2,r) &= \sum_{mnl\mu\nu} F^{mnl}_{\mu\nu}(r)\Phi^{mnl}_{\mu\nu}(\boldsymbol{\omega}_1,\boldsymbol{\omega}_2,0) \\ &= \sum_{mnl\mu\nu} F^{mnl}_{\mu\nu}(r) f^m f^n \sum_\chi \begin{pmatrix} m & n & l \\ \chi & -\chi & 0 \end{pmatrix} R^m_{\chi\mu}(\boldsymbol{\omega}_1) R^n_{\underline{\chi}\nu}(\boldsymbol{\omega}_2) \end{aligned} \tag{F.19}$$

and the inverse equation is:

$$\begin{aligned} F^{mnl}_{\mu\nu}(r) &= \int \mathrm{d}\boldsymbol{\omega}_1 \mathrm{d}\boldsymbol{\omega}_2 F(\boldsymbol{\omega}_1,\boldsymbol{\omega}_2,r)\Phi^{mnl*}_{\mu\nu}(\boldsymbol{\omega}_1,\boldsymbol{\omega}_2,0) \\ &= f^m f^n \sum_\chi \begin{pmatrix} m & n & l \\ \chi & -\chi & 0 \end{pmatrix} \times \\ &\quad \int \mathrm{d}\boldsymbol{\omega}_1 R^{m*}_{\chi\mu}(\boldsymbol{\omega}_1) \int \mathrm{d}\boldsymbol{\omega}_2 R^{n*}_{\underline{\chi}\nu}(\boldsymbol{\omega}_2) F(\boldsymbol{\omega}_1,\boldsymbol{\omega}_2,r) \end{aligned} \tag{F.20}$$

The function $F(\boldsymbol{\omega}_1,\boldsymbol{\omega}_2,r)$ and the projections $F^{mnl}_{\mu\nu}(r)$ can be transformed into each other by 2 simple steps.

Transform between $F^{mnl}_{\mu\nu}(r)$ and $F'^{mn}_{\mu\nu,\chi}(r)$

Suppose

$$F'^{mn}_{\mu\nu,\chi}(r) = \sum_l \begin{pmatrix} m & n & l \\ \chi & -\chi & 0 \end{pmatrix} F^{mnl}_{\mu\nu}(r) \tag{F.21}$$

Using property of 3j-symbol [61]

$$\sum_\chi \begin{pmatrix} m & n & l' \\ \chi & -\chi & 0 \end{pmatrix} \begin{pmatrix} m & n & l \\ \chi & -\chi & 0 \end{pmatrix} = \frac{\delta_{l'l}}{2l+1} \tag{F.22}$$

we have as the inverse transform

$$F^{mnl}_{\mu\nu}(r) = (2l+1)\sum_\chi \begin{pmatrix} m & n & l \\ \chi & -\chi & 0 \end{pmatrix} F'^{mn}_{\mu\nu,\chi}(r) \tag{F.23}$$

Thus eq. (F.19) becomes

$$\begin{aligned} F(\boldsymbol{\omega}_1,\boldsymbol{\omega}_2,r) &= \sum_{mnl\mu\nu}(2l+1)\sum_{\chi'}\begin{pmatrix} m & n & l \\ \chi' & -\chi' & 0\end{pmatrix} F'^{mn}_{\mu\nu,\chi'}(r)\times \\ &\quad \sum_{\chi}\begin{pmatrix} m & n & l \\ \chi & -\chi & 0\end{pmatrix} f^m f^n R^m_{\chi\mu}(\boldsymbol{\omega}_1)R^n_{\underline{\chi}\nu}(\boldsymbol{\omega}_2) \\ &= \sum_{mn\mu\nu}\sum_{\chi'}\sum_{\chi} F'^{mn}_{\mu\nu,\chi'}(r) f^m f^n R^m_{\chi\mu}(\boldsymbol{\omega}_1)R^n_{\underline{\chi}\nu}(\boldsymbol{\omega}_2)\times \\ &\quad \sum_{l}(2l+1)\begin{pmatrix} m & n & l \\ \chi' & -\chi' & 0\end{pmatrix}\begin{pmatrix} m & n & l \\ \chi & -\chi & 0\end{pmatrix} \end{aligned} \tag{F.24}$$

As

$$\sum_{l}(2l+1)\begin{pmatrix} m & n & l \\ \chi' & -\chi' & 0\end{pmatrix}\begin{pmatrix} m & n & l \\ \chi & -\chi & 0\end{pmatrix} = \delta_{\chi'\chi} \tag{F.25}$$

we have

$$F(\boldsymbol{\omega}_1,\boldsymbol{\omega}_2,r) = \sum_{mn\mu\nu\chi} F'^{mn}_{\mu\nu,\chi}(r) f^m f^n R^m_{\chi\mu}(\boldsymbol{\omega}_1)R^n_{\underline{\chi}\nu}(\boldsymbol{\omega}_2) \tag{F.26}$$

and

$$F'^{mn}_{\mu\nu,\chi}(r) = \int \mathrm{d}\boldsymbol{\omega}_1\mathrm{d}\boldsymbol{\omega}_2 F(\boldsymbol{\omega}_1,\boldsymbol{\omega}_2,r) f^m f^n R^{m*}_{\chi\mu}(\boldsymbol{\omega}_1)R^{n*}_{\underline{\chi}\nu}(\boldsymbol{\omega}_2) \tag{F.27}$$

Thus eq. (F.26, F.27) can be performed either by fast generalized spherical harmonic transform (FGSHT), or by being developed into

$$F(\boldsymbol{\omega}_1,\boldsymbol{\omega}_2,r) = \sum_{mn\mu\nu\chi} F'^{mn}_{\mu\nu,\chi}(r) f^m f^n r^m_{\chi\mu}(\theta_1)r^n_{\underline{\chi}\nu}(\theta_2)e^{-i\chi(\phi_{12}\equiv\phi_1-\phi_2)}e^{-i\mu\psi_1}e^{-i\nu\psi_2} \tag{F.28}$$

and transformed with FFT-3D.

Rotational invariant transform with FFT-3D

Suppose

$$F'^{m}_{\mu\nu,\chi}(r,\theta_2) = \sum_{n} F'^{mn}_{\mu\nu,\chi}(r) f^n r^n_{\underline{\chi}\nu}(\theta_2) \tag{F.29}$$

then we have

$$F(\boldsymbol{\omega}_1,\boldsymbol{\omega}_2,r) = \sum_{m\mu\nu\chi} F'^{m}_{\mu\nu,\chi}(r,\theta_2) f^m r^m_{\chi\mu}(\theta_1)e^{-i\chi\phi_{12}}e^{-i\mu\psi_1}e^{-i\nu\psi_2} \tag{F.30}$$

The inverse transform should be

$$F'^{mn}_{\mu\nu,\chi}(r) = \frac{1}{2}\int \mathrm{d}(\cos\theta_2) F'^{m}_{\mu\nu,\chi}(r,\theta_2) r^n_{\underline{\chi}\nu}(\theta_2) \tag{F.31}$$

In the same way, suppose

$$F'_{\mu\nu,\chi}(r,\theta_1,\theta_2) = \sum_{m} F'^{m}_{\mu\nu,\chi}(r,\theta_2) r^m_{\chi\mu}(\theta_1) \tag{F.32}$$

and the inverse transform

$$F'^{m}_{\mu\nu,\chi}(r,\theta_2) = \frac{1}{2}\int \mathrm{d}(\cos\theta_1) F'_{\mu\nu,\chi}(r,\theta_1,\theta_2) r^m_{\chi\mu}(\theta_1) \tag{F.33}$$

then we have

$$F(r,\boldsymbol{\omega}_1,\boldsymbol{\omega}_2) = \sum_{\mu\nu\chi} F'_{\mu\nu,\chi}(r,\theta_1,\theta_2)e^{-i\chi\phi_{12}}e^{-i\mu\psi_1}e^{-i\nu\psi_2} \tag{F.34}$$

which can be treated as a normal FFT of 3 dimensions.

f.4 TRANSFORM IN FIXED FRAME

Similarly, in the laboratory coordinate system

$$\Phi_{\mu\nu}^{mnl}(0,\mathbf{\Omega},\hat{\mathbf{r}}) = \sum_{\eta} \begin{pmatrix} m & n & l \\ \mu & \eta & -\mu-\eta \end{pmatrix} f^m f^n R_{\eta,\nu}^{n}(\mathbf{\Omega}) R_{-\mu-\eta,0}^{l}(\hat{\mathbf{r}}) \tag{F.35}$$

The rotational invariant does not take advantage of the χ transform as $\mu \neq 0$. The expansion on rotational invariants should be calculated directly.

Expansion of $F(\mathbf{r},\mathbf{\Omega})$ on rotational invariants

The total equation of the forward transform is:

$$F_{\mu\nu}^{mnl}(r) = f^m f^n \sum_{\eta} \begin{pmatrix} m & n & l \\ \mu & \eta & -\mu-\eta \end{pmatrix} \int \mathrm{d}\hat{\mathbf{r}} R_{-\mu-\eta,0}^{l*}(\hat{\mathbf{r}}) \int \mathrm{d}\mathbf{\Omega} F(r,\hat{\mathbf{r}},\mathbf{\Omega}) R_{\eta,\nu}^{n*}(\mathbf{\Omega}) \tag{F.36}$$

Firstly, the FGSHT is performed:

$$F_{\eta\nu}^{n}(\mathbf{r}) = \int \mathrm{d}\mathbf{\Omega} f^n F(\mathbf{r},\mathbf{\Omega}) R_{\eta,\nu}^{n*}(\mathbf{\Omega}) \tag{F.37}$$

Then the spherical harmonic transform by histogram should give

$$F_{\eta\nu,\lambda}^{nl}(r) = \int \mathrm{d}\hat{\mathbf{r}} R_{\lambda 0}^{l*}(\hat{\mathbf{r}}) F_{\eta\nu}^{n}(r,\hat{\mathbf{r}}) \tag{F.38}$$

As $F_{\eta\nu}^{n}(\mathbf{r})$ values are tabulated in the Cartesian grid, we cannot use a quadrature approach without interpolation, so the histogram approach is used.

Histogram for a function f gives:

$$\overline{f}(r) = \int \mathrm{d}\theta_r \mathrm{d}\phi_r f(x,y,z) \tag{F.39}$$

so if we want to compute

$$\overline{F}(r) = \int \mathrm{d}\theta_r \mathrm{d}\phi_r R_{\lambda 0}^{l*}(x,y,z) F(x,y,z) \tag{F.40}$$

we just need to propose

$$f(x,y,z) = R_{\lambda 0}^{l*}(x,y,z) F(x,y,z) \tag{F.41}$$

For complex numbers $F_{\eta\nu}^{n}(\mathbf{r})$, the real and imaginary parts can be calculated separately.

The rotational matrices $R_{\lambda 0}^{l*}(\mathbf{r})$ in Cartesian coordinate system can be pre-generated by recurrence as detailed in appendix G.

Finally, the combination of projections gives:

$$F_{\mu\nu}^{mnl}(r) = f^m \sum_{\eta} \begin{pmatrix} m & n & l \\ \mu & \eta & -\mu-\eta \end{pmatrix} F_{\eta\nu,-\mu-\eta}^{nl}(r) \tag{F.42}$$

Rebuilding of $F(\mathbf{r},\mathbf{\Omega})$ from projections

and the rebuilding of $F(\mathbf{r},\mathbf{\Omega})$ in a certain orientation is as simple as its definition

$$F(\mathbf{r},\mathbf{\Omega}) = \sum_{mnl\mu\nu} F_{\mu\nu}^{mnl}(r) f^m f^n \sum_{\eta} \begin{pmatrix} m & n & l \\ \mu & \eta & -\mu-\eta \end{pmatrix} R_{\eta\nu}^{n}(\mathbf{\Omega}) R_{-\mu-\eta,0}^{l}(\hat{\mathbf{r}}) \tag{F.43}$$

f.5 SYMMETRY

In IET and MDFT, the rotational invariants are used to describe the solvent. It possesses symmetric rules, introduced by the indistinguishability of the two particles, symmetry properties of the single particle, and its real number property as a physical quantity. Here we list all the symmetric rules concerning the 2-molecule system.

F.5.1 *Symmetric rules of $F(\boldsymbol{\omega}_1, \boldsymbol{\omega}_2)$ in intermolecular form*

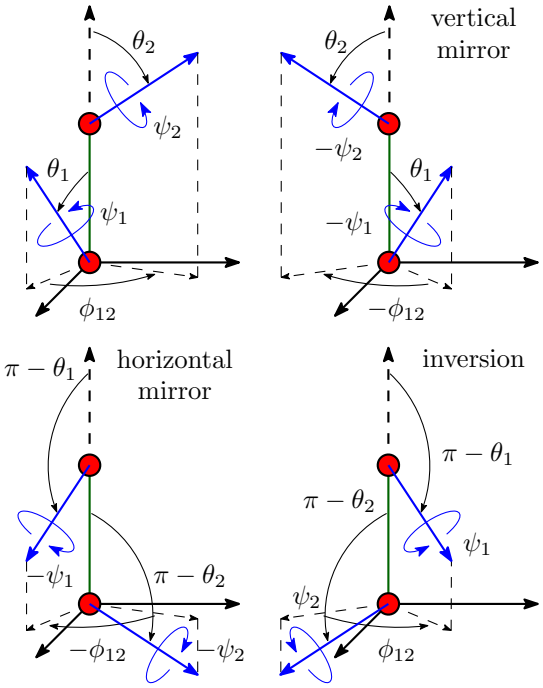

Figure F.1: Symmetry operations of a 2-molecule system

As shown in figure F.1, if a function in intermolecular coordinate system $F(\boldsymbol{\omega}_1, \boldsymbol{\omega}_2) \equiv F(\cos\theta_1, \cos\theta_2, \phi, \psi_1, \psi_2)$ is a physical quantity in r-space, it possesses symmetry rules:

1. Symmetry of vertical mirror (if the molecule possesses a vertical mirror v):

$$F(\theta_1, \theta_2, \phi, \psi_1, \psi_2) = F(\theta_1, \theta_2, -\phi, -\psi_1, -\psi_2) \tag{F.44}$$

2. Symmetry of inversion (if the molecules are interchangeable):

$$F(\theta_1, \theta_2, \phi, \psi_1, \psi_2) = F(\pi - \theta_2, \pi - \theta_1, \phi, \psi_2, \psi_1) \tag{F.45}$$

And an additive symmetric rule is owned by particles having

3. Symmetry axe C_2:

$$F(\theta_1, \theta_2, \phi, \psi_1, \psi_2) = F(\theta_1, \theta_2, \phi, \psi_1 + \pi, \psi_2 + \pi) \tag{F.46}$$

F.5.2 *Symmetric rules of rotational invariant projections*

We can deduce all the symmetries with the definition of $F(r, \boldsymbol{\omega}_1, \boldsymbol{\omega}_2) \Leftrightarrow F'^{mn}_{\mu\nu,\chi}(r)$ in eq. (F.26,F.27), $F^{mnl}_{\mu\nu} \Leftrightarrow F'^{mn}_{\mu\nu,\chi}$ in eq. (F.21,F.23), and the definition of Hankel transform:

$$\hat{F}^{mnl}_{\mu\nu}(k) = 4\pi i^l \int \mathrm{d}r\, r^2 j_l(kr) F^{mnl}_{\mu\nu}(r) \tag{F.47}$$

1. With the symmetry of GSH (eq. (H.12)) and the fact that $F(r, \boldsymbol{\omega}_1, \boldsymbol{\omega}_2)$ is real,

$$F'^{mn}_{\mu\nu,\chi}(r) = (-)^{\mu+\nu} F'^{mn*}_{\underline{\mu\nu},\underline{\chi}}(r) \tag{F.48}$$

$$F^{mnl}_{\mu\nu}(r) = (-)^{m+n+l+\mu+\nu} F^{mnl*}_{\underline{\mu\nu}}(r) \tag{F.49}$$

As the the spherical Bessel function $j_l(kr)$ is real and $\left(i^l\right)^* = (-)^l i^l$,

$$\hat{F}^{mnl}_{\mu\nu}(k) = (-)^{m+n+\mu+\nu} \hat{F}^{mnl*}_{\underline{\mu\nu}}(k) \tag{F.50}$$

Therefore

$$\hat{F}'^{mn}_{\mu\nu,\chi}(k) = (-)^{m+n+\mu+\nu} \hat{F}'^{mn*}_{\underline{\mu\nu},\chi}(k) \tag{F.51}$$

2. With the symmetry in eq. (F.45), which adapts to pure solvents, as well as the symmetry of GSH:

$$r^m_{\chi\mu}(\pi - \theta) = (-)^{m+\mu} r^m_{\underline{\chi}\mu}(\theta) \tag{F.52}$$

we can find

$$F'^{nm}_{\nu\mu,\chi}(r) = (-)^{m+n+\mu+\nu} F'^{mn}_{\mu\nu,\chi}(r) \tag{F.53}$$

$$F^{nml}_{\nu\mu}(r) = (-)^{m+n+\mu+\nu} F^{mnl}_{\mu\nu}(r) \tag{F.54}$$

Of course, if the particles 1 and 2 belong to two different species α and β, the term on the right refers to the PDF of $\alpha\beta$ and the one on the left refers to the PDF of $\beta\alpha$.

3. With C_{2v} symmetry as water, according to the C_2 symmetry, μ, ν is even; then as the molecule possesses a symmetry of vertical mirror v, with the symmetry in eq. (F.44),

$$F'^{mn}_{\mu\nu,\chi}(r) = F'^{mn*}_{\mu\nu,\chi}(r) \tag{F.55}$$

which implies that $F'^{mn}_{\mu\nu,\chi}(r)$ and $F^{mnl}_{\mu\nu}(r)$ are real, and according to eq. (F.47), $F^{mnl}_{\mu\nu}(k)$ is real if l is even, and pure imaginary if l is odd. According to Blum [16], we also have:

$$F^{mnl}_{\mu\nu}(r) = F^{mnl}_{\underline{\mu\nu}}(r) \tag{F.56}$$

$$F'^{mn}_{\mu\nu,\chi}(r) = F'^{mn}_{\underline{\mu\nu},\chi}(r) \tag{F.57}$$

And in k-space,

$$\hat{F}^{mnl}_{\mu\nu}(k) = (-)^l \hat{F}^{mnl*}_{\mu\nu}(k) \tag{F.58}$$

$$\hat{F}'^{mn}_{\mu\nu,\chi}(k) = (-)^{m+n} \hat{F}'^{mn*}_{\mu\nu,\underline{\chi}}(k) \tag{F.59}$$

G

Calculation of Rotation Matrix Elements $R^m_{\mu\mu'}$ by Recurrence

$\mathbf{R}^m(\mathbf{\Omega}) \equiv \left\{R^m_{\mu'\chi}(\mathbf{\Omega})\right\}$ is the rotation matrix of dimension $(2m+1)\times(2m+1)$, defined in Messiah and other books [13, 61, 90].

In MDFT, evaluation of $R^m_{\mu'\chi}(\hat{\mathbf{k}})$ for each m, μ', χ and $\mathbf{k}$ by its definition:

$$R^m_{\mu'\chi}(\hat{\mathbf{k}}) = r^m_{\mu'\chi}(\theta_k)e^{-i\mu'\phi_k} \tag{G.1}$$

is too costly to be done in iterations; on the other hand, to directly stock the value of every element is taxing in terms of memory. An algorithm of $R^m_{\mu\mu'}(\hat{\mathbf{k}})$ evaluation by recurrence described by Choi *et al.* [91] suggests an acceptable cost during the computation, by generating the rotation matrix elements from these of lower order to avoid extra calculation.

g.1 Case of $m_{\max} \leq 1$

According to the definition in eq. (G.1), it is easy to find

$$R^0_{00} = 1 \tag{G.2}$$

For $m = 1$, $\mathbf{R}^1(\hat{\mathbf{k}})$ depends only on the 3×3 orthogonal matrix $\mathbf{R}$ that defines the rotation from the basis vectors of laboratory frame to those of $\mathbf{k}$-frame:

$$\mathbf{R} = \begin{bmatrix} R_{xx} & R_{yx} & R_{zx} \\ R_{xy} & R_{yy} & R_{zy} \\ R_{xz} & R_{yz} & R_{zz} \end{bmatrix} = \begin{bmatrix} \cos\theta_k\cos\phi_k & -\sin\phi_k & \sin\theta_k\cos\phi_k \\ \cos\theta_k\sin\phi_k & \cos\phi_k & \sin\theta_k\sin\phi_k \\ -\sin\theta_k & 0 & \cos\theta_k \end{bmatrix} \tag{G.3}$$

The matrix $\mathbf{R}$ can be calculated by the cross products of basis vectors as shown in figure 6.3

$$\begin{bmatrix} \mathbf{e}''_1 & \mathbf{e}'_2 & \mathbf{e}''_3 \end{bmatrix} = \begin{bmatrix} \mathbf{e}_1 & \mathbf{e}_2 & \mathbf{e}_3 \end{bmatrix} \mathbf{R} = \mathbf{R} \tag{G.4}$$

The rotation matrix $\mathbf{R}^m$ can be separated into the real $\mathbf{F}^m$ and imaginary $\mathbf{G}^m$ parts, which can be given by the relations

$$R^m_{\chi\chi'} = F^m_{\chi\chi'} + iG^m_{\chi\chi'} \tag{G.5}$$

$$\begin{bmatrix} F^1_{\underline{1}\underline{1}} & F^1_{\underline{1}0} & F^1_{\underline{1}1} \\ F^1_{0\underline{1}} & F^1_{00} & F^1_{01} \\ F^1_{1\underline{1}} & F^1_{10} & F^1_{11} \end{bmatrix} = \begin{bmatrix} (R_{yy}+R_{xx})/2 & R_{xz}/\sqrt{2} & (R_{yy}-R_{xx})/2 \\ R_{zx}/\sqrt{2} & R_{zz} & -R_{zx}/\sqrt{2} \\ (R_{yy}-R_{xx})/2 & -R_{xz}/\sqrt{2} & (R_{yy}+R_{xx})/2 \end{bmatrix} \tag{G.6}$$

$$\begin{bmatrix} G^1_{\underline{1}\underline{1}} & G^1_{\underline{1}0} & G^1_{\underline{1}1} \\ G^1_{0\underline{1}} & G^1_{00} & G^1_{01} \\ G^1_{1\underline{1}} & G^1_{10} & G^1_{11} \end{bmatrix} = \begin{bmatrix} (R_{yx}-R_{xy})/2 & R_{yz}/\sqrt{2} & -(R_{yx}+R_{xy})/2 \\ -R_{zy}/\sqrt{2} & 0 & -R_{zy}/\sqrt{2} \\ (R_{yx}+R_{xy})/2 & R_{yz}/\sqrt{2} & (R_{xy}-R_{yx})/2 \end{bmatrix} \tag{G.7}$$

g.2 CASE OF $m_{\max} > 1$

Recurrence relation for $-m+1 \leq \chi' \leq m-1$

The recurrence relation for $-m \leq \chi \leq m$, $-m+1 \leq \chi' \leq m-1$ between matrix elements is:

$$R^m_{\chi\chi'} = a^m_{\chi\chi'} R^1_{00} R^{m-1}_{\chi\chi'} + b^m_{\chi\chi'} R^1_{10} R^{m-1}_{\chi-1,\chi'} + b^m_{-\chi,\chi'} R^1_{-1,0} R^{m-1}_{\chi+1,\chi'} \tag{G.8}$$

where

$$\begin{aligned} a^m_{\chi\chi'} &= \left[\frac{(m+\chi)\,(m-\chi)}{(m+\chi')\,(m-\chi')}\right]^{\frac{1}{2}} \qquad (-m+1 \leq \chi \leq m-1) \\ b^m_{\chi\chi'} &= \left[\frac{(m+\chi)\,(m+\chi-1)}{2\,(m+\chi')\,(m-\chi')}\right]^{\frac{1}{2}} \qquad (-m+2 \leq \chi \leq m-2) \end{aligned} \tag{G.9}$$

To separate the real and imaginary parts, suppose

$$H^m_{\chi\chi'}(i,j) = F^1_{ij} F^{m-1}_{\chi\chi'} - G^1_{ij} G^{m-1}_{\chi\chi'} \tag{G.10}$$

$$K^m_{\chi\chi'}(i,j) = F^1_{ij} G^{m-1}_{\chi\chi'} + G^1_{ij} F^{m-1}_{\chi\chi'} \tag{G.11}$$

therefore

$$F^m_{\chi\chi'} = a^m_{\chi\chi'} H^m_{\chi\chi'}(0,0) + b^m_{\chi\chi'} H^m_{\chi-1,\chi'}(1,0) + b^m_{-\chi,\chi'} H^m_{\chi+1,\chi'}(-1,0) \tag{G.12}$$

$$G^m_{\chi\chi'} = a^m_{\chi\chi'} K^m_{\chi\chi'}(0,0) + b^m_{\chi\chi'} K^m_{\chi-1,\chi'}(1,0) + b^m_{-\chi,\chi'} K^m_{\chi+1,\chi'}(-1,0) \tag{G.13}$$

In the case of $\chi = \pm m$, certain terms in eq. (G.8) are out of definition. They are supposed to be zero. Another way is to suppose that

$$\begin{aligned} a^m_{\chi\chi'} &= 0 \quad \text{for } \chi = \pm m \\ b^m_{\chi\chi'} &= 0 \quad \text{for } \chi = \pm m \text{ and } \chi = \mp(m-1) \end{aligned} \tag{G.14}$$

Recurrence relation for $-m+2 \leq \chi' \leq m$

For the case $\chi' = \pm m$ that are not covered in eq. (G.8), another recurrence relation supposes that:

$$R^m_{\chi\chi'} = c^m_{\chi\chi'} R^1_{0,1} R^{m-1}_{\chi,\chi'-1} + d^m_{\chi\chi'} R^1_{1,1} R^{m-1}_{\chi-1,\chi'-1} + d^m_{-\chi,\chi'} R^1_{-1,1} R^{m-1}_{\chi+1,\chi'-1} \tag{G.15}$$

$$F^m_{\chi\chi'} = c^m_{\chi\chi'} H^m_{\chi,\chi'-1}(0,1) + d^m_{\chi\chi'} H^m_{\chi-1,\chi'-1}(1,1) + d^m_{-\chi,\chi'} H^m_{\chi+1,\chi'-1}(-1,1) \tag{G.16}$$

$$G^m_{\chi\chi'} = c^m_{\chi\chi'} K^m_{\chi,\chi'-1}(0,1) + d^m_{\chi\chi'} K^m_{\chi-1,\chi'-1}(1,1) + d^m_{-\chi,\chi'} K^m_{\chi+1,\chi'-1}(-1,1) \tag{G.17}$$

with

$$\begin{aligned} c^m_{\chi\chi'} &= \left[\frac{2\,(m+\chi)\,(m-\chi)}{(m+\chi')\,(m+\chi'-1)}\right]^{\frac{1}{2}} \qquad (-m+1 \leq \chi \leq m-1) \\ d^m_{\chi\chi'} &= \left[\frac{(m+\chi)\,(m+\chi-1)}{(m+\chi')\,(m+\chi'-1)}\right]^{\frac{1}{2}} \qquad (-m+2 \leq \chi \leq m-2) \end{aligned} \tag{G.18}$$

and

$$\begin{aligned} c^m_{\chi\chi'} &= 0 \quad \text{for } \chi = \pm m \\ d^m_{\chi\chi'} &= 0 \quad \text{for } \chi = \pm m \text{ and } \chi = \mp(m-1) \end{aligned} \tag{G.19}$$

which is available for $-m+2 \leq \chi' \leq m$.

Symmetries

The symmetries of $R^m_{\chi\chi'}$ allow us to calculate only half of the elements:

$$R^l_{\underline{mm'}} = (-1)^{m+m'} R^{l*}_{mm'} \tag{G.20}$$

which gives

$$F^l_{\underline{mm'}} = (-1)^{m+m'} F^l_{mm'} \tag{G.21}$$

$$G^l_{\underline{mm'}} = -(-1)^{m+m'} G^l_{mm'} \tag{G.22}$$

H

Properties of Wigner 3j-Symbol and GSH

The properties of Wigner 3j-symbol and Wigner generalized spherical harmonics (GSH, Wigner D-symbol) play a huge role in the reduction of molecular Ornstein-Zernike equation as well as finding the relation between rotational invariant projections. Their main properties, presented in Messiah [61], Gray & Gubbins [13] and Edmonds [90], are listed here.

h.1 properties of wigner 3j-symbol

Wigner 3j-symbols are equivalent to Clebsch-Gordon (CG) coefficients multiplied by the phase factor:

$$\begin{pmatrix} m & n & l \\ \mu & \nu & -\lambda \end{pmatrix} = \frac{(-)^{m-n+\lambda}}{\sqrt{2l+1}} < mn\mu\nu \mid l\lambda > \tag{H.1}$$

and can be calculated with the Racah formula [61].

Reality

The 3j-symbols are real.

$$\begin{pmatrix} m & n & l \\ \mu & \nu & \lambda \end{pmatrix} = \begin{pmatrix} m & n & l \\ \mu & \nu & \lambda \end{pmatrix}^* \tag{H.2}$$

Selection rules

$$\begin{pmatrix} m & n & l \\ \mu & \nu & \lambda \end{pmatrix} = 0 \text{ if } \begin{cases} \mu+\nu+\lambda = 0 \\ |m-n| < l < m+n \\ \text{(triangular inequalities)} \end{cases} \text{ are not meet.} \tag{H.3}$$

Permutation

1. Even permutation

$$\begin{pmatrix} m & n & l \\ \mu & \nu & \lambda \end{pmatrix} = \begin{pmatrix} n & l & m \\ \nu & \lambda & \mu \end{pmatrix} = \begin{pmatrix} l & m & n \\ \lambda & \mu & \nu \end{pmatrix} \tag{H.4}$$

2. Odd permutation

$$\begin{aligned} (-)^{m+n+l} \begin{pmatrix} m & n & l \\ \mu & \nu & \lambda \end{pmatrix} &= \begin{pmatrix} n & m & l \\ \nu & \mu & \lambda \end{pmatrix} \\ = \begin{pmatrix} m & l & n \\ \mu & \lambda & \nu \end{pmatrix} &= \begin{pmatrix} l & n & m \\ \lambda & \nu & \mu \end{pmatrix} \end{aligned} \tag{H.5}$$

3. Simultaneous change of signs of μ, ν and λ

$$\begin{pmatrix} m & n & l \\ \mu & \nu & \lambda \end{pmatrix} = (-)^{m+n+l} \begin{pmatrix} m & n & l \\ -\mu & -\nu & -\lambda \end{pmatrix} \tag{H.6}$$

Orthogonality

$$\sum_{l=|m-n|}^{m+n} \sum_{\lambda=-l}^{l} (2l+1) \begin{pmatrix} m & n & l \\ \mu & \nu & \lambda \end{pmatrix} \begin{pmatrix} m & n & l \\ \mu' & \nu' & \lambda \end{pmatrix} = \delta_{\mu\mu'}\delta_{\nu\nu'} \tag{H.7}$$

$$\sum_{\mu=-m}^{m} \sum_{\nu=-n}^{n} \begin{pmatrix} m & n & l \\ \mu & \nu & \lambda \end{pmatrix} \begin{pmatrix} m & n & l' \\ \mu & \nu & \lambda' \end{pmatrix} = (2l+1)^{-1} \delta_{ll'}\delta_{\lambda\lambda'} \tag{H.8}$$

h.2 PROPERTIES OF GSH

There are many different definitions of GSH given in lectures. Here we adopt the definition proposed by Messiah:

$$R^m_{\mu'\mu}(\phi\theta\psi) = e^{-i\mu'\phi} r^m_{\mu'\mu}(\theta) e^{-i\mu\psi} \tag{H.9}$$

where $r^m_{\mu\mu'}$ is the generalized Legendre polynomial (GLP), which is real, and can be evaluated using the Wigner formula:

$$\begin{aligned} r^m_{\mu'\mu}(\theta) \;=\; & \left[(m+\mu')!\,(m-\mu')!\,(m+\mu)!\,(m-\mu)!\right]^{\frac{1}{2}} \times \\ & \sum_i \frac{(-)^i\,(\cos\theta/2)^{2m+\mu'-\mu-2i}\,(\sin\theta/2)^{2i-\mu'+\mu}}{(m+\mu'-i)!\,(m-\mu-i)!\,i!\,(i-\mu'+\mu)!} \end{aligned} \tag{H.10}$$

Symmetries of $r^m_{\mu'\mu}(\theta)$

$$r^m_{\mu\mu'}(\theta) = (-)^{\mu'-\mu} r^m_{\mu'\mu}(\theta) \tag{H.11}$$

$$r^m_{\underline{\mu'\mu}}(\theta) = (-)^{\mu'-\mu}\, r^m_{\mu'\mu}(\theta) \tag{H.12}$$

$$r^m_{\mu'\mu}(\theta) = r^m_{\mu\mu'}(-\theta) \tag{H.13}$$

$$r^m_{\mu'\mu}(\theta+\pi) = (-)^{m+\mu} r^m_{\mu'\underline{\mu}}(\theta) \tag{H.14}$$

where $\underline{\mu} \equiv -\mu$.

Symmetries of $R^m_{\mu'\mu}(\phi\theta\psi)$

$$R^m_{\mu'\mu}(\phi\theta\psi) = (-)^{\mu'-\mu}\, R^{m*}_{\underline{\mu'\mu}}(\phi\theta\psi) \tag{H.15}$$

$$R^m_{\mu'\mu}(\phi\theta\psi) = (-)^{\mu'-\mu}\, R^{m*}_{\mu\mu'}(\phi\theta\psi) \tag{H.16}$$

$$R^m_{\mu'\mu}(\phi\theta\psi) = (-)^{m+\mu'} R^m_{\underline{\mu'}\mu}(-\phi,\theta+\pi,\psi) = (-)^{m+\mu} R^m_{\mu'\underline{\mu}}(\phi,\theta+\pi,-\psi) \tag{H.17}$$

Unitarity and orthogonality

$$\sum_{\mu'} R^m_{\mu'\mu}(\phi\theta\psi) R^{m*}_{\mu'\mu''}(\phi\theta\psi) = \delta_{\mu\mu''} \tag{H.18}$$

$$\sum_{\mu} R^m_{\mu'\mu}(\phi\theta\psi) R^{m*}_{\mu''\mu}(\phi\theta\psi) = \delta_{\mu'\mu''} \tag{H.19}$$

$$\sum_{m\mu'\mu} R^m_{\mu'\mu}(\phi\theta\psi) R^{m*}_{\mu'\mu'}(\phi'\theta'\psi') = \delta_{\phi\phi'}\delta_{\theta\theta'}\delta_{\psi\psi'} \tag{H.20}$$

$$\frac{1}{8\pi^2}\int \mathrm{d}\cos\theta \mathrm{d}\phi \mathrm{d}\psi R^m_{\mu'\mu}(\phi\theta\psi) R^{n*}_{\nu'\nu}(\phi\theta\psi) = \frac{\delta_{mn}\delta_{\mu'\nu'}\delta_{\mu\nu}}{2n+1} \tag{H.21}$$

$r^m_{\mu'\mu}(\theta)$ *in terms of* $\cos\theta$ *and* $\sin\theta$

1. If $(-)^{\mu'+\mu} = +1$, $r^m_{\mu'\mu}(\theta)$ is a polynomial of degree m in $\cos\theta$.
2. If $(-)^{\mu'+\mu} = -1$, $r^m_{\mu'\mu}(\theta)/\sin\theta$ is a polynomial of degree $(m-1)$ in $\cos\theta$.

Rotation and product

$$R^m_{\mu'\mu}(\boldsymbol{\omega}) = \sum_{\chi} R^m_{\mu'\chi}(\boldsymbol{\omega_2}) R^m_{\chi\mu}(\boldsymbol{\omega_1}) \tag{H.22}$$

where $\boldsymbol{\omega}$ is the result of the successive application of $\boldsymbol{\omega}_1$ and $\boldsymbol{\omega_2}$ in order.

$$\begin{aligned} R^m_{\chi\mu}(\boldsymbol{\omega}) &= \sum_{\mu'} R^{m*}_{\mu'\chi}(\hat{\mathbf{k}}) R^m_{\mu'\mu}(\boldsymbol{\Omega}) \\ R^m_{\mu'\mu}(\boldsymbol{\Omega}) &= \sum_{\chi} R^{m*}_{\chi\mu'}(\hat{\mathbf{k}}^{-1}) R^m_{\chi\mu}(\boldsymbol{\omega}) = \sum_{\chi} R^m_{\mu'\chi}(\hat{\mathbf{k}}) R^m_{\chi\mu}(\boldsymbol{\omega}) \end{aligned} \tag{H.23}$$

Composition relation for GSHs

$$\sum_{\mu'\nu'\lambda'} \begin{pmatrix} m & n & l \\ \mu' & \nu' & \lambda' \end{pmatrix} R^m_{\mu'\mu}(\phi\theta\psi) R^n_{\nu'\nu}(\phi\theta\psi) R^l_{\lambda'\lambda}(\phi\theta\psi) = \begin{pmatrix} m & n & l \\ \mu & \nu & \lambda \end{pmatrix} \tag{H.24}$$

h.3 CONVENTION OF GSH

The convention of GSH in books and articles used in this thesis varies depending on the source. In Messiah [61] and Gray & Gubbins [13], it is defined as in eq. (H.9). In Edmonds [90], it is defined as:

$$D^m_{\mu'\mu}(\phi\theta\psi) = e^{i\mu'\psi} d^m_{\mu'\mu}(\theta) e^{i\mu\phi} \tag{H.25}$$

which can be seen as the inverse rotation matrix of $R^m_{\mu'\mu}$.

In Blum [16, 17], the equation

$$D^l_{m0}(\phi\theta\psi) = (-)^m \left(\frac{4\pi}{2l+1}\right)^{\frac{1}{2}} Y^l_m(\theta\phi) \tag{H.26}$$

is adopted, which means it shares the same definition as Edmonds, where

$$R^m_{\mu'\mu}(\phi\theta\psi) = D^{m*}_{\mu\mu'}(\phi\theta\psi) \tag{H.27}$$

In Fries & Patey [19], the definition of Messiah is used.

Bibliography

[1] Trenton H. Parsell, Meng-Yin Yang, and A. S. Borovik. "C-H Bond Cleavage with Reductants: Re-Investigating the Reactivity of Monomeric MnIII/IV-Oxo Complexes and the Role of Oxo Ligand Basicity." In: *Journal of the American Chemical Society* 131.8 (2009). PMID: 19196005, pp. 2762–2763. DOI: 10.1021/ja8100825 (cit. on pp. 1, 100).

[2] Sebastiao Formosinho and Monica Barroso, eds. *Proton-Coupled Electron Transfer. A Carrefour of Chemical Reactivity Traditions*. RSC Catalysis Series. The Royal Society of Chemistry, 2012, P001–157. DOI: 10.1039/9781849733168. URL: http://dx.doi.org/10.1039/9781849733168 (cit. on p. 1).

[3] GermanL Perlovich and Annette Bauer-Brandl. "Solvation of Drugs as a Key for Understanding Partitioning and Passive Transport Exemplified by NSAIDs." In: *Chemical Processes with Participation of Biological and Related Compounds*. CRC Press, 2008, pp. 291–325. DOI: doi:10.1201/b12241-9. URL: http://dx.doi.org/10.1201/b12241-9 (cit. on p. 1).

[4] German L. Perlovich, Tatyana V. Volkova, and Annette Bauer-Brandl. "Towards an understanding of the molecular mechanism of solvation of drug molecules: A thermodynamic approach by crystal lattice energy, sublimation, and solubility exemplified by paracetamol, acetanilide, and phenacetin." In: *Journal of Pharmaceutical Sciences* 95.10 (), pp. 2158–2169. DOI: 10.1002/jps.20674 (cit. on p. 1).

[5] Laura D. Hughes, David S. Palmer, Florian Nigsch, and John B. O. Mitchell. "Why are some properties more difficult to predict than others? A study of QSPR models of solubility, melting point, and Log P." In: *Journal of Chemical Information and Modeling* 48.1 (Jan. 2008), pp. 220–232. DOI: 10.1021/ci700307p (cit. on p. 1).

[6] A. D. Mcnaught and A. Wilkinson. *IUPAC. Compendium of Chemical Terminology, 2nd ed. (the "Gold Book")*. WileyBlackwell; 2nd Revised edition edition (cit. on p. 1).

[7] Frank Jensen. *Introduction to Computational Chemistry*. John Wiley & Sons, 2006 (cit. on pp. 1, 7–9).

[8] Christopher J. Cramer and Donald G. Truhlar. "Implicit Solvation Models: Equilibria, Structure, Spectra, and Dynamics." In: *Chemical Reviews* 99.8 (1999). PMID: 11849023, pp. 2161–2200. DOI: 10.1021/cr960149m (cit. on pp. 1, 7).

[9] Jacopo Tomasi and Maurizio Persico. "Molecular Interactions in Solution: An Overview of Methods Based on Continuous Distributions of the Solvent." In: *Chemical Reviews* 94.7 (1994), pp. 2027–2094. DOI: 10.1021/cr00031a013 (cit. on pp. 2, 7, 8).

[10] Jacopo Tomasi, Benedetta Mennucci, and Roberto Cammi. "Quantum Mechanical Continuum Solvation Models." In: *Chemical Reviews* 105.8 (2005), pp. 2999–3094. DOI: 10.1021/cr9904009 (cit. on pp. 2, 8).

[11] William L. Jorgensen and Julian Tirado-Rives. "Free energies of hydration for organic molecules from Monte Carlo simulations." In: *Perspectives in Drug Discovery and Design* 3.1 (1995), pp. 123–138. DOI: 10.1007/BF02174470 (cit. on p. 2).

[12] Jean-Pierre Hansen and Ian R. McDonald. *Theory of Simple Liquids*. Ed. by Jean-Pierre Hansen and Ian R. McDonald. Fourth Edition. Oxford: Academic Press, 2013 (cit. on pp. 2, 10, 16).

[13] C.G. Gray and K.E. Gubbins. *Theory of Molecular Fluids: I: Fundamentals*. International Series of Monographs on Chemistry. OUP Oxford, 1984. URL: http://books.google.de/books?id=3mz2RcnnMGwC (cit. on pp. 2, 7, 10, 13, 34, 109, 115, 116, 121, 124, 126).

[14] David Chandler and Hans C. Andersen. "Optimized Cluster Expansions for Classical Fluids. II. Theory of Molecular Liquids." In: *The Journal of Chemical Physics* 57.5 (1972), pp. 1930–1937. DOI: http://dx.doi.org/10.1063/1.1678513 (cit. on p. 2).

[15] Fumio Hirata, ed. *Molecular Theory of Solvation*. en. Vol. 24. Understanding Chemical Reactivity. Dordrecht: Kluwer Academic Publishers, 2004. URL: http://link.springer.com/10.1007/1-4020-2590-4 (visited on 08/10/2016) (cit. on pp. 3, 22).

[16] L. Blum and A. J. Torruella. "Invariant Expansion for Two-Body Correlations: Thermodynamic Functions, Scattering, and the Ornstein-Zernike Equation." In: *The Journal of Chemical Physics* 56.1 (1972), pp. 303–310. DOI: http://dx.doi.org/10.1063/1.1676864 (cit. on pp. 3, 25, 26, 37, 38, 45, 109, 114, 120, 126).

[17] L. Blum. "Invariant Expansion. II. The Ornstein Zernike-Equation for Nonspherical Molecules and an Extended Solution to the Mean Spherical Model." In: *The Journal of Chemical Physics* 57.5 (1972), pp. 1862–1869. DOI: http://dx.doi.org/10.1063/1.1678503 (cit. on pp. 3, 25, 38, 39, 110, 126).

[18] L. Blum. "Invariant expansion III: The general solution of the mean spherical model for neutral spheres with electostatic interactions." In: *The Journal of Chemical Physics* 58.8 (1973), p. 3295 (cit. on pp. 3, 25).

[19] P. H. Fries and G. N. Patey. "The solution of the hypernetted-chain approximation for fluids of nonspherical particles. A general method with application to dipolar hard spheres." In: *The Journal of Chemical Physics* 82.1 (Jan. 1985), pp. 429–440. DOI: doi:10.1063/1.448764. (Visited on 01/15/2013) (cit. on pp. 3, 25, 38, 114, 126).

[20] N. David Mermin. "Thermal Properties of the Inhomogeneous Electron Gas." In: *Physical Review* 137.5A (Mar. 1965), A1441–A1443. DOI: 10.1103/PhysRev.137.A1441. (Visited on 02/10/2014) (cit. on p. 3).

[21] R. Evans. "The nature of the liquid-vapour interface and other topics in the statistical mechanics of non-uniform, classical fluids." In: *Advances in Physics* 28.2 (1979), pp. 143–200. DOI: 10.1080/00018737900101365 (cit. on pp. 3, 16).

[22] J. P. Hansen. "Basic Statistical Theory of Liquids." In: *The Physics and Chemistry of Aqueous Ionic Solutions*. Ed. by M.-C Bellissent-Funel and G. W. Neilson. Dordrecht: Springer Netherlands, 1987, pp. 1–59. DOI: 10.1007/978-94-009-3911-0_1. URL: http://dx.doi.org/10.1007/978-94-009-3911-0_1 (cit. on p. 3).

[23] Lionel Gendre, Rosa Ramirez, and Daniel Borgis. "Classical density functional theory of solvation in molecular solvents: Angular grid implementation." In: *Chemical Physics Letters* 474.4-6 (June 2009), pp. 366–370. DOI: 10.1016/j.cplett.2009.04.077 (cit. on pp. 3, 28, 33).

[24] Guillaume Jeanmairet, Maximilien Levesque, Rodolphe Vuilleumier, and Daniel Borgis. "Molecular Density Functional Theory of Water." In: *The Journal of Physical Chemistry Letters* 4 (Jan. 2013), pp. 619–624. DOI: 10.1021/jz301956b (cit. on pp. 3, 28).

[25] Guillaume Jeanmairet, Maximilien Levesque, Volodymyr Sergiievskyi, and Daniel Borgis. "Molecular density functional theory for water with liquid-gas coexistence and correct pressure." In: *The Journal of Chemical Physics* 142.15 (Apr. 2015), p. 154112. DOI: 10.1063/1.4917485. (Visited on 04/17/2015) (cit. on pp. 3, 28).

[26] Guillaume Jeanmairet, Nicolas Levy, Maximilien Levesque, and Daniel Borgis. "Molecular density functional theory of water including density–polarization coupling." In: *Journal of Physics: Condensed Matter* 28.24 (June 2016), p. 244005. DOI: 10.1088/0953-8984/28/24/244005 (cit. on pp. 3, 28).

[27] Guillaume Jeanmairet. "A molecular density functional theory to study solvation in water." Theses. Université Pierre et Marie Curie - Paris VI, July 2014 (cit. on pp. 3, 28).

[28] Maximilien Levesque, Virginie Marry, Benjamin Rotenberg, Guillaume Jeanmairet, Rodolphe Vuilleumier, and Daniel Borgis. "Solvation of complex surfaces via molecular density functional theory." In: *The Journal of Chemical Physics* 137.22 (Dec. 2012), pp. 224107–224107–8. DOI: doi:10.1063/1.4769729. (Visited on 12/13/2012) (cit. on pp. 3, 28).

[29] Rosa Ramirez, Ralph Gebauer, Michel Mareschal, and Daniel Borgis. "Density functional theory of solvation in a polar solvent: Extracting the functional from homogeneous solvent simulations." In: *Physical Review E* 66.3 (2002), pp. 031206–031206–8. DOI: 10.1103/PhysRevE.66.031206 (cit. on pp. 3, 28).

[30] Rosa Ramirez and Daniel Borgis. "Density Functional Theory of Solvation and Its Relation to Implicit Solvent Models." In: *The Journal of Physical Chemistry B* 109.14 (2005), pp. 6754–6763. DOI: 10.1021/jp045453v. (Visited on 07/05/2010) (cit. on pp. 3, 28).

[31] Volodymyr P. Sergiievskyi, Guillaume Jeanmairet, Maximilien Levesque, and Daniel Borgis. "Fast Computation of Solvation Free Energies with Molecular Density Functional Theory: Thermodynamic-Ensemble Partial Molar Volume Corrections." In: *The Journal of Physical Chemistry Letters* 5.11 (2014), pp. 1935–1942. DOI: 10.1021/jz500428s (cit. on pp. 3, 28).

[32] Shuangliang Zhao, Rosa Ramirez, Rodolphe Vuilleumier, and Daniel Borgis. "Molecular density functional theory of solvation: From polar solvents to water." In: *The Journal of Chemical Physics* 134.19, 194102 (2011). DOI: http://dx.doi.org/10.1063/1.3589142 (cit. on pp. 3, 14, 28, 31, 33, 54, 85).

[33] Michiel Sprik and Michael L. Klein. "A polarizable model for water using distributed charge sites." In: *The Journal of Chemical Physics* 89.12 (1988), pp. 7556–7560. DOI: http://dx.doi.org/10.1063/1.455722 (cit. on p. 3).

[34] Liem X. Dang, Julia E. Rice, and Peter A. Kollman. "The effect of water models on the interaction of the sodium–chloride ion pair in water: Molecular dynamics simulations." In: *The Journal of Chemical Physics* 93.10 (1990), pp. 7528–7529. DOI: http://dx.doi.org/10.1063/1.459714 (cit. on p. 3).

[35] Kevin R Hadley and Clare McCabe. "Coarse-Grained Molecular Models of Water: A Review." In: *Molecular simulation* 38.8-9 (2012), pp. 671–681. DOI: 10.1080/08927022.2012.671942 (cit. on p. 7).

[36] B. Lee and F.M. Richards. "The interpretation of protein structures: Estimation of static accessibility." In: *Journal of Molecular Biology* 55.3 (1971), 379 –IN4. DOI: http://dx.doi.org/10.1016/0022-2836(71)90324-X (cit. on p. 8).

[37] Robert B. Hermann. "Theory of hydrophobic bonding. II. Correlation of hydrocarbon solubility in water with solvent cavity surface area." In: *The Journal of Physical Chemistry* 76.19 (1972), pp. 2754–2759. DOI: 10.1021/j100663a023 (cit. on p. 8).

[38] *Gaussian 09 keyword: SCRF*. 2014. URL: http://www.gaussian.com/g_tech/g_ur/k_scrf.htm (cit. on p. 8).

[39] MJ Holst. "The Poisson-Boltzmann Equation." In: () (cit. on pp. 8, 9).

[40] Benoit Roux and Thomas Simonson. "Implicit solvent models." In: *Biophysical Chemistry* 78.1–2 (Apr. 1999), pp. 1–20. DOI: 10.1016/S0301-4622(98)00226-9. (Visited on 04/29/2014) (cit. on p. 9).

[41] Massimo Marchi, Daniel Borgis, Nicolas Levy, and Pietro Ballone. "A dielectric continuum molecular dynamics method." In: *The Journal of Chemical Physics* 114.10 (2001), pp. 4377–4385. DOI: http://dx.doi.org/10.1063/1.1348028 (cit. on p. 9).

[42] Nicolas Levy, Daniel Borgis, and Massimo Marchi. "A dielectric continuum model of solvation for complex solutes." In: *Computer Physics Communications* 169.1–3 (2005). Proceedings of the Europhysics Conference on Computational Physics 2004CCP 2004Europhysics Conference on Computational Physics 2004, pp. 69 –74. DOI: http://dx.doi.org/10.1016/j.cpc.2005.03.018 (cit. on p. 9).

[43] J. Miyazaki, J. A. Barker, and G. M. Pound. "A new Monte Carlo method for calculating surface tension." In: *The Journal of Chemical Physics* 64.8 (1976), pp. 3364–3369. DOI: http://dx.doi.org/10.1063/1.432627 (cit. on p. 11).

[44] E.G.D. Cohen, R. Verberg, and I.M.de Schepper. "Viscosity and diffusion in hard-sphere-like colloidal suspensions." In: *Physica A: Statistical Mechanics and its Applications* 251.1–2 (1998), pp. 251 –265. DOI: http://dx.doi.org/10.1016/S0378-4371(97)00609-2. URL: http://www.sciencedirect.com/science/article/pii/S0378437197006092 (cit. on p. 11).

[45] Snehasis Chowdhuri, Ming-Liang Tan, and Toshiko Ichiye. "Dynamical properties of the soft sticky dipole-quadrupole-octupole water model: A molecular dynamics study." In: *The Journal of Chemical Physics* 125.14 (2006). DOI: http://dx.doi.org/10.1063/1.2357117 (cit. on p. 13).

[46] Martin Chaplin. *Water Model*. URL: http://www1.lsbu.ac.uk/water/water_models.html (cit. on p. 13).

[47] H. J. C. Berendsen, J. R. Grigera, and T. P. Straatsma. "The missing term in effective pair potentials." In: *The Journal of Physical Chemistry* 91.24 (1987), pp. 6269–6271. DOI: 10.1021/j100308a038 (cit. on pp. 13, 14, 47, 66, 90).

[48] H.J.C. Berendsen, J.P.M. Postma, W.F. van Gunsteren, and J. Hermans. "Interaction models for water in relation to protein hydration." In: *Intermolecular Forces*. Ed. by B. Pullman. D. Reidel, 1981, pp. 331–342 (cit. on p. 14).

[49] Pier Luigi Silvestrelli and Michele Parrinello. "Structural, electronic, and bonding properties of liquid water from first principles." In: *The Journal of Chemical Physics* 111.8 (1999), pp. 3572–3580. DOI: http://dx.doi.org/10.1063/1.479638 (cit. on p. 14).

[50] Steven W. Rick, Steven J. Stuart, and B. J. Berne. "Dynamical fluctuating charge force fields: Application to liquid water." In: *The Journal of Chemical Physics* 101.7 (1994), pp. 6141–6156. DOI: http://dx.doi.org/10.1063/1.468398 (cit. on p. 14).

[51] Jean-Pierre Hansen and Ian R. McDonald. "{CHAPTER} 6 - Perturbation Theories." In: *Theory of Simple Liquids (Second Edition)*. Ed. by Jean-Pierre Hansen and Ian R. McDonald. Second Edition. London: Academic Press, 1986, pp. 145 –192. DOI: http://dx.doi.org/10.1016/B978-0-08-057101-0.50010-X. URL: http://www.sciencedirect.com/science/article/pii/B978008057101050010X (cit. on p. 16).

[52] P. Tarazona and R. Evans. "A simple density functional theory for inhomogeneous liquids." In: *Molecular Physics* 52.4 (1984), pp. 847–857. DOI: 10.1080/00268978400101601 (cit. on p. 16).

[53] R. Evans. "Density Functionals in the Theory of Nonuniform Fluids." In: *Fundamentals of inhomogeneous fluids*. Ed. by Douglas. Henderson. Marcel Dekker, 1992 (cit. on p. 16).

[54] J.Z. Wu. "Density Functional Theory for Liquid Structure and Thermodynamics." In: *Molecular Thermodynamics of Complex Systems*. Ed. by Xiaohua Lu and Ying Hu. Berlin, Heidelberg: Springer Berlin Heidelberg, 2009, pp. 1–73. DOI: 10.1007/978-3-540-69116-7_1. URL: http://dx.doi.org/10.1007/978-3-540-69116-7_1 (cit. on p. 16).

[55] URL: https://en.wikipedia.org/wiki/Correlation_function (cit. on p. 18).

[56] Song-Ho Chong and Sihyun Ham. "Thermodynamic-Ensemble Independence of Solvation Free Energy." In: *Journal of Chemical Theory and Computation* 11.2 (2015), pp. 378–380. DOI: 10.1021/ct500876x (cit. on pp. 19, 86).

[57] Richard H. Byrd, Peihuang Lu, Jorge Nocedal, and Ciyou Zhu. "A Limited Memory Algorithm for Bound Constrained Optimization." In: *SIAM J. Sci. Comput.* 16.5 (Sept. 1995), pp. 1190–1208. DOI: 10.1137/0916069 (cit. on pp. 28, 56).

[58] Ciyou Zhu, Richard H. Byrd, Peihuang Lu, and Jorge Nocedal. "Algorithm 778: L-BFGS-B: Fortran subroutines for large-scale bound-constrained optimization." In: *ACM Transactions on Mathematical Software* 23.4 (Dec. 1997), pp. 550–560. DOI: 10.1145/279232.279236. (Visited on 06/09/2011) (cit. on pp. 28, 56).

[59] M. Frigo and S.G. Johnson. "The Design and Implementation of FFTW3." In: *Proceedings of the IEEE* 93.2 (2005), pp. 216–231. DOI: 10.1109/JPROC.2004.840301 (cit. on pp. 29, 44).

[60] Daniel Borgis, Lionel Gendre, and Rosa Ramirez. "Molecular Density Functional Theory: Application to Solvation and Electron-Transfer Thermodynamics in Polar Solvents." In: *The Journal of Physical Chemistry B* 116.8 (Mar. 2012), pp. 2504–2512. DOI: 10.1021/jp210817s (cit. on p. 33).

[61] Albert Messiah. *Quantum Mechanics*. Quantum Mechanics vol. 2. North-Holland, 1981. URL: https://books.google.fr/books?id=VR93vUk8d_8C (cit. on pp. 34, 109, 111, 114–116, 121, 124, 126).

[62] William H. Press, Saul A. Teukolsky, William T. Vetterling, and Brian P. Flannery. *Numerical Recipes 3rd Edition: The Art of Scientific Computing*. 3rd ed. New York, NY, USA: Cambridge University Press, 2007 (cit. on pp. 41, 77, 112).

[63] M. A. Kastenholz and Philippe H. Hünenberger. "Computation of methodology-independent ionic solvation free energies from molecular simulations. I. The electrostatic potential in molecular liquids." In: *The Journal of Chemical Physics* 124.12, 124106 (2006). DOI: http://dx.doi.org/10.1063/1.2172593 (cit. on pp. 47, 48).

[64] Mika A. Kastenholz and Philippe H. Hünenberger. "Computation of methodology-independent ionic solvation free energies from molecular simulations. II. The hydration free energy of the sodium cation." In: *The Journal of Chemical Physics* 124.22, 224501 (2006). DOI: http://dx.doi.org/10.1063/1.2201698 (cit. on p. 47).

[65] Philippe Hunenberger and Maria Reif. "Chapter 2 Fundamental Experimental Problems." In: *Single-Ion Solvation: Experimental and Theoretical Approaches to Elusive Thermodynamic Quantities*. The Royal Society of Chemistry, 2011, pp. 8–38. DOI: 10.1039/9781849732222-00008. URL: http://dx.doi.org/10.1039/9781849732222-00008 (cit. on p. 47).

[66] Peter G. Kusalik and Igor M. Svishchev. "The Spatial Structure in Liquid Water." In: *Science* 265.5176 (1994), pp. 1219–1221. DOI: 10.1126/science.265.5176.1219 (cit. on p. 47).

[67] B. R. A. Nijboer and Th. W. Ruijgrok. "On the energy per particle in three- and two-dimensional Wigner lattices." In: *Journal of Statistical Physics* 53.1 (), pp. 361–382. DOI: 10.1007/BF01011562 (cit. on p. 47).

[68] V.R. Saunders, C. Freyria-Fava, R. Dovesi, L. Salasco, and C. Roetti. "On the electrostatic potential in crystalline systems where the charge density is expanded in Gaussian functions." In: *Molecular Physics* 77.4 (1992), pp. 629–665. DOI: 10.1080/00268979200102671 (cit. on p. 48).

[69] Lorenzo Maschio, Bernard Kirtman, Roberto Orlando, and Michel Rèrat. "Ab initio analytical infrared intensities for periodic systems through a coupled perturbed Hartree-Fock/Kohn-Sham method." In: *The Journal of Chemical Physics* 137.20, 204113 (2012). DOI: http://dx.doi.org/10.1063/1.4767438 (cit. on p. 48).

[70] R E Raab and O L De Lange. *Multipole theory in electromagnetism: classical, quantum, and symmetry aspects, with applications*. International series of monographs on physics. Oxford: Clarendon Press, 2005. URL: https://cds.cern.ch/record/859649 (cit. on p. 48).

[71] Shuangliang Zhao, Honglai Liu, Rosa Ramirez, and Daniel Borgis. "Accurate evaluation of the angular-dependent direct correlation function of water." In: *The Journal of Chemical Physics* 139.3 (July 2013), pp. 034503–1–034503–10. DOI: doi:10.1063/1.4813400 (cit. on pp. 54, 55, 60, 104, 106).

[72] Joël Puibasset and Luc Belloni. "Bridge function for the dipolar fluid from simulation." In: *The Journal of Chemical Physics* 136.15 (Apr. 2012), p. 154503. DOI: doi:10.1063/1.4703899. (Visited on 10/14/2013) (cit. on pp. 54, 55, 60, 104–106).

[73] D. Asthagiri, Safir Merchant, and Lawrence R. Pratt. "Role of attractive methane-water interactions in the potential of mean force between methane molecules in water." In: *The Journal of Chemical Physics* 128.24 (2008), p. 244512. DOI: 10.1063/1.2944252 (cit. on p. 66).

[74] Luc Belloni and Ioulia Chikina. "Efficient full Newton–Raphson technique for the solution of molecular integral equations – example of the SPC/E water-like system." In: *Molecular Physics* 112.9-10 (May 2014), pp. 1246–1256. DOI: 10.1080/00268976.2014.885612 (cit. on p. 67).

[75] Jonathan G. Harris and Kwong H. Yung. "Carbon Dioxide's Liquid-Vapor Coexistence Curve And Critical Properties as Predicted by a Simple Molecular Model." In: *The Journal of Physical Chemistry* 99.31 (1995), pp. 12021–12024 (cit. on pp. 74, 90).

[76] Y. Boutard, Ph. Ungerer, J.M. Teuler, M.G. Ahunbay, S.F. Sabater, J. Pérez-Pellitero, A.D. Mackie, and E. Bourasseau. "Extension of the anisotropic united atoms intermolecular potential to amines, amides and alkanols: Application to the problems of the 2004 Fluid Simulation Challenge." In: *Fluid Phase Equilibria* 236.1–2 (2005). Fluid Properties Simulation Challenge Special Issue Section, pp. 25 – 41. DOI: http://dx.doi.org/10.1016/j.fluid.2005.06.009. URL: http://www.sciencedirect.com/science/article/pii/S0378381205001925 (cit. on pp. 74, 90).

[77] William L Briggs and Van E. Henson. *The DFT: An Owner's Manual for the Discrete Fourier Transform*. Philadelphia: Society for Industrial and Applied Mathematics, 1995 (cit. on p. 77).

[78] Maximilien Levesque, Rodolphe Vuilleumier, and Daniel Borgis. "Scalar fundamental measure theory for hard spheres in three dimensions: Application to hydrophobic solvation." In: *The Journal of Chemical Physics* 137.3 (July 2012) (cit. on p. 85).

[79] Dominik Horinek, Shavkat I. Mamatkulov, and Roland R. Netz. "Rational design of ion force fields based on thermodynamic solvation properties." In: *The Journal of Chemical Physics* 130.12 (Mar. 2009), p. 124507. DOI: 10.1063/1.3081142 (cit. on p. 87).

[80] Yizhak Marcus. "A simple empirical model describing the thermodynamics of hydration of ions of widely varying charges, sizes, and shapes." In: *Biophysical Chemistry* 51.2 (1994), pp. 111 –127. DOI: http://dx.doi.org/10.1016/0301-4622(94)00051-4. URL: http://www.sciencedirect.com/science/article/pii/0301462294000514 (cit. on p. 87).

[81] Richard M. Noyes. "Thermodynamics of Ion Hydration as a Measure of Effective Dielectric Properties of Water." In: *Journal of the American Chemical Society* 84.4 (1962), pp. 513–522 (cit. on p. 87).

[82] Michael D. Tissandier, Kenneth A. Cowen, Wan Yong Feng, Ellen Gundlach, Michael H. Cohen, Alan D. Earhart, James V. Coe, and Thomas R. Tuttle. "The Proton's Absolute Aqueous Enthalpy and Gibbs Free Energy of Solvation from Cluster-Ion Solvation Data." In: *J. Phys. Chem. A* 102.40 (1998), pp. 7787–7794. DOI: 10.1021/jp982638r (cit. on p. 87).

[83] Yizhak Marcus. "Ionic radii in aqueous solutions." In: *Chemical Reviews* 88.8 (1988), pp. 1475–1498 (cit. on p. 87).

[84] William L. Jorgensen, James M. Briggs, and M. Leonor. Contreras. "Relative partition coefficients for organic solutes from fluid simulations." In: *The Journal of Physical Chemistry* 94.4 (Feb. 1990), pp. 1683–1686. DOI: 10.1021/j100367a084 (cit. on p. 90).

[85] M. Diraison, G. J. Martyna, and M. E. Tuckerman. "Simulation studies of liquid ammonia by classical ab initio, classical, and path-integral molecular dynamics." In: *The Journal of Chemical Physics* 111.3 (1999), pp. 1096–1103 (cit. on p. 90).

[86] Christophe Chipot, Richard Jaffe, Bernard Maigret, David A. Pearlman, and Peter A. Kollman. "Benzene Dimer: A Good Model for pi-pi Interactions in Proteins? A Comparison between the Benzene and the Toluene Dimers in the Gas Phase and in an Aqueous Solution." In: *Journal of the American Chemical Society* 118.45 (1996), pp. 11217–11224 (cit. on p. 90).

[87] Thorsten Schnabel, Anupam Srivastava, Jadran Vrabec, and Hans Hasse. "Hydrogen Bonding of Methanol in Supercritical CO2: Comparison between 1H NMR Spectroscopic Data and Molecular Simulation Results." In: *The Journal of Physical Chemistry B* 111.33 (2007), pp. 9871–9878 (cit. on p. 90).

[88] J. L. F. Abascal and C. Vega. "A general purpose model for the condensed phases of water: TIP4P/2005." In: *The Journal of Chemical Physics* 123.23 (2005) (cit. on p. 90).

[89] Peter Gács and László Lovász. *Complexity of Algorithms*. Lecture Notes. 1999 (cit. on p. 103).

[90] A. R. Edmonds. *Angular Momentum in Quantum Mechanics*. 1960 (cit. on pp. 114–116, 121, 124, 126).

[91] Cheol Ho Choi, Joseph Ivanic, Mark S. Gordon, and Klaus Ruedenberg. "Rapid and stable determination of rotation matrices between spherical harmonics by direct recursion." In: *The Journal of Chemical Physics* 111.19 (1999), pp. 8825–8831. DOI: http://dx.doi.org/10.1063/1.480229 (cit. on p. 121).

Université Paris-Saclay
Espace Technologique / Immeuble Discovery
Route de l'Orme aux Merisiers RD 128 / 91190 Saint-Aubin, France

université PARIS-SACLAY | ÉCOLE DOCTORALE INTERFACES Approches Interdisciplinaires : Fondements, Applications et Innovation

Titre : Théorie de la fonctionnelle de la densité moléculaire sous l'approximation du fluide de référence homogène

Mots clés : fonctionnelle densité classique, solvatation, hypernetted-chain, équations intégrales

Résumé : Les propriétés de solvatation jouent un rôle important dans les problèmes chimiques et biochimiques. La théorie fonctionnelle de la densité moléculaire (MDFT) est l'une des méthodes frontières pour évaluer ces propriétés, dans laquelle une fonction d'énergie libre de solvatation est minimisée pour un soluté arbitraire dans une boîte de solvant cubique périodique. Dans cette thèse, nous travaillons sur l'évaluation du terme d'excès de la fonctionnelle d'énergie libre sous l'approximation du fluide de référence homogène (HRF), équivalent à l'approximation de la chaîne hypernettée (HNC) dans la théorie des équations intégrales. Deux algorithmes sont proposés: le premier est une extension d'un algorithme précédent, qui permet de traiter le cas d'un solvant moléculaire à trois dimensions (en fonction de trois angles d'Euler) au lieu d'un solvant linéaire (selon deux angles); L'autre est un nouvel algorithme qui intègre le traitement de la convolution angulaire de l'équation Ornstein-Zernike (OZ) moléculaire dans MDFT, et en fait développe la densité du solvant et le gradient fonctionnel en harmoniques sphériques généralisées (GSHs). On montre que le nouvel algorithme est beaucoup plus rapide que le précédent. Les deux algorithmes sont appropriés pour des solutés arbitraires tridimensionnel dans l'eau liquide, et pour prédire l'énergie libre et la structure de solvatation d'ions et de molécules.

Title : Molecular Density Functional Theory under homogeneous reference fluid approximation

Keywords : Classical density functional theory, solvation, hypernetted-chain, integral equations

Abstract : Solvation properties play an important role in chemical and bio-chemical issues. The molecular density functional theory (MDFT) is one of the frontier numerical methods to evaluate these properties, in which the solvation free energy functional is minimized for an arbitrary solute in a periodic cubic solvent box. In this thesis, we work on the evaluation of the excess term of the free energy functional under the homogeneous reference fluid (HRF) approximation, which is equivalent to hypernetted-chain (HNC) approximation in integral equation theory. Two algorithms are proposed: the first one is an extension of a previously implemented algorithm, which makes it possible to handle full 3D molecular solvent (depending on three Euler angles) instead of linear solvent (depending on two angles); the other one is a new algorithm that integrates the molecular Ornstein-Zernike (OZ) equation treatment of angular convolution into MDFT, which in fact expands the solvent density and the functional gradient on generalized spherical harmonics (GSHs). It is shown that the new algorithm is much more rapid than the previous one. Both algorithms are suitable for arbitrary three-dimensional solute in liquid water, and are able to predict the solvation free energy and structure of ions and molecules.

Université Paris-Saclay
Espace Technologique / Immeuble Discovery
Route de l'Orme aux Merisiers RD 128 / 91190 Saint-Aubin, France